

# Multimodality Imaging of Tumour Pathophysiology and Response to Pharmacological Intervention

Sean Peter Johnson

Submitted for the degree of Doctor of Philosophy in  
Oncology

Cancer Institute, University College London, September  
2014

# Declaration

---

I, Sean Peter Johnson, confirm that the work presented in this thesis is my own. Any work conducted by others or in collaboration with myself is clearly stated in this thesis. When information has been derived from other sources I confirm that this has been indicated in the thesis. This thesis represents work conducted by myself at the University College London Cancer Institute and University College London Centre for Advanced Biomedical Research between the dates of September 2009 and September 2014.

Sean Peter Johnson, September 2014

# Abstract

---

This thesis describes the need for imaging the tumour pathophysiological microenvironment in order to understand response to treatment. Specifically looking at tumour vascularisation in *in vivo* murine xenograft models of disease, response to treatment with vascular disruption is assessed via photoacoustic tomography (PAT) and magnetic resonance imaging (MRI).

Photoacoustic imaging is a novel imaging modality based on the detection of ultrasound waves created by the absorption of nano-second pulsed laser energy within tissue chromophores. It has the spectral specificity of optical techniques whilst also achieving the high resolution of ultrasound. Haemoglobin is the main chromophore found in biological tissue and this modality is therefore ideally suited to imaging tumour vascularisation. Using a Fabry-Perot interferometer this thesis demonstrates for the first time the feasibility of using PAT for pre-clinical research and the characterisation of typical tumour vascular features in a non-invasive non-ionising manner. Response to different concentrations of a vascular disrupting drug is then demonstrated, with novel insights in to how tumours recover from vascular damage observed.

MRI of response to vascular disruption is also presented. As MRI is widely used in the clinic it can serve as a translational tool of novel imaging biomarkers, and serves to further understand the differences in response of pathologically vascularised of tumours. This thesis looks at markers associated with disruption of haemodynamics, using apparent diffusion (ADC) to elucidate onset of necrosis, increase in haemoglobin concentration ( $R2^*$ ) as indication of impaired flow, and arterial spin labelling (ASL) as a marker of tumour blood perfusion. This is shown in both subcutaneous and clinically relevant liver metastasis models.

Taken as whole, the results from this thesis indicate that whilst understanding the response of the tumour vasculature to pharmacological intervention is complex, novel imaging techniques can provide invaluable translational information on the pathophysiology of tumours.

# Acknowledgements

---

I would first of all like to thank my supervisor Professor Barbara Pedley for taking me on as a student and guiding me through my PhD; your time was given freely and your advice much appreciated, and for that I am truly grateful. To everyone else at the Cancer Institute; Vineeth Rajkumar, Vessela Vassileva, Geoff Boxer, Seckou Diocou, Mathew Robson, Mario Mazzantini, Uzma Qureshi, Rashid Mohammed, Amit Jathoul and Annette Magnussen, many thanks for all your help over the years, your patience in explaining and demonstrating techniques, and the many discussions we have had, without which this work would not have been possible.

To my friends and colleagues at the UCL Centre for Advanced Biomedical Imaging, especially Simon Walker-Samuel who supervised my imaging studies and work, but also Rajiv Ramasawmy and Miguel Gonçalves for their assistance in experiments and general amiability throughout my time at CABI. To CABI director Professor Mark Lythgoe and to all members past and present with which I have had the good fortune to work; Adam Badar, Tammy Kalber, Daniel Stuckey, Bernard Siow, Jack Wells, Niall Colgan, Simon Richardson, Niraj Patel, Isabel Christie, Adrienne Campbell-Washburn, and too many more to mention, thank you all for helping me shape my thoughts on molecular imaging and for sharing all the great work you do.

To the Photoacoustic Imaging group at UCL Medical Physics and Biomedical Engineering under Professor Paul Beard, I have eternal gratitude for sharing with me the wonders of photoacoustic imaging. Especial thanks to Jan Laufer, Olumide Ogunlade and Edward Zhang for helping me along with experiments, technical understanding and interpretation of experimental data.

And finally, I would like to acknowledge the help from my friends and family, and thank them for their unwavering support, their ability to take my mind away from academia when needed, and their faith in that all would be completed. In regards to this I would especially like to thank my girlfriend Katharina Schulz, whose love and understanding has helped me be able to finish this thesis.

# Publications resulting from this thesis

---

- **Johnson SP**, Ogunlade O, Zhang E, Laufer J, Rajkumar V, Pedley RB, Beard P (2014). Photoacoustic tomography of vascular therapy in a preclinical mouse model of colorectal carcinoma, *Proc. of SPIE*, Vol. 8943, paper 89431R.
- **S. P. Johnson**, O. Ogunlade, E. Zhang, J. Laufer, V. Rajkumar, S. Walker-Samuel, M. F. Lythgoe, R. B. Pedley and P. C. Beard (2013). Photoacoustic tomography assessment of vascular targeted therapy to determine vessel regrowth following treatment, *Proc. SPIE, ECBO 2013: Opto-Acoustic Methods and Applications* 8800.
- J. Laufer, **P. Johnson**, E. Zhang, B. Treeby, B. Cox, B. Pedley, and P. Beard (2012). In vivo preclinical photoacoustic imaging of tumor vasculature development and therapy, *J. Biomed. Opt.* 17, 056016.
- J. Laufer, **P. Johnson**, E. Zhang, B. Treeby, B. Cox, B. Pedley and P. Beard (2011). In vivo longitudinal photoacoustic imaging of subcutaneous tumours in mice, *Proc. SPIE*, Photons Plus Ultrasound: Imaging and Sensing 7899 .

# Table of contents

---

Declaration.....	1
Abstract.....	2
Acknowledgements.....	3
Publications resulting from this thesis.....	4
Table of contents .....	5
List of figures.....	11
Abbreviations.....	11
Chapter 1 Introduction .....	16
1.1 Introduction and scope of this thesis.....	16
1.2 Cancer biology.....	17
1.3 Tumour microenvironment.....	19
1.4 Tumour angiogenesis.....	20
1.5 Vascular targeted therapy .....	21
1.6 Colorectal cancer .....	22
1.7 Translational imaging.....	23
1.7.1 Magnetic resonance imaging.....	24
1.7.1.1 Basic principles of MRI imaging .....	25
1.7.2 Contrast enhance computed tomography.....	27
1.7.3 Ultrasound .....	27
1.7.4 Optical imaging .....	28
1.9 Hypothesis and aims of this thesis.....	28
1.10 References .....	30
Chapter 2 General materials & methodology.....	37
2.1 Introduction .....	37
2.2 Tissue culture .....	37
2.2.1 Equipment.....	37
2.2.1.1 Haemocytometer & Countess cell counter.....	37
2.2.1.2 Centrifuge .....	37
2.2.2 Techniques.....	38
2.2.2.1 Cell lines .....	38
2.2.2.2 Cell sub-culture .....	38
2.2.2.3 Frozen storage procedure.....	39

2.2.2.4 Preparation for in vivo work .....	39
2.3 Animal experiments .....	40
2.3.1 Animal handling .....	40
2.3.2 Pre-clinical tumour models .....	41
2.3.2.1 Subcutaneous tumour model .....	41
2.3.2.2 Orthotopic liver metastases model .....	41
2.4 In vivo imaging .....	43
2.4.1 Magnetic Resonance Imaging .....	43
2.4.2 Photoacoustic Imaging .....	43
2.4.3 Bioluminescence Imaging .....	44
2.5 Tissue collection .....	45
2.5.1 Formalin fixation of samples .....	45
2.5.2 Frozen storage of samples .....	45
2.5.3 Haematoxylin and eosin staining .....	46
2.5.4 Double fluorescence immunohistochemistry .....	46
2.5.5 Injected biological markers .....	47
2.5.5.1 Perfusion .....	47
2.5.5.2 Hypoxia .....	47
2.6 Microscopy .....	47
2.6.1 Brightfield .....	47
2.6.2 Fluorescence .....	47
2.7 References .....	48
Chapter 3 In vivo photoacoustic imaging of tumour pathophysiology .....	49
3.1 Introduction .....	49
3.1.1 The applicability of photoacoustic tomography for <i>in vivo</i> imaging .....	49
3.1.2 Photoacoustic effect .....	50
3.1.2.1 Laser principles .....	51
3.1.2.2 Interaction with tissue .....	52
3.1.2.3 Tissue chromophores .....	53
3.1.2.4 Physics of chromophore PA signal production .....	54
3.1.3 Advantages of PA tomography systems .....	55
3.1.4 Why it should be used for tumour pathophysiology .....	56
3.2 Methods .....	57
3.2.1 System design .....	57

3.2.1.1 PC controller .....	58
3.2.1.2 Laser excitation source .....	58
3.2.1.3 Planar sensor detection system .....	58
3.2.1.4 Interrogation laser .....	60
3.2.2 Signal acquisition and processing/DSO .....	61
3.2.3 Physiological monitoring .....	61
3.2.4 Experimental design .....	63
3.2.4.1 Initial PA scanner imaging capabilities .....	63
3.2.4.2 Inhalational gas experiments .....	63
3.2.4.3 In vivo imaging of tumours .....	64
3.3 Results .....	65
3.3.1 Ex vivo blood analysis .....	65
3.3.2 Typical reconstruction of normal tissue vasculature .....	66
3.3.3 In vivo effect of melanin .....	67
3.3.4 Inhalation oxygen content effect on PA scanning .....	70
3.3.5 Three dimensional imaging of subcutaneous tumours .....	72
3.3.6 Maximum depth imaged .....	73
3.3.7 Comparative pathological features of tumour vasculature .....	74
3.3.8 Development of tumours over time by PAT .....	76
3.3.9 Spectroscopic analysis of tumours in vivo .....	77
3.3.10 PA imaging of other organs .....	78
3.4 Discussion .....	79
3.4.1 PA can image structural haemoglobin in vivo .....	79
3.4.2 Melanin is a strong in vivo optical absorber .....	80
3.4.3 Blood oxygenation does not affect PA structural images .....	82
3.4.4 Subcutaneous tumours can be resolved in vivo with PAT .....	82
3.4.5 PAT can differentiate different tumour vascular pathophysiologies in vivo .....	83
3.4.6 In vivo spectroscopy can provide qualitative data on tumour oxygenation .....	85
3.4.7 Imaging of different organs and locations is difficult with PAT .....	85
3.5 Summary .....	86
3.6 References .....	86
Chapter 4 Photoacoustic imaging of vascular targeted therapy .....	89
4.1 Introduction .....	89
4.1.1 Assessing response of VDA drug efficacy .....	89



4.1.1.1 Vessel Angiography with MRI .....	89
4.1.1.2 Computed Tomography Angiography.....	90
4.1.1.3 Ultrasound .....	91
4.1.2 Potential of PAT for assessing vascular response to treatment .....	91
4.2 Methods.....	92
4.2.1 Drug treatment .....	92
4.2.2 Acute response to vascular disruption .....	92
4.2.3 Tumour blood vessel destruction .....	93
4.2.4 Vessel regrowth following vascular disruption.....	93
4.2.5 PAT for dose response of VDAs.....	94
4.3 Results.....	95
4.3.1 Acute Assessment of vascular disruption .....	95
4.3.2 Response to OXi4503 .....	96
4.3.3 Vessel regrowth following treatment.....	102
4.3.4 Effect of different OXi4503 doses can be observed in vivo by PAT .....	107
4.3.5 PA signal intensity corresponds to regrowth of tumours.....	111
4.4 Discussion.....	113
4.4.1 Destruction of tumour associated vasculature can be assessed by PAT .....	113
4.4.2 Internal tumour vasculature is required for outward growth of the tumour ....	115
4.4.3 Efficacy of vascular targeted treatment can be observed with PAT.....	116
4.5 Conclusion.....	117
4.6 References .....	120
Chapter 5 Magnetic resonance imaging parameters associated with tumour vascular pathophysiology.....	123
5.1 Introduction .....	123
5.1.1 MRI of tumour vasculature .....	123
5.1.1 Arterial spin labelling .....	124
5.2.2 Intrinsic susceptibility MRI.....	125
5.1.3 Diffusion weighted MRI .....	126
5.1.4 Hypothesis of vascular functional parameters in response to OXi4503.....	127
5.2 Methods.....	128
5.2.1 MRI pulse sequences .....	128
5.2.1.1 High resolution morphological sequence .....	128
5.2.1.2 Arterial spin labelling sequence.....	129

5.2.1.3 Intrinsic susceptibility sequence .....	129
5.2.1.4 Diffusion weighted imaging sequence .....	130
5.2.2 In vivo procedure .....	130
5.3 Results .....	131
5.3.1 High resolution and segmentation .....	131
5.3.2 ASL acute .....	132
5.3.3 R2* acute .....	133
5.3.4 ADC acute .....	135
5.3.5 Baseline vs 90min response .....	136
5.3.6 Longitudinal MRI assessment of response .....	137
5.4 Discussion .....	139
5.4.1 MRI Sequences function as predicted .....	139
5.4.2 Vascular shutdown can be observed using R2* and ADC .....	140
5.4.3 Longitudinal analysis .....	141
5.5 Conclusion .....	142
5.6 Reference List .....	143
Chapter 6 Functional MRI biomarkers of vascular disruption in a liver metastatic model of cancer .....	147
6.1 Introduction .....	147
6.2 Method .....	148
6.2.1 Validation of luciferase transduction .....	148
6.2.2 Characterisation of liver metastasis model .....	148
6.2.3 Functional assessment of response to vascular disruption .....	149
6.3 Results .....	150
6.3.1 Expression of luciferase activity .....	150
6.3.2 Development of orthotopic model .....	153
6.3.3 Monitoring of functional response within tumour deposits .....	155
6.3.4 Response of metastases to vascular disruption .....	157
6.3.5 Effect of tumour location .....	162
6.4 Discussion .....	165
6.4.1 Correct transduction of cells lines was achieved .....	165
6.4.2 Functional MRI biomarkers can be measured on individual tumour deposits .....	165
6.4.3 Effect of tumour location .....	167
6.4.4 Further work on hepatic ASL .....	168

6.5 References .....	170
Chapter 7 Conclusion .....	172
7.1 Vascular anatomy with photoacoustic tomography.....	172
7.1.1 Future PAT work.....	173
7.2 Translation of vascular associated MRI sequences.....	173
7.2.1 Future MRI work .....	175
7.3 Concluding remarks .....	176
I Appendix .....	177
I.I Cell growth kinetics.....	177
I.II Kinetics of luciferase activity.....	178
I.III Luciferase correlation to cell number .....	180
I.IV Lower limit of luciferase detection.....	182
I.V Subcutaneous growth comparison .....	184

# List of figures

---

<b>Figure 1.1</b>	Hallmarks of cancer	18
<b>Figure 1.2</b>	Nuclear magnetic spin in MRI	26
<b>Figure 3.1</b>	Imaging modality depth penetration and spatial resolution comparison	50
<b>Figure 3.2</b>	Light interaction with biological tissue	52
<b>Figure 3.3</b>	Absorption coefficient for tissue chromophores	53
<b>Figure 3.4</b>	Schematic of PAT Scanner set up	57
<b>Figure 3.5</b>	Reflectance characteristics of the Fabry-Perot Interferometer sensor	59
<b>Figure 3.6</b>	Phase biasing of the Fabry-Perot interferometer	60
<b>Figure 3.7</b>	Depiction of PA scanner and photoacoustic detection principle	62
<b>Figure 3.8</b>	Ex vivo PAT spectroscopy of whole blood	65
<b>Figure 3.9</b>	Typical reconstruction of PA vascular image	66
<b>Figure 3.10</b>	In vivo effect of melanin	68
<b>Figure 3.11</b>	In vivo effect of melanin on PA imaging at increasing wavelength	69
<b>Figure 3.12</b>	Effect of inhalational oxygen on PA image acquisition	71
<b>Figure 3.13</b>	3D PA imaging of subcutaneous tumours	72
<b>Figure 3.14</b>	Maximum PA depth imaging	73
<b>Figure 3.15</b>	Pathological features of tumours	75
<b>Figure 3.16</b>	Development of tumours over time by PAT	76
<b>Figure 3.17</b>	Spectroscopic analysis of tumours in vivo	77
<b>Figure 3.18</b>	PA imaging of other organs	78
<b>Figure 4.1</b>	Acute effect of vascular disruption with OXi4503 by PAT	95
<b>Figure 4.2</b>	Initial response to saline sham dose	97
<b>Figure 4.3</b>	Initial response to vascular disruption – SW1222	98
<b>Figure 4.4</b>	Histology of initial response – SW1222	99
<b>Figure 4.5</b>	Initial response to vascular disruption – LS174T	101
<b>Figure 4.6</b>	Histology of initial response – LS174T	102
<b>Figure 4.7</b>	Vessel regrowth following vascular disruption – SW1222	104
<b>Figure 4.8</b>	Vessel regrowth following vascular disruption – LS174T	105
<b>Figure 4.9</b>	Comparison of Tumour volume vs PA signal intensity	106
<b>Figure 4.10</b>	PAT assessment of different doses of OXi4503 – SW1222	108
<b>Figure 4.11</b>	PAT assessment of different doses of OXi4503 – LS174T	109
<b>Figure 4.12</b>	Histological assessment of different doses of OXi4503	110

<b>Figure 4.13</b>	Dose response to OXi4503 compared to PA signal	112
<b>Figure 5.1</b>	High resolution morphological MRI images & segmentation	131
<b>Figure 5.2</b>	Tumour perfusion maps	132
<b>Figure 5.3</b>	Acute measurement of R2*	134
<b>Figure 5.4</b>	Acute measurement of ADC	135
<b>Figure 5.5</b>	Spatial correlation of R2* and ADC values	136
<b>Figure 5.6</b>	Confirmation of longitudinal MRI feasibility	137
<b>Figure 5.7</b>	Longitudinal R2* and ADC measurements	138
<b>Figure 6.1</b>	Fluorescence activated cell sorting analysis of luciferase gene transduction	151
<b>Figure 6.2</b>	Bioluminescence monitoring of liver metastatic burden	152
<b>Figure 6.3</b>	Magnetic resonance monitoring of liver metastatic deposits	153
<b>Figure 6.4</b>	Segmentation of tumour deposits and total tumour burden	154
<b>Figure 6.5</b>	Mapping of functional MRI measurements on to tumour deposits	156
<b>Figure 6.6</b>	Functional response of tumour deposits – Sham dose	157
<b>Figure 6.7</b>	Functional response of tumour deposits – SW1222	158
<b>Figure 6.8</b>	Functional response of tumour deposits – LS174T	159
<b>Figure 6.9</b>	Baseline vs change correlation in perfusion	160
<b>Figure 6.10</b>	Baseline vs change correlation in R2*	161
<b>Figure 6.11</b>	Change in R2* vs change in perfusion	161
<b>Figure 6.12</b>	Histological assessment of multiple tumours within a liver section	162
<b>Figure 6.13</b>	Functional response of tumour deposits categorised by location	164
<b>Table I.I</b>	Viability of parental and luciferase transduced SW1222 cells	177
<b>Table I.II</b>	Viability of parental and luciferase transduced LS174T cells	177
<b>Figure I.I</b>	In vitro kinetics of luciferase activity	179
<b>Figure I.II</b>	In vitro correlation between cell number and luciferase activity	181
<b>Figure I.III</b>	In vitro lower limits of cell detection	183
<b>Figure I.IV</b>	In vivo subcutaneous average photon radiance	184
<b>Figure I.V</b>	In vivo growth comparison	185
<b>Figure I.VI</b>	In vivo growth comparison vs bioluminescence	186

# Abbreviations

---

<b>ADC</b>	Apparent diffusion coefficient
<b>AIA</b>	Angiogenesis inhibiting agent
<b>ANOVA</b>	Analysis of variance
<b>ASL</b>	Arterial spin labelling
<b>BOLD</b>	Blood oxygenation level dependent
<b>BSU</b>	Biological services unit
<b>CA1P</b>	Combretastatin A-1 Phosphate
<b>CA4P</b>	Combretastatin A-4 Phosphate
<b>CABI</b>	Centre for Advanced Biomedical Imaging
<b>CEUS</b>	Contrast-enhanced ultrasound
<b>CRC</b>	Colorectal carcinoma
<b>CT</b>	Computed tomography
<b>DCE</b>	Dynamic contrast-enhanced
<b>DMEM</b>	Dulbecco's modified eagles media
<b>DMSO</b>	Dimethylsulphoxide
<b>DMXAA</b>	Vadimezan, ASA404, vascular disrupting agent
<b>DNA</b>	Deoxyribonucleic acid
<b>DSO</b>	Digital storage oscilloscope
<b>DWI</b>	Diffusion weighted imaging
<b>EDTA</b>	Ethylenediaminetetraacetic acid
<b>EGF</b>	Epidermal growth factor
<b>FACS</b>	Fluorescence activated cell sorting
<b>FAIR</b>	Flow-alternating inversion recovery
<b>FBS</b>	Foetal bovine serum
<b>FGF</b>	Fibroblast growth factor

<b>FPI</b>	Fabry-Perot interferometer
<b>FSR</b>	Free spectral range
<b>i.v.</b>	Intravenous
<b>IDL</b>	Interactive data language
<b>IMS</b>	Industrial methylated spirits
<b>IS</b>	Intrinsic susceptibility
<b>ITF</b>	Interferometer transfer function
<b>IVC</b>	Individually ventilated cages
<b>MATLAB</b>	Matrix laboratory
<b>MIP</b>	Maximum intensity projection
<b>MR</b>	Magnetic resonance
<b>MRA</b>	Magnetic resonance angiography
<b>MRI</b>	Magnetic resonance imaging
<b>NK</b>	Natural killer
<b>NMR</b>	Nuclear magnetic resonance
<b>OCT</b>	Optical coherence tomography
<b>OPO</b>	Optical parametric oscillator
<b>OXi4503</b>	Combretastatin A-1 Phosphate, CA1P, vascular disrupting agent
<b>PA</b>	Photoacoustic
<b>PAI</b>	Photoacoustic imaging
<b>PAM</b>	Photoacoustic microscopy
<b>PAT</b>	Photoacoustic tomography
<b>PBS</b>	Phosphate buffered saline
<b>PCR</b>	Polymerase chain reaction
<b>PDGF</b>	Platelet derived growth factor
<b>PET</b>	Positron emission tomography
<b>PIL</b>	Personal individual licence

<b>PPL</b>	Procedure project licence
<b>RECIST</b>	Response evaluation criteria in solid tumours
<b>ROI</b>	Region of interest
<b>SPECT</b>	Single photon emission computed tomography
<b>TE</b>	Echo time
<b>TNM</b>	Tumour-node-metastasis
<b>TOF</b>	Time of flight
<b>TR</b>	Repetition time
<b>US</b>	Ultrasound
<b>VDA</b>	Vascular disrupting agent
<b>VEGF</b>	Vascular endothelial growth factor
<b>VEGFR</b>	Vascular endothelial growth factor receptor
<b>YAG</b>	Yttrium aluminium garnet



# Chapter 1 Introduction

---

## 1.1 Introduction and scope of this thesis

Cancer is often described in terms of a genetic disease (1, 2), although it is better considered as a group of inherently associated diseases that share a characteristic phenotype: uncontrolled cell growth and proliferation (3). Once a cell attains a cancerous pre-disposition the progression of the disease will be to spread to other parts of the body, a process known as metastasis, and develop into further solid tumour deposits. The major sites of metastasis are lung, liver, and bone, although there are many different metastatic locations, with primary tumours generally predisposed to form metastasis in certain target tissues (4); once cancer spreads to these organs it reduces their function by replacing functional cells with tumour tissue. Metastatic spread of disease is the main cause of mortality in patients with cancer, causing 90% of human cancer-related deaths (5). The latest global figures, for 2012, show that there were 14.1 million new cases of cancer diagnosed, 8.2 million cancer deaths, and 32.6 million people living with cancer that had been diagnosed within the previous 5 years (6). It is therefore an important clinical need and a highly active area of research, with much emphasis on development of new therapies with which to treat patients, and methods capable of assessing response of these therapies. Given the wide range of different types of cancer that can arise – each individual cell type in the human body can become cancerous – and the myriad of possible underlying genetic mutations that can give rise to a cancerous state, a common feature amongst tumours is often sought for targeting therapeutically. This is possible, as all cancers will possess certain characteristic pathological features, allowing treatment in relation to cancer biology without involving the specific genetic cause or cell origin. This thesis aims to demonstrate the therapeutic response to targeting one of these pathological characteristic features of cancer cells, namely angiogenesis and the vascular network in tumours. In order to do this the novel imaging modality ‘Photo-Acoustic Tomography’, and new vascular associated Magnetic Resonance Imaging scanning sequences, will be employed in pre-clinical models of disease, and their potential translation to human use shown. Therapeutic response will be assessed following vascular disruption with the Vascular Disrupting Agent (VDA) OXi4503 (combretastatin A1 di-phosphate /CA1P). A review of the cancer biology and pathophysiological target, the novel drugs used to treat the disease, and the imaging techniques employed, will first be reviewed in this introduction, followed by the original research conducted in to this area of oncology.

## 1.2 Cancer biology

Cancer can be considered as an evolutionary accumulation of genetic changes; mutations in genes or epigenetic regulation of gene expression which confers a growth advantage to a cell allow it to out-compete other cells and expand into a cancerous neoplasm. The causative genetic mutations can either be hereditary, known as germline mutations, or caused directly in the cells, known as somatic mutations, by carcinogens (7). The first described carcinogen was noted in 1775 by the London surgeon Sir Percival Pott (8), with the association between soot and testicular cancer in chimney sweeps. The progression of a cancerous neoplasm has long been thought of as a multistep sequence of cellular events, with various mutations required for tumourigenesis. Evidence that this is the case can be found in the fact that tumours are monoclonal, as a result of clonal expansion of the neoplastic cells (9, 10). Mutations affecting either oncogenes, genes that drive cell proliferation and increase the possibility of errors in genetic encoding, or tumour suppressor genes, genes that can halt the cellular cycle and cause apoptosis, will increase the chance of acquiring the necessary growth advantages needed for a cancer cell to progress to a tumour (11, 12). This progressive accumulation of genetic alterations in cells thus enables tumour growth and possible metastatic dissemination. Although this provides an underlying genetic profile of disease progression which should enable precise individually-tailored personalised therapy, the exact genetic mutations observed vary enormously, even within similar tumour types, and may not follow a sequential pathway to tumourigenesis. The mutations required for cancer progression can however also be classed according to the acquired capabilities or survival advantages conveyed to the cell. These capabilities were described as characteristic hallmarks of cancer in the seminal paper by Hanahan and Weinberg (13); knowledge of specific genetic alterations is therefore not required as such, but assumed as causative of hallmark abilities conferred to the cell that are common across all tumours. These hallmark abilities as originally set out are: the ability to sustain proliferative cellular signalling, evading the action of growth suppressors, enabling replicative immortality, activation of local tissue invasion and distant metastatic spread, the induction of blood vessels to supply the growing tumour via angiogenesis to supply oxygen and nutrients to the nascent tumour, and resisting cell death signals. An update of the hallmarks of cancer in 2011 (14) added two further hallmark characteristics of cancer biology, namely the avoidance of destruction by the immune system and deregulation of cellular energetics, and described two contributing 'enabling characteristics' of tumour formation in genome instability and tumour promoting inflammation. **Figure 1.1** shows an adaptation of the now iconic image of these 'Hallmarks

of cancer' (14). These reviews give great insight in to the genetic mutations of different cancers and how they can create the different hallmarks, showing the potential of genetically defined personalised medicine; on the other hand it also provides a framework in which to target tumours based on the acquired capabilities as a whole without knowing the genetic cause. As this thesis is concerned with imaging pathophysiology and response to treatment in order to enhance current translation of novel cancer therapies, the genetic aspect of cancer development, whilst acknowledged here, is not further discussed.

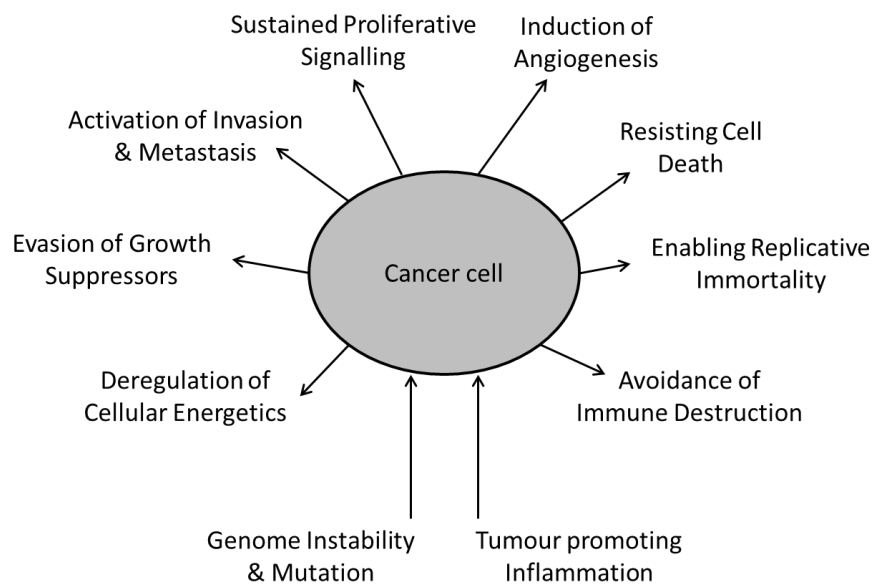


**Figure 1.1 Hallmarks of cancer**

The acquired capabilities of cancerous cells are depicted by the arrows leaving the 'Cancer cell', with the two enabling characteristic named outside and contributing to the formation of the cancer cell.

### **1.3 Tumour microenvironment**

The acquired capabilities of cancerous cells alone cannot fully explain the complexity of the developing tumour; of the  $\approx 10$  trillion cells in the human body, many may have acquired genetic mutations from exposure to radiation, oxidative stress and successive replication, and may have formed pre-cancerous micro-lesions. The reason why some of these and not others develop into tumours and advanced stage cancers is due, in large part, to the microenvironment of the surrounding tissue and associated non-malignant cells (15). The tumour microenvironment is an evolving concept that defines the behaviour of cancer not by the genetics of the cancer cells alone, but by the surrounding milieu that the tumour cells need for survival, growth, proliferation and metastasis. This microenvironment of non-cancerous cells can account for upwards of 50% of the total mass of primary and metastatic tumours. These can be divided into three main categories of stromal cell type: 1) infiltrating immune cells, consisting of macrophages, T and B lymphocytes, natural-killer NK and NKT cells, inflammatory monocytes, neutrophils, mast cells and platelets; 2) Cancer associated fibroblastic cells, consisting of activated fibroblasts, cancer associated adipocytes and mesenchymal stem cells; 3) angiogenic vascular cells, consisting of endothelial cells and pericytes (16). Other microenvironment components present are the malignant cells themselves, endothelial cells associated with lymphatics, dendritic cells, red blood cells, and the extracellular matrix (16). The interaction of this tumour microenvironment with the malignant cells influences the progression of the cancerous neoplasm, with often a tumour promoting effect due to growth factors such as platelet-derived (PDGF), vascular-endothelial (VEGF), fibroblast (FGF) and epidermal (EGF) (17, 18). Traditional chemotherapy and radiotherapy will affect all cells within the tumour microenvironment, with reaction of the tumour-associated cells also affecting outcome of treatment (19, 20). Targeting of the tumour microenvironment as well as the hallmark characteristics of tumours is therefore an attractive option, which could increase the action of chemotherapy drugs (21).

## 1.4 Tumour angiogenesis

Of the hallmarks of cancer as established by Hanahan and Weinberg, arguably the one of most clinical importance is angiogenesis. The angiogenic formation of new blood vessels is a normal biological process through which avascular tissues are supplied with blood flow. It has a physiological role in wound healing, foetal development and in the reproductive cycle (22). Angiogenesis can however be pathological in nature, and has been associated with psoriasis, endometriosis, ischemic heart disease, rheumatoid arthritis, hepatitis and solid tumour development. It has long been known that for solid tumours to develop beyond a size of  $\approx 1\text{mm}^3$  new blood vessels must supply nutrients and oxygen to the cancerous cells (23). The neo-vasculature created to enable tumour growth is chaotically formed and pathologically different from normal vasculature (24), with resulting impaired flow of blood to the tumour that has implications for therapeutic intervention, such as re-oxygenation for radiotherapy and delivery of chemotherapeutics. As well as permitting tumour growth and affording a degree of resistance to therapy, the tumour vascular, crucially, gives tumour cells the ability to disseminate into the systemic circulation, allowing the metastatic spread which is the major cause of patient mortality. With regards to solid tumour development and progression, the relationship between tumour cells and the vascular network was first described in 1907 by Professor E Goldman (25). The invasion of malignant tumour cells into local blood vessels, followed by the development of metastases at distant sites, was described via histological and *ex vivo* techniques; it was noted that tumour cells disseminated through the vascular system by cell infiltration into nearby arterial vessels. How these cells entered the vascular system was put down to a general vascular degeneration at the site of malignancy and the function of the lymphatic system. The second point of note in this paper concerned the distribution of tumour blood vessels and the general conditions of circulation within tumours; while the architecture of blood vessels within specific normal organs was known to be characteristically organised, the presence of a tumour leads to uncontrolled development and chaotic irregularity, with the growing tumour periphery developing extensive new blood vessels. The majority of the tumour does not receive a rich supply of blood; the peripheral vessels branch irregularly into small abnormal vessels, and blood supply to the core is diminished, leading to localised necrosis in many tumours. The degree of vascularisation is also related to the tumour location; the level of pre-existing vasculature at the site of tumour development determines how vascular that tumour will initially become. The one common feature of tumour blood vessels observed was a structural one; in the tumour periphery, and in normal tissue surrounding the growing tumour, the vessels would coil around themselves

in a spiral fashion and send capillary shoots towards tumour. The appearance of the whole tumour blood vessel network was also found to differ depending upon tumour type; carcinoma tumours were found to be more vascular towards the periphery with fewer vessels penetrating into the tumour, whilst sarcomas showed an even distribution throughout the tumour. Because the vascular architecture differed between tumours, though derived from the same endothelial cells, Goldman concluded that this was the result of host tissue remodelling, due to action of the tumour environment. These initial observations have been corroborated many times in subsequent years, notably by Judah Folkman (23, 26, 27), and further expanded by more recent work demonstrating the involvement of further stromal cell elements of the tumour microenvironment in relation to tumour neo-vasculature angiogenesis, all of which validates the targeting of the vascular microenvironment as a therapeutic approach (28, 29).

## **1.5 Vascular targeted therapy**

Given the importance of the tumour vascular microenvironment, cancer therapies that target tumour blood vessels have been actively sought (30, 31). The two main classes of drug that have emerged in the vascular targeting area are angiogenesis-inhibiting agents (AIAs) and vascular disrupting agents (VDAs) (32, 33). AIAs aim to stop further growth of the tumour vasculature and thereby inhibit tumour progression. There are many molecular targets within the AIA group of drugs, with the major ones being the vascular-endothelial growth factor (VEGF) (34, 35) and its receptor (VEGFR) (36), receptor tyrosine kinases (37), angiopoietin/Tie-2 (38) and plasma membrane integrins (39). Although promising novel therapeutics, AIAs have been largely ineffective at stopping tumour progression as single therapies (40-42). However an intriguing concept of 'vascular normalisation' has emerged (43); it has been noted that combination of AIAs with traditional cancer therapies such as chemotherapy (44-46) can show increased survival in patients when compared to stand-alone treatment, the theory being that AIAs can normalise the aberrant pro-angiogenic signalling in the tumour microenvironment and create a vasculature that is more susceptible to drug delivery and re-oxygenation for purposes of radiotherapy.

VDAs on the other hand target established tumour vasculature with the aim of destroying it. VDAs cause direct apoptosis of vascular endothelial cells, thereby destroying tumour vasculature, and reduce the blood flow to tumours, causing ischaemia and subsequent central tumour necrosis (32). An additional anti-mitotic effect has also been noted with certain VDAs. There are two main classes of VDA, those that bind to tubulin and those that

do not. VDAs that are independent of tubulin binding are part of the flavonoid class, with the lead compound being DMXAA (5,6-dimethylxanthenone-4-acetic acid, ASA404, vadimezan). Direct and indirect anti-vascular activity is caused by apoptosis of tumour blood vessel endothelial cells (47). Tubulin binding VDAs bind at the colchicine site of tubulin (48) and cause depolymerisation of tubulin, cytoskeleton re-arrangement and changes to cell morphology (49). The lead compounds in this category are the combretastatin family of drugs, including combretastatin A-4 phosphate (CA4P) (50) and combretastatin A-1 phosphate (CA1P, OXi4503) (51). These agents selectively target proliferating tumour endothelial cells, causing blebbing and rounding of endothelial cells, increased vessel permeability, Rho-mediated vasoconstriction and cessation of blood flow, and ultimate destruction of tumour neo-vascularisation (52, 53). Reduction in tumour perfusion following VDA treatment can be observed within minutes, with a dose dependent response observed in functional tumour blood vessels, resulting in widespread central necrosis by 24-48 hours (54). A characteristic rim of surviving tumour cells remains however following treatment (49, 52), which is thought to survive due to receiving oxygen and nutrients from surrounding normal tissue vasculature, which is not affected. This frequently leads to repopulation of the tumour vasculature and viable cancer cells, and progression of the tumour. The use of VDAs therefore generally requires combination with radiotherapy or other chemotherapy for successful treatment of cancer. Many VDAs are still being developed, and the questions surrounding how they affect tumour vasculature, and how best to combine them with other therapies, remain. Monitoring of response, both in preclinical animal models and in patients, should help to answer these questions and increase the translational throughput of novel VDA treatment strategies (55).

## **1.6 Colorectal cancer**

Colorectal carcinoma (CRC), the subject of this thesis, is one of the most prevalent forms of cancer in the world; in the region of 1.2 million patients are diagnosed with CRC worldwide each year, making it the 3<sup>rd</sup> most common cancer globally (56). In Europe it is the third most common cause of cancer related death (56). The associated metastatic spread is high and usually to the liver, with 14-20% of patients at diagnosis already with hepatic metastases and a further third with localised disease which subsequently progresses to liver metastatic stage (57, 58). Using the 'Tumour-Node-Metastasis' or TNM system, the 7<sup>th</sup> revision of which was recently published (59), patients with liver metastases are classed as stage IV disease, where survival at 5 years is only 6%, although if surgically resectable this

increases to around 25%-40% (60). Management of this CRC with synchronous liver metastases is difficult (61): whether the metastases are resectable or not, treatment usually entails surgical removal of the primary colorectal tumour followed by interval chemotherapy, with liver resection performed at a later date if possible (62, 63). For patients where resection is not possible, either due to advanced stage liver burden or metastatic disease that has spread beyond the liver, guidelines for treatment are to use systemic chemotherapy either to reduce the size of liver burden for potential surgical resection, or as palliative treatment for symptoms of disease and increased quality of life (64). Further development of chemotherapy strategies, especially vascular targeted therapies mentioned previously, are therefore of great need. Preclinical models for investigating therapy of colorectal cancer are usually one of two types: spontaneous, induced or transplanted mouse models (syngeneic models), or transplanted human tumour cells in immune deficient animals (xenograft models) (65). The use of vascular targeted therapy for CRC and advanced liver metastases in human xenograft studies has shown that OXi4503 causes vascular shutdown and massive central necrosis (66, 67); however, the monitoring of this response has been in an invasive manner that is not applicable to human use. In patients with liver metastases treated with OXi4503 limited data is available, although the use of dynamic contrast magnetic resonance imaging (DCE-MRI) in a phase I clinical trial of OXi4503 has shown that non-invasive assessment of response is possible (68). Further elucidation of the mechanism of action of vascular targeted therapy and response to treatment of individual tumours would therefore greatly enhance translational ability of novel drug treatments and biomarkers of response.

## **1.7 Translational imaging**

Staging of the extent of cancer, and assessing the response of tumours to therapy, is an important part of clinical oncology. Assessment usually takes the form of a decrease in tumour volume or progression of the disease. This is based on the observation that therapies that cause a regression of the tumour volume will generally demonstrate an increase in patient survival (69, 70); standardisation of measurements was therefore needed, and resulted in the publication of the 'Response evaluation criteria in solid tumours' (RECIST) (71) for accurately measuring response to treatment based upon differences in measured size of tumours. Volumetric changes in tumours following successful treatment may take weeks to become apparent, or in the case of cytostatic therapies show no change at all, meaning lost time, unnecessary side effects and



unsuccessful clinical trials in the former, or a missed opportunity in the translation of potentially effective new therapeutic strategies in the latter. Imaging strategies have evolved that are capable of providing functional markers of response for specific targeted drugs for this reason. Many reviews have been published describing these advances in oncology imaging (72-75); the following subsections of examples of imaging modalities for translational imaging that, whilst not exhaustive, describes those that have the most relevance to imaging the response of the tumour vasculature microenvironment to therapy with the aim of clinical translation.

### **1.7.1 Magnetic resonance imaging**

Magnetic resonance imaging (MRI) was developed in the 1970s by Paul Lauterbur and Peter Mansfield, for which they were awarded the Nobel prize in 2003 (76). The basic principles of MRI imaging are outlined below in section 1.8; the fundamental concept is that of detecting nuclear spin re-orientation in a magnetic field. As water is abundant in tissue and very sensitive to MR detection, imaging protocols are predominantly linked to imaging water (72). Anatomical images can therefore be generated with MRI, however the real strength is the ability to change imaging parameters in order to bias the detection towards functional differences of different tissues. The main techniques developed to image tumour vasculature are MR angiography (77) and dynamic contrast-enhanced MRI (DCE-MRI) (78). MR angiography is concerned primarily with imaging vessel structure, and is discussed at more length in the corresponding part of this thesis, chapter 4. DCE-MRI is a more common technique that is employed to assess density, integrity and leakiness of tissue vasculature based on exogenous contrast agent kinetics in tissue. It is commonly used in the clinic for the diagnosis and evaluation of cancer (79) with many contrast agents developed for use in patients. A quantitative analysis of DCE data is therefore highly dependent upon the distribution and elimination of the contrast agent employed; gadolinium-based compounds for example have a distribution half-life of around 90 minutes in humans and 27 minutes in mice (80). DCE-MRI is therefore based on several assumptions, the main being that the contrast agent flows freely between different compartments whose volumes do not change over the course of the scan. Differences in contrast agent used, success of injection, route and biodistribution of the compound, plus many other variables, make DCE-MRI difficult, although not impossible, to compare across studies. An inherent measure of the vascular components of tumours would therefore be highly preferable.

### 1.7.1.1 Basic principles of MRI imaging

There are many sources that describe in detail the fundamental concepts of MRI imaging for a comprehensive review (101-103). It is beyond the scope of this thesis to explain in depth the exhaustive information on this topic, but the basic principles will be established here, with more detailed information in the relevant chapters. MRI is based on the principle of nuclear spin; certain nuclei spin on their axis creating a magnetic dipole moment. These can essentially be thought of as small magnets. When inside a strong magnetic field, denominated  $B_0$ , the majority of these nuclei align with the direction of the major field, called the Z axis, and process around it. The frequency of process around the Z axis depends on the specific nuclei imaged and the microenvironment in which it is found. If the number of protons plus the number of neutrons is an odd number, then the spin is designated as  $\frac{1}{2}$ ; the spins will be either of lower energy and align with  $B_0$  or of higher energy and align opposite to  $B_0$ . There is a net magnetisation along the Z axis as the number of spins aligning with  $B_0$  is higher than those opposing it. By applying an oscillating magnetic field radiofrequency pulse perpendicular to  $B_0$ , which is rotating at the resonant frequency of the nuclear spin around the Z axis, the net magnetisation 'tips' from the Z axis in to the X-Y plane. These three concepts are illustrated in **figure 1.2**. The receiver coil in MR systems detects magnetisation in this X-Y plane and signal is produced. Net magnetisation will initially be in phase in this transverse plane, but as the pulsed magnetic field is switched off the spins will dephase due to magnetic field inhomogeneities, and the net magnetisation will be restored to the  $B_0$  field. Characteristic times can be described based on the dephasing of these spins, and used to discern differences in tissue structure, as different tissues will possess different values (72).

T1 is the time taken for the longitudinal (Z axis) magnetisation to return to 63% [ $1-(1/e)$ ] of its initial value after being tipped into the X-Y plane. It is known as spin-lattice, as the energy from the radiofrequency pulse is dissipated into the surrounding nuclear lattice in order to regain magnetisation. Water containing tissue will have long T1 times, of around 400-1200ms, fluid even longer at around 1500-2000ms, and fat containing tissue shorter T1 times, at around 100-150ms. In order to bias MR imaging to be T1 weighted images, parameters can be set by creating a short repetition time TR for repeat of the radiofrequency pulse and short echo time TE.

T2 is the time taken for the transverse magnetisation in the X-Y plane to decay by 37% ( $1/e$ ) of its initial value after the radiofrequency pulse. It is called spin-spin relaxation, as it occurs due to the loss of phase between nuclear spins. T2\* is the same as T2 but with the added

dephasing effect of field inhomogeneities. T2 is generally faster than T1. In biological tissue water-containing tissue has a T2 in the order of seconds, whilst fat-containing tissue is in the range of 10-100ms. To bias an MR scan for T2 weighting the TE is set long, which then allows imaging of tissues with long T2 times, such as water, that will appear bright on imaging.

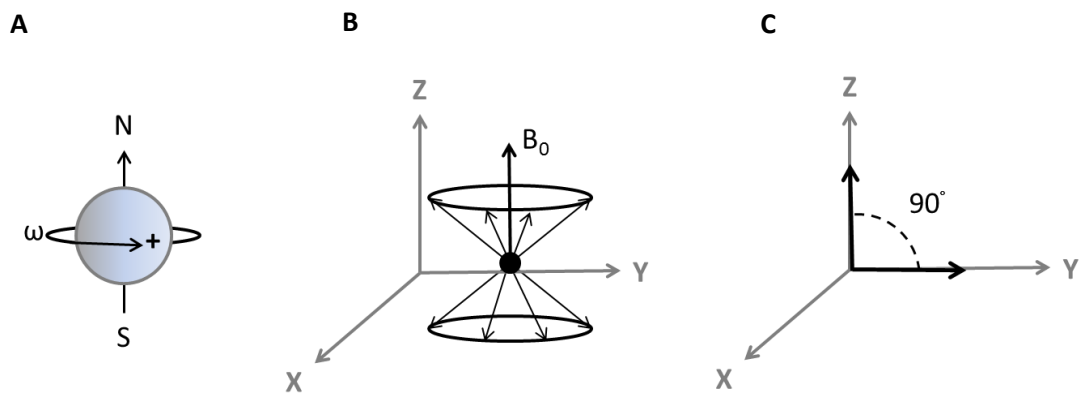


**Figure 1.2 Nuclear magnetic spin in MRI**

Nuclei spin on their axis with an angular momentum  $\omega$ , creating a magnetic dipole north and south (**A**). When placed in a strong magnetic field  $B_0$  the majority of nuclear spins line up with the field in the Z axis direction (**B**). In order to achieve an MR signal the magnetisation vector is flipped over on to the transverse X-Y plane by applying a radiofrequency pulse (**C**).

### **1.7.2 Contrast enhance computed tomography**

Computed tomography (CT) is an imaging modality that uses X-ray imaging to reconstruct three dimensional data based on differentiation of tissues due to high or low enhancement (81); x-rays pass through the tissue and are attenuated by absorption or scatter of photons. Low attenuation occurs in soft tissue, allowing most of the x-ray to pass through to the detector, whilst hard structures such as bone possess higher attenuation properties. Contrast enhancement can be used to observe how different structures handle the passage of the contrast agent. As exogenous contrast agents are required, as with DCE-MRI but using iodine based compounds, many of the same concepts of contrast agent kinetics can be applied (82, 83). One advantage of DCE-CT is that the signal intensity, measured in Hounsfield units, is linear over a large range, meaning that concentrations of contrast agent are proportional to the change observed in the signal intensity (84). Disadvantages include the use of ionising radiation and the need for repeated image acquisitions for dynamic screening (85). For vascular studies micro-CT can provide high resolution quantitative measures of vascular volume, density and branching patterns (86), however concerns remain regarding the use of radiation and the standardisation of exogenous contrast administration.

### **1.7.3 Ultrasound**

Ultrasound (US) is a low cost, sensitive and easy to use *in vivo* imaging technique (87). High frequency mechanical oscillations of sound in short pulses are transmitted into a tissue of interest, and an echo return detected via a transducer which creates electrical signals for processing into an image. The echo produced is dependent upon the different echogenicity within the tissue, allowing structural images to be produced. With regards to functional measurements of angiogenesis, power Doppler measurements can be used to assess blood flow (88) and micro-bubbles can be used as a contrast agent (89). These microbubbles are able to circulate within blood vessels and, due to their large acoustic impedance difference with biological tissue, can be used as a strong echogenic marker, forming the basis for contrast-enhanced US (CEUS) (90). CEUS has been used to measure blood perfusion and flow rate in tumours and organs (91) and has been targeted at tumour-induced angiogenesis through conjugation to a peptide targeting  $\alpha_v\beta_3$  (92). However, molecular imaging is limited to the intravascular space due to compartmentalisation issues, with the aforementioned problems of exogenous contrast still problematic for CEUS.

### **1.7.4 Optical imaging**

Optical techniques for imaging tumour pathophysiology are generally the preserve of pre-clinical research, as human studies using optical imaging have been limited in ability. A few optical imaging systems have recently had an impact on patient imaging however, with the main modality being fluorescence imaging, such as the development of microscopic-endoscope fluorescence imaging (93). However, the only fluorescent molecules approved for human use are indo-cyanine green, fluorescein, photofrin and 5-aminolevulinic acid (94), limiting the ability of research. On the macroscopic level only intra-operative imaging has been achieved, with liver metastases from CRC accurately identified (95). Non-fluorescence based systems such as optical coherence tomography are based on the scattering of photons, and can be used to image structures *in vivo* (96), however the field of view is small and data acquisition slow (73). A novel imaging modality combines both optical and ultrasound imaging capabilities: photoacoustic imaging (PAI). This can either be in the form of microscopy (PAM) (97) or full tomographic mode (PAT) (98). Whilst PAM allows greater resolution of images, the area of interest is focussed on to one plane, and the imaging area therefore restricted. PAT, on the other hand, is able to image larger areas of tissue and does not focus onto a particular plane, but rather receives all data possible within the region of interest. The underlying principle of both PAM and PAT is the generation of sound from the absorption of light, known as the photoacoustic effect. This was first described by 1880 Alexander Graham Bell when he published his work on the invention of the 'photophone' in the American journal of science (99). Bell's work in to the transmission of sound by modulation of sunlight effectively demonstrated the principle of information encoded onto light, and is the precursor to today's medical imaging use of the photoacoustic effect (100). Modern biomedical imaging scanners are able to achieve spatial resolution similar to ultrasound imaging, but with addition of the high specificity and spectral ability of optical techniques.

### **1.8 Hypothesis and aims of this thesis**

The hypothesis of this thesis is that non-invasive imaging of tumour pathophysiology will provide novel translational imaging biomarkers for vascular targeted therapy. Having reviewed aspects of oncology related to the abnormal biology of cancer and assessment of response, the aims of this thesis are to further the translational ability of preclinical research, and provide response markers for prognosis and clinical intervention. In order to achieve this, the work will concentrate on one of the hallmarks of cancer, which is

applicable to many different disease situations. As the main cause of tumour growth and metastatic spread is the formation of neo-vasculature within the tumour, this thesis will look at vascular development and growth, and the therapeutic targeting of tumour blood vessels. It is envisaged that this will provide greater understanding of the underlying vascular pathophysiology, and provide markers of response to therapeutic intervention. The therapeutic approach to be used is that of vascular disruption, as this can be used for targeting solid tumour growth of both known and undetected micro-metastatic cancerous lesions. As OXi4503 is an advanced VDA in clinical use which causes a large degree of vascular shutdown in preclinical models, which should aid detection of response, this compound has been selected for investigation. This thesis will concentrate on colorectal carcinoma, as this has important and direct clinical relevance, but it is envisaged that any findings will be applicable to all solid cancer types, as it is the tumour vasculature that is being assessed. For this study two distinct CRC cancers will be employed, SW1222 and LS174T, as they possess different vascular pathophysologies when forming tumours *in vivo*. The models to be used are 1) subcutaneous, which is easy to use and interpret, and widely employed, therefore can be compared across preclinical studies, and 2) a model of liver metastatic disease which will be more relevant for clinical translation. The assessment of these models will be by non-invasive molecular imaging; whilst great advances have been made with various modalities this has mainly been through use of exogenous contrast agents. One of the aims of this thesis is to develop imaging biomarkers of vessel growth and assessment of response that are based on inherent tumour vascular characteristics. To this end the novel imaging modality of photoacoustic tomography will be employed to give greater insight into the structure of tumour vascular networks, and the response of these to treatment with OXi4503. Novel use of MRI sequences will also be used to demonstrate that inherent characteristics of the tumour vasculature can be assessed for response criteria to vascular targeted therapy. The layout of this thesis includes a general Materials and Methods section (chapter 2) that applies to all subsequent research. The basic physical principles of PAT are then discussed, and its suitability for imaging tumours *in vivo* assessed (chapter 3) followed by PAT assessment of vascular disruption (chapter 4). Focus is then placed on the development of MRI imaging sequences capable of assessing vascular function without exogenous contrast agents (chapter 5), and assessment of the liver metastatic model response to VDA treatment (chapter 6). The overarching results and implications of this research, coupled with future work that would improve the translational ability of these concepts, is presented in the final section (chapter 7).

## 1.9 References

- (1) Futreal PA, Coin L, Marshall M, Down T, Hubbard T, Wooster R, et al. A census of human cancer genes. *Nat Rev Cancer* 2004;4:177-83.
- (2) Vogelstein B, Papadopoulos N, Velculescu VE, Zhou S, Diaz LA, Jr., Kinzler KW. Cancer genome landscapes. *Science* 2013;339:1546-58.
- (3) Chial H. Genetic regulation of cancer. *Nature Education* 2008;1(1):67.
- (4) Chen LL, Blumm N, Christakis NA, Barabasi AL, Deisboeck TS. Cancer metastasis networks and the prediction of progression patterns. *Br J Cancer* 2009;101:749-58.
- (5) Mehlen P, Puisieux A. Metastasis: a question of life or death. *Nat Rev Cancer* 2006;6:449-58.
- (6) Website: [http://globocan.iarc.fr/Pages/fact\\_sheets\\_cancer.aspx](http://globocan.iarc.fr/Pages/fact_sheets_cancer.aspx) accessed 01/05/14
- (7) Harrington KJ. Biology of cancer. *Medicine* 2011;39:689-92.
- (8) Pott P. Chirurgical observations relative to the cataract, the polypus of the nose, the cancer of the scrotum, the different kinds of ruptures, and the mortification of the toes and feet. 1775 Available from: URL: <http://galenet.galegroup.com/servlet/ECCO?c=1&stp=Author&ste=11&af=BN&a e=T007127&tiPG=1&dd=0&dc=flc&docNum=CW107455718&vrsn=1.0&srchtp=a&d4=0.33&n=10&SU=0LRM&locID=ureginalib>
- (9) Meacham CE, Morrison SJ. Tumour heterogeneity and cancer cell plasticity. *Nature* 2013;501:328-37.
- (10) Greaves M, Maley CC. Clonal evolution in cancer. *Nature* 2012;481:306-13.
- (11) Weinberg RA. Oncogenes and tumor suppressor genes. *CA: A Cancer Journal for Clinicians* 1994;44:160-70.
- (12) Lee EY, Muller WJ. Oncogenes and tumor suppressor genes. *Cold Spring Harb Perspect Biol* 2010;2:a003236.
- (13) Hanahan D, Weinberg RA. The Hallmarks of Cancer. *Cell* 2000;100:57-70.
- (14) Hanahan D, Weinberg RA. Hallmarks of cancer: the next generation. *Cell* 2011;144:646-74.
- (15) Bissell MJ, Hines WC. Why don't we get more cancer? A proposed role of the microenvironment in restraining cancer progression. *Nat Med* 2011;17:320-9.
- (16) Balkwill FR, Capasso M, Hagemann T. The tumor microenvironment at a glance. *J Cell Sci* 2012;125:5591-6.

- (17) Hanahan D, Coussens LM. Accessories to the crime: functions of cells recruited to the tumor microenvironment. *Cancer Cell* 2012;21:309-22.
- (18) Zhang X, Nie D, Chakrabarty S. Growth factors in tumor microenvironment. *Front Biosci (Landmark Ed)* 2010;15:151-65.
- (19) Devaud C, Westwood JA, John LB, Flynn JK, Paquet-Fifield S, Duong CP, et al. Tissues in different anatomical sites can sculpt and vary the tumor microenvironment to affect responses to therapy. *Mol Ther* 2014;22:18-27.
- (20) Nakasone ES, Askautrud HA, Kees T, Park JH, Plaks V, Ewald AJ, et al. Imaging tumor-stroma interactions during chemotherapy reveals contributions of the microenvironment to resistance. *Cancer Cell* 2012;21:488-503.
- (21) Provenzano PP, Cuevas C, Chang AE, Goel VK, Von Hoff DD, Hingorani SR. Enzymatic targeting of the stroma ablates physical barriers to treatment of pancreatic ductal adenocarcinoma. *Cancer Cell* 2012;21:418-29.
- (22) Carmeliet P, Jain RK. Angiogenesis in cancer and other diseases. *Nature* 2000;407:249-57.
- (23) Folkman J. Tumor Angiogenesis: Therapeutic Implications. *N Engl J Med* 1971;285:1182-6.
- (24) De BK, Cauwenberghs S, Carmeliet P. Vessel abnormalization: another hallmark of cancer? Molecular mechanisms and therapeutic implications. *Curr Opin Genet Dev* 2011;21:73-9.
- (25) Goldmann E. The growth of malignant disease in man and the lower animals, with special reference to the vascular system. *The Lancet* 1907;170:1236-40.
- (26) Folkman J, Klagsbrun M. Angiogenic factors. *Science* 1987;235:442-7.
- (27) Folkman J, Watson K, Ingber D, Hanahan D. Induction of angiogenesis during the transition from hyperplasia to neoplasia. *Nature* 1989;339:58-61.
- (28) Junttila MR, de Sauvage FJ. Influence of tumour micro-environment heterogeneity on therapeutic response. *Nature* 2013;501:346-54.
- (29) Albini A, Sporn MB. The tumour microenvironment as a target for chemoprevention. *Nat Rev Cancer* 2007;7:139-47.
- (30) Ruoslahti E. Specialization of tumour vasculature. *Nat Rev Cancer* 2002;2:83-90.
- (31) Randal J. Antiangiogenesis drugs target specific cancers, mechanisms. *J Natl Cancer Inst* 2000;92:520-2.
- (32) Siemann DW. The unique characteristics of tumor vasculature and preclinical evidence for its selective disruption by Tumor-Vascular Disrupting Agents. *Cancer Treat Rev* 2011;37:63-74.
- (33) Thorpe PE. Vascular targeting agents as cancer therapeutics. *Clin Cancer Res* 2004;10:415-27.



- (34) Dickson PV, Hamner JB, Sims TL, Fraga CH, Ng CY, Rajasekeran S, et al. Bevacizumab-induced transient remodeling of the vasculature in neuroblastoma xenografts results in improved delivery and efficacy of systemically administered chemotherapy. *Clin Cancer Res* 2007;13:3942-50.
- (35) Wildiers H, Guetens G, De BG, Verbeken E, Landuyt B, Landuyt W, et al. Effect of antivascular endothelial growth factor treatment on the intratumoral uptake of CPT-11. *Br J Cancer* 2003;88:1979-86.
- (36) Tvorogov D, Anisimov A, Zheng W, Leppanen VM, Tammela T, Laurinavicius S, et al. Effective suppression of vascular network formation by combination of antibodies blocking VEGFR ligand binding and receptor dimerization. *Cancer Cell* 2010;18:630-40.
- (37) Kamoun WS, Ley CD, Farrar CT, Duyverman AM, Lahdenranta J, Lacorre DA, et al. Edema control by cediranib, a vascular endothelial growth factor receptor-targeted kinase inhibitor, prolongs survival despite persistent brain tumor growth in mice. *J Clin Oncol* 2009;27:2542-52.
- (38) Falcon BL, Hashizume H, Koumoutsakos P, Chou J, Bready JV, Coxon A, et al. Contrasting actions of selective inhibitors of angiopoietin-1 and angiopoietin-2 on the normalization of tumor blood vessels. *Am J Pathol* 2009;175:2159-70.
- (39) Skuli N, Monferran S, Delmas C, Favre G, Bonnet J, Toulas C, et al. Alpha5beta3/alpha5beta5 integrins-FAK-RhoB: a novel pathway for hypoxia regulation in glioblastoma. *Cancer Res* 2009;69:3308-16.
- (40) Cobleigh MA, Langmuir VK, Sledge GW, Miller KD, Haney L, Novotny WF, et al. A phase I/II dose-escalation trial of bevacizumab in previously treated metastatic breast cancer. *Seminars in Oncology* 2003;30, Supplement 16:117-24.
- (41) Jain RK, Duda DG, Clark JW, Loeffler JS. Lessons from phase III clinical trials on anti-VEGF therapy for cancer. *Nat Clin Prac Oncol* 2006;3:24-40.
- (42) Giantonio BJ, Catalano PJ, Meropol NJ, O'Dwyer PJ, Mitchell EP, Alberts SR, et al. Bevacizumab in combination with oxaliplatin, fluorouracil, and leucovorin (FOLFOX4) for previously treated metastatic colorectal cancer: results from the Eastern Cooperative Oncology Group Study E3200. *J Clin Oncol* 2007;25:1539-44.
- (43) Goel S, Duda DG, Xu L, Munn LL, Boucher Y, Fukumura D, et al. Normalization of the vasculature for treatment of cancer and other diseases. *Physiol Rev* 2011;91:1071-121.
- (44) Hurwitz H, Fehrenbacher L, Novotny W, Cartwright T, Hainsworth J, Heim W, et al. Bevacizumab plus Irinotecan, Fluorouracil, and Leucovorin for Metastatic Colorectal Cancer. *N Engl J Med* 2004;350:2335-42.
- (45) Saltz LB, Clarke S, Diaz-Rubio E, Scheithauer W, Figer A, Wong R, et al. Bevacizumab in combination with oxaliplatin-based chemotherapy as first-line therapy in metastatic colorectal cancer: a randomized phase III study. *J Clin Oncol* 2008;26:2013-9.

- (46) Tebbutt NC, Wilson K, GebSKI VJ, Cummins MM, Zannino D, Van Hazel GA, et al. Capecitabine, bevacizumab, and mitomycin in first-line treatment of metastatic colorectal cancer: results of the Australasian Gastrointestinal Trials Group Randomized Phase III MAX Study. *J Clin Oncol* 2010;28:3191-8.
- (47) Ching LM, Zwain S, Baguley BC. Relationship between tumour endothelial cell apoptosis and tumour blood flow shutdown following treatment with the antivascular agent DMXAA in mice. *Br J Cancer* 2004;90:906-10.
- (48) Lippert JW, III. Vascular disrupting agents. *Bioorg Med Chem* 2007;15:605-15.
- (49) Siemann DW. Therapeutic strategies that selectively target and disrupt established tumor vasculature. *Hematology/Oncology Clinics of North America* 2004;18:1023-37.
- (50) Gaya A, Daley F, Taylor NJ, Tozer G, Qureshi U, Padhani A, et al. Relationship between human tumour angiogenic profile and combretastatin-induced vascular shutdown: an exploratory study. *Br J Cancer* 2008;99:321-6.
- (51) Salmon HW, Siemann DW. Effect of the second-generation vascular disrupting agent OXi4503 on tumor vascularity. *Clin Cancer Res* 2006;12:4090-4.
- (52) Tozer GM, Kanthou C, Baguley BC. Disrupting tumour blood vessels. *Nat Rev Cancer* 2005;5:423-35.
- (53) Tozer GM, Kanthou C, Parkins CS, Hill SA. The biology of the combretastatins as tumour vascular targeting agents. *Int J Exp Pathol* 2002;83:21-38.
- (54) Siemann DW, Horsman MR. Vascular targeted therapies in oncology. *Cell Tissue Res* 2009;335:241-8.
- (55) McKeage MJ, Fong P, Jeffery M, Baguley BC, Kestell P, Ravic M, et al. 5,6-Dimethylxanthenone-4-acetic acid in the treatment of refractory tumors: a phase I safety study of a vascular disrupting agent. *Clin Cancer Res* 2006;12:1776-84.
- (56) Ferlay J, Shin HR, Bray F, Forman D, Mathers C, Parkin DM. Estimates of worldwide burden of cancer in 2008: GLOBOCAN 2008. *Int J Cancer* 2010;127:2893-917.
- (57) Manfredi S, Lepage C, Hatem C, Coatmeur O, Faivre J, Bouvier AM. Epidemiology and management of liver metastases from colorectal cancer. *Ann Surg* 2006;244:254-9.
- (58) Leporrier J, Maurel J, Chiche L, Bara S, Segol P, Launoy G. A population-based study of the incidence, management and prognosis of hepatic metastases from colorectal cancer. *Br J Surg* 2006;93:465-74.
- (59) EdgeSB, ByrdDR, ComptonCC, et al (eds). *AJCC Cancer Staging Manual*, 7th edn. Springer: New York, 2010
- (60) Cancer Research UK. *Statistics and outlook for bowel cancer*, (2013) <http://www.cancerresearchuk.org/cancer-help/type/bowel-cancer/treatment/statistics-and-outlook-for-bowel-cancer> accessed 01/05/14

- (61) Siriwardena AK, Mason JM, Mullamitha S, Hancock HC, Jegatheeswaran S. Management of colorectal cancer presenting with synchronous liver metastases. *Nat Rev Clin Oncol* 2014;11:446-59.
- (62) Adam R, Lucidi V, Bismuth H. Hepatic colorectal metastases: methods of improving resectability. *Surg Clin North Am* 2004;84:659-71.
- (63) de Haas RJ, Adam R, Wicherts DA, Azoulay D, Bismuth H, Vibert E, et al. Comparison of simultaneous or delayed liver surgery for limited synchronous colorectal metastases. *Br J Surg* 2010;97:1279-89.
- (64) Schmoll HJ, Van CE, Stein A, Valentini V, Glimelius B, Haustermans K, et al. ESMO Consensus Guidelines for management of patients with colon and rectal cancer. a personalized approach to clinical decision making. *Ann Oncol* 2012;23:2479-516.
- (65) Li ZY, Ni S, Yang X, Kiviat N, Lieber A. Xenograft models for liver metastasis: Relationship between tumor morphology and adenovirus vector transduction. *Mol Ther* 2004;9:650-7.
- (66) Chan LS, Malcontenti-Wilson C, Muralidharan V, Christophi C. Effect of vascular targeting agent Oxi4503 on tumor cell kinetics in a mouse model of colorectal liver metastasis. *Anticancer Res* 2007;27:2317-23.
- (67) Malcontenti-Wilson C, Chan L, Nikfarjam M, Muralidharan V, Christophi C. Vascular targeting agent Oxi4503 inhibits tumor growth in a colorectal liver metastases model. *J Gastroenterol Hepatol* 2008;23:e96-e104.
- (68) Patterson DM, Zweifel M, Middleton MR, Price PM, Folkes LK, Stratford MR, et al. Phase I clinical and pharmacokinetic evaluation of the vascular-disrupting agent OXi4503 in patients with advanced solid tumors. *Clin Cancer Res* 2012;18:1415-25.
- (69) Goffin J, Baral S, Tu D, Nomikos D, Seymour L. Objective responses in patients with malignant melanoma or renal cell cancer in early clinical studies do not predict regulatory approval. *Clin Cancer Res* 2005;11:5928-34.
- (70) El-Maraghi RH, Eisenhauer EA. Review of phase II trial designs used in studies of molecular targeted agents: outcomes and predictors of success in phase III. *J Clin Oncol* 2008;26:1346-54.
- (71) Eisenhauer EA, Therasse P, Bogaerts J, Schwartz LH, Sargent D, Ford R, et al. New response evaluation criteria in solid tumours: revised RECIST guideline (version 1.1). *Eur J Cancer* 2009;45:228-47.
- (72) Brindle K. New approaches for imaging tumour responses to treatment. *Nat Rev Cancer* 2008;8:94-107.
- (73) Weissleder R, Pittet MJ. Imaging in the era of molecular oncology. *Nature* 2008;452:580-9.
- (74) Histed SN, Lindenberg ML, Mena E, Turkbey B, Choyke PL, Kurdziel KA. Review of functional/anatomical imaging in oncology. *Nucl Med Commun* 2012;33:349-61.

- (75) Yankeelov TE, Abramson RG, Quarles CC. Quantitative multimodality imaging in cancer research and therapy. *Nat Rev Clin Oncol* 2014.
- (76) Riederer SJ. MR imaging: its development and the recent Nobel Prize. *Radiology* 2004;231:628-31.
- (77) Brubaker LM, Bullitt E, Yin C, Van DT, Lin W. Magnetic resonance angiography visualization of abnormal tumor vasculature in genetically engineered mice. *Cancer Res* 2005;65:8218-23.
- (78) Yankeelov TE, Gore JC. Dynamic Contrast Enhanced Magnetic Resonance Imaging in Oncology: Theory, Data Acquisition, Analysis, and Examples. *Curr Med Imaging Rev* 2009;3:91-107.
- (79) Gillies RJ, Bhujwala ZM, Evelhoch J, Garwood M, Neeman M, Robinson SP, et al. Applications of magnetic resonance in model systems: tumor biology and physiology. *Neoplasia* 2000;2:139-51.
- (80) Aime S, Caravan P. Biodistribution of gadolinium-based contrast agents, including gadolinium deposition. *J Magn Reson Imaging* 2009;30:1259-67.
- (81) Wolbarst A. *Physics of Radiology*. 2nd ed Medical Physics Publishing; Madison Wisconsin: 2005
- (82) Sahani DV, Kalva SP, Hamberg LM, Hahn PF, Willett CG, Saini S, et al. Assessing tumor perfusion and treatment response in rectal cancer with multisection CT: initial observations. *Radiology* 2005;234:785-92.
- (83) Korporeal JG, van VM, van den Berg CA, van der Heide UA. Tracer kinetic model selection for dynamic contrast-enhanced computed tomography imaging of prostate cancer. *Invest Radiol* 2012;47:41-8.
- (84) Ingrisch M, Sourbron S. Tracer-kinetic modeling of dynamic contrast-enhanced MRI and CT: a primer. *J Pharmacokinet Pharmacodyn* 2013;40:281-300.
- (85) Brix G, Griebel J, Delorme S. [Dynamic contrast-enhanced computed tomography. Tracer kinetics and radiation hygienic principles]. *Radiologe* 2012;52:277-94.
- (86) Zagorchev L, Mulligan-Kehoe MJ. Molecular imaging of vessels in mouse models of disease. *Eur J Radiol* 2009;70:305-11.
- (87) Widmann G, Riedl A, Schoepf D, Glodny B, Peer S, Gruber H. State-of-the-art HR-US imaging findings of the most frequent musculoskeletal soft-tissue tumors. *Skeletal Radiol* 2009;38:637-49.
- (88) Kaushik S, Miller TT, Nazarian LN, Foster WC. Spectral Doppler Sonography of Musculoskeletal Soft Tissue Masses. *Journal of Ultrasound in Medicine* 2003;22:1333-6.
- (89) Calliada F, Campani R, Bottinelli O, Bozzini A, Sommaruga MG. Ultrasound contrast agents: basic principles. *Eur J Radiol* 1998;27 Suppl 2:S157-S160.

- (90) Postema M, Gilja OH. Contrast-enhanced and targeted ultrasound. *World J Gastroenterol* 2011;17:28-41.
- (91) Feleppa EJ, Alam SK, Deng CX. Emerging ultrasound technologies for early markers of disease. *Dis Markers* 2002;18:249-68.
- (92) Kaufmann BA, Lindner JR. Molecular imaging with targeted contrast ultrasound. *Curr Opin Biotechnol* 2007;18:11-6.
- (93) Yelin D, Rizvi I, White WM, Motz JT, Hasan T, Bouma BE, et al. Three-dimensional miniature endoscopy. *Nature* 2006;443:765.
- (94) Murahari MS, Yegeri MC. Identification and usage of fluorescent probes as nanoparticle contrast agents in detecting cancer. *Curr Pharm Des* 2013;19:4622-40.
- (95) Ishizawa T, Fukushima N, Shibahara J, Masuda K, Tamura S, Aoki T, et al. Real-time identification of liver cancers by using indocyanine green fluorescent imaging. *Cancer* 2009;115:2491-504.
- (96) Huang D, Swanson EA, Lin CP, Schuman JS, Stinson WG, Chang W, et al. Optical coherence tomography. *Science* 1991;254:1178-81.
- (97) Zhang HF, Maslov K, Stoica G, Wang LV. Functional photoacoustic microscopy for high-resolution and noninvasive in vivo imaging. *Nat Biotechnol* 2006;24:848-51.
- (98) Zhang E, Laufer J, Beard P. Backward-mode multiwavelength photoacoustic scanner using a planar Fabry-Perot polymer film ultrasound sensor for high-resolution three-dimensional imaging of biological tissues. *Appl Opt* 2008;47:561-77.
- (99) Bell AG. On the production and reproduction of sound by light. *Am.J.Sci.* 20, 305-324. 1880.
- (100) Bell AG. Production of sound by radiant energy. *Journal of the Franklin Institute* 1881;CXI:401-28.
- (101) Haacke EM, Brown RW, Thompson MR, Venkatesan R. *Magnetic Resonance Imaging: Physical Principles and Sequence Design*. New York: Wiley-Liss; 1999.
- (102) Abragam A. *Principles of Nuclear Magnetism*. Oxford: Clarendon Press; 1961.
- (103) Callaghan PT. *Principles of nuclear magnetic resonance microscopy*. Oxford: Clarendon Press; 1991.

# Chapter 2 General materials & methodology

---

## 2.1 Introduction

The approach and experimental set up of all research work is specified in detail in each chapter. The following paragraphs set out basic materials and methods used, and cover elements of equipment, techniques and models employed. All work was performed in the UCL Cancer Institute, the UCL Centre for Advanced Biomedical Imaging (UCL CABI), and the UCL Biological Services Unit (BSU).

## 2.2 Tissue culture

All cell tissue culture work, for both preliminary *in vitro* studies and preparation of cells for *in vivo* studies, was performed under sterile technique. Cell lines grown *in vitro* were reanimated from a stock of frozen aliquots stored in liquid nitrogen. Cells were grown in ventilated flasks (Corning, Sigma-Aldrich, Gillingham, UK) under simulated physiological conditions of 37°C and 5% CO<sub>2</sub>.

### 2.2.1 Equipment

#### 2.2.1.1 Haemocytometer & Countess cell counter

In order to ascertain the number of cells within a given volume of media a Countess automated cell counter (Invitrogen, Limited, Paisley, UK) was used. A cell suspension/trypan blue (Sigma-Aldrich, Gillingham, UK) 1:1 mixture was loaded into a Countess slide and inserted into the machine. Correct focus was defined and automated cell count sequence selected. Results were checked to ensure correct identification of viable and non-viable cells via trypan blue exclusion, and results of total cells/ml and cell viability saved electronically.

#### 2.2.1.2 Centrifuge

In order to concentrate cell densities, cell suspensions were pelleted by centrifugation at 455g for 5 minutes, supernatant removed via vacuum aspiration, and cell pellets resuspended at the desired concentration.

## **2.2.2 Techniques**

### **2.2.2.1 Cell lines**

The human colorectal carcinoma cell lines SW1222 and LS174T were acquired from UCL Cancer Institute stocks at passages p2 and p5 respectively. Transduction of SW1222 and LS174T cell lines with the firefly luciferase gene had been performed (Dr Martin Pule, UCL Cancer Institute) and these were also acquired, at passages p5 and p8 respectively. All cell lines were shown to be negative for mycoplasma infection by an in house polymerase chain reaction (PCR) test before collection, and at subsequent checks. Growth conditions were checked with the American Type Cell Culture website (1). Medium used was D-Modified Eagles Media (DMEM, Sigma-Aldrich, Gillingham, UK) with the addition of 10% foetal bovine serum (FBS), 1% L-glutamine (100x) and 1% non-essential amino acids (100x, all from Invitrogen, Paisley, UK). Anti-bacterial infection agents, such as the commonly used antibiotics penicillin-streptomycin, were not used during tissue culture as these could mask possible infections and become a detriment to any subsequent *in vivo* studies in immune-compromised animals. Instead, any flasks thought to be potentially infected were discarded.

### **2.2.2.2 Cell sub-culture**

Cells were passaged under sterile conditions within the class II down-flow ventilated biosafety cabinet (ESCO model no LP2-4S1, Hatboro PA, USA). At each passage cell flasks were checked under a brightfield microscope for signs of infection. Flask medium was also inspected for signs of potential infection, such as a cloudy or milky appearance. At any indication of possible infection cells were discarded immediately. Cell medium was changed every 2 to 3 days to maintain nutrient levels. To prevent contact-growth inhibition and ensure exponential growth, cells at  $\approx 80\%$  confluency were split as follows: medium was removed via aspiration and adherent cells rinsed with phosphate buffered saline (PBS, Lonza, UK) to remove dead cell debris, growth factors and any remaining media. This PBS was then removed and 1ml of trypsin-EDTA (Source Bioscience UK Ltd) added per  $\approx 30\text{cm}^2$  surface area of flask. Flasks were placed in the incubator for 5-10 minutes until the cells had detached from the monolayer of the flask and were in suspension. The action of trypsin was then inhibited by the addition of an equal amount of FBS containing media as trypsin used, and as much of a single cell suspension as possible achieved by pipetting. Between 1:2 and 1:8 dilution, based on apparent confluency of the flask monolayer, was

then passaged into a new flask and returned to the incubator. A complete record of passage number, date and dilution factor was kept every time cells were split.

### **2.2.2.3 Frozen storage procedure**

In order to maintain a personal stock of cell lines a repository was created, with aliquots of each cell line frozen down for cryogenic storage. Briefly, healthy, exponentially growing cells were detached from a flask and a single cell suspension created. The suspension was pelleted by centrifugation, washed in PBS, re-pelleted, resuspended in a known volume of serum free medium and total cell number determined by Countess automated cell counter. The suspension was then centrifuged and the pellet re-suspended in freezing medium (10% dimethylsulphoxide (DMSO, ThermoFisher Scientific, Cambridge, UK) and 90% FBS) at a concentration of  $2 \times 10^6$  cells/ml. . This solution was then placed in 1ml aliquots in cryotube vials (Nalgene, SLS Ltd, UK) labelled with cell line, freeze date, concentration, and passage number. Aliquots were then frozen inside cryo-freezing containers to allow a slow gradual freezing process in a -80°C freezer (New Brunswick Scientific, Eppendorf, Enfield CT, USA), and subsequently stored in liquid nitrogen storage facility (UCL Cancer Institute).

### **2.2.2.4 Preparation for in vivo work**

For *in vivo* experimentation the number of required cells was calculated and flasks expanded accordingly to provide sufficient total cells. An upper passage limit of 25 was used in case differential growth characteristics and/or tumour forming capability had been introduced due to excessive *in vitro* handling and/or cell adaptation after multiple cell divisions. Cells were detached, pelleted, washed in PBS, re-pelleted and counted. The cell suspension was then pelleted by centrifugation and resuspended in the desired volume of serum free media, depending upon the *in vivo* experimental procedure. The final cell suspension was used *in vivo* as soon as possible In order to preserve cell viability and limit any potential cell aggregations.



## **2.3 Animal experiments**

All *in vivo* experiments were performed in accordance with UK regulations and UK Home Office Scientific Procedures act (1986) under PIL 40/8141 and PPL 70/7309 'Targeted Cancer Therapies'. For all animal experiments the Workman P *et al* (2) 'Guidelines for the welfare and use of animals in cancer research' were adhered to. Animals strains used were immune-deficient Nu/Nu mice lacking T-cells due to developmental absence of a thyroid gland. The background species of the mice were either MF1, procured from an in house breeding colony, or CD1 mice, procured from Charles River Laboratories, both species being ultimately outbred colonies of Swiss Webster stock (3).

Animals were housed in barrier conditions within UCL BSU facilities in individual ventilated cages (IVC) with food and water *ad libitum*. Daytime conditions were simulated by a 12 hour light/dark cycle. Animals for experimentation were females between the ages of 8-10 weeks, with a seven day acclimatisation period allowed between arrival at biological services facilities and experimental use.

### **2.3.1 Animal handling**

All *in vivo* techniques were acquired through previous training and tuition at the royal veterinary college London, resulting in a home office licence for modules 1-4 (PIL 40:8141). Typical procedures performed included restraint via scruffing, injection of substances (cell suspensions, drug solutions, contrast agents, etc.) via subcutaneous (s.c.), intraperitoneal (i.p.) and intravenous (i.v.) routes of administration, and induction of anaesthesia for routine imaging procedures. Animals were checked daily when under procedure and at no point showed signs of suffering or lasting harm due to experimental procedures. Termination was carried out via cervical dislocation via a schedule 1 method.

## 2.3.2 Pre-clinical tumour models

### 2.3.2.1 Subcutaneous tumour model

Cell lines were prepared through tissue culture techniques to a concentration of  $5 \times 10^6$  per 100 $\mu$ l of serum free media. A 100 $\mu$ l bolus of cells was injected subcutaneously into the right flank above the hind leg via a 1ml syringe with a 25 gauge x 16mm needle, within a sterile down-flow cabinet (Techniplast, UK). Animals were returned to IVCs and checked daily for tumour growth, with typical values being a growth to 0.1cm<sup>3</sup> in 14-16 days.

A set of digital callipers were used to measure tumour volume; animals were restrained and tumour length, breadth and height measured. To calculate volume the ellipsoid formula from three distinct measurements, as seen below, was used as this has been shown to provide the most accurate estimate of relative and actual tumour mass (4). The maximum volume permissible was 1.5cm<sup>3</sup>, after which the mice were killed by schedule 1 cervical dislocation.

$$v = L \times B \times H \times \left(\frac{\pi}{6}\right)$$

### 2.3.2.2 Orthotopic liver metastases model

Cell lines were prepared through tissue culture techniques to a concentration of  $1 \times 10^6$  per 100 $\mu$ l of serum free media. A surgery suite was prepared in advance by disinfecting all surfaces with Mikrozid AF spray (Schülke & Mayr, Meadowhall, UK). Sterile surgical drapes were placed over the operating table. All surgical instruments to be used were sterilised by autoclaving. Sterile surgical gown, mask and gloves were used at all times within the surgical suite. Animals were taken individually in to the surgical suite and anaesthetised with 4% isoflurane (Abbott Laboratories, USA) in oxygen (BOC, UK) at a flow rate of 1L/min. Anaesthetised mice were placed on the operating table with an individual nose cone supplying 1-2% isoflurane in 0.5L/min O<sub>2</sub> for maintenance of anaesthesia. The flank of the animal was swabbed with chlorhexidine solution above the location of the spleen in order to sterilise the skin before operation. Pre-operative analgesia was provided through subcutaneous injection of 0.1mg/kg buprenorphine (Vetergesic, Reckitt Benckiser, UK) just above the site of incision. Depth of anaesthesia was monitored by a paw-pinch response; surgery commenced when no pinch response was observed. A set of surgical scissors and tweezers were used to make a  $\approx$ 1cm incision through the skin above the spleen; these were then considered to be 'outside' instruments and therefore not used internally. A further set

of 'internal' round-edged scissors and non-toothed tweezers were used to make an incision through the exposed muscle wall. The spleen was located and gently held in place in order to allow intrasplenic injection of cells; a fine gauge 27g needle was introduced into the spleen and 100µl of cell suspension injected. Care was taken to inject at a steady pressure, with correct injection noted by a paling of the spleen with no spillage of liquid into the opened cavity. Following injection cells were allowed to wash through to the liver for 2 minutes, after which the splenic artery and vein were ligated with undyed, absorbable, coated vicryl sutures (Ethicon, Johnson & Johnson, UK) and splenectomy performed to prevent formation of an intrasplenic tumour. The muscle wall was then sutured with PC-5 4-0 coated vicryl sutures (Ethicon, Johnson & Johnson, UK). The skin layer was securely closed using the Autoclip wound closure system (Harvard apparatus Ltd, UK), the area swabbed with chlorhexadine, and mice returned to a recovery box. Full recovery of the animals was checked before returning the IVCs to the holding room and at 24 hours post operation. One week following surgery, when wounds had completely healed, the wound clips were removed.

## **2.4 In vivo imaging**

### **2.4.1 Magnetic Resonance Imaging**

All magnetic resonance imaging (MRI) experiments were performed on a dedicated small animal Agilent 9.4T MRI scanner (Agilent Technologies, Santa Clara, USA) located within the UCL Centre for Advanced Biomedical Imaging (UCL CABI,). Animals were taken to the preparation room adjacent to the MRI scanner room and, when ready for imaging, placed in an anaesthetic induction box with 4% isoflurane in 1L/min O<sub>2</sub>. Once anaesthesia was achieved animals were transferred to the MRI cradle designed to fit into the bore of the MRI scanner magnet, with anaesthetic gas flow changed to the incorporated nose-cone face mask and reduced to 1-2% isoflurane in 0.5L/min O<sub>2</sub>. A rectal probe was inserted into the animals to monitor body temperature, and respiratory bellows placed immediately inferior to the diaphragm to measure respiration rate. In order to maintain animal temperature a heated fan set to 36.8°C using feedback measured from the rectal probe was used to blow warm air down the bore of the magnet. Both body temperature and respiration rate were monitored remotely via SAM PC software (SA Instruments, USA) in the MRI control room throughout all data acquisitions. Small bore MRI gradients were used with a 39mm birdcage coil (RAPID Biomed, Rimpar, Germany) to transmit radiofrequency pulses and receive MRI signals. If mice had subcutaneous tumours image motion artefacts produced from respiration were reduced by setting the tumour within silicone rubber impression paste (CharmFlex, Dentkist Inc, UK). If an intravenous or intraperitoneal injection was required a primed remote line was set up before image acquisition and secured in place with tape and/or rubber impression paste. This allowed administration of substances at a later timepoint after baseline data acquisition. Total scan time including experimental set up was limited to 3 hours anaesthesia per animal as stipulated in the project licence. Following MRI scans animals were placed in a recovery box and monitored for a minimum of 20min before returning to the IVC and holding facility.

### **2.4.2 Photoacoustic Imaging**

All photoacoustic imaging (PAI) experiments were performed on the in-house system built by the UCL Department of Medical Physics and Bioengineering located within CABI. The system set up and specifications are discussed in greater depth in the relevant chapter. Animals were taken in IVCs to the preparation section within the PAI room, with experimental flow designed to allow one animal at a time to then be taken to the anaesthetic induction box. Animals were anaesthetised with 4% isoflurane in 1L/min O<sub>2</sub>.

Once anaesthesia was achieved animals were placed on a cradle specifically designed to fit the PAI sensor, with a window 15x15mm permitting access to area to be imaged. The area of interest, either a subcutaneous tumour or physiologically normal mouse flank, was then wiped with a water based lubricant (Johnson&Johnson, USA) to enable acoustic coupling with the PAI sensor, and the cradle put in to place within the scanner. When in position the animal received 1-2% isoflurane in 0.5L/min O<sub>2</sub> via nose-cone face mask. A warm air blower coupled to a thermal chamber was used to maintain animal temperature, and respiration monitored visually through the Perspex wall of the chamber. Data acquisition was then performed via the associated computer control system. Total scan time including experimental set up was limited to 3 hours anaesthesia per animal as stipulated in the project licence, but was typically much less than this, with 1hr usually enough to acquire multiple scans. Following PAI scans animals were left within the heated chamber, and isoflurane switched off to allow breathing of O<sub>2</sub> until recovery. Animals were then returned to IVCs and monitored for a minimum of 20min before returning to the holding facility.

### **2.4.3 Bioluminescence Imaging**

An IVIS Lumina system (PerkinElmer, USA) was used to acquire bioluminescence images of firefly luciferase gene transfected cell lines. For whole body *in vivo* images animals were administered D-luciferin (Biosynth, USA) from a stock concentration of 30mg/ml prepared in sterile saline solution and injected intraperitoneally (i.p.) at 5ml/kg for a total dose of 150mg/kg. The substrate was allowed to biodistribute for 15 minutes to allow a plateau of peak emission before image acquisition. Animals were anaesthetised at 12 minutes post injection with inhalational isoflurane at 4% in O<sub>2</sub> then placed within the imaging chamber with nose cone isoflurane supply reduced to 1.5% for maintenance. Imaging parameters were set for 1s, 30s and 60s exposure time with no binning. Photon count was calculated over a user defined region of interest (ROI) using VivoVision software (PerkinElmer, USA) with photon emitted per second per steradian (p/s/str) used to define total photon flux and average radiance.

## **2.5 Tissue collection**

In order to investigate *ex vivo* any changes in pathophysiology observed *in vivo* mice were sacrificed and biological tissue specimens were excised and kept for analysis as either fixed or frozen samples.

### **2.5.1 Formalin fixation of samples**

Samples to be used for morphological immunohistochemistry were preserved via formalin fixation. Samples were placed in sterilin containers (ThermoFisher Scientific, Cambridge, UK) containing 10% neutral buffered formalin (Sigma-Aldrich, Gillingham, UK ) and left for a minimum of 48hrs before processing to allow full fixation. Samples were then processed at UCL Department of Histopathology by dehydration through a series of increasing ethanol solutions, following which they were embedded in paraffin blocks and sectioned on a microtome (model RM 2135, Leica, UK) at 5µm thickness, and transferred to a heated section-bath for around 5 minutes. Individual sections were then picked up onto polysine microscope slides (VWR international, Leicestershire, UK) and placed onto a hotplate for ≈10min before placing into an oven set to 65°C for a minimum of 1 hour. Slides were then stored at room temperature until required for staining.

### **2.5.2 Frozen storage of samples**

For fluorescence immunohistochemistry, samples were snap-frozen in order to preserve localisation of both tissue antigens and injected markers of perfusion and hypoxia. For this the sample was excised and placed in pre-cooled isopentane (Sigma-Aldrich, Gillingham, UK), then lowered gradually in to a dewer containing liquid nitrogen (BOC, UK). Once frozen, samples were transferred to labelled sterilin containers and stored in a -80°C freezer (model U570 premium, New Brunswick Scientific) until sectioned. For sectioning, frozen samples were mounted in OCT embedding matrix (Lamb RA, ThermoFisher Scientific, Cambridge, UK) and cut on a cryostat (model CM3050 s, Leica, UK) at 10µm thickness and picked up via contact on to polysine microscope slides (VWR international, Leicestershire, UK). Slides were then stored at -80°C until required for histochemistry.

### **2.5.3 Haematoxylin and eosin staining**

For basic cell morphology and tissue structure haematoxylin and eosin (H&E) staining was performed. Below are the steps used for the H&E protocol staining:

- 1) Deparaffinise slides in histoclear for 10 minutes and rehydrate by 5 minutes each in 100% IMS, 70% IMS, H<sub>2</sub>O.
- 2) Place slides in distilled H<sub>2</sub>O for 5 minutes.
- 3) Place slides in haematoxylin for 5-10 minutes.
- 4) Wash thoroughly in tap H<sub>2</sub>O.
- 5) Dip in acid/alcohol (1% HCL/70% IMS) for a 1 second.
- 6) Wash thoroughly in tap H<sub>2</sub>O.
- 7) Place slides in eosin for 30 seconds.
- 8) Wash thoroughly in tap H<sub>2</sub>O.
- 9) Dehydrate slides in 70% and 100% IMS
- 10) Place slides in histoclear for 5-10 minutes.
- 11) Mount coverslips on to slides with DPX.
- 12) Visualise and capture microscopy image.

### **2.5.4 Double fluorescence immunohistochemistry**

For specific CD31 antigen marker for blood vessels and hypoxia via anti-pimonidazole immunohistochemistry the following protocol was used:

- 1) Fix sections in acetone for 10 minutes.
- 2) Air dry sections for a few seconds and circle with wax pen.
- 3) Rehydrate sections in PBS.
- 4) Apply 3% normal goat serum/PBS for 20 minutes.
- 5) Tap off excess and apply Rat anti Mouse CD31 1:2 (Gift from Montevani lab) and Rabbit anti-pimonidazole (Hypoxypore, USA) 1:400. Leave for 1hr at room temperature.
- 6) Wash in PBS 3 Times (5 minutes each).
- 7) Apply Goat anti Rat 546 and Goat anti Rabbit 488 secondary antibodies (AlexaFluor, Invitrogen, Life Technologies, UK) both at 1:200. Leave for 1hr at room temperature.
- 8) Wash in PBS 3 Times (5 minutes each).
- 9) Visualise and capture microscopy image.

## **2.5.5 Injected biological markers**

### **2.5.5.1 Perfusion**

In order to visualise perfusion of a specific tissue of interest the fluorescent dye Hoechst 33342, used to stain the DNA of perfused cells, (Cambridge Bioscience, UK) was injected i.v. 60 seconds prior to schedule 1 killing and tissue snap freezing. A stock concentration was made up at 6.25mg/ml, covered from light and stored at 4°C. Animals were dosed at 2ml/kg (e.g. for an average 25g mouse 50µl would be injected) for a final dose of 12.5mg/kg. Tissue samples frozen with injected Hoechst 33342 were kept shielded from light at all times where possible.

### **2.5.5.2 Hypoxia**

To visualise areas of hypoxia within the tissue of interest the small molecule pimonidazole (Hypoxyprom, USA), shown to be strongly correlated with oxygen electrode measurements in mouse tumours (5), was injected at least 30 minutes before schedule 1 of the animal. Stock concentration was prepared to 10mg/ml and animals dosed at 6ml/kg (e.g. for an average 25g mouse 150µl would be injected) for a final dose of 60mg/kg.

## **2.6 Microscopy**

### **2.6.1 Brightfield**

For all brightfield microscopy, slides were visualised on a Zeiss Axioskop2 microscope (Carl Zeiss, UK) using 10x and 20x objectives, with images captured using an AxioCam (Carl Zeiss, UK) high resolution digital camera. For data acquisition Axiovision software v 4.8(Carl Zeiss, UK) was used. Composite images of whole tumour sections were acquired on an Axioskop 2 microscope by stitching together a large number of individual tiles at high resolution.

### **2.6.2 Fluorescence**

Slides were visualised on a Zeiss AxioImager microscope (Carl Zeiss, UK) using 10x and 20x objectives, with images captured using an AxioCam (Carl Zeiss, UK) high resolution digital camera. For data acquisition Axiovision software (Carl Zeiss, UK) was used. Multi-fluorescence high resolution composite tiled images of whole tumour sections were then acquired.



## 2.7 References

- (1) [http://www.lgcstandards-atcc.org/?geo\\_country=gb](http://www.lgcstandards-atcc.org/?geo_country=gb) , accessed 2013.
- (2) Workman P, Aboagye EO, Balkwill F, Balmain A, Bruder G, Chaplin DJ, et al. Guidelines for the welfare and use of animals in cancer research. *Br J Cancer* 2010;102:1555-77.
- (3) Chia R, Achilli F, Festing MF, Fisher EM. The origins and uses of mouse outbred stocks. *Nat Genet* 2005;37:1181-6.
- (4) Tomayko MM, Reynolds CP. Determination of subcutaneous tumor size in athymic (nude) mice. *Cancer Chemother Pharmacol* 1989;24:148-54.
- (5) Raleigh JA, Chou SC, Arteel GE, Horsman MR. Comparisons among pimonidazole binding, oxygen electrode measurements, and radiation response in C3H mouse tumors. *Radiat Res* 1999;151:580-9.

# Chapter 3 In vivo photoacoustic imaging of tumour pathophysiology

---

## 3.1 Introduction

### 3.1.1 The applicability of photoacoustic tomography for *in vivo* imaging

Photoacoustic tomography is ideally suited to assessing tumour pathophysiology *in vivo*; it is completely non-ionising and non-invasive, with no detrimental effects through its use. Using the high tissue-based contrast and spectroscopic capability of optical techniques and the spatial resolution of ultrasound, PA imaging can provide highly detailed structural and functional information on the tumour microenvironment (1). The imaging niche in which this fits is one of tens to hundreds of micron resolution and millimetre depth penetration (2), making it well placed to provide macro-environment changes at the tumour-localised level. **Figure 3.1** shows the depth penetration and spatial resolution of PAI in comparison to other common biomedical imaging approaches (3). As can be seen PAI is well suited to imaging specific biological phenomena such as tumour angiogenesis and progression of disease. Previously published studies using PA systems have shown preliminary tumour imaging data (4-7); however the results of these studies were unsatisfactory in terms of imaging depth, which was limited to a few hundred microns, which is insufficient to encompass whole growing tumours, and gives poor image quality. The vascular anatomy was not clearly defined, making tumour vasculature differentiation from normal tissue virtually impossible. These PA systems were based on detection of ultrasound waves using piezoelectric detectors, which limits image quality due to insufficient broadband detection of most clinical piezoelectric devices, and limited apertures of available arrays (8).

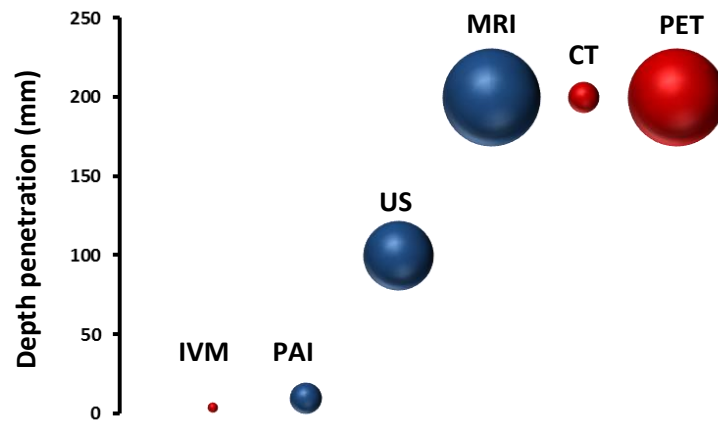


**Figure 3.1 Imaging modality depth penetration and spatial resolution comparison**

Imaging modalities are: Intra-vital Microscopy (IVM), Photoacoustic Imaging (PAI), Ultrasound (US), Magnetic Resonance Imaging (MRI), Computed tomography (CT) and Positron Emission Tomography (PET). Penetration through tissue can be seen on the Y axis, with MRI, CT and PET considered whole body imaging. Size of sphere relates to spatial resolution possible with each modality (IVM 1-2μm, PAT 5-500μm, US 500-1000μm, MRI 1000μm, CT 100μm, PET 1000μm). Colour of sphere denotes whether the modality is invasive or uses ionising radiation (Red) or non-invasive (Blue).

This chapter introduces the basic physics of PAI before expanding on the concept of photoacoustic tomography (PAT) imaging through an all-optical, non-piezoelectric detector based system used at UCL. Basic *in vivo* experiments then demonstrate the increased suitability of the PAT system over other optical imaging systems for imaging tumour vascular pathophysiology in a longitudinal manner.

### 3.1.2 Photoacoustic effect

The photoacoustic effect is the production of sound following absorption of optical energy, first noted by Alexander Graham Bell in 1880 (9). In the realm of biomedical imaging this phenomenon is utilised to acquire images and functional information on the location of certain energy absorbers within tissue. Significant advances in utilising the photoacoustic effect for scientific and technological research were only possible following the creation of the first laser in the 1960s (10). The reasons for this can be found in the fundamental characteristics of laser light and its interaction with biological tissue. These aspects central to PA imaging are described below.

### 3.1.2.1 Laser principles

The light used by Bell in 1880 was simply sunlight condensed and modulated through a series of mirrors. The problem with this light source is a lack of consistent power which is also often of low intensity, a multiple-wavelength or polychromatic spectrum, and an incoherent and divergent means of propagation. Light amplification by the simulated emission of radiation, first proposed by Einstein in 1917 (11) and now commonly known by its acronym *laser*, overcomes these problems: laser light is produced when an electron, orbiting its atom in a high energy state, is struck by a photon. This leads to the electron returning to a resting state around the atom and emitting two photons with the same energy, frequency and direction (12). These emitted photons stimulate the emission of subsequent photons, leading to the light characteristics that make it ideal for PA imaging:

- Spectral purity: all forms of energy that propagate through space as waves can be represented on the electromagnetic spectrum. ‘White light’ or sunlight is a mix of different wavelengths within the visible range. Laser light in contrast is emitted at a single wavelength. This can be in the hundreds of nanometre range for visible light (400-700nm) through to infrared (700nm-1mm). This spectral purity allows PA excitation systems to be tuneable and to interrogate samples at different wavelengths with high specificity.
- Coherence and collimation: light emitted through stimulated emission of radiation produces wavelengths that are in phase in both time and space. This creates a directionality of laser beam excitation. Laser beams are emitted in parallel and therefore have a defined beam diameter. No divergence from this beam occurs, allowing the energy to be identical over any distance, with no decrease in energy intensity until deposited within the tissue of interest (13).
- High intensity: a final attribute of lasers worth noting is the high peak power attainable. This allows high energy to be contained within each nanosecond pulse, thereby achieving higher PA wave production due to increased signal to noise whilst staying within safety limits (14).

### 3.1.2.2 Interaction with tissue

Laser light incident on biological tissue will result in a number of consequences. These are depicted in **figure 3.2** and described below (13):

- Reflection: approximately 4-7% of laser light incident on skin will simply be reflected back from the tissue (15). This depends on the angle at which it interacts with the skin surface, and affects how much energy is absorbed within the tissue.
- Scattering: once in biological tissue, laser light is spread from its original beam through refraction in different tissue areas, mainly through striking dermal collagen, which alters the path of the photons. This results in increased spatial distribution of the energy of the applied laser beam. The larger the beam diameter size the less scattering occurs and deeper penetration depths achieved. The laser light is also scattered less with increased wavelength, as scattering is inversely proportional to the incident light wavelength (16).
- Absorption: the first law of photobiology, known as the Grotthus-Draper law, states that only absorption of incident laser light will produce a biological effect. Reflection and scattering will affect the initial distribution of the absorbed deposited energy however, so should also be taken into consideration. Absorption occurs at particular molecules known as chromophores; biological chromophores are discussed below.
- Transmission: any light from the laser that is not reflected, scattered or absorbed will pass through the tissue either to deeper lying structures or completely.

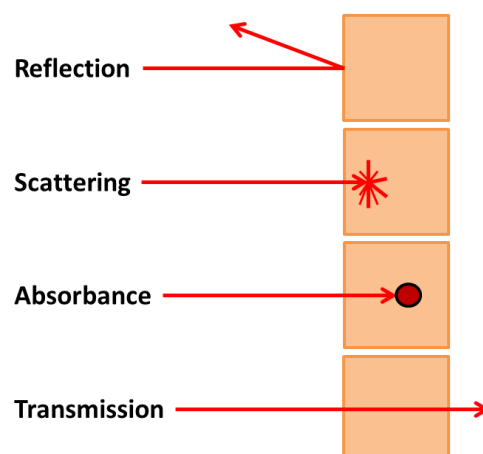


**Figure 3.2 Light interaction with biological tissue**

Light that is incident on biological tissue will have a combination of the effects shown above; it can be reflected from the surface of the tissue, photons that do penetrate the tissue will be scattered and either absorbed or transmitted through to the other side. For the purpose of PAT imaging absorption is the main effect required.

### 3.1.2.3 Tissue chromophores

Energy from the deposited laser light will be absorbed by specific chromophores. In biological tissue the most frequent chromophores are water, melanin, oxyhaemoglobin, deoxyhaemoglobin, lipids, collagen and elastin. The absorption coefficient for these chromophores over a range of wavelengths can be seen in **figure 3.3** (8).

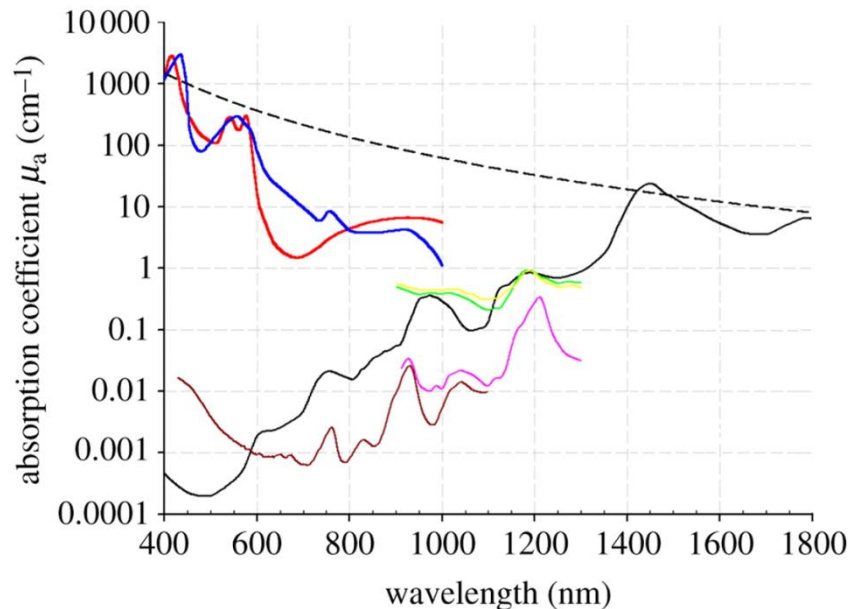


**Figure 3.3 Absorption coefficient for tissue chromophores**

The graph shows absorption in  $\mu_a$  (cm<sup>-1</sup>) for a range of tissue chromophores, at excitation wavelengths from 400nm to 1800nm. Chromophores shown are: oxyhaemoglobin (red), deoxyhaemoglobin (blue), melanin (dashed black), 80% water in tissue (black), 20% water in tissue (brown), elastin (yellow), collagen (green), and lipid (pink).

As can be seen from **figure 3.3** the main tissue chromophores in the 600-900nm section of the spectrum are oxyhaemoglobin, deoxyhaemoglobin and melanin. All other major chromophores are at least one order of magnitude lower than these three; this creates a biological imaging ‘window’ in which haemoglobin and melanin are the predominant PA signal-producing chromophores. These images will therefore reflect the deposition of haemoglobin within the vascular network of the tissue, and also areas of melanin, if present, in the form of pigmentation. Absorbance of light energy by a chromophore can result in the following biological responses:

- Photothermal: this is one result from the conversion of light energy to heat. It is dependent on the wavelength and pulse duration used, and therefore the fluence (J/cm<sup>2</sup>) or energy density achieved. Photothermal effects can severely damage tissue if the fluence is too great. Significant increases in temperature are therefore

not desired when acquiring PA images, and are kept below the Maximum Permissible Exposure (17) through the use of pulsed laser excitation beams.

- Photochemical: certain chromophores, either directly or following a change in conformation upon absorbing energy, elicit chemical reactions within the tissue. Although not a common result of laser light absorption, this has been used for photodynamic therapy, through the use of photosensitizers generating reactive oxygen species (18).
- Photomechanical: this response occurs when high energy and short pulse duration laser excitation is used. Thermal expansion of the chromophore occurs which creates an initial pressure distribution and waves of ultrasound to propagate outward through the tissue from the absorber.

#### 3.1.2.4 Physics of chromophore PA signal production

Once laser energy is deposited in the tissue chromophores it produces a rapid photomechanical response with a temperature increase of less than 0.1K due to the nanosecond pulsed nature of the beam. This is not sufficient to cause photothermal destruction of tissue, but does lead to a photomechanical induced distribution of pressure. This pressure is released in the form of acoustic waves in the tens of megahertz range with amplitudes of less than 10 kilo-pascals. These acoustic waves propagate back through the tissue and can be detected by various ultrasound sensor systems. The physics of photoacoustic signal production for a specific point  $r$  can therefore be described as the initial pressure distribution  $p_0$ , given by the thermodynamic conversion efficiency  $\Gamma$  of the absorbed optical energy at that point  $H(r)$ ;

$$p_0(r) = \Gamma H(r)$$

The thermodynamic conversion efficiency  $\Gamma$  is known as the Grüneisen coefficient, and is a dimensionless constant that describes the degree of conversion of heat to pressure. It is formulated as;

$$\Gamma = \frac{\beta c^2}{C_p}$$

In this equation  $\beta$  is the volume of thermal expanse,  $c$  is the speed of sound within the tissue, and  $C_p$  is the specific heat capacity at constant pressure. These parameters account

for the conversion efficiency of the deposited energy. However, the absorbed optical energy  $H(r)$  is also dependent upon a number of factors;

$$H(r) = \mu_a(r)\theta(r; \mu_a, \mu_s, g)$$

In this equation  $\mu_a(r)$  is the local absorption coefficient of the chromophore and the remaining  $\theta(r; \mu_a, \mu_s, g)$  is the optical fluence of the applied laser beam, where  $\mu_a$  is the absorption coefficient,  $\mu_s$  is the scattering coefficient, and  $g$  is the anisotropy factor.

This shows that the initial pressure distribution  $p_0$  is dependent upon mechanical and thermodynamic properties of the tissue, and optical parameters of the applied laser beam. The greatest source of variance in PA imaging however can be found in the applied laser beam, as the Grüneisen coefficient  $\Gamma$  is thought to change minimally. PA imaging is therefore often described as absorption based, as it is the spatial absorption of photons encoded onto acoustic waves that provides the PA signal for image reconstruction. It is not however a simple measure of the local absorption coefficient  $\mu_a$ , as this is dependent on the fluence  $\theta$  which is also dependent on  $\mu_a$ ; the initial pressure distribution  $p_0$  is therefore a non-linear function of  $\mu_a$ . The assumption that the thermodynamic conversion efficiency (Grüneisen coefficient  $\Gamma$ ) is non-variant within tissue is also of importance; whilst it is true that PA images correspond primarily to optical absorption and photon scattering it is recognised that the Grüneisen coefficient may have a role in image contrast (8). This is therefore a major caveat to any attempt at estimation of quantitative spectroscopy using PA imaging (19).

### 3.1.3 Advantages of PA tomography systems

The in-house PA system developed by UCL Medical Physics and Bioengineering (Prof Beard's group (20)) is a tomography- mode PA scanner. It has many advantages over other PA imaging approaches; the laser incident upon the tissue sample is of large diameter which provides full field illumination, giving a larger tissue volume irradiated by diffuse light. This enables imaging of greater fields of view than PA systems that concentrate on microscopic imaging. PA microscopy leads to images with very high resolution, but the area of interest that it is possible to image is small. On the other hand, other tomographic PA systems that use standard ultrasound detectors are capable of imaging large areas but with limited resolution of detected ultrasound.

Another advantage of the UCL PA scanner is that it is 'backward mode', so that the PA signal is detected in the opposite direction of the applied laser beam. This eliminates the



need for complex ultrasound detection arrays, and allows the characterisation of the area of interest that is directly in front of the sensor. By using an all optical Fabry-Perot interferometer the laser excitation light can be applied directly to this area of interest, making the UCL scanner suited to imaging superficial anatomy. It is the least restrictive of all current PA systems available, and therefore well suited to image the developing tumour vasculature over time.

### **3.1.4 Why it should be used for tumour pathophysiology**

PA tomography through the system developed at UCL Medical Physics has the potential to provide detailed structural and functional information on living tissue in greater detail than systems already described. The major advantages are that it is a backward-mode system that facilitates illumination of the area of interest, and therefore gives superior imaging of superficial anatomical features, and in addition it is an all-optical system which provides better acoustic performance compared to piezoelectric receivers.

The superficial vascular network of tissues can be readily imaged with this system, as has been previously demonstrated *ex vivo* (21); this should translate to imaging whole tumours *in vivo*, with the abnormal pathophysiological and progression of these tumours evident over time. It is the aim of this chapter, therefore, to apply the PAT system to the study of subcutaneous tumours *in vivo* and establish what is possible using this approach. Through a series of experiments, the parameters affecting *in vivo* tumour visualisation will be tested, in order to determine what structural and functional information can be obtained in preclinical studies of tumour pathophysiology, with the ultimate aim of clinical translation.



#### **3.2.1.1 PC controller**

All aspects of image acquisition were fully automated via PC control; the wavelength of laser excitation was controlled via the optical parametric oscillator (OPO), phase-bias optimisation of the interrogation laser and optical x-y scanner for detection of PA signal, and digital storage oscilloscope (DSO) for PA waveform raw data capture and storage, were all fully controlled remotely from the PC via LabVIEW (National Instruments, US) and Matlab (MathWorks, US) software. Reconstruction of raw data was performed in Matlab using established algorithms for correction of sound attenuation in tissue (22, 23).

#### **3.2.1.2 Laser excitation source**

The laser energy used to induce photoacoustic signals was created using a Q-switched-Nd:YAG (Quality-switched Neodymium-doped Yttrium aluminium garnet) laser (Quanta-Ray PRO-270, Newport Spectra Physics), the output of which was used to pump a fibre-coupled optical parametric oscillator (OPO, GWU-Lasertechnik, Germany). This creates optical pulses of 8ns duration at a repetition frequency of 10Hz tuneable over the wavelength range 410-2100nm. The optical fibre produced a beam of 2cm diameter which was incident on the underside of the planar detection sensor and bathed the tissue of interest in broad-field illumination.

#### **3.2.1.3 Planar sensor detection system**

The sensor used to detect generated PA signals was a Fabry-Perot interferometer (FPI), acoustically coupled to the tissue of interest via a droplet of water. The Fabry-Perot sensor head was created by vacuum deposition of a 38µm parylene C polymer film between two dichroic mirrors. The dichroic mirrors are highly reflective between 1500nm and 1650nm but transparent in the wavelength range 590nm-1200nm. This allows the laser excitation source to pass through the sensor head when it is between 590nm-1200nm and create PA signals that propagate backwards to the FPI and induce changes in its optical thickness, and therefore the reflected power intensity of the interrogation laser (**Figure 3.5**) (20). A fundamental limit of the lateral resolution with this system is the spot size of the light from the interrogation laser incident on the FPI and the step size used for the point-to-point raster scanning of the FPI. A 100µm interrogation laser step size will support a lateral frequency content up to 7.5 MHz. The bandwidth of the FPI sensor must be able to detect this frequency content. The standard FPI sensor is 40 microns thick which allows a bandwidth of 22 MHz, sufficient to detect all higher frequency content in the lateral dimension induced by changes in the FPI sensor thickness. This permits a lateral resolution

in the region of 100 microns. For the axial resolution, a sampling time of 10nS, which corresponds roughly to axial scan step size of 15 $\mu$ m, was used. This axial resolution worsens with imaging depth, as the high frequency contents of the PA signal gets attenuated more in tissue. Even if high frequency PA signals are generated in tissue at depth they will become attenuated as they travel through tissue to the sensor.

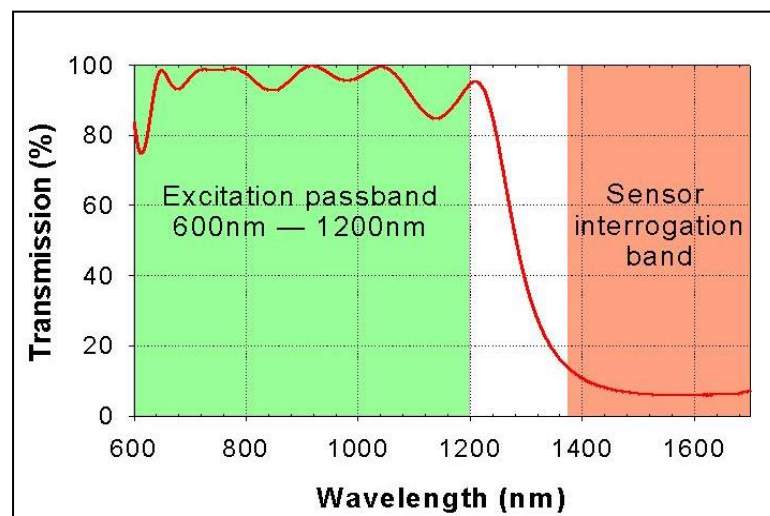


**Figure 3.5 Reflectance characteristics of the Fabry-Perot Interferometer sensor**

The graph shows the transmission through the Fabry-Perot interferometer sensor head for a range of laser wavelengths. For the laser excitation source at 600nm-1200nm the interferometer is transparent, whilst for the sensor interrogation laser the interferometer is 95% reflective.

#### 3.2.1.4 Interrogation laser

In order to detect the PA-induced changes in sensor optical thickness, a continuous wave focussed interrogation laser beam produced from an external laser (Thorlabs ECL5000DT), nominally at 1550nm, was raster scanned across the FPI using a galvanometer mirror-based x-y scanner. At 1550nm the dichroic mirrors are highly reflective (95%) to the laser light and therefore the interrogation laser does not pass through into the tissue. The interrogation laser is only nominally at 1550nm because in practice at each point of the x-y scan the polymer film spacer of the sensor has a different optical thickness, so the wavelength is set to that which provides the maximum slope on the interferometer transfer function, thus achieving the optimal sensitivity. This phase biasing is achieved by first scanning a range of wavelengths that is greater than the free spectral range (FSR) of the interferometer (in the case of our 38 $\mu$ m FPI this is 18.8nm), which provides the wavelength dependent measure of reflectivity  $R(\lambda)$ . This measured reflectance is then plotted as a function of phase to get normalised interferometer transfer function (ITF), a derivative of which is normalised phase sensitivity  $S(\lambda)$ . The interrogation laser can then be set to  $\lambda_{opt}$ , the value which will give the maximum sensitivity. The whole process of phase-biasing takes  $\approx$ 50ms for each point (20).

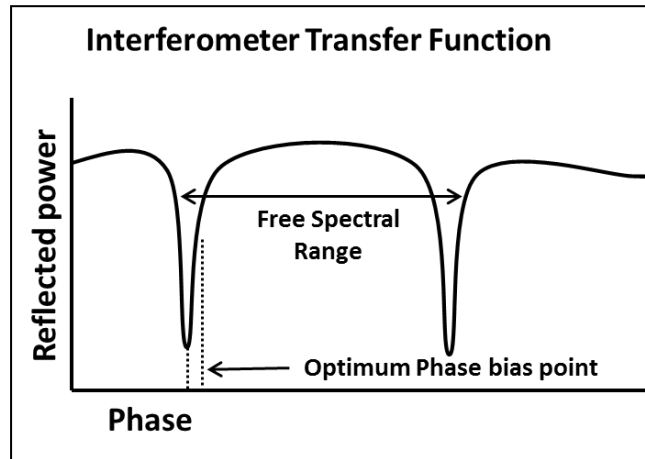


**Figure 3.6 Phase biasing of the Fabry-Perot interferometer**

The graph shows the interferometer transfer function for the Fabry-Perot sensor head. As each point of the sensor will have a different optical thickness, an optimal phase is selected for maximum sensitivity to reflected power for each point. This is achieved by first scanning a range of excitation wavelengths that cover the free spectral range (FSR) of the sensor point.

### 3.2.2 Signal acquisition and processing/DSO

The acquisition and processing of the PA signal is performed by the Digital Storage Oscilloscope (DSO); once a specific point is selected the  $\lambda_{\text{opt}}$  is set and the excitation laser fired at the same time as the DSO is triggered to record the PA waveform. A photodiode-transimpedance amplifier unit detects changes in the reflected power intensity and this is stored in the DSO. Once the waveform has been acquired the interrogation laser beam is moved to the next point and the procedure repeated, thereby recording the 2D (x and Y) pattern of acoustic waves incident on the sensor in a time (t) varying manner. The maximum scan size was 14mm by 14mm, with a usual scan comprising 20,000 waveforms and taking 8 minutes to acquire. Image reconstruction in 3D is therefore an inverse k-space method based on a Fourier transform of the x-y detected time-resolved photoacoustic signal, to recreate the initial pressure distribution caused by the absorbed energy.

### 3.2.3 Physiological monitoring

*In vivo* experiments were achieved by first anaesthetising the animals in an induction box at 4% Isoflurane before transferring them on to a specifically designed 3D-printed holder that clipped straight in to position on top of the planar detection system. This incorporated a nose-cone for maintenance of anaesthesia at 1-2% Isoflurane. A rectal probe was used to determine body temperature with a heated chamber maintaining animal core temperature to a constant 37°C. This chamber was made of Perspex, allowing respiration rate to be monitored visually. A depiction of the system set-up and photoacoustic detection principle can be seen in **figure 3.7**.

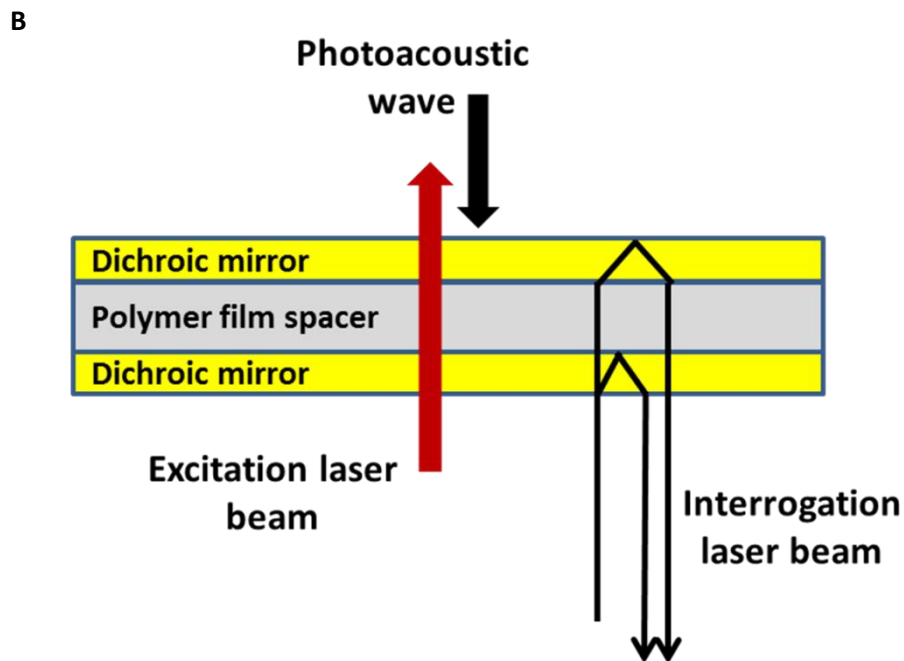
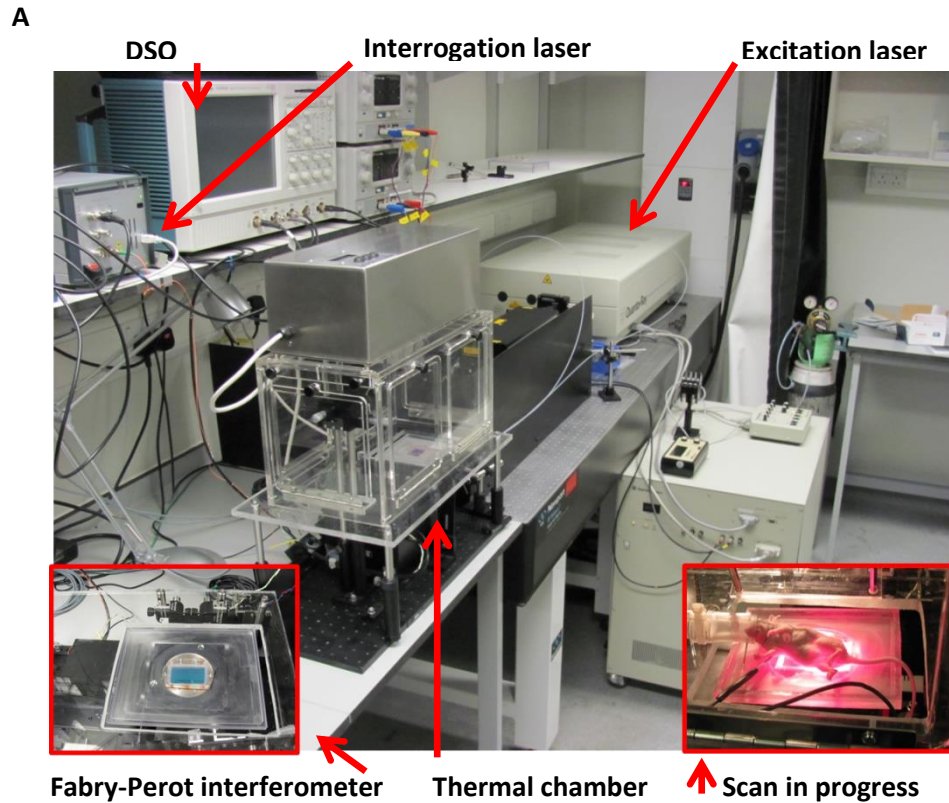


**Figure 3.7 Depiction of PA scanner and photoacoustic detection principle**

Panel **A** shows the PA scanner with major parts described in section 3.2.1 indicated. Panel **B** shows the functioning of the Fabry-Perot sensor head; the excitation laser is able to pass both dichroic mirrors of the sensor and produce a PA effect in the tissue of interest. This causes a PA wave to propagate back to the sensor, changing the thickness of the polymer film spacer. This change in optical thickness causes the reflected power intensity to vary, which can be detected by raster scanning an interrogation beam across the surface of the sensor.

### 3.2.4 Experimental design

#### 3.2.4.1 Initial PA scanner imaging capabilities

To compare the imaging ability of the UCL PA scanner to published data on absorption coefficient of haemoglobin, an initial *ex vivo* blood spectrum was acquired. Mouse blood obtained via cardiac puncture exsanguination (n=2, ~1ml each) was put in a well-slide and placed on top of the PA scanner sensor. A spectroscopic experiment was then performed at a single excitation point of the sensor, starting at 600nm and proceeding in steps of 2nm up to a maximum of 1000nm. Two data series were acquired, with results plotted as absorption coefficient ( $\mu_a \text{ cm}^{-1}$ ) at each wavelength, using published data for comparison (24).

The ability of the scanner to image blood vessels *in vivo* was initially demonstrated by imaging the superficial vasculature of the palm of my hand. A suitable location was found and a single scan at 600nm excitation was acquired for reconstruction.

A further exploratory experiment was performed to assess the effect of melanin on image acquisition prior to the main aim of investigating tumour vascular development and subsequent tumour imaging studies. A single C57BL/6 female 25g mouse was anaesthetised and the fur on the flank removed with hair removal cream. The flank of the animal was then imaged at 590nm, 600nm, 620nm, 640nm, 660nm, 680nm and 700nm excitation wavelengths.

#### 3.2.4.2 Inhalational gas experiments

To observe the effect of the inhalation gas, used to carry the anaesthetic, on systemic oxygen status of animals during *in vivo* blood vessel imaging, a series of experiments measured the acquired PA signal intensity over time with both pure oxygen (100% O<sub>2</sub>, BOC Healthcare, UK) and medical air (20.9%  $\pm$  0.5% O<sub>2</sub>, BOC Healthcare, UK). For this study n=3 mice were used for both oxygen and medical air over one hour of 1% Isoflurane anaesthesia for each gas, during which 5 scans per gas were acquired. The reconstructed data were used to visually assess any potential structural changes due to increased oxygen. Measures of PA signal were also taken from the data and an ANOVA two-factor with replication statistical test performed to check for any variation in signal between the inspired gasses. This was then compared to an external measure of systemic oxygenation status measured via a PulseOx laser Doppler system. N=6 animals were anaesthetised and the systemic blood oxygenation measured via a tail vein cuff. Results were plotted as percentage oxygenation status over time, and compared to PA acquired data.



#### **3.2.4.3 In vivo imaging of tumours**

After initial experiments on scanner capability and reconstruction of acquired data sets, the system was used to characterise the *in vivo* pathophysiological appearance of tumours. N=6 SW1222 and n=6 LS174T tumours were established in the flank of nude mice. Caliper measurements were used to monitor growth of the tumours, and PA scans acquired when tumours were palpable ( $\approx 0.1\text{cm}^3$  after 7 days). PA scans were continued every few days as the tumours developed until the animals were terminated via a schedule I method due to tumour size (maximum volume  $1.5\text{cm}^3$ ). In addition to the flank containing the tumour, *in vivo* images of selected normal tissues were acquired. Liver, kidney and spleen were all scanned both *in vivo* and *ex vivo*. PA images of tumour pathophysiology were compared with known immunohistological fluorescence images of hypoxia, perfusion and blood vessels, and also to vascular casts of the tumour blood vessel network. Raw data of micro-CT scanned tumour polymer casts were a kind gift from Dr Amos Folarin (25); this data was re-analysed, reconstructed and visualised with MatLab software alongside the acquired PA data sets.

### 3.3 Results

#### 3.3.1 Ex vivo blood analysis

**Figure 3.8** shows the acquired absorption coefficient  $\mu_a$  for whole mouse blood containing the anti-coagulant heparin across the excitation wavelength spectrum from 600nm to 1000nm using the in house system. The two acquired measurements are shown in yellow and green, whilst the known absorption coefficients for oxy-haemoglobin and deoxy-haemoglobin are shown in red and blue respectively. The acquired measurements lie initially between the oxy- and deoxy- haemoglobin spectra, between 600-675nm. After 675nm and up to the maximum 1000nm the acquired measurements are higher than the known haemoglobin spectra. The pattern of acquired data closely follows that of oxy-haemoglobin, albeit constantly 20-30  $\mu_a$  (cm<sup>-1</sup>) higher.

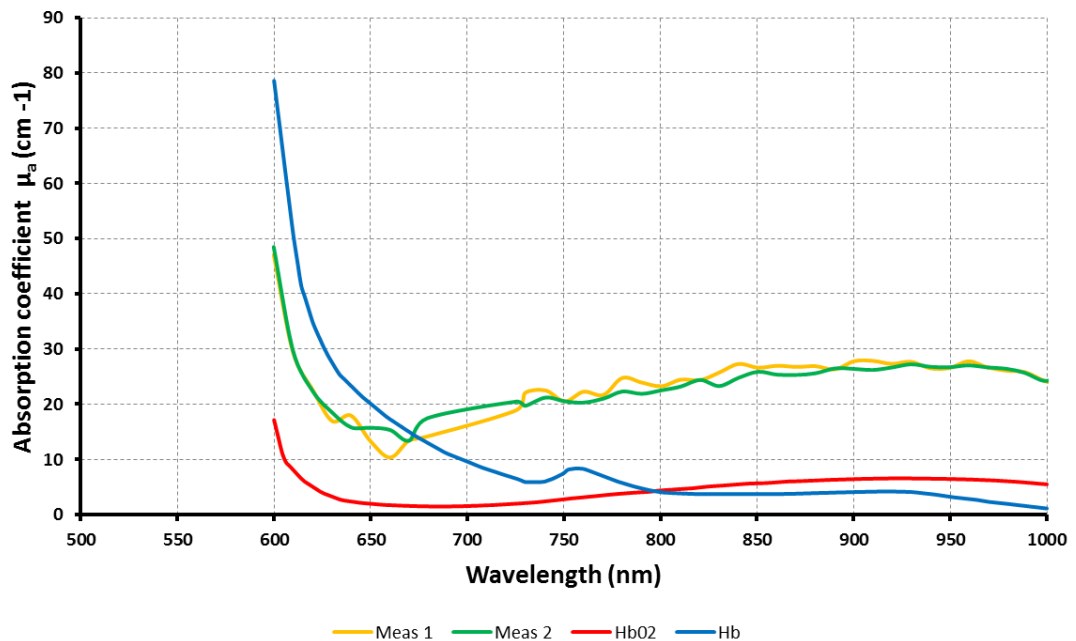


**Figure 3.8 Ex vivo PAT spectroscopy of whole blood**

Whole mouse blood acquired from cardiac puncture was used to obtain absorption coefficient ( $\mu_a$  cm<sup>-1</sup>) spectra of whole blood from the in-house PAT system (2 measurements taken, shown in yellow and green). This is compared to known absorption coefficients for oxy- and deoxy-haemoglobin (red and blue respectively)

### 3.3.2 Typical reconstruction of normal tissue vasculature

Represented in **figure 3.9** is a typical superficial vascular network from the palm of my hand. Both panel **A** and **B** are Maximum Intensity Projections (MIPs) in the Z direction of a 14mm by 14mm area in the X and Y direction. Resolution in the X and Y is 33.3 $\mu$ m, with resolution in the Z direction of 15.6 $\mu$ m. Panel **A** is of the entire Z-stack and shows a striated pattern across the entire figure, similar to that observed in finger printing, and a few tubular structures throughout the image. The striated pattern corresponds to the skin surface of my hand, whilst the tubular structures arise from the haemoglobin within the blood vessels. This is clearly shown by panel **B** where the top 100 $\mu$ m of the Z-stack has been removed; the majority of the signal from the skin has been removed, with the vascular network much more clearly defined. The origin of the observed striations is not clear, and thought to be potentially caused by a number of factors; chromophores within the skin, such as pigmentation, may be a cause but are unlikely at this wavelength of 600nm. As the signal is present within the striations of the skin it could be due to the lipids and oily nature of the dermis, or some chromophore such as carbon (e.g. from work surface dirt, etc) on the palm. Another possibility is that the contact achieved between the skin surface and the sensor is affected by the skin striations, resulting in the observed patterns. Whatever the cause the effect is easily removed from the acquired data, and not generally seen in subsequent imaging studies.

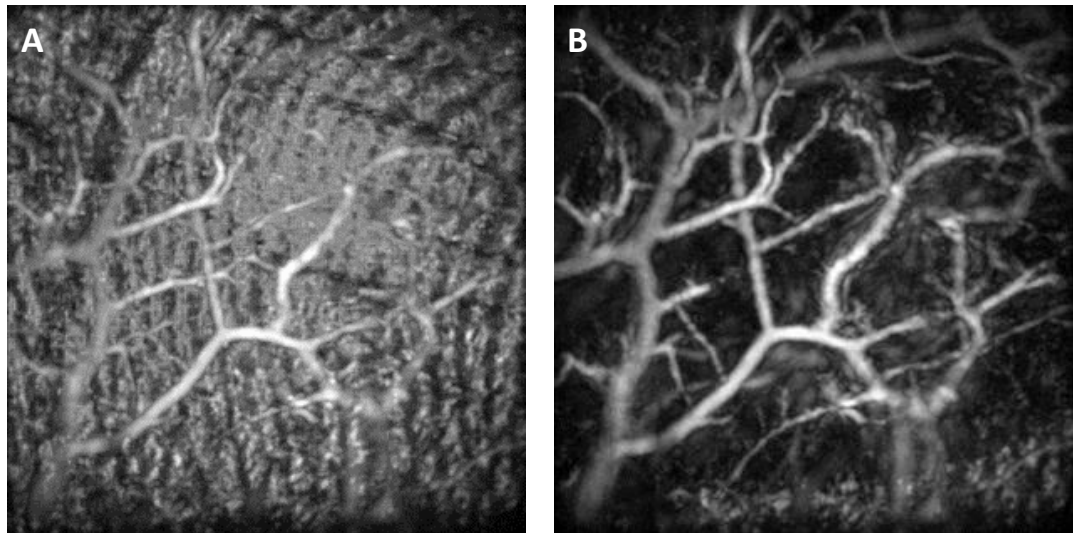


**Figure 3.9 Typical reconstruction of PA vascular image**

Maximum intensity projections (MIPs) are shown for a typical *in vivo* PA image at 600nm. Both images depict a 14mm by 14mm section of human palm. Panel **A** shows the entire Z direction, with the image in panel **B** having the top 100 $\mu$ m section removed. PA signal from both skin pigmentation and haemoglobin is observed.

### 3.3.3 In vivo effect of melanin

The effect of melanin on imaging with the PAT system can be seen in **figures 3.10** and **3.11**. Panel **A** of **figure 3.10** shows the species used and an example of the area imaged demarked by the red rectangle. Although the melanin pigmentation of the hair is clear to see, the skin appears to be non-pigmented. This translates to an *in vivo* image of the flank at 590nm excitation wavelength seen in panel **B**, which shows a 14x14mm MIP in the X-Y direction. Superficial blood vessel networks are evident, as well as patches of small globular signal highlighted by the red arrows. The blood vessels are visible due to the haemoglobin content, with the small globular areas being caused by the melanin present in the hair follicles within the skin. The speckled nature of signal caused by the melanin is potentially due to distribution of hair follicles or glandular structures containing melanin within the skin. Panel **C** shows an MIP in the X and Z direction on the right hand side, depicting the depth capabilities of the acquired data. A measure of PA signal magnitude in arbitrary units has been drawn through this data set, and the peaks of signal related to the features of the PA data set with red arrows. Whilst the skin surface is visible there are also many superficial vessels clearly defined within the image.

**Figure 3.11** represents a series of MIP images from the same mouse as in **figure 3.10**, acquired at increasing excitation wavelengths from 600nm up to 700nm. All panels are 14x14mm X and Y with 33.3 $\mu$ m resolution, and have displayed next to them the same line of PA signal magnitude drawn through at the same point of the data set. All peaks on the PA signal amplitude graph correspond to features within the data set; the main skin peak has been highlighted in all graphs with the red arrow. Some blood vessels are still visible at 600nm, as seen in the reconstructed image and also the signal peaks in the associated graph. At all excitation wavelengths above this the signal from the melanin in the skin dominates, and is the only thing visible in the reconstructed data. The graph of feature-corresponding PA signal shows that below the level of the skin the ability to discern vessels decreases as the excitation wavelength increases. This has been depicted by the blue line which shows signal at the level of background noise, which increases with higher excitation wavelengths.

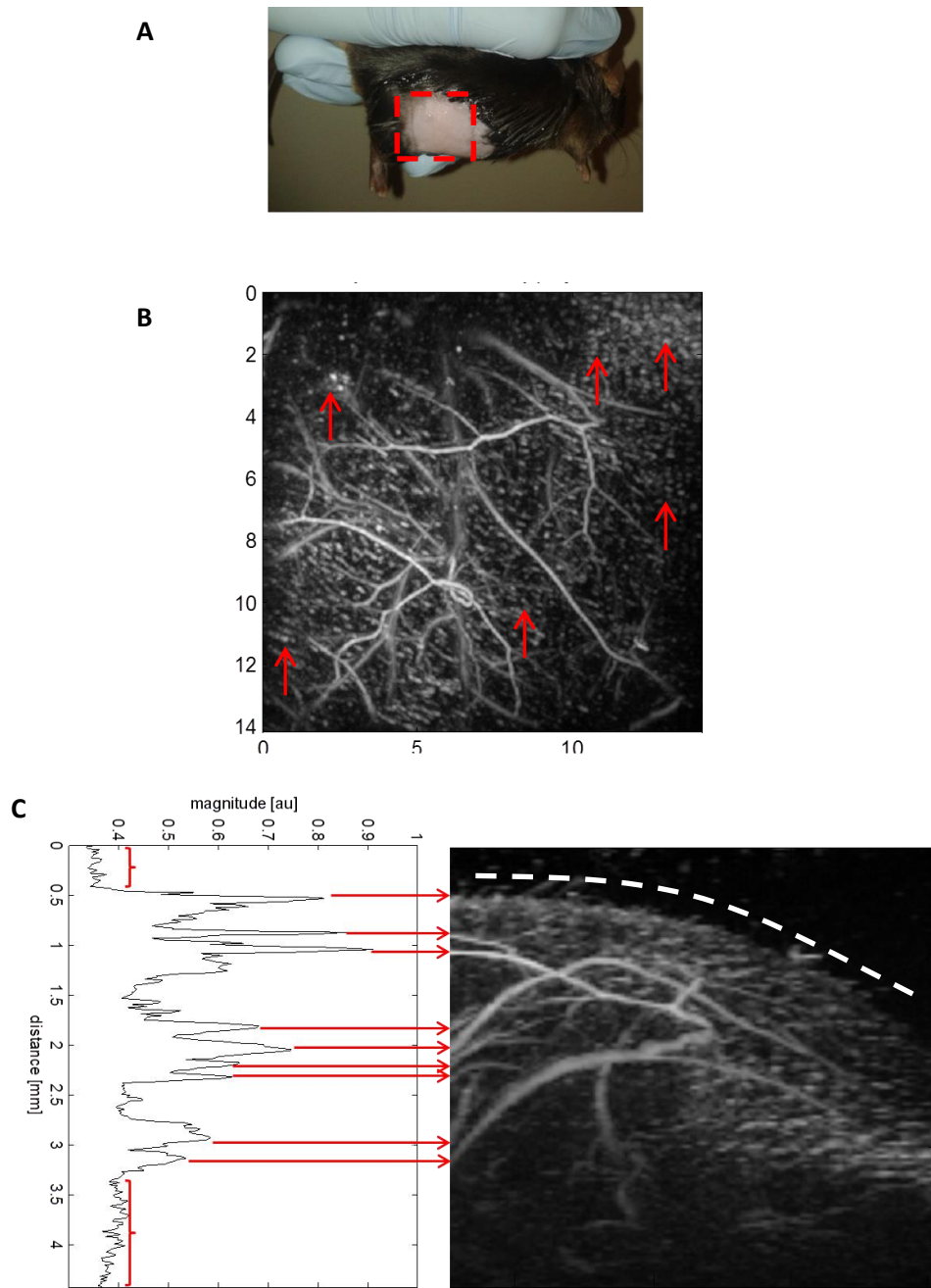


**Figure 3.10 In vivo effect of melanin**

Panel **A** shows the imaged area ( $n=1$ ) of a C57BL/6 mouse. Although the flank appears to have no pigmentation present the MIP image at 590nm, panel **B** clearly shows vessel structures and small globular regions of melanin deposition (examples highlighted by the red arrows). Panel **C** shows the magnitude of PA signal from the top of the Z-stack to the bottom of the acquired data, with peaks in the graph linked via red arrows to the anatomical feature they represent in the PA image. The skin surface is denoted by the dotted white line.

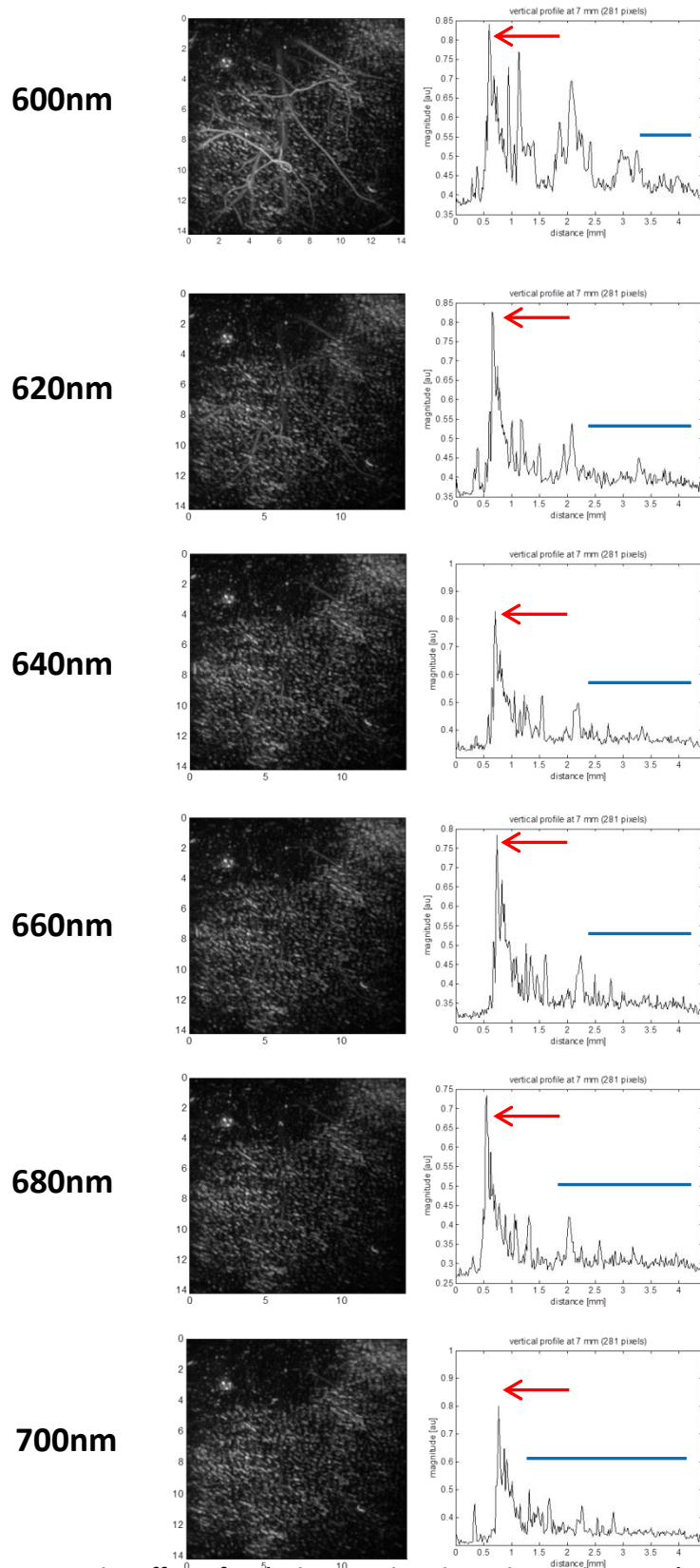


**Figure 3.11 In vivo effect of melanin on PA imaging at increasing wavelength**

The same area as shown in Fig. 3.10 is depicted here at increasing wavelengths. As the wavelengths increases above 600nm the signal from melanin is predominant and dominates the image. The corresponding graphs of Z-stack PA signals show that features below the level of the skin, shown by the peak highlighted by the red arrow, are lost, with an increasing PA signal waveform that is the same as background highlighted by the increasing blue bar.

### 3.3.4 Inhalation oxygen content effect on PA scanning

The effect of using either medical air or pure oxygen for animal anaesthesia on PA imaging can be seen in **Figure 3.12**. Panel **A** and **B** are MIP images acquired at 680nm after 60 minutes of breathing oxygen or medical air respectively. The structure and pattern of the observed vasculature is similar between the two images. An area of tissue, highlighted by the red discontinuous circle, does appear to vary in signal intensity between the two images. A measure of PA signal amplitude was taken across a clear vessel at the point indicated by the red line. A graph of the n=5 measures during the 60 minutes for each mouse and each gas can be observed in panel **C**, where box plots of these values are given for oxygen 1-3 (O1, O2 and O3) and medical air 1-3 (A1, A2 and A3). This shows similar values when compared across gasses with no significant difference observed. A level of variance within the 60 minute time window is observed for each animal, demonstrating a degree of variability in measured PA signal amplitude. The systemic oxygenation levels from pulseOx measurement can be seen in panels **D** (oxygen) and **E** (medical air). Error bars denote standard deviation of the mean, with the plot for oxygen being much more consistent and homogeneous through the group, with an average O<sub>2</sub> saturation for the group over the 60 minute period of 98.5%. The graph for medical air shows much more variability between animals, with average O<sub>2</sub> saturation being between 96 and 98%.

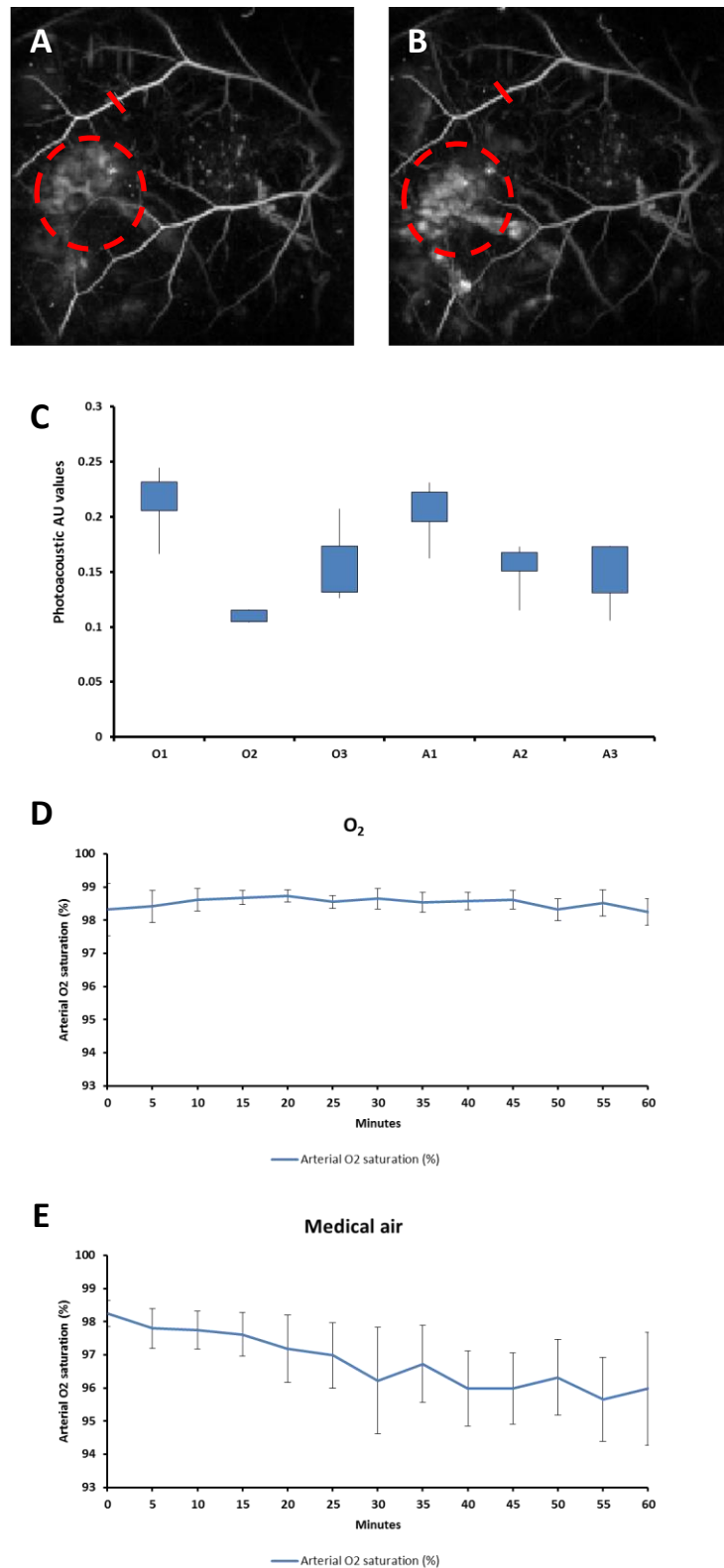


**Figure 3.12 Effect of inhalational oxygen on PA image acquisition**

Panel **A** and **B** show MIP PA images acquired at 680nm after 60 minutes of either oxygen or medical air respectively. The graph in panel **C** shows the PA signal amplitude measurements (n=5) for the same vessel over the 60min period for all animals (n=3, 1-3) for both oxygen (O) and medical air (A). No significant difference is observed between the two groups of measurements. Panels **D** and **E** show PulseOx measure systemic oxygenation status over 60min for n=6 animals. Error bars denote mean±SDM.



### 3.3.5 Three dimensional imaging of subcutaneous tumours

Imaging of subcutaneous tumours was achieved in all n=6 SW1222 and n=6 LS174T animals. **Figure 3.13** panel **A** shows a reconstructed 3D representation of an LS174T tumour at day 7 post injection of cells at an excitation wavelength of 610nm. The tumour is located in the centre of the image and is highlighted with a white arrow. Non-tumour associated superficial blood vessels of the skin are visible either side of the central tumour. A large diffuse PA signal is located beneath both the blood vessels and the tumour; this corresponds to the underlying muscle wall of the flank of the animal, highlighting that the tumour is in the subcutaneous space. As the data set is three dimensional, it is possible to optically section the data set at any point. This has been done for the present data set and can be seen in panel **B**. This shows that there is PA signal from every point of the 3D reconstruction. The image can be sectioned at any point through the tumour and provide information of the PA signal from that location. The image reconstructed here shows a maximum imaging depth of 6.5mm.

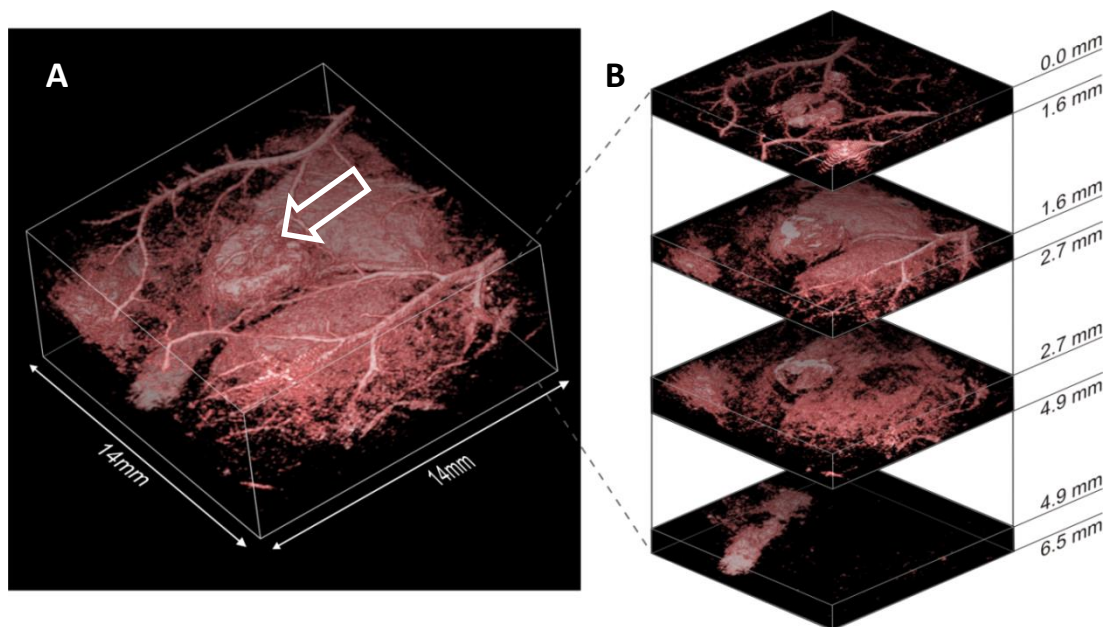


**Figure 3.13 3D PA imaging of subcutaneous tumours**

Panel **A** shows the three dimensional reconstruction of a subcutaneous LS174T tumour at 7 days after cell injection imaged at 610nm. The growing tumour is indicated by the white arrow. The data set can be optically sectioned, as is demonstrated in panel **B**; the data can be sectioned at any depth of the 6.5mm acquired and the PA signal information at that point observed.

### 3.3.6 Maximum depth imaged

Over the course of imaging the growing tumours, various depths were achieved depending upon signal detection. **Figure 3.14** shows the maximum depth imaged during these acquisitions. The tumour depicted is an SW1222 at 17 days after cell injection acquired at 793nm excitation wavelength. The high excitation wavelength of 793nm was used to increase tissue penetration and decrease attenuation effects, thereby allowing greater depth imaging. A scan area of 12x12mm is shown in the X-Y MIP (panel **A**), with the tumour located in the centre of the image. In the Y-Z and X-Z MIP images (**B** and **C** respectively) the spherical tumour can be seen to a depth of 9mm as depicted by the dotted line. When reconstructed in 3D in panel **D** it is clear that the tumour occupies the entire acquired data set.

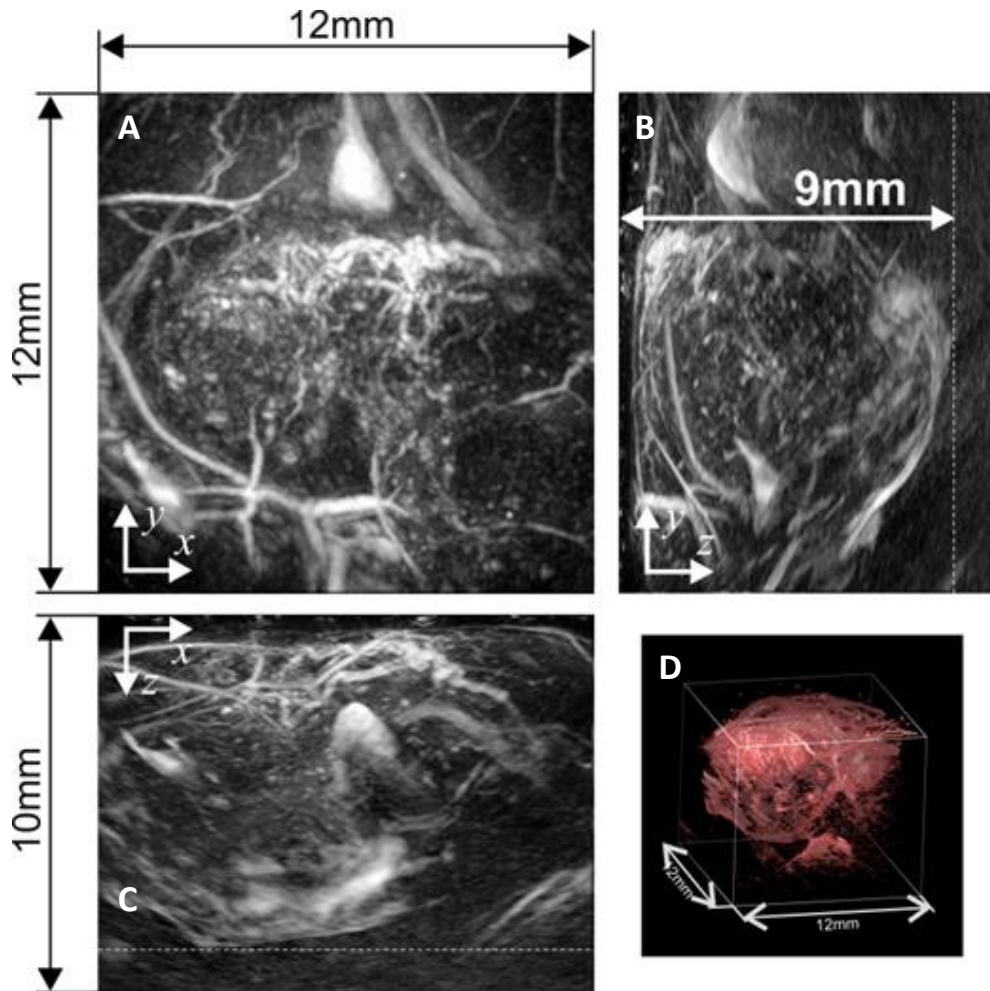


**Figure 3.14 Maximum PA depth imaging**

Panel **A, B** and **C** shows the three dimensional reconstruction of a subcutaneous SW1222 tumour at 17 days after cell injection imaged at 793nm. The orientation in XYZ is indicated by the white arrow. 3D reconstruction of this data set can be observed in panel **D**.

### 3.3.7 Comparative pathological features of tumour vasculature

When comparing the *in vivo* PA images of the two tumour types various pathological features were observed. **Figure 3.15** highlights these, and compares them to *ex vivo* analysis by micro-CT imaging of vascular casts and immunohistological staining of tumour sections. In the PA images (**A** and **B**) the location of the tumour has been indicated by the dotted red circle. The PA signal from within SW1222 tumours (**A**) shows a fine distribution of small areas of signal, with a few areas of signal drop-out. In contrast LS174T tumours show large areas of no signal, with a few large invading vessels within the tumour. Both SW1222 and LS174T tumours show typical angiogenic ‘corkscrew’ shape vessels outside of the solid tumour, highlighted by the red arrows. Reconstruction of the micro-CT polymer cast raw data of these two tumour types shows a similar pattern for extent of tumour vasculature. SW1222 tumours (**C**) show a homogeneous spread of fine tumour micro-vessels, with a few small areas of non-vascularised tissue. LS174T tumours on the other hand (**D**) have a heterogeneous pattern of smaller vessels and large areas of non-vascularised tissue, with a few very large thick invading blood vessels. When this is compared to immunofluorescence of the same tumour types a similar pattern is observed. Whilst this was observed by my own fluorescence imaging, the quality of image from experienced colleagues, such as Dr El Emir et al, allows greater comparison, and these are therefore presented in panels **E** and **F**. The images in panels **E** and **F** show CD31 for detection of blood vessels in red, perfusion by the injected marker Hoechst 33342 in blue, and anti-pimonidazole for the detection of hypoxia in green (data adapted from raw data acquired from El Emir et al (32)). SW1222 tumours (**E**) have a widespread expression of blood vessels, most of which is also perfused, shown by the co-localisation of the red and blue fluorescence. In the few areas of non-perfusion there is also hypoxia, shown by the green signal where no blue is apparent. LS174T tumours by contrast (**F**) have large hypoxic areas shown by the green, with only a few large intruding blood vessels that are perfused. These patterns of blood vessel expression are consistent across imaging modalities, and across the different tumour types imaged. The relative lack of spatial resolution for the PAT images when compared to images of CT casts and microscopy is outweighed by the fact that the process is completely non-invasive and carried out *in situ*. An example of this is the associated cork-screw vessels in the surrounding tissue, which is not imaged by the *ex vivo* modalities. As each modality is imaging the same associated parameters of vascular function the similarity achieved is notable and shows PA can be used to image tumour vasculature.

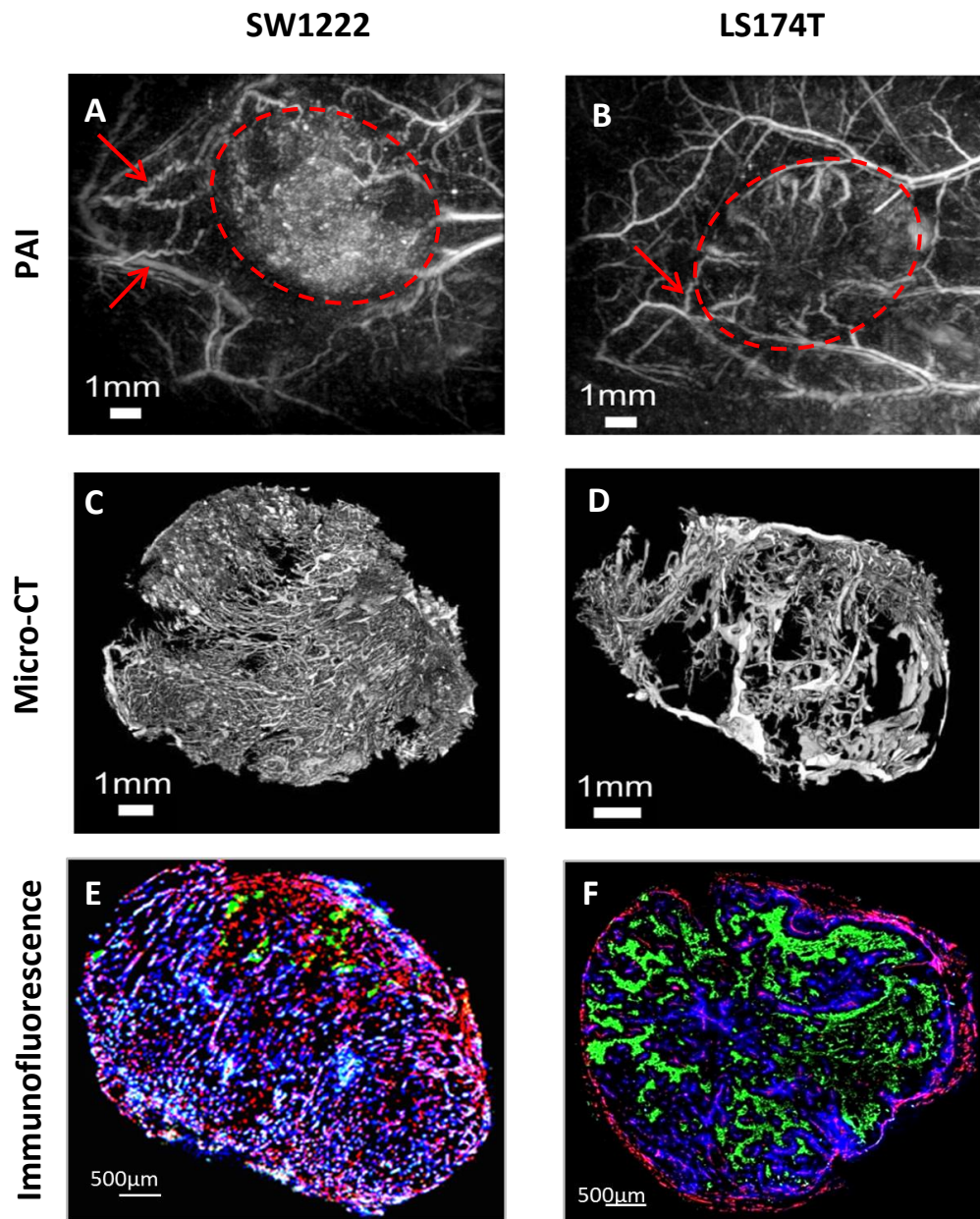


**Figure 3.15 Pathological features of tumours**

The top row **A** and **B** show *in vivo* images from PAI for SW1222 and LS174T tumours respectively. This is compared to *ex vivo* micro-CT imaged polymer casts of the microvasculature of these tumour types (**C** and **D** respectively) and immunofluorescence of tumour sections (**E** and **F**) showing CD31 for blood vessels in red, perfusion by Hoechst 33342 in blue and hypoxia by anti-pimonidazole in green.



### 3.3.8 Development of tumours over time by PAT

As tumours were imaged over a number of days it was possible to observe the progression of the developing tumour and the associated vasculature. **Figure 3.16** shows an example of this for both LS174T and SW1222 tumours imaged at day 7, 8 and 12. Arrows in red or green denote similar locations between scans for orientation purposes. The exact wavelength used is denoted at the bottom left hand corner of each image. The images from day 7 and 8 are clearly of the same area of the flank, and show a diffuse pattern of PA signal at the location of the tumour for both tumour types, albeit more pronounced in the LS174T. Images from day 12 show identifiable architecture from previous days in the surrounding non-tumour associated vasculature. The PA signal from the centre of the tumour and the angiogenic feeding vessels however is vastly changed, with a more defined location of signal.

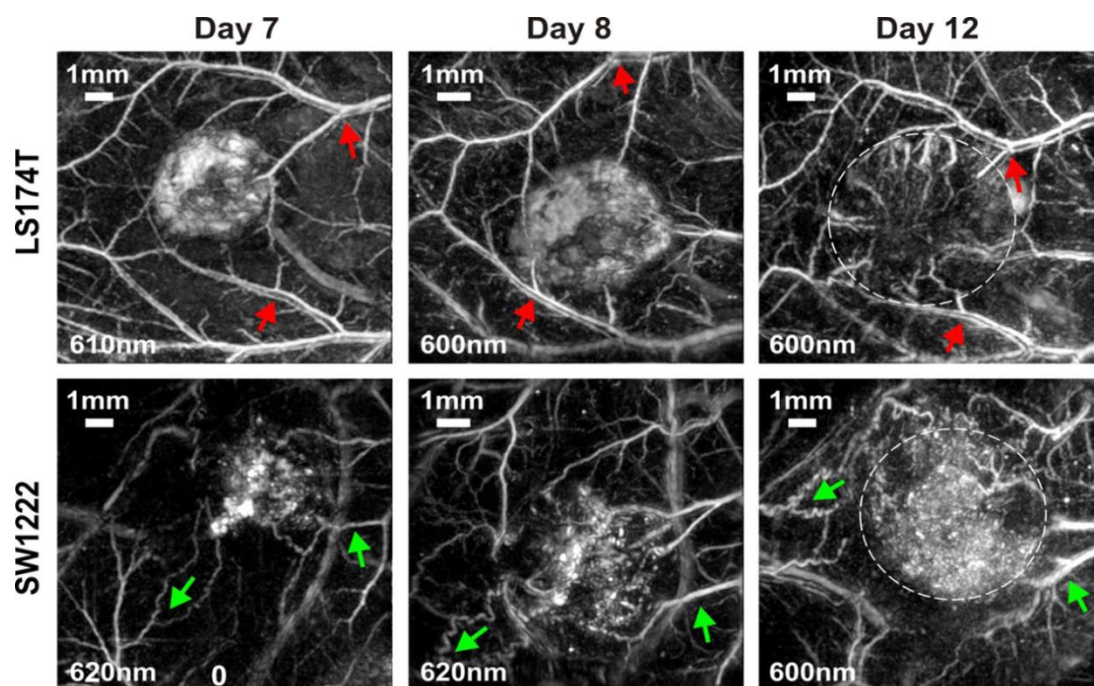


**Figure 3.16 Development of tumours over time by PAT**

The top row **A** depicts growth of an LS174T tumour by PAT, whilst the bottom row depicts the growth of an SW1222 tumour. Both are shown at day 7, 8 and 12, with exact excitation wavelength shown in the bottom left of each image. Arrows in red and green depict architectural features that are identifiable throughout the imaging sequence.

### 3.3.9 Spectroscopic analysis of tumours in vivo

The ability to acquire spectroscopic data from tumours *in vivo* was also examined. **Figure 3.17** shows an example of an SW1222 tumour imaged at multiple excitation wavelengths, without moving the animal between scans, 8 days after cell injection. Four wavelengths are shown, 600nm (**A**), 620nm (**B**), 640nm (**C**) and 670nm (**D**), with three common features indicated in each; the red arrow highlights an angiogenic associated vessel outside of the tumour, the signal intensity of which appears to decrease as the wavelength increases. The centre of the tumour is highlighted by the interior of the red circle, with signal intensity from this area increasing as the wavelength increases. The third feature is a large deep-lying vessel, indicated by the green arrow, that is not initially visible but that appears as the wavelength increases. Also of note is that many of the smaller superficial skin vasculature also disappears as the wavelength increases to 670nm.

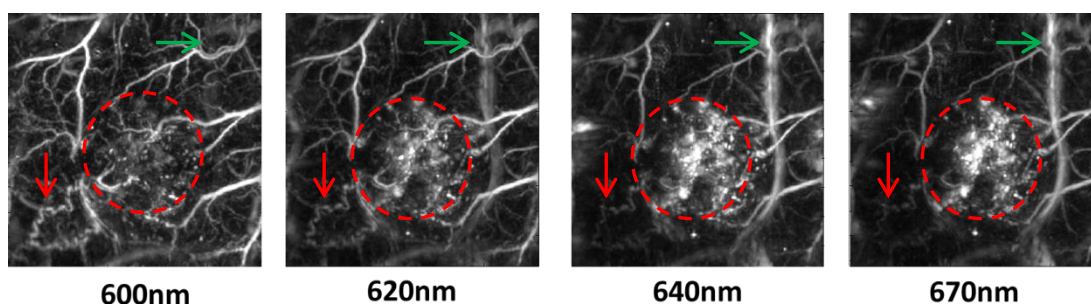


**Figure 3.17 Spectroscopic analysis of tumours in vivo**

The same tumour (SW1222 8 days after cell injection) is imaged increasing PA excitation wavelengths. The red arrow indicates an angiogenic feeding vessel, the red circle the centre of the tumour, and the green arrow a large deep-lying vessel, all of which vary in intensity depending on the excitation wavelength.

### 3.3.10 PA imaging of other organs

In order to assess the suitability of PAT for imaging internal tumours imaging of organs other than subcutaneous tumours by PAT was also performed. **Figure 3.18** shows an example of some of the results achieved at 680nm. The top row is *in vivo* imaging, with panel **A** being of the flank of a mouse in the area of the spleen and panel **B** the abdomen of a mouse in the area of the liver. A feature in **A**, to the top left and indicated by the red arrow, is potentially the spleen, as it appears to have a unique pattern of PA signal and a rounded smooth edge. Visible in **B** are the major blood vessels running down the length of the abdomen from head (left hand side of the image) to tail (right hand side). A structure to the right of the vessels is presumed to be intestines (highlighted by the red arrow). The bottom row of panel **C** and **D** depict *ex vivo* PA images acquired from excised organs placed on the scanner sensor. Highlighted in **C** is a spleen, heart, lungs and kidney, whilst **D** is a section of excised liver. All organs in **C** appear homogeneous with regards to PA signal pattern and intensity. The excised liver section in **D** shows fine detail of the liver blood vessels that is unlike the *in vivo* setting.

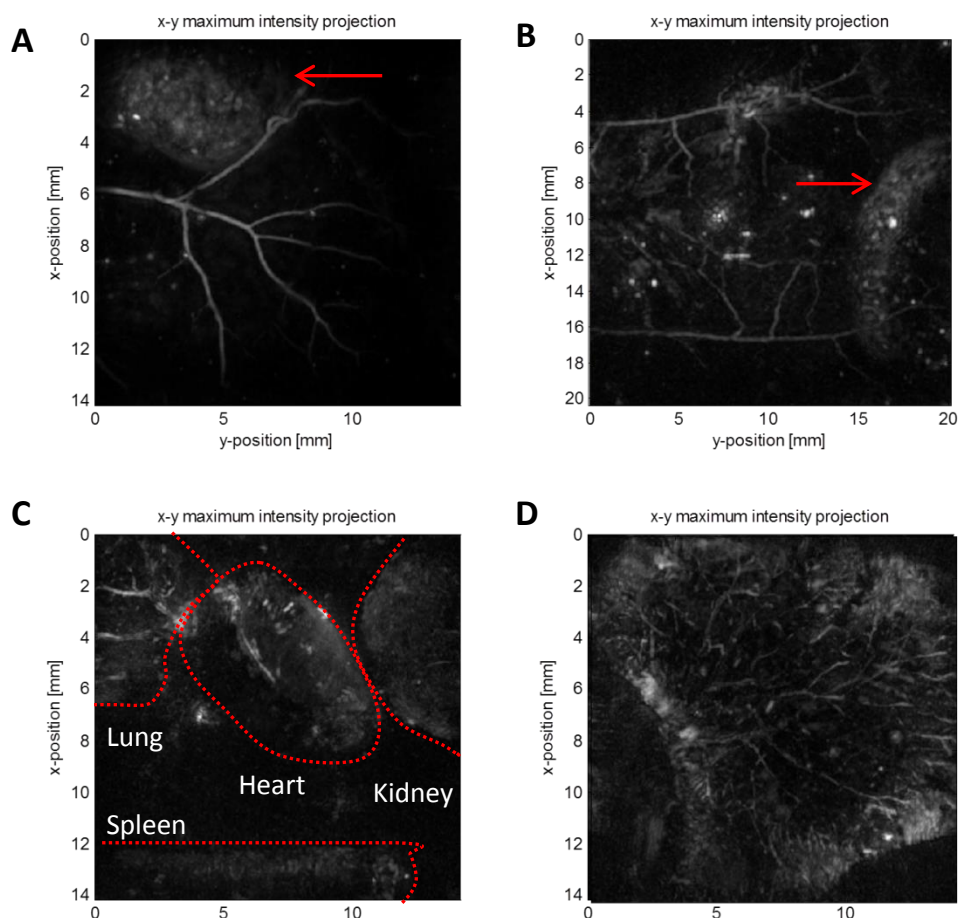


**Figure 3.18 PA imaging of other organs**

PA imaging at 680nm of mouse *in vivo* spleen (**A**), *in vivo* abdomen showing liver and intestines (**B**), *ex vivo* excised lung, heart, kidney and spleen (**C**), and *ex vivo* liver section (**D**)

## 3.4 Discussion

### 3.4.1 PA can image structural haemoglobin in vivo

The natural contrast created for PA imaging *in vivo* is chromophores in biological tissue; within the optical imaging window of around 600nm to 800nm both haemoglobin and melanin are the main absorbers in tissue, so these were therefore the first to be assessed by the PA scanner system. **Figure 3.8** shows the absorption coefficient spectrum in  $\mu_a$  from a single point at the centre of the sensor. Information about the Z dimension is contained in the time series acquired at each scanned point of the sensor; knowing the speed of sound the Z distance can be calculated. The photoacoustic signal is proportional to the absorbed energy, as it is the time derivative of the energy. For a one dimensional acquisition such as this, and in a homogenous medium such as the blood samples used, the absorbed energy follows an exponential decay with time. The constant term of the exponential decay is the absorption coefficient  $\mu_a$ , which can be calculated by fitting an exponential to the PA signal at different wavelengths to obtain the  $\mu_a$  spectrum. Working out the chromophore concentration from the observed absorption coefficient is challenging (19); relating the absorption coefficient to the concentration of the chromophores is possible, but only if their relative contributions within a composite image and their individual absorption profiles are known. Within the blood sample used a combination of oxyhaemoglobin, deoxyhaemoglobin, anticoagulant, and water was present in an unknown composition. The spectra for pure oxyhaemoglobin and deoxyhaemoglobin were plotted against the experimental data from known published values (24).

The *ex vivo* blood spectrum shown in **figure 3.8** lies initially from 600nm to around 660nm between the expected absorption coefficients for oxygenated and deoxygenated haemoglobin, for both of the measurements taken. This would suggest that the exsanguinated blood is a mixture of both oxy- and deoxy- haemoglobin. Above this wavelength however, from around 675nm to 1000nm, the signal is above the expected absorption coefficient, although it does track with oxy-haemoglobin, albeit  $20\text{--}30\mu_a \text{ (cm}^{-1}\text{)}$  above the expected value. This would suggest that there is something else within the sample that is also acting as an optical absorber at these wavelengths. It is possible that either the anticoagulant used, heparin, or some other element such as red blood cell aggregations within the sample, could cause an increase in the observed absorbance. It may also be an issue of comparing whole blood, with its component of water and plasma as well as haemoglobin, to measurements of pure haemoglobin that confounds the comparison. The results also demonstrate the difficulty in obtaining accurate quantitative



measures of chromophore concentration even from a simple standardised sample; quantitative PA imaging (QPAI) has been of importance and desired in the field of PA imaging for some time (26). The difficulty in normalising the energy applied to the tissue by the laser, and the scattering and absorption of the photons once in the tissue, coupled with not knowing how much conversion efficiency from light to heat has been achieved, i.e. the Grunesian coefficient, makes accurate measurements of chromophore concentration by PA imaging extremely challenging. This difficulty has been noted in the literature previously (27). Straightforward assumptions about PA images and quantitative measures of absorption coefficient, like presented here in our *ex vivo* blood spectrum assay, will therefore always be an approximation and always semi-quantitative, as has already been shown experimentally (28). The observed measurements, however, are within a reasonable range of expected values, and given that the structure and architecture of healthy and pathological blood vessel networks, rather than any intrinsically flawed measure of functionality/quantitation, are the main interest of this research, it is realistic to assume that we have obtained an accurate assessment of the presence of haemoglobin. This is further validated by the *in vivo* measurements obtained from the palm, where reconstruction of acquired data showed a 33.3 $\mu$ m high resolution image of superficial vascular networks. Of interest here is the finger-print type patterns created in the image due to signal in the striated grooves of the skin surface of the palm. The effect of melanin on image reconstruction is well known, as it is also a biological chromophore; even when no pigmentation is apparent the effect on image reconstruction was pronounced. This was either due to inherent small concentrations of melanin, or potentially some other absorber contained within the lipids of the skin microstructure. The imaging of melanin however was considered to be of further interest.

### **3.4.2 Melanin is a strong *in vivo* optical absorber**

Melanin is known to be a strong optical absorber, and therefore useful as a PA contrast-providing agent. The effect of melanin on imaging with our system was therefore warranted. As seen in **fig. 3.10 A**, even C57BL/6 mice, with significant amounts of melanin pigmentation present in their fur, have little apparent pigment in the skin, and therefore imaging of the superficial skin vasculature is possible at 590nm wavelength (**fig. 3.10 B**), where the contribution from haemoglobin is still relatively high (see **fig. 3.3**). It is even possible to get a PA signal from deeper structures such as blood vessels (**fig. 3.10 C**). However, as the excitation wavelength increases this signal from melanin becomes too strong to be able to detect anything else; all signal is generated by the first few

micrometres of the skin layer, and no deeper haemoglobin signal was observed. Melanin is therefore very strongly picked up by the UCL PA system, which would not be useful to have melanin present when studying the tumour vasculature as it would provide too much contrast for the purposes of observing pathophysiology. As a reporter for PA scanning however, we have also shown that melanin is a strong optical absorber with this approach. This could therefore be used to study inherent cases of melanin expression, such as attempted by others in the field for melanoma metastases in lymph nodes (29) and detection of melanomas via photoacoustic microscopy (30). The problem with PA microscopy has already been discussed, and imaging of melanomas is interesting due to their inherent melanin. However, another approach taken at UCL is to use tyrosinase, the rate limiting step in melanin production, as a genetic reporter in order to be able to track any cell engineered to express the gene (31). As strong as this approach may be, it is not applicable to this study of the pathological environment of tumour vasculature in nude mice.

### 3.4.3 Blood oxygenation does not affect PA structural images

As both the tumour vascular environment and the acquired PA images are both susceptible to oxygenation status, the effect of the oxygen used during anaesthesia of the animals was evaluated. **Fig. 3.12** shows no discernible difference in structure or vessel size between pure oxygen and medical air breathing even after 60 minutes. A small area highlighted does appear to increase slightly in PA contrast within the medical air image, however this is put down to inherent variability within the PA system. This is further evidence that exact quantitation of signal is not entirely possible. However, a measure of PA signal amplitude of the same vessel throughout the hour acquisition in arbitrary units, taking in to account the caveat that the measurements are not fully quantitative, shows no significant difference between inhalational gases. Using a systemic measure of blood oxygenation shows that when using oxygen as the inhalational gas for anaesthesia the results are much more stable and consistent across animals. It was therefore decided that oxygen would be used for all further studies as it did not affect the qualitative nature of the acquired data.

### 3.4.4 Subcutaneous tumours can be resolved in vivo with PAT

The PAT can identify solid subcutaneous tumours *in vivo* based on the detection of haemoglobin. As can be seen in **fig. 3.13 A**, the location of the tumour between the skin vasculature and the underlying muscle wall clearly shows that it is in the subcutaneous space. **Fig. 3.13 B** also shows that the data can be optically sectioned at any point, providing information on the presence of haemoglobin from the centre of the tumour. This is the first time that an all-optical photoacoustic tomography system has imaged tumours *in vivo* purely based on the haemoglobin signal from the blood contained within the vasculature. What is more, as this is a tomography set up, and not a microscopy system that can only image a few hundred microns depth, this system was able to encompass the entire tumour. The deepest image acquired in this study can be seen in **fig. 3.14** with the tumour clearly resolved to an imaging depth of 9mm which, considering it is an optical based system, is substantially better than other optical modalities.

### 3.4.5 PAT can differentiate different tumour vascular pathophysiologies *in vivo*

One of the aims of this research was to investigate the different architecture and extent of tumour vascularisation, its interaction with the surrounding microenvironment, and how this affects progression of the solid tumour. This study demonstrated that imaging with PA tomography can distinguish between two very different tumour vascular pathophysiologies through imaging of the haemoglobin content of the tumours. SW1222 and LS174T cell lines are both colorectal carcinomas, but they present very different states of vascularisation when grown as tumours *in vivo*. The SW1222 xenograft is well differentiated, and forms glandular structures when grown *in vivo* that reflect the colorectal origin of the initial cells. They also present a more 'normal' tissue organisation pattern and greater degree of vascularisation. The vasculature is extensive throughout the tumour, with little or no hypoxic regions or necrotic tissue. The LS174T cells on the other hand form a moderate to poorly differentiated xenograft with a disorganised structure, many avascular regions, and poor organisation of any existing vasculature (32, 33). Reconstructed PA images of SW1222 tumours, as shown in **fig. 3.15**, show a fine resolution of signal throughout the solid tumour, with few areas of non-signal; this would correspond to the tumour being fully vascularised with small vessels, as the signal corresponds directly to the presence of haemoglobin within the vasculature. In contrast, established LS174T tumours exhibit large areas of no signal, indicating large non-vascularised regions of the tumour, with a few large irregular vessels intruding in to the tumour mass. These images correspond well to *ex vivo* analysis of these tumour types with reconstructed data from other imaging sources; micro-CT of SW1222 vascular polymer casts also show SW1222 tumours to have a smaller vessel size but more extensive coverage of vasculature, compared to LS174T tumours that have fewer and thicker vessels with large avascular regions between them. When compared to immunofluorescence imaging, the *in vivo* PA images also compare favourably. By pimonidazole, Hoechst 33342 and CD31 immunofluorescence, large areas of the LS174T tumours are shown to be hypoxic due to lack of blood vessels and perfusion, whilst the SW1222 tumours are more extensively covered with perfused blood vessels and have few hypoxic regions. This corresponds to the PA data, where areas of non-signal in the LS174T tumours are presumed to be avascular and therefore hypoxic or necrotic, whilst SW1222 tumours have extensive PA contrast. This emphasises the ability of PAT to discriminate between two very different tumour vascular pathophysiologies with a simple non-invasive and non-ionising *in vivo* scan, which only requires anaesthetising of the animals during data acquisition. What is also advantageous with the *in vivo* PA scans is that the

microenvironment surrounding the tumour is also imaged. This allows the effect of angiogenesis within the normal skin vasculature to be imaged, with highlighted vessels from the tumour periphery showing the characteristic 'corkscrew-like' appearance of co-opted blood vessels. These are directed towards the growing tumours and are therefore tumour-associated, being affected by tumour released growth factors. The ability to longitudinally acquire data is also a major advantage, as the vasculature development can be imaged along with the tumour growth. **Fig 3.16** demonstrates that the imaging between subsequent days is possible, and registration of similar features permits assessment of vascular change. Of interest here is how the appearance of the injected cells changes over time; at early time points of around a week after cell injection for both models the tumour appears to have a diffuse pattern, with blood vessels of the normal skin vasculature showing signs of angiogenic attraction towards the agglomeration of cells. The diffuse 'fuzzy' signal from the haemoglobin within the tumour mass is thought to come from blood pooling within the nascent tumour that does not have an established vascular architecture. At 12 days after the injection of cells the tumours appear to have a completely different PA haemoglobin signal from the centre of the tumours; the 'tumour-associated' vessels are much closer to the edge of the growing solid tumour, and it is postulated that the internal structure of tumour vasculature is more developed and defined, and therefore more able to handle blood flow, leading to a change in PA pattern. This is somewhat substantiated by the appearance of a fine-mesh pattern in the SW1222 tumours and thick intruding vessels in the LS174T tumours at day 12.

Imaging with PA tomography can therefore be used to assess the differing pathological vascular states of tumours *in vivo*, and it is shown to be ideally suited to imaging not only the developing tumour but also the vascular development in surrounding tissues. This lends itself to following tumour vascular development, differentiating vascular architecture between tumour types, and assessing therapies that exploit the interaction of the tumour vasculature with the surrounding microenvironment. It may also be used to assess tumour vascular states of patients and aid in therapy selection.

### 3.4.6 In vivo spectroscopy can provide qualitative data on tumour oxygenation

When looking at the spectroscopic ability of PA imaging, as in **fig. 3.17**, valuable information regarding the tumour vascular pathophysiology can also be acquired. It is worth restating the caveat that this data can only be semi-quantitative at the present moment due to the complex interaction of *in vivo* chromophores and the conversion of light into heat and therefore pressure distribution; however, qualitative data suggests that detection of vessel oxygenation status *in vivo* is possible. As the PA excitation wavelength is increased the relative contribution to PA signal generation of oxyhaemoglobin vs deoxyhaemoglobin goes down (**fig. 3.3**). It is therefore logical to assume that any decrease in vessel PA magnitude can be said to be predominantly oxygenated, whilst any increase can be assumed to be deoxygenated. In **fig. 3.17** the vessels that decrease in signal are those tumour associated vessels that are directly linked to the tumour, or are the smallest vessels resolved which are assumed to be arterioles and capillaries. The areas that increase in signal as the wavelength is increased are the tumour core and a larger deeper lying vessel that is assumed to be a vein. Whilst spectrally un-mixing these two signals is difficult, the qualitative data suggests an important future potential for PA imaging of tumour oxygenation status. This application is further complicated however by the attenuation of different chromophores within the tissue at the different wavelengths and the difficulty in measuring their relative concentrations.

### 3.4.7 Imaging of different organs and locations is difficult with PAT

Imaging of different locations with PAT would enable a variety of different models to be employed, such as orthotopic models of cancer that more accurately reflect the clinical situation (34). Of interest to this work was imaging of the liver, as this would allow use of the more clinically relevant liver metastatic model of colorectal cancer. Results in **fig. 3.18** however show that PAT imaging of the liver *in vivo* was not achieved with this system. Whilst the surface of the spleen (**fig. 3.18 A**) can be seen, and also the vasculature of the abdomen and to some extent the intestines (**fig. 3.18 B**), the surface of the liver remained undetected. This was potentially due to motion artefacts from respiration or an issue of depth penetration of the photons into biological tissue, as the *ex vivo* data suggests that haemoglobin content within the lung, heart, kidney and spleen (**fig. 3.18 C**), and especially the liver (**fig. 3.18 D**), is sufficient to produce detailed images. However, at the current time PAT remains limited to imaging subcutaneous superficial tumours to a depth of  $\approx 1\text{cm}$ .

### 3.5 Summary

In this chapter it has been shown that photoacoustic tomography is ideally suited to imaging tissue chromophores *in vivo*. I have demonstrated for the first time *in vivo* that PAT is able to visualise whole subcutaneous tumours with a simple non-invasive, non-ionising scan that detects tumour haemoglobin content. Imaging of tumour vasculature and the tumour-associated blood vessels in the surrounding microenvironment has been achieved. This included the growth of typical angiogenic structures from co-opted blood vessels towards the tumour. Longitudinal monitoring of tumour progression and development of vascular state was also shown. Different vascular pathophysiologies can be detected using PAT, highlighting its potential in assisting vascular targeted therapy selection. The ability to assess oxygenation *in vivo* in a qualitative manner has also been demonstrated. All of these capabilities point to the use of PAT to evaluate vascular targeted therapies. Whilst PA imaging is not currently in clinical use, this will undoubtedly occur in the future, and it is an excellent technique for investigating preclinical models with the aim of increased translation of novel therapies. The subsequent work stemming from this research was therefore to evaluate the response to a tumour vasculature targeted drug in preclinical models, in order to demonstrate the utility of PAT for the translation of novel therapies.

### 3.6 References

- (1) Laufer J, Johnson P, Zhang E, Treeby B, Cox B, Pedley B, et al. In vivo preclinical photoacoustic imaging of tumor vasculature development and therapy. *J Biomed Opt* 2012;17:056016.
- (2) Wang LV, Hu S. Photoacoustic tomography: in vivo imaging from organelles to organs. *Science* 2012;335:1458-62.
- (3) Hu S, Wang LV. Photoacoustic imaging and characterization of the microvasculature. *Journal of Biomedical Optics* 2010;15:011101-15.
- (4) Lao Y, Xing D, Yang S, Xiang L. Noninvasive photoacoustic imaging of the developing vasculature during early tumor growth. *Phys Med Biol* 2008;53:4203-12.
- (5) Siphanto RI, Thumma KK, Kolkman RG, Van Leeuwen TG, de Mul FF, van Neck JW, et al. Serial noninvasive photoacoustic imaging of neovascularization in tumor angiogenesis. *Opt Express* 2005;13:89-95.
- (6) Lungu GF, Li ML, Xie X, Wang LV, Stoica G. In vivo imaging and characterization of hypoxia-induced neovascularization and tumor invasion. *Int J Oncol* 2007;30:45-54.

- (7) Ku G, Wang X, Xie X, Stoica G, Wang LV. Imaging of tumor angiogenesis in rat brains in vivo by photoacoustic tomography. *Appl Opt* 2005;44:770-5.
- (8) Beard P. Biomedical photoacoustic imaging. *Interface Focus* 2011;1:602-31.
- (9) Bell AG. Upon the production and reproduction of sound by light. *Telegraph Engineers, Journal of the Society of* 1880;9:404-26.
- (10) Maiman TH. Stimulated Optical Radiation in Ruby. *Nature* 1960;187:493-4.
- (11) Einstein A, Zur Quantentheorie der Strahlung, *Physiol Z*; 18:121-8
- (12) Stoker MR. Basic principles of lasers. *Anaesthesia & Intensive Care Medicine* 2005;6:402-4.
- (13) Bogdan A, I, Kaufman J. Laser principles. *Curr Probl Dermatol* 2011;42:7-23.
- (14) Oraevsky A and Karabutov A. Ultimate sensitivity of time-resolved optoacoustic detection, biomedical optoacoustics. *Proc. SPIE*. 2000;0277-786x 3916:228-239
- (15) Anderson RR, Parrish JA. The optics of human skin. *J Invest Dermatol* 1981;77:13-9.
- (16) Herd RM, Dover JS, Arndt KA. Basic laser principles. *Dermatol Clin* 1997;15:355-72.
- (17) BS EN 60825-1:2007 Safety of laser products. Equipment classification and requirements, BSI, 2007
- (18) Thomas G, Isaacs R. Basic principles of lasers. *Anaesthesia & Intensive Care Medicine* 12:574-7.
- (19) Cox BT, Laufer JG, Beard PC. The challenges for quantitative photoacoustic imaging. 2009 p. 717713-9.
- (20) Zhang E, Laufer J, Beard P. Backward-mode multiwavelength photoacoustic scanner using a planar Fabry-Perot polymer film ultrasound sensor for high-resolution three-dimensional imaging of biological tissues. *Appl Opt* 2008;47:561-77.
- (21) Zhang EZ, Laufer JG, Pedley RB, Beard PC. In vivo high-resolution 3D photoacoustic imaging of superficial vascular anatomy, *Physics in Medicine and Biology* 2009;54:1035-1046
- (22) Treeby BE, Cox BT. k-Wave: MATLAB toolbox for the simulation and reconstruction of photoacoustic wave fields. *J Biomed Opt* 2010;15:021314.
- (23) Treeby BE. Acoustic attenuation compensation in photoacoustic tomography using time-variant filtering. *J Biomed Opt* 2013;18:036008.
- (24) <http://omlc.org/spectra/hemoglobin/summary.html>.
- (25) Folarin AA, Konerding MA, Timonen J, Nagl S, Pedley RB. Three-dimensional analysis of tumour vascular corrosion casts using stereoimaging and micro-computed tomography. *Microvasc Res* 2010;80:89-98.



- (26) Wang LV. Prospects of photoacoustic tomography. *Med Phys* 2008;35:5758-67.
- (27) Cox B, Laufer JG, Arridge SR, Beard PC. Quantitative spectroscopic photoacoustic imaging: a review. *J Biomed Opt* 2012;17:061202.
- (28) Laufer J, Delpy D, Elwell C, Beard P. Quantitative spatially resolved measurement of tissue chromophore concentrations using photoacoustic spectroscopy: application to the measurement of blood oxygenation and haemoglobin concentration. *Phys Med Biol* 2007;52:141-68.
- (29) Grootendorst DJ, Jose J, Wouters MW, van Boven H, Van der Hage J, Van Leeuwen TG, et al. First experiences of photoacoustic imaging for detection of melanoma metastases in resected human lymph nodes. *Lasers Surg Med* 2012;44:541-9.
- (30) Oh JT, Li ML, Zhang HF, Maslov K, Stoica G, Wang LV. Three-dimensional imaging of skin melanoma in vivo by dual-wavelength photoacoustic microscopy. *J Biomed Opt* 2006;11:34032.
- (31) Laufer J, Jathoul A, Pule M, Beard P. In vitro characterization of genetically expressed absorbing proteins using photoacoustic spectroscopy. *Biomed Opt Express* 2013;4:2477-90.
- (32) El-Emir E, Boxer GM, Petrie IA, Boden RW, Dearling JL, Begent RH, et al. Tumour parameters affected by combretastatin A-4 phosphate therapy in a human colorectal xenograft model in nude mice. *Eur J Cancer* 2005;41:799-806.
- (33) El-Emir E, Qureshi U, Dearling JL, Boxer GM, Clatworthy I, Folarin AA, et al. Predicting response to radioimmunotherapy from the tumor microenvironment of colorectal carcinomas. *Cancer Res* 2007;67:11896-905.
- (34) Bibby MC. Orthotopic models of cancer for preclinical drug evaluation: advantages and disadvantages. *Eur J Cancer* 2004;40:852-7.

# Chapter 4 Photoacoustic imaging of vascular targeted therapy

---

## 4.1 Introduction

The ability of imaging modalities to provide information on the efficacy of drug action has been discussed at length in the introduction to this thesis. As established previously, the research presented in this thesis is focussed on assessing the reaction of the tumour vascular microenvironment to therapy, so it was therefore decided to limit the scope of the work to concentrate on Vascular Disrupting Agents (VDAs), as this class of drug would potentially create the largest detectable difference in vascular function. Also previously discussed was the action of the combretastatin class of VDAs, and in particular OXi4503. Having shown in the previous chapter that PAT is capable of acquiring detailed images of the tumour vascular microenvironment and the interaction of this with the surrounding normal tissue, this chapter aims to demonstrate the ability of PAT to monitor the effects of vascular targeted therapy with OXi4503. An initial recap of techniques used to image tumour vasculature after VDA therapy will be described first, followed by a comparison with assessment via PAT. The methods used to demonstrate the ability of PAT to monitor response to vascular targeted therapy will then be set out and shown within the results section of this chapter.

### 4.1.1 Assessing response of VDA drug efficacy

Imaging modalities used to assess the tumour microenvironment were discussed in the introduction; what follows is a quick overview of those used to assess response to VDA therapy through directly imaging the tumour blood vessels. Other modalities that acquire quantitative measurements on the tumour microenvironment though assessing parameters associated with tumour vasculature, such as MRI and bioluminescence, are described in the following chapters.

#### 4.1.1.1 Vessel Angiography with MRI

Imaging of tumour vasculature with MRI is possible by acquiring Magnetic Resonance Angiography (MRA) images. MRA can be used to resolve the large vessels of the tumour microenvironment macroscopically, allowing visualisation of the tumour-associated vasculature (1). This can be either based on 'Time-of-flight' MRA (TOF-MRA) to measure vessel tortuosity (2) or through injection of exogenous contrast agents (3, 4). These approaches are able to image vascular morphology, but have disadvantages and certain

limitations when imaging tumour microvasculature. With TOF-MRA small tumour blood vessels with a slow rate of blood perfusion will not be readily visualised, as TOF-MRA is a flow dependent technique that is insensitive to slow rates of blood flow (5). Contrast-enhanced MRA has the added confounding factor of administration of a contrast agent. This is typically gadolinium, which quickly compartmentalises in the interstitial space due to a short intravascular half-life, making it ill-suited to high resolution MRA. Other contrast agents, such as iron oxide nanoparticles (6), can provide resolution of the microvasculature to around 100µm, but are still dependent on exogenous contrast and flow parameters of the tumour microenvironment.

Based on MRA, parameters of the tumour microvasculature can be identified and classified, such as an fractional volume of blood content, index of vessel size (7), tumour vessel density (8), and vascular permeability (9, 10). These are generally considered to be vascular associated parameters however, and are discussed in more depth in the following chapter. The main disadvantage of these approaches is the lack of three-dimensional information regarding the architectural arrangement of tumour blood vessels.

#### **4.1.1.2 Computed Tomography Angiography**

Tumour blood vessel angiography can also be performed using Dynamic Contrast-Enhanced Computed Tomography (DCE-CT). As with MRA the microvascular structure of the tumour blood vessel network is not defined, but physiological parameters of regional tumour blood flow, mean blood transit time, and permeability of the vessel surface area can all be measured using DCE-CT (11). This is possible due to analysis of the temporal changes observed in a succession of images acquired after administration of an exogenous contrast agent, typically an iodinated contrast material. DCE-CT has been shown to be reproducible in peripheral tumours, compared to various reference measures of blood flow, in both preclinical models and human studies (12-14), although three-dimensional vessel architecture of the tumour-associated vasculature is not observed. CT also requires the use of ionising radiation, so although DCE-CT can be used to assess vascular targeted therapy (15), the accumulation of radiation damage due to repeated measurements is a potential risk to the patient. The use of exogenous contrast agents also has the potential of causing nephrotoxicity.

#### **4.1.1.3 Ultrasound**

Contrast enhanced US (CEUS) imaging, using microbubbles as a contrast agent, is a comparatively inexpensive imaging modality that can provide information on the vascular structure of tissues and potentially angiogenesis within tumours (16). CEUS has been shown to provide quantitative estimation of tumour blood flow in response to treatment with VDAs (17, 18), however only regional enhancements were observed with no link between structure and function of the vascular disruption.

#### **4.1.2 Potential of PAT for assessing vascular response to treatment**

The ability of PAT to assess the microvasculature of tumours *in vivo* was demonstrated in the previous chapter. It follows that PAT should be able to image the response of these tumours to vascular disruption with VDAs over time. Other modalities are able to image the tumour vascular microenvironment, as described above, but all have certain drawbacks that make them less than ideal for observing the effect of the tumour microvasculature and its interaction with the surrounding tissue following treatment. The main disadvantage of these modalities is a lack of resolution with regards to the vasculature and an inability to resolve three-dimensional tumour vascular networks *in vivo* without the addition of exogenous contrast. This chapter describes the use of PAT to assess the tumour microvasculature and associated feeding vessels following treatment with OXi4503, with the aim of providing greater detail on vessel response, and demonstrating the utility of this entirely non-invasive technique for assessing vascular targeted treatment.

## **4.2 Methods**

All PAT was performed on the system previously described in chapter 3. Experiments were performed at a number of excitation wavelengths, however those represented in this chapter are all at 680nm, as this wavelength afforded the greatest tissue penetration for PA imaging. Female CD1 nu/nu mice were acquired through UCL BSU services, transferred to the CABI, and subcutaneous tumours established via injection of either SW1222 or LS174T colorectal cells. As these experiments were longitudinal in nature, animals were kept in IVCs within CABI for the duration of the experiments under the same monitored conditions as outlined in chapter 2.

### **4.2.1 Drug treatment**

The VDA OXi4503 was a kind gift from Dr David Chaplin (OXiGENE, San Francisco, USA). For dosing, a stock concentration of 4mg/ml was prepared in sterile saline and vortexed for 2 minutes. The drug was readily soluble, with no particulates present following preparation. Drug solutions were made fresh for each session, kept in the dark in light tight containers and used within an hour of preparation. Animals were injected i.v. at a ratio of 10ml/kg for a total dose of 40mg/kg. If lower doses were required the stock concentration was diluted accordingly, with rate of i.v. dose kept at 10ml/kg and therefore an equivalent volume, dependent on animal weight, injected. Sham doses consisted of i.v. sterile saline injected at 10ml/kg. For longitudinal experiments, where PAT data was acquired on subsequent days, animals were placed in a heated recovery box following dosing and monitored for adverse effects for 15 minutes before returning to IVCs. At the end of the experiment animals were terminated via a schedule I method and tumours excised for histological assessment as previously described. The experimental design for assessing response to VDA therapy can be found in the following subsections.

### **4.2.2 Acute response to vascular disruption**

To observe with PAT the immediate effect on tumour blood perfusion due to vascular disruption with OXi4503, n=2 SW1222 and n=2 LS174T s.c. tumours were dosed i.v. with 40mg/kg of the VDA, and PA images acquired at 1hr post dose. Further SW1222 subcutaneous tumours (n=4) were also dosed in the same manner and imaged at 6hr post dose. Acquired PA data were reconstructed, and changes in signal and structure of tumour blood vessels analysed.

### **4.2.3 Tumour blood vessel destruction**

In order to extend our observations on the effect of blood vessel destruction caused by VDA treatment a longitudinal experiment following the same tumours was devised. SW1222 s.c. tumours (n=4) and LS174T s.c. tumours (n=2) were used for this study. Animals were imaged at baseline and then dosed with 40mg/kg of OXi4503 (n=2 for both SW1222 and LS174T tumours) or sham dosed with saline (n=2 SW1222). Subsequent PAT imaging was performed at 24hr and 48hr following dosing. Identification of blood vessels was achieved in a qualitative manner through interrogation of reconstructed data sets. Initial reconstruction of PA data was performed in order to ascertain that changes in induced signal had occurred, at which point (48hrs) the mice were killed and tumours excised. Histological assessment of tumour structure and viability via H&E staining was performed. Perfusion and distribution of tumour blood vessels were also assessed via immunofluorescence.

### **4.2.4 Vessel regrowth following vascular disruption**

Having established the utility of PAT to assess initial vascular disruption in response to VDA treatment, the ability to monitor subsequent behaviour of the tumour blood vessels was then studied. N=4 SW1222 and n=4 LS174T s.c. tumours were dosed i.v. with 40mg/kg of OXi4503 and imaged by PAT every two to three days after dosing. PA data was acquired up to day 16 following the dose of VDA, with caliper measurements for tumour volume also acquired over the same time course. At day 16 animals were killed via a schedule I method and tumours excised for histology. Analysis of PA data was performed to include PA signal intensity on a voxel by voxel basis across the tumour region. The tumour was selected as a region of interest (ROI) through a combined manual and automated process. Broad tumour regions were first segmented using reconstruction software Amira 5.4.0, followed by a threshold limit of the data set. A background measure of signal intensity was acquired, with a subjective measure of 10% used to reject any voxels within the tumour ROI containing PA signal above this, thereby acquiring volume measurements of internal tumour areas of signal void. For a positive measure of PA signal, an arbitrary blood vessel outside the tumour was selected in each image at a depth of 1-1.5mm. This provided a PA signal intensity measure for selection of tumour ROI voxels, which was then plotted against the total tumour volume as measured by caliper measurements and the extent of signal void within the tumour.

#### **4.2.5 PAT for dose response of VDAs**

The applicability of PAT to discern the effects of different doses of VDA on the level of vascular disruption following treatment was then investigated. For this, n=6 SW1222 and n=4 LS174T s.c. tumours were dosed i.v. with 10mg/kg of OXi4503 and a further n=6 SW1222 and n=4 LS174T were dosed i.v. with 1mg/kg. As with the study of vessel regrowth, these tumours were all imaged every two to three days until 16 days after treatment or until schedule I termination due to licence regulations. This data was compared to that previously acquired for 40mg/kg OXi4503. Caliper measurements of tumour volume, and PA analysis of voxel signal intensity, were also compared to the maximum dose of 40mg/kg. For histological assessment of vascular disruption, n=2 SW1222 s.c. tumours dosed with 10mg/kg and n=2 dosed with 1mg/kg OXi4503 were excised at 48hr after dosing. These tumour samples were assessed for markers of perfusion and extent of remaining blood vessel network by immunofluorescence, and tissue morphology by H&E. These images were then compared to previously acquired analysis of 48hr post dose with 40mg/kg OXi4503 in SW1222 and LS174T, and with the sham dose of saline in SW1222 tumours (section 4.2.2).

## 4.3 Results

### 4.3.1 Acute Assessment of vascular disruption

Visualisation of the acute effects of vascular disruption with OXi4503 can be seen in **Figure 4.1**. Each panel is 14mm x 14mm in the XY direction, with the Z direction being a maximum intensity projection (MIP) of the acquired data. The first row depicts the entire Z-stack within the MIP, whilst the second row has had the top 0.5mm layer removed and is therefore representative of PA signal from the centre of the tumour mass. The first column shows an LS174T tumour at 1hr post dose, the second shows an SW1222 at 1hr post dose, and the third shows the SW1222 at 6hr after dosing. All figures are representative of the specific tumour type and time point, as each effect was noted for all tumours imaged. All the images at 1hr post OXi4503 show typical PAT results with no obvious effect of vascular disruption, comparable to untreated tumours. At 6hr post treatment in the SW1222 there already appears to be an area with some loss of signal at the centre of the tumour, highlighted by the red arrow.

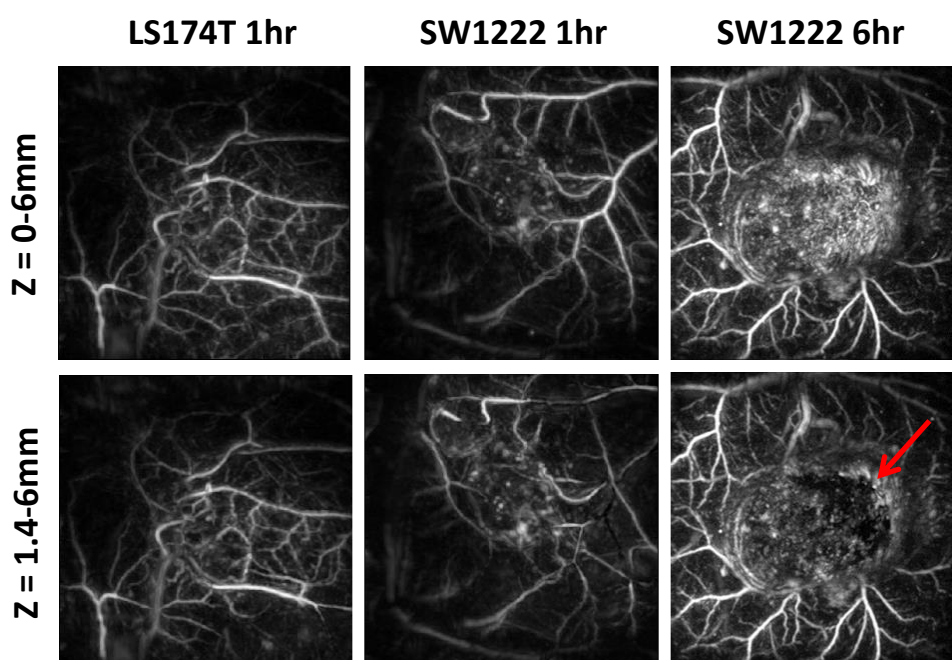


**Figure 4.1 Acute effect of vascular disruption with OXi4503 by PAT**

Representative PAT images of LS174T (n=2) and SW1222 (n=6) s.c. tumours following 40mg/kg of the VDA OXi4503 i.v. Each panel is 14x14mm XY and MIP in the Z direction. The first row is of the entire Z-stack whilst the second row has had the first 0.5mm removed.



### 4.3.2 Response to OXi4503

The response to vascular disruption with 40mg/kg OXi4503 over 24hr-48hr, as assessed by PAT, can be seen in **figure 4.2** (sham dose), **fig. 4.3** (SW1222 tumours) and **fig. 4.5** (LS174T tumours). Each panel is an MIP of the acquired and reconstructed PA data. The first row depicts a 14x14mm panel in the XY and 6mm in the Y direction at baseline, at 24 and 48 hours after dosing. The large circular area of signal corresponds to the tumour mass, and is imaged in the same location at each time point as confirmed by the similarity of the surrounding vascular features. No change in signal intensity or distribution is seen in **figure 4.2** (sham dose) over the 48 hour time-course. The second row is the same data set but with the initial 1.4mm of data removed, showing the PA signal corresponding to the blood vessels within the tumour. Again, no difference in appearance, either of signal intensity or distribution, is seen. The third row shows the tumour from the XZ direction in a 14x6mm panel, with the whole 14mm of the Y direction shown as an MIP. This angle clearly shows the depth imaging encompassing the whole subcutaneous tumour, which again shows no difference in signal across the 48hrs, confirming the presence of vessels throughout the tumour. **Figure 4.3** (SW1222 tumours) shows the same layout as described for **fig. 4.2**, although in this case only a 1mm top slice of data has been removed in order to observe the internal tumour PA signal. At baseline acquisition the tumour is clearly visible in the X and Y directions as a spherical mass at the centre of the image, with surrounding superficial skin vasculature also clearly defined. In the Y direction the whole tumour is encompassed by the PAT image and can be seen to be protruding slightly from the level of the skin surface. The signal from the centre of the tumour is finely speckled and present across the entire tumour mass, as previously observed with this tumour type. At 24hr and 48hr post VDA the signal from the centre of the tumour location, corresponding to the internal tumour blood vessels, is completely absent, as can be seen from the second row of images that have the top removed. Signal intensity in this region has changed from high and evenly spread across the tumour to a large area of no signal. The area around the tumour location has increased in PA signal, and shows a large band of diffuse signal for a few millimetres surrounding the tumour. This is also seen in the first row of images where the entire Z-stack is depicted. Although the tumour location is visible, the appearance has changed from a fine speckle pattern to a diffuse patchy signal. This PA signal is from the remaining outer rim of the tumour, which inhibits clear visualisation of the more central, signal-void area. This is observed in the depth imaging in the third row, where the lack of PA signal can be seen in the centre of the tumour, but with PA signal present both above and beneath the tumour.

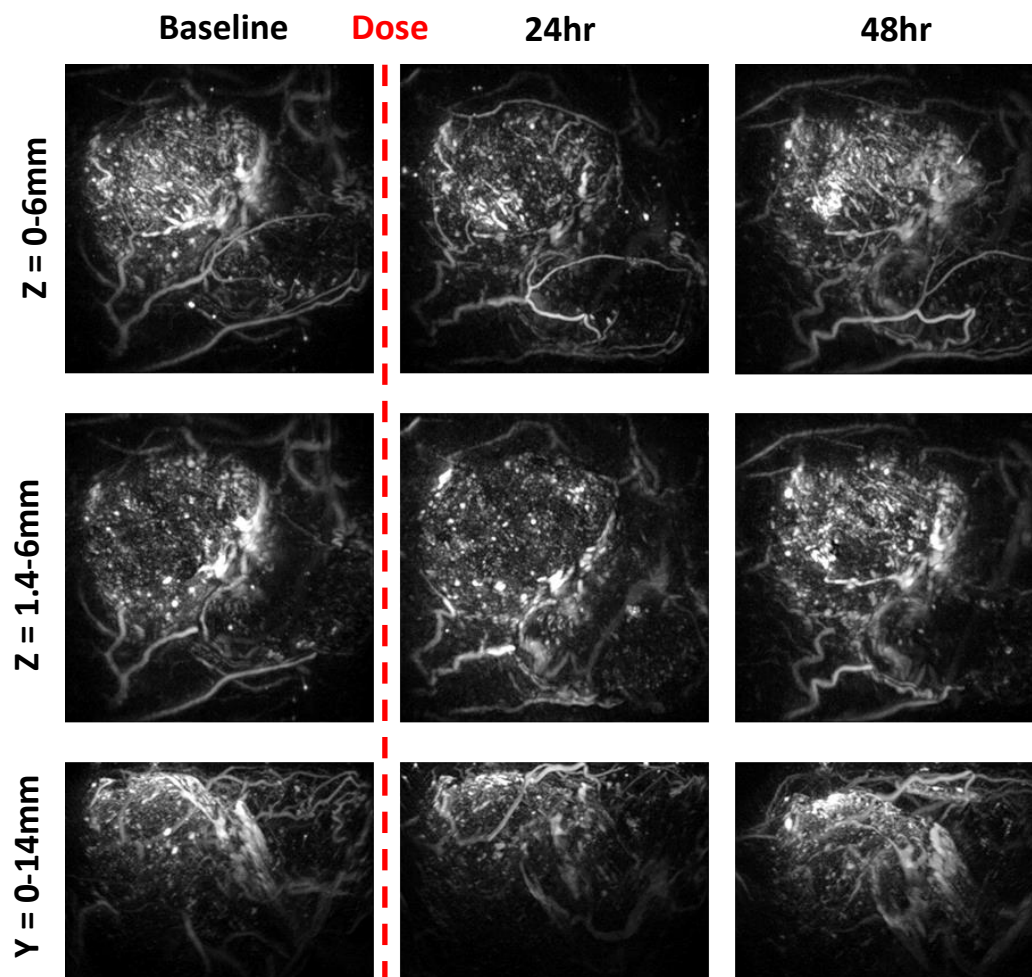


**Figure 4.2 Initial response to saline sham dose**

Representative PAT images of SW1222 s.c. tumours following 10ml/kg of saline sham dose i.v. (n=2). The first and second rows are 14x14mm in the XY and 0-6mm and 1.4-6mm in the Y direction MIPs, whilst the third row is 14x6mm in the XZ with 14mm in the Y as an MIP. Each row shows baseline images followed by 24 and 48hr post dose.

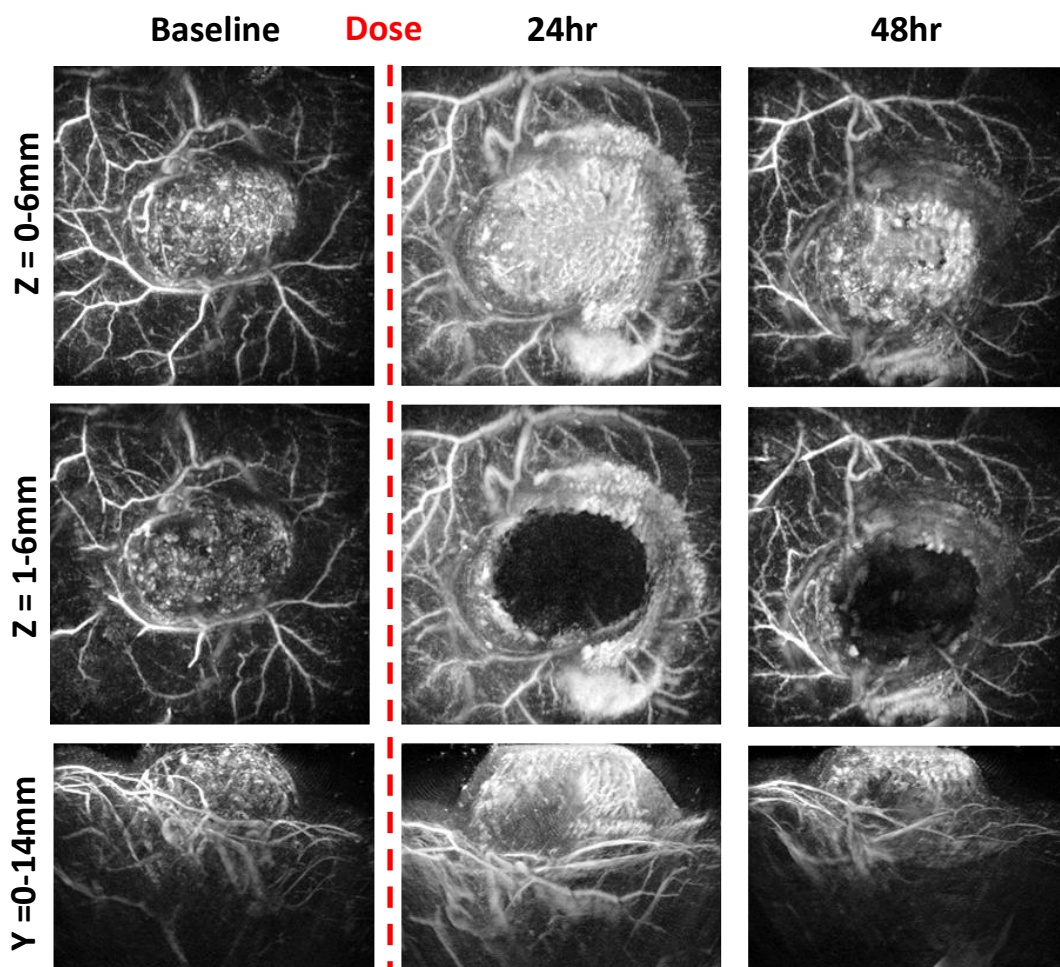


**Figure 4.3 Initial response to vascular disruption – SW1222**

Representative PAT images of SW1222 s.c. tumours following 40mg/kg of OXi4503 i.v. (n=4). The first and second rows are 14x14mm in the XY and 0-6mm and 1-6mm in the Y direction MIPs, whilst the third row is 14x6mm in the XZ with 14mm in the Y as an MIP. Each row shows baseline images followed by 24 and 48hr post dose.

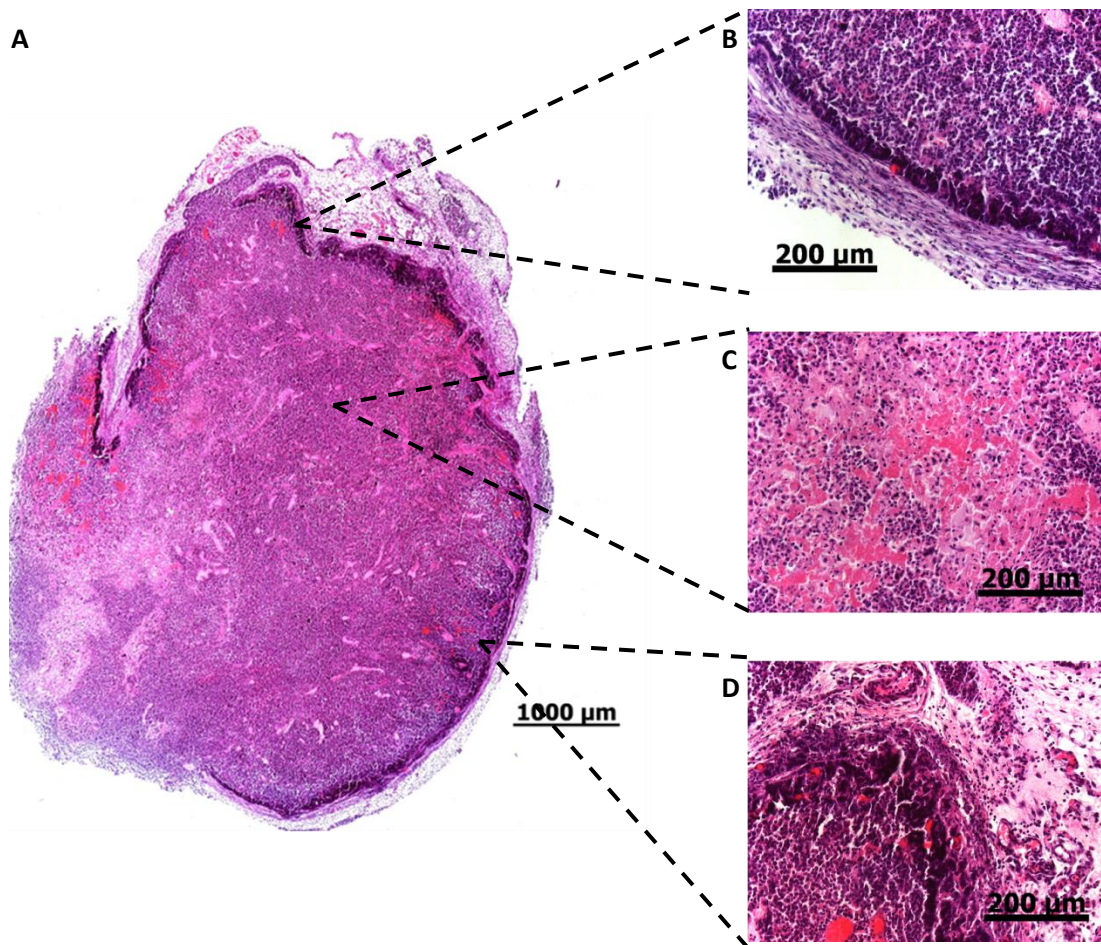


**Figure 4.4 Histology of initial response – SW1222**

Haematoxylin and Eosin staining of the n=4 SW1222 tumours used for initial response to vascular disruption by PAT was performed, an example cross section of which can be seen in panel **A** (10x magnification). A highlighted section of the surviving rim of tumour cells can be seen in panel **B** (20x). Panel **C** shows the central tumour necrosis and cellular debris present within the tumour core (20x). Panel **D** shows evidence of red blood cells within the tumour surviving rim and periphery of the tumour necrotic area.

Histological analysis of tumour structure by Haematoxylin and Eosin staining at 48hr following treatment for these SW1222 tumours can be seen in **Figure 4.4**. Panel **A** shows a whole tumour cross section at 10x magnification. A darker edge can be seen around the tumour section, which when seen at 20x magnification (panel **B**) shows a rim of viable cells at the periphery of the tumour. The centre of the tumour section, also seen highlighted in panel **C**, shows cells that have rounded up, lost cell contact and typical glandular structure. Also present is evidence of cell breakdown and cellular debris in the form of non-specific protein staining in the intercellular spaces. Observed towards the edge of the tumour, either just inside or associated with the surviving rim of cells, are red blood cells either

within vessels or pooled within the intercellular space. This can be seen mainly in the upper half of panel **A** and also highlighted in panel **D**.

The PAT data for LS174T tumours can be seen in **figure 4.5**. The layout is as previously stated, with 0.75mm removed from the surface data in the second row. At baseline imaging the tumour is visible as the spherical mass of PA signal intensity at the centre of the image. Following dosing with OXi4503 the PA signal within the tumour mass is disrupted, with areas of no signal appearing at 24 and 48hours. This drop in signal is more pronounced at 48 hours, where a 'rim' effect can be observed, with diffuse PA signal appearing around the tumour location. This is not as marked an effect as seen in the SW1222 tumours, however, with some PA signal apparently still present within the centre of the tumour mass. The change in internal PA signal pattern is again obscured by signal from the surviving outer rim, and therefore although present it is not easily defined in the entire Z-stack MIP (first row) or depth imaging (third row) images. Also apparent is the survival of a few large feeding vessels close to the periphery of the tumour and surviving tumour rim. Histological analysis of tumour structure by Haematoxylin and Eosin staining at 48hr following treatment for these LS174T tumours can be seen in **Figure 4.6**. Panel **A** shows a whole tumour cross section at 10x magnification. Certain areas appear unaffected by treatment with OXi4503, in that they appear well stained and organised, as highlighted in panel **B**. Other areas are lighter in staining, and upon closer inspection (panel **C**, 20x magnification) have lost structure and cell contact, cells have rounded up, and a necrotic appearance is apparent. This is similar to the observed effect in SW1222 tumours, however the extent of tumour necrosis is not the whole centre of the tumour, as with SW1222 tumours, but more patchy and spread out across the tumour cross section. Once again, red blood cells can be seen, as highlighted in panel **D**, at the edge of these necrotic areas of tumour, within the surviving tumour tissue, or outside of the tumour within normal skin structures.



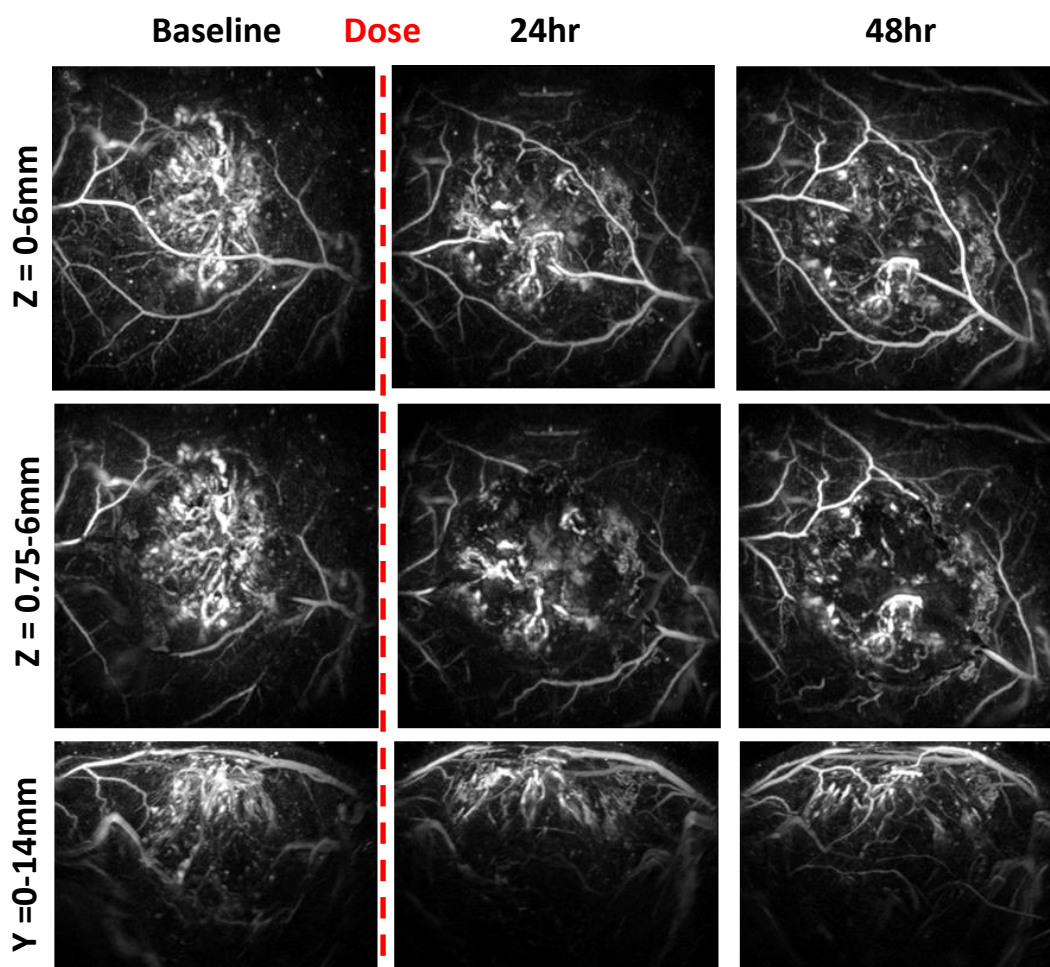


**Figure 4.5 Initial response to vascular disruption – LS174T**

Representative PAT images of LS174T s.c. tumours following 40mg/kg of OXi4503 i.v. (n=4). The first and second rows are 14x14mm in the XY and 0-6mm and 1-6mm in the Y direction MIPs, whilst the third row is 14x6mm in the XZ with 14mm in the Y as an MIP. Each row shows baseline images followed by 24 and 48hr post dose.

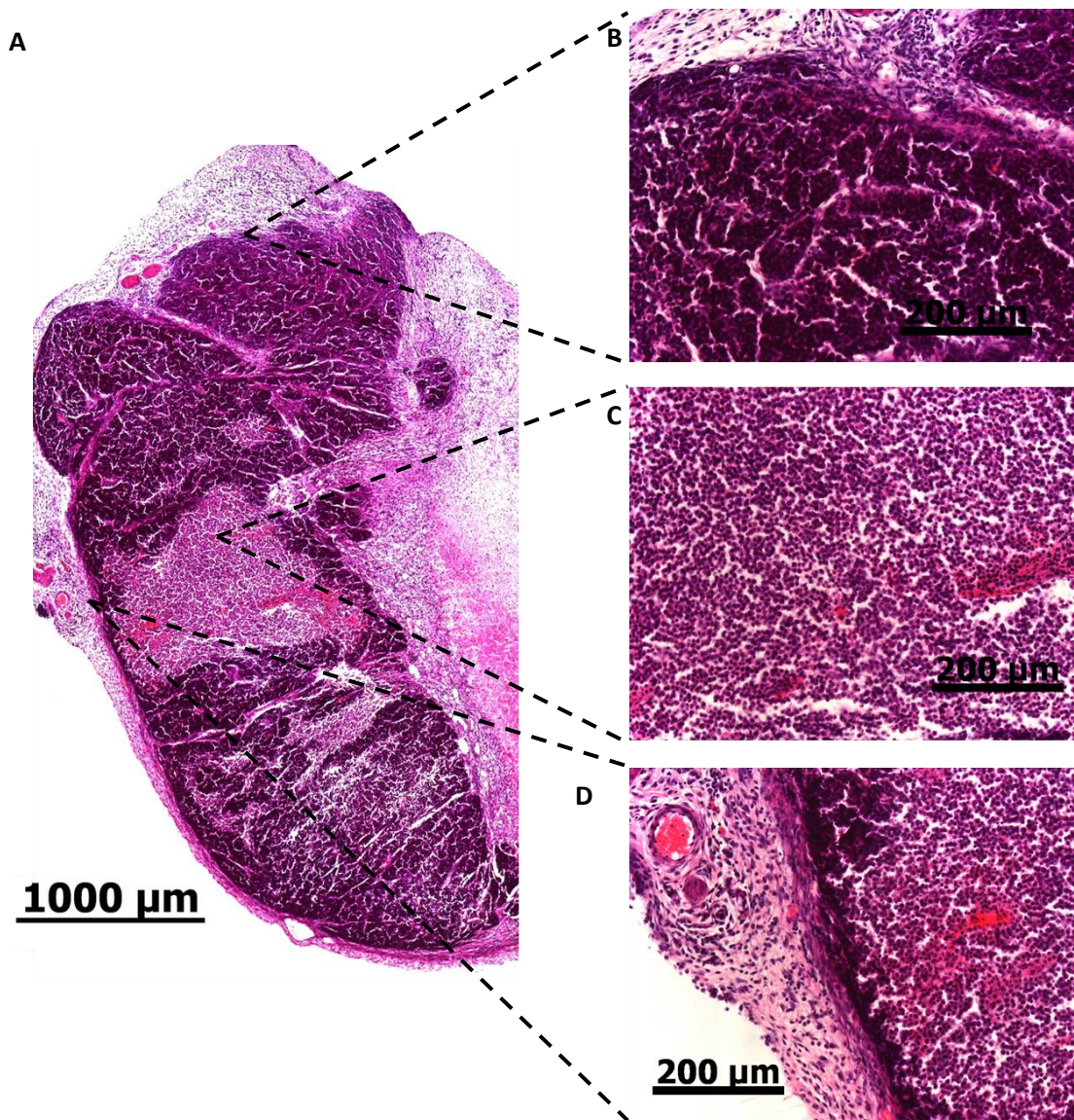


**Figure 4.6 Histology of initial response – LS174T**

Haematoxylin and Eosin staining of the n=4 LS174T tumours used for initial response to vascular disruption by PAT was performed, an example cross section of which can be seen in panel **A** (10x magnification). A highlighted section of surviving tumour tissue can be seen in panel **B** (20x). Panel **C** shows the necrosis and cellular debris that has occurred within areas of the tumour (20x). Panel **D** shows evidence of red blood cells within the tumour surviving tissue and periphery of the tumour necrotic area.

### 4.3.3 Vessel regrowth following treatment

Results from the longitudinal experiment on vessel regrowth can be observed in the representative tumours shown in **figure 4.7** (SW1222) and **figure 4.8** (LS174T). These panels are 14x14mm MIP in the XY direction and 1-6mm and 0.75-6mm in the Z direction respectively, acquired at 680nm excitation wavelength, and at the time points indicated above each panel. The SW1222 tumours all initially exhibited the central lack of signal after dosing with 40mg/kg OXi4503. However, over the 16 days of the experiment this area of signal void became smaller, as signal returned to the centre of the tumour from the outside edge of the tumour mass. The tumour regrowth appeared similar to the baseline image, but with a small necrotic central area remaining. The response of the LS174T tumours appears similar to the initial results of dosing with OXi4503 over 48 hours; signal pattern is disrupted within the tumour interior, but with smaller areas devoid of signal compared with SW1222, and a lesser degree of tumour periphery enhancement. Tumour recovery over time is also not as clear as in the SW1222 tumours, with overall pattern of PA signal distribution within the LS174T tumours not returning to baseline-like appearance within the 16 days. Signal from the 'void' areas does return to some extent, albeit with an irregular distribution, and appears to have returned to most areas of the tumour at around 10 days post dose, but with fewer vessels and a different pattern of distribution. This area of signal void, for both SW1222 and LS174T tumours, was plotted against measures of 'haemoglobin positive' tumour voxels and tumour volume, as can be seen in **figure 4.9**. The blue line shows average total tumour volume and the red line shows average total area of internal tumour without signal, shown as a percentage of the baseline measurement at day 0 measured on the left side Y axis, with error bars denoting standard error of the mean. Positive tumour voxels, as a measure of tumour haemoglobin within vessels, expressed as percentage of total tumour ROI voxels, can be seen in the black line measured on the right side Y axis. As can be seen, for the SW1222 tumours outward growth of the tumours does not occur whilst the area of internal signal void is still present. An initial decrease in tumour volume is accompanied by an increase in the internal areas of signal void and a decrease of percentage positive 'haemoglobin' voxels. Towards the end of this timeframe all parameters appear to be returning to baseline values, with volume increasing and positive voxels returning to the tumour core. Areas of void remain high but appear to be on a downward trend. For the LS174T tumours growth of the tumours starts at around 10 days post dose, although the voxels of positive 'haemoglobin' signal are still below baseline



values. Areas of PA signal void appear to initially decrease and stay at or below baseline values for the duration of the experiment.

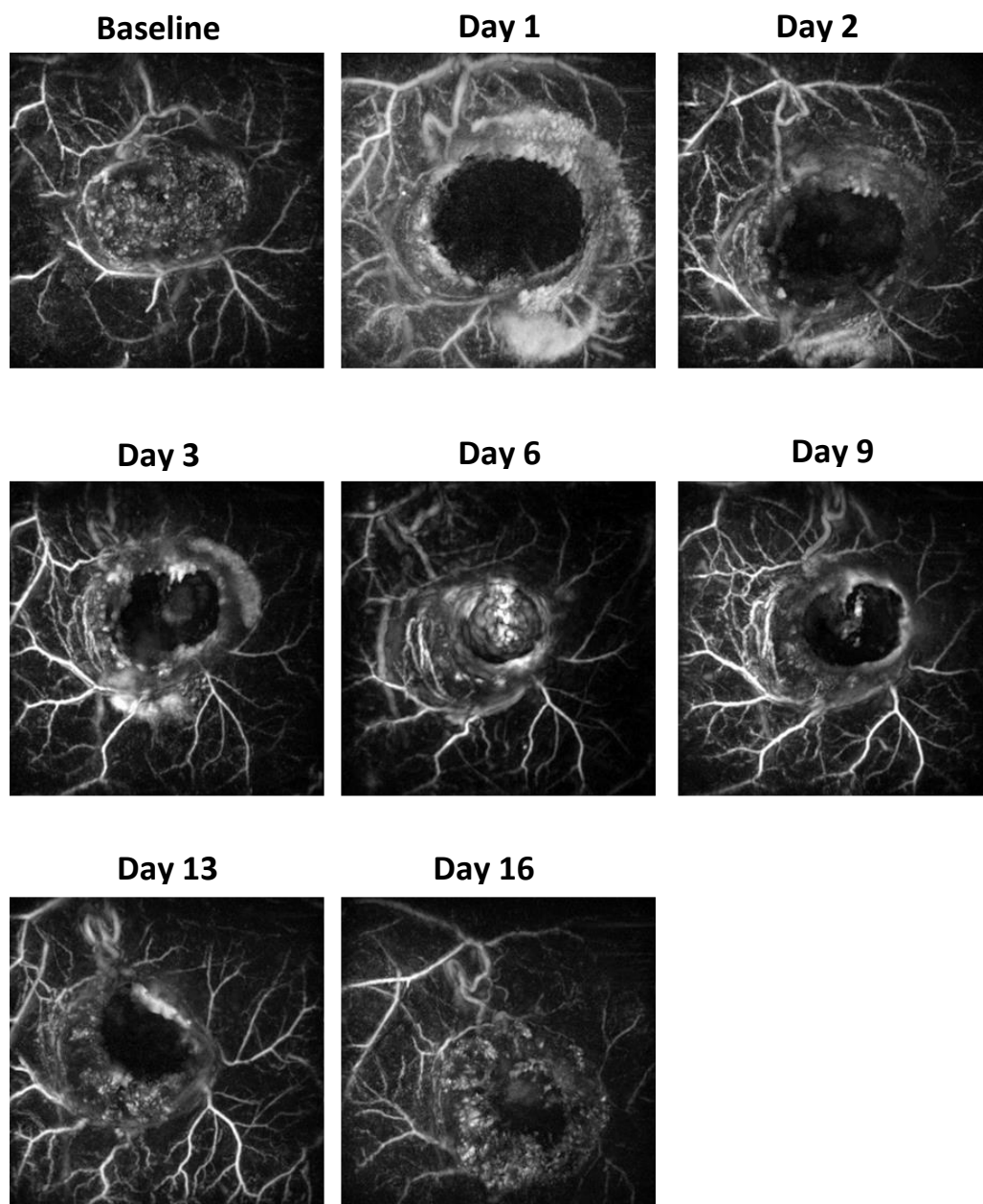


**Figure 4.7 Vessel regrowth following vascular disruption – SW1222**

Representative PAT images of SW1222 s.c. tumours following 40mg/kg of OXi4503 i.v. (n=6). Each panel is 14x14mm in the XY and 1-6mm in the Y direction MIPs reconstructed from PAT data acquisition. Time points are indicated above each panel, from baseline to 16 days after administration of dose.

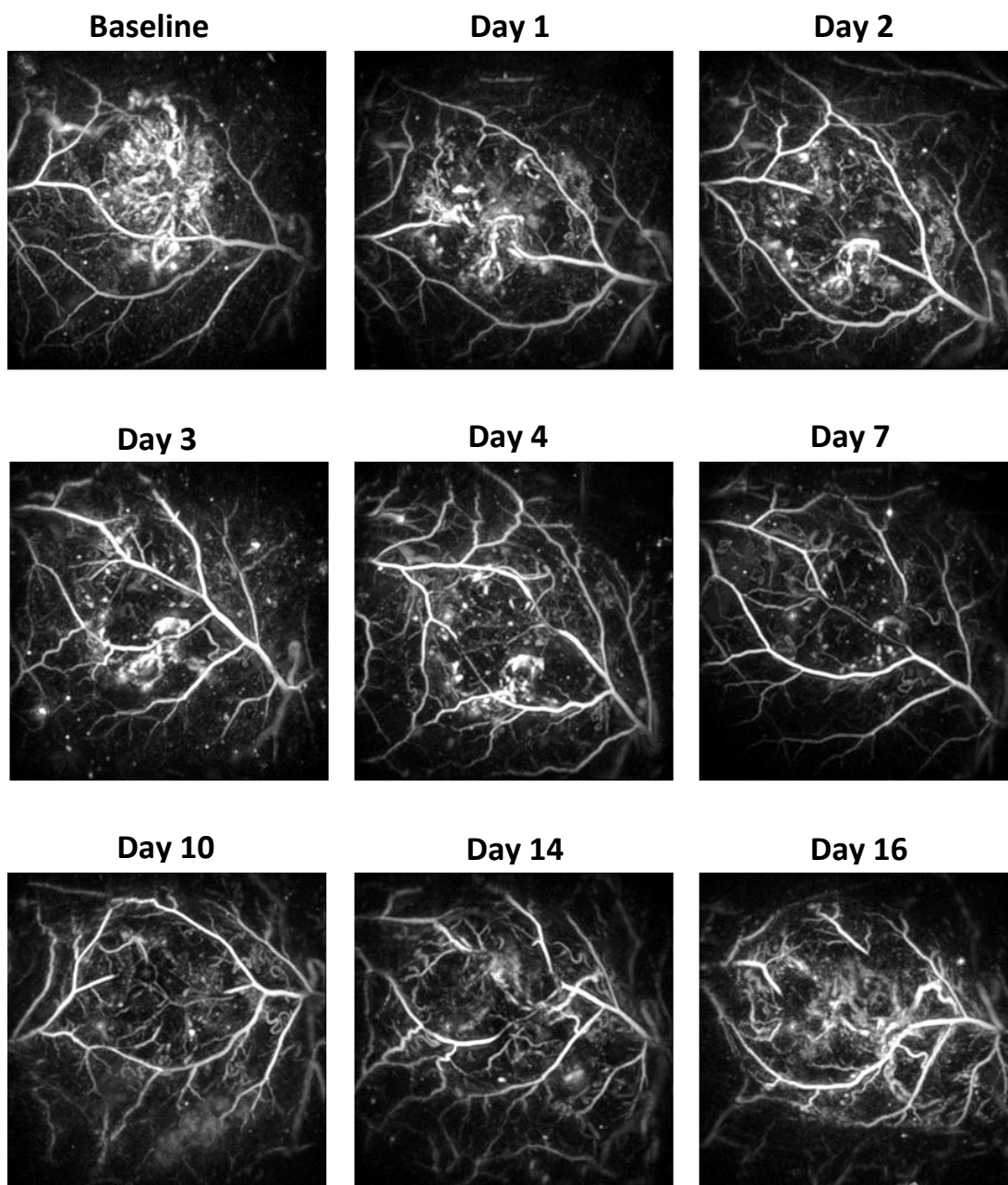


**Figure 4.8 Vessel regrowth following vascular disruption – LS174T**

Representative PAT images of LS174T s.c. tumours following 40mg/kg of OXi4503 i.v. (n=6). Each panel is 14x14mm in the XY and 0.75-6mm in the Y direction MIPs reconstructed from PAT data acquisition. Time points are indicated above each panel, from baseline to 16 days after administration of dose.

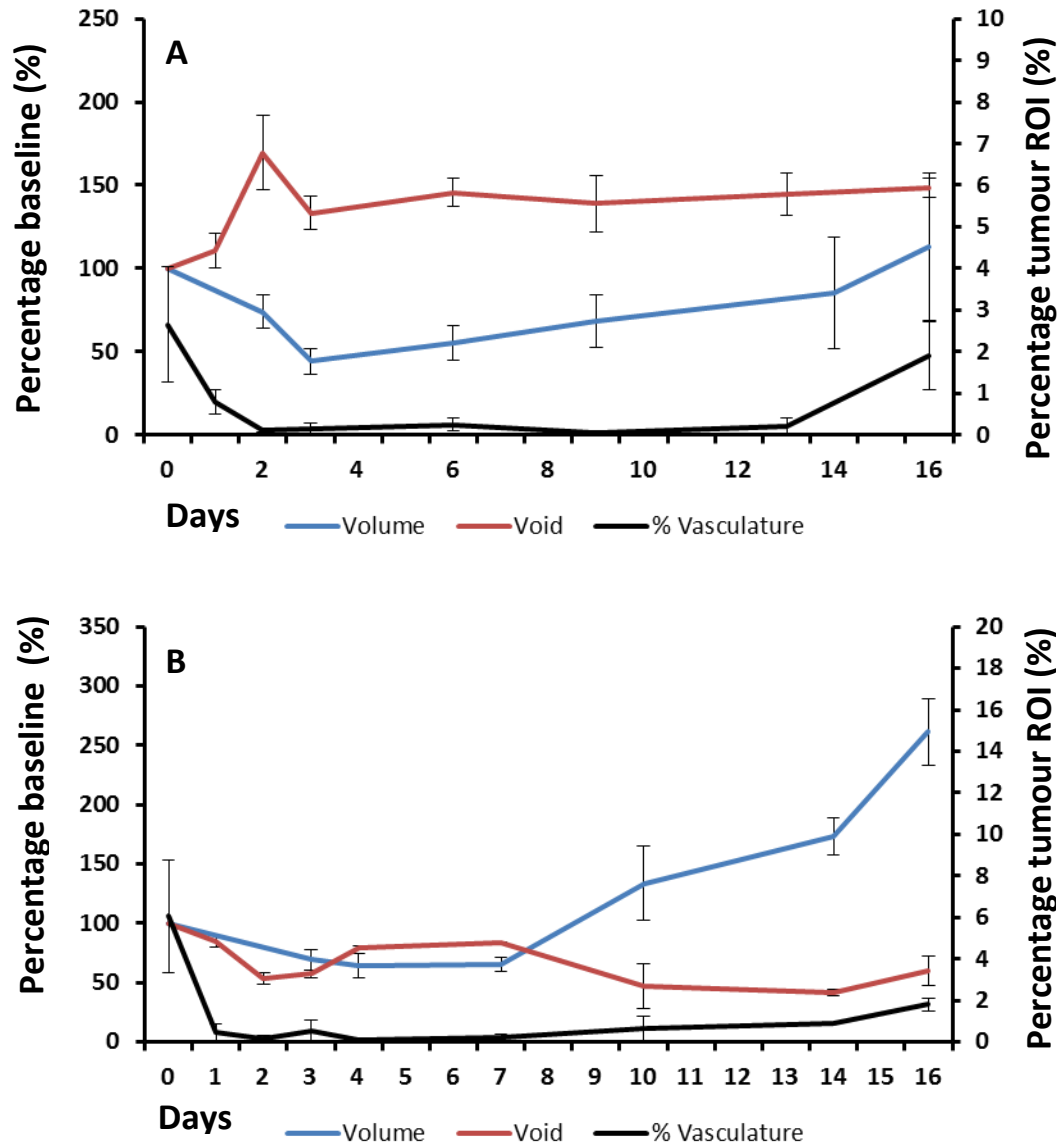


**Figure 4.9 Comparison of tumour volume vs PA signal intensity**

Graph **A** shows data for the SW1222 tumours and graph **B** shows data for the LS174T tumours (n=4 respectively). Tumour volume assessed by caliper measurement is shown across the n=4 tumours as percentage of baseline volume (Blue). The measure of PA signal intensity void within the tumour also as a measure of baseline is shown in red (left side axis). The percentage of tumour ROI at or above a reference PA signal measurement made in a superficial blood vessel is shown by the black line (right side axis). Error bars denote standard error of the mean.

#### 4.3.4 Effect of different OXi4503 doses can be observed in vivo by PAT

The effect of different degrees of vascular disruption on the signal intensity and distribution of PAT images caused by different concentrations of OXi4503, at 48hr post dose, can be seen in **figure 4.10** for SW1222 tumours and **figure 4.11** for LS174T tumours. The top row in each figure (**A**) shows an example PAT MIP images (14x14mm in the X and Y) for baseline, sham dose (for SW1222 only), and 1mg/kg, 10mg/kg, and 40mg/kg OXi4503. Each PAT image was acquired at 680nm and has had the top 1mm of the Z-stack removed. Voxel analysis of the tumour region was performed by manual segmentation, with intensity values for all voxels within this region displayed on a histogram of grey-scale intensity (0-256). An example histogram for the PAT image shown is presented in the second row. This shows a marked reduction in range of values within the tumour region for the 40mg/kg group (**C**) when compared to sham dose values (**B**). Average percentage of the tumour ROI that contained voxels of an intensity equal to or above the positive 'haemoglobin' reference measurement across the whole groups can therefore be measured; this is shown by the graph **D** of **figures 4.10** and **4.11**, with the error bars denoting the standard error of the mean. These graphs show the average sham-dose value to be  $8.5 \pm 0.8\%$  for SW1222, which is consistent with baseline values measured of  $8.3 \pm 1.25\%$ . Baseline values for LS174T tumours were  $10.25 \pm 1.75\%$ . All treated groups are lower in value in a dose dependent manner, with the 40mg/kg groups being  $0.11 \pm 0.1\%$  and  $0.15 \pm 0.3\%$  for SW1222 and LS174T tumours respectively, the 10mg/kg groups being  $2.5 \pm 0.5\%$  and  $2.89 \pm 0.6\%$ , and the 1mg/kg groups being  $8.17 \pm 1\%$  and  $8.65 \pm 0.95\%$ .

Histological analysis of these tumours for all dose levels in the SW1222 tumour can be seen in **figure 4.12**. The first column shows haematoxylin and eosin staining for basic tissue morphology. The sham dose tumour is composed of viable tissue which has a highly nucleated and densely packed structure. The 1mg/kg tumour consists of two distinct tumour lobules that resemble the untreated tumour. The 10mg/kg and 40mg/kg groups resemble each other, both possessing a tumour core that has less nuclear staining from haematoxylin, typical of areas of induced necrosis, and an outer capsule of connective tissue. However, a thin rim of viable tumour tissue around the necrosis can be seen, which appears to be slightly thicker for the 10mg/kg than the 40mg/kg dose. The second column shows dual fluorescence microscopy, with perfusion in blue (Hoechst 33342) and blood vessels in red (CD31). These channels are depicted separately in the subsequent two columns respectively. Within the tumour region in the sham and 1mg/kg groups both blood

vessels and perfusion are present across the tumour, indicating the presence of viable tissue and corresponding well with the H&E stain. In the 10mg/kg and 40mg/kg groups the central tumour region appears as a void of signal, indicating a lack of blood vessels and perfusion in the core, albeit with perfused blood vessels around the tumour periphery and in the connective tissue.

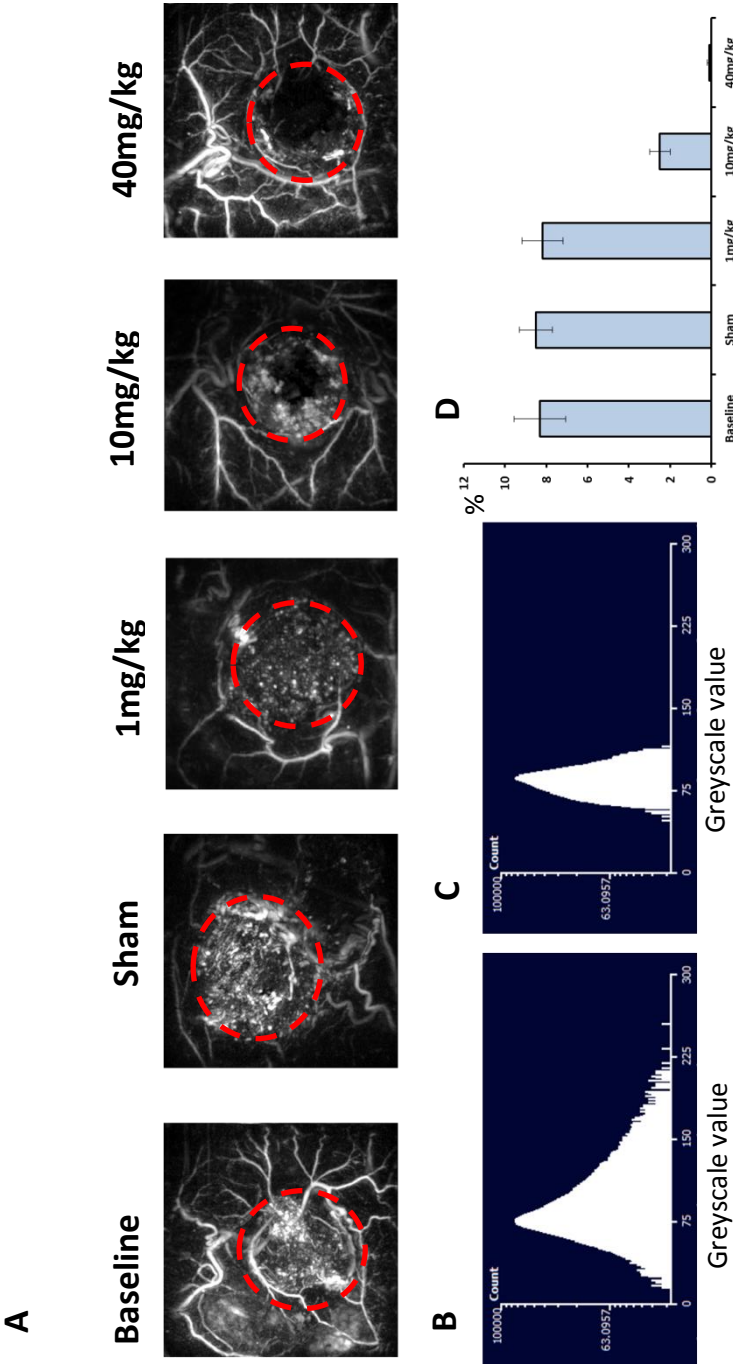


**Figure 4.10 PAT assessment of different doses of OXi4503 – SW1222**  
Assessment of the tumour microenvironment by PAT imaging; the first row **A** shows representative PAT images at 680nm of SW1222 tumours at baseline and after dosing with saline sham or 1mg/kg, 10mg/kg and 40mg/kg of OXi4503 (n=4 for each dose, panels are MIP projections, 14x14 XY, with 1mm removed in the Z direction). Histograms **B** and **C** show voxel analysis of manually segmented tumour regions for baseline and 40mg/kg groups respectively. From this, and using an external blood vessel as a 'haemoglobin positive' test, tumour voxels containing haemoglobin positive signal can be quantified. This is depicted in graph **D** for all groups, and shows a dose dependent reduction in percentage of tumour area positive for haemoglobin (error bars denote mean ± SDM).

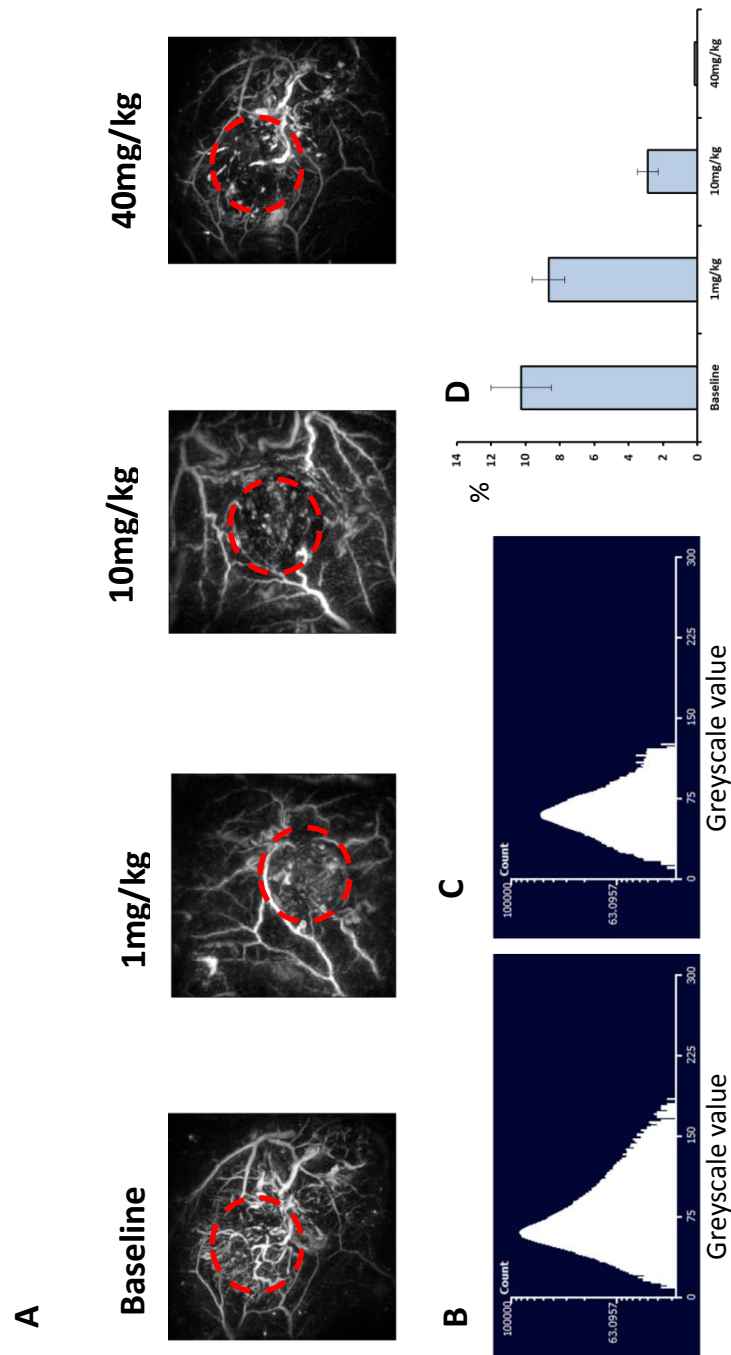


**Figure 4.11 PAT assessment of different doses of OXi4503 – LS174T**

Assessment of the tumour microenvironment by PAT imaging; the first row **A** shows representative PAT images at 680nm of LS174T tumours at baseline and after dosing with 1mg/kg, 10mg/kg and 40mg/kg of OXi4503 (n=4 for each dose, panels are MIP projections, 14x14 XY, with 1mm removed in the Z direction). Histograms **B** and **C** show voxel analysis of manually segmented tumour regions for baseline and 40mg/kg groups respectively. From this, and using an external blood vessel as a 'haemoglobin positive' test, tumour voxels containing haemoglobin positive signal can be quantified. This is depicted in graph **D** for all groups, and shows a dose dependent reduction in percentage of tumour area positive for haemoglobin (error bars denote mean $\pm$ SDM)



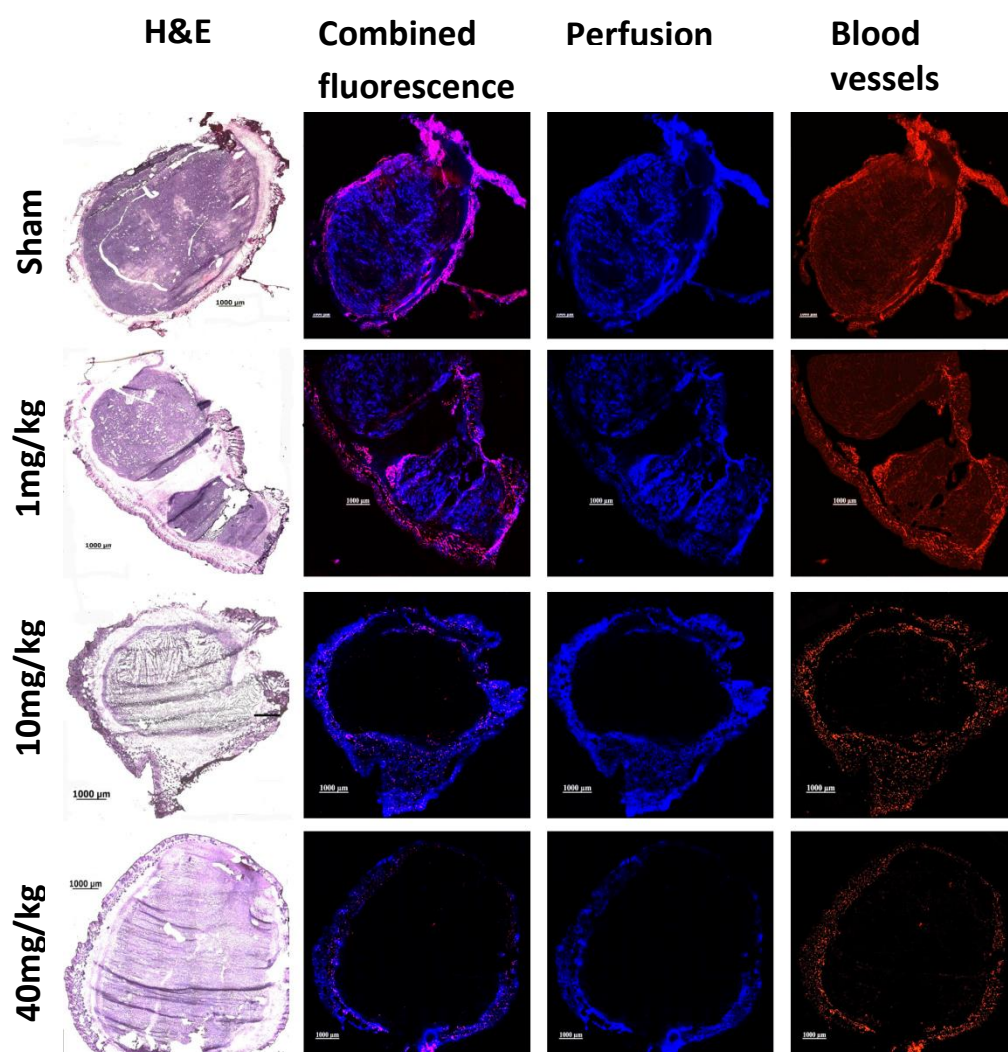


**Figure 4.12 Histological assessment of different doses of OXi4503**

Assessment of the tumour microenvironment by histological staining and immunofluorescence; the first column shows haematoxylin and eosin staining for tissue morphology representative of SW1222 tumours after dosing with saline control or 1mg/kg, 10mg/kg and 40mg/kg of OXi4503. The same tumours can be seen in column 2, which shows combined immunofluorescence for perfusion by Hoechst 33342 in blue, and blood vessel by CD31 in red. These channels are shown separately in columns 3 and respectively.

#### 4.3.5 PA signal intensity corresponds to regrowth of tumours

Measurement of tumour volume across the dose response groups can be seen in **figure 4.13**. Graph **A** shows the tumour growth data for the SW1222 tumours and graph **B** the growth data for the LS174T tumours. Volume is expressed as the average percentage of baseline volume, with error bars denoting standard error. In each graph the 40mg/kg OXi4503 is depicted by the blue line, the 10mg/kg group by the red line, the 1mg/kg group by the green line, and a control group, measured from  $n = 8$  size matched tumours of each type over the same time frame, shown in purple. A typical dose response curve can be seen in both tumour types, with the 40mg/kg dose having the greatest effect on tumour volume, followed by the 10mg/kg and finally the 1mg/kg groups. The 1mg/kg group for both SW1222 and LS174T tumours is similar to the control group. Using 200% of initial tumour volume as a measure of doubling time (so as to be confident of actual tumour growth as opposed to measurement inaccuracy or tumour swelling/blood pooling due to treatment) the graph shows that the SW1222 40mg/kg group does not double within the 16 day timeframe, the 10mg/kg group takes 13.9 days and the 1mg/kg group takes 3.8 days. Doubling time for the SW1222 control group was measured as 3.9 days. For the LS174T tumours doubling time was calculated as 12.2 days for the 40mg/kg group, 6.7 days for the 10mg/kg group, 3.5 days for the 1mg/kg group, and 4.3 days for the control group. Using the PA images to calculate return of increased signal intensity to tumour voxels, as shown in **figure 4.10** and **4.11**, the time taken for tumours to return to a 'normal' proportion of 'haemoglobin positive' PA signal across the tumour can be determined. This was calculated as 65% of baseline values for the SW1222 10mg/kg group at day 13, a time point at which the tumours are re-growing by caliper measurement. For the 1mg/kg group the values at 48 hours post VDA are 98.3% of baseline values, with the growth of the tumour almost matching control volumes. For the LS174T tumours, at time points where the tumours appear to be re-growing, this is 51.9% at day 10 for the 40mg/kg group, 70.8% at day 10 for the 10mg/kg group, and 84.4% at 48 hours for the 1mg/kg group.



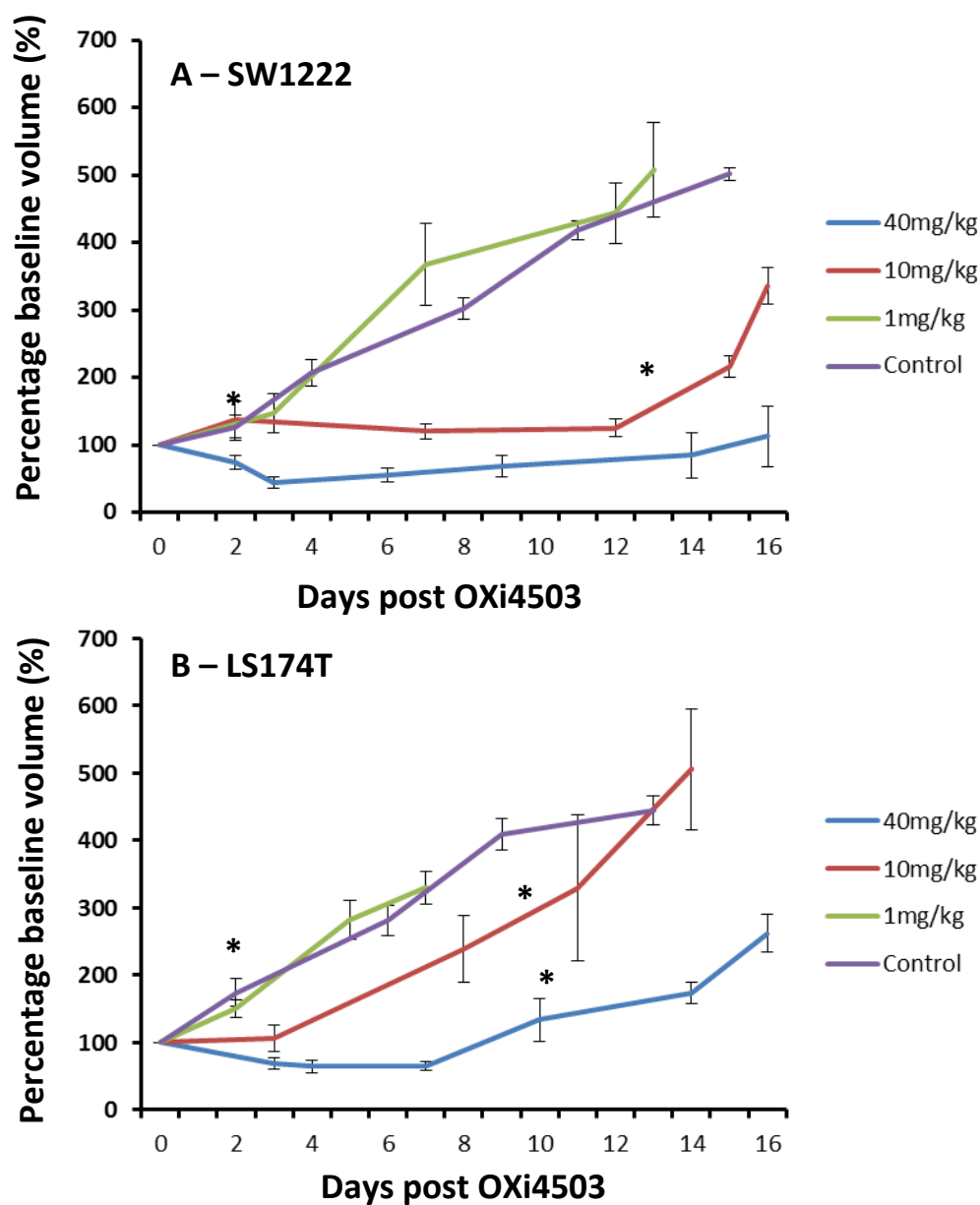


**Figure 4.13 Dose response to OXi4503 compared to PA signal**

Tumour volume calculated by caliper measurement is shown for control (n=6, purple) and 40mg/kg (blue), 10mg/kg (red) and 1mg/kg (green) of OXi4503 for both SW1222 (A) and LS174T (B) (n=4 for each group). Using PA signal intensity as a measure of internal tumour blood vessel structure, the point at which tumour return to a 'normal' growth can be linked to the PA tumour expression, as highlighted by the star above each group.

## 4.4 Discussion

### 4.4.1 Destruction of tumour associated vasculature can be assessed by PAT

It is well known that OXi4503 causes tumour specific destruction of blood vessels (19, 20). Studies that have shown this pre-clinically however are invasive, may alter the tumour microenvironment due to experimental procedure, and may not accurately reflect the tumour blood vessel three dimensional networks, associated feeding vessels and interaction with its surroundings. Invasive studies are unable to image developing tumours over a significant period of time, unlike PAT. In this study, cancer cells were subcutaneously injected and left to develop as solid primary tumours, a model of disease that is a well-established animal representation of cancer. These models are often difficult to translate into clinical use, so correct interpretation of model data is crucial (21, 22). Another caveat is that this tumour location is ectopic, and therefore the tumour-surrounding milieu does not reflect the microenvironment in which the tumour would originally develop; however, the progression of neo-angiogenesis and the growth of the internal tumour vasculature is representative of the clinical situation. Previous work has shown that VDAs (23-26), and specifically OXi4503 (27), start to affect the structure and viability of tumour vascular endothelial cells within 1-4 hours of treatment, and cause blood vessel destruction and tumour necrosis from 6-24 hours onwards. In order to observe this with PAT, a dose sufficient to cause massive central destruction of tumour blood vessels was used. At 40mg/kg, the dose of OXi4503 is higher than the 25mg/kg required to cause a reduction of 90% in tumour perfusion in KHT sarcomas (28), and greater than the ED50 for tumour vessel shutdown of 3mg/kg in MDA-MB-231 adenocarcinomas and MHEC5-T hemangio-endotheliomas (29). This dose of 40mg/kg was also close to the dose of 50mg/kg shown to be effective at reducing functional vascular volume by over 80% (19), and was therefore deemed sufficient to cause maximum effect within the colorectal tumours tested. Initial response to this dose at 1 hour for both SW1222 and LS174T, as seen in **figure 4.1**, did not appear to cause any change in PA signal or image quality. If the effect of OXi4503 within this hour was to slow and/or stop the flow of blood within the tumour blood vessels, as is the mechanism of action of VDAs (30), with no physical destruction of blood vessels, then the haemoglobin still within the blood located in the vessels would be sufficient to maintain PA signal. A real-time video assessment of blood flow would be able to distinguish this; however, as currently each PA image requires around 8 minutes to acquire the full data set, any changes in flow are not detected by this system. Other PA imaging

approaches using ultrasound detection arrays have recently reported real-time imaging capabilities (31) although, as is the case with piezoelectric detectors, the image quality and resolution is not sufficient for imaging subcutaneous tumours in great detail. The ability to image in real time on this all optical system would therefore be a major advantage, and studies are underway to improve this aspect of the UCL PA scanner in order to image blood flow within tissue (32).

At 6 hours post dosing, when vessel destruction is expected, a slight change in PA signal was noted in the SW1222 tumours. While this is likely to indicate the onset of vessel destruction, the effect was variable and not sufficient to confidently state it was the result of VDA action. However, at the later times of 24 and 48 hours post injection (**figures 4.3 and 4.5**), the effect of vascular disruption with OXi4503 was clearly apparent; the signal from the internal section of the tumour has completely disappeared, compared to the saline sham dose that has maintained signal intensity. The effect was most pronounced in the SW1222 tumours, which showed a complete void of signal, correlating to a total destruction of tumour blood vessels. A high intensity signal from the tumour periphery is also present, which is thought to be due to a combination of factors: firstly, vessels in the remaining viable tumour rim; secondly, blood destined for the tumour no longer having a vascular structure through which to diffuse and simply pooling at the tumour edge; and thirdly, the haemoglobin from the destroyed central blood vessels being pushed out towards the rim of the necrotic area due to high intra-tumour pressure. This is verified by the histological assessment of these tumours in **figures 4.4 and 4.6**; in the SW1222 tumours a clear boundary is set by the rim of surviving cells around the tumour cross section. Inside of this the tumour is necrotic, with a loss of structure, rounding of cells, and cellular breakdown products. Any red blood cells are either within vessels of the normal tissue or very close to the surviving rim. Of note is the fact that no PAT signal from the destroyed tumour blood vessels remains in the tumour core which is consistent with the histological analysis, and therefore the haemoglobin must have either been removed or shifted to the tumour edge, even though previous work (33) has shown remnants of endothelial cells to exist within the necrotic area. This increased presence of haemoglobin and supposed blood around the periphery of the tumour is consistent with the known effect of a viable surviving rim following treatment with OXi4503 (34). The change in PA signal within LS174T tumours also shows a decrease in signal from within the tumour and areas of signal void, however the effect is much less pronounced than in the SW1222 tumours. Histology shows that the necrotic areas appear in a patchy manner, and the obvious central necrosis in the

SW1222 tumours is not replicated. Necrotic areas do appear however, and the red blood cell distribution around the periphery of these necrotic areas is similar to the SW1222 tumours. A peripheral rim effect is however still present in the PAT data, demonstrating this destruction of internal blood vessels and the pooling of blood at the tumour edge. The difference in response also reflects the ability of PAT to distinguish between two tumours with differing vascular pathophysiologies, and also different levels of response within the same tumour, which may both be clinically translatable as prognostic factors for response to vascular targeted therapies. This aspect of research would need to be examined in greater depth in future studies.

#### **4.4.2 Internal tumour vasculature is required for outward growth of the tumour**

Longitudinal studies following the regrowth of internal blood vessels, seen up to day 16 following the highest dose of 40mg/kg in **figures 4.7** and **4.8** for qualitative assessment of response in both SW1222 and LS174T respectively, and in **figure 4.9** for a semi-quantitative assessment of lack of internal PA signal and return of high-signal voxels compared to actual tumour volume, provide novel insights in to the effect of targeting the tumour vasculature with VDA treatment. Firstly, the tumours are not completely eradicated by a single dose; whilst this is a known effect of VDA treatment, and the tumours regrow from a surviving viable rim of cells (35), the manner in which this occurs has not been previously demonstrated. From this work I have shown that the avascular areas of tumour are repopulated from the surviving rim, with angiogenic vessels growing inwards from the tumour periphery. This is evident from qualitative assessment of the PAT images and the shrinkage of the internal areas of signal void. From the semi-quantitative assessment of tumour voxels the return of high-signal voxels, comparable to haemoglobin containing voxels outside of the tumour location and therefore assumed to be areas of haemoglobin containing vasculature, appears to have a greater significance than the detection of signal void voxels. For SW1222 tumours the void areas remain high at day 16 post dose, and whilst there is no outward growth of the tumours the content of vascular voxels within the tumour ROI is increasing, signalling return of a normal vascular distribution. The LS174T tumours by contrasts appear to have fewer or similar areas of signal void, equating to avascular and necrotic sections of the tumour, and a decreased percentage of vascular regions. The areas of vascular voxels, whilst not returning to baseline values, do appear to increase from around day 7 which is consistent with outward increase in tumour volume. Whilst the inward growth of tumour vasculature from the surviving rim may seem logical, it

is nonetheless only demonstrable by longitudinal *in vivo* studies such as those presented here. Of importance is also the fact that for certain vascular pathophysiologies, such as the well organised SW1222 tumours, whilst this central avascular area remains outward growth of the solid tumour does not occur whilst the avascular tumour areas remain; **figure 4.9** clearly shows that the SW1222 tumours do not grow over this period of time and that the internal PA signal is only just returning to baseline values. For other types of tumour vasculature extent, such as the more chaotic LS174T tumours, an increase in haemoglobin containing regions appears sufficient to allow growth of the tumour. This method of assessing return of vasculature is a straightforward approach, but is thus shown to be effective. The structure of the new vasculature however is not observed; although the PA signal has returned, the appearance of the LS174T tumours is visually different to baseline images. It is possible that, as LS174T tumours are more chaotic with regards to neo-angiogenesis and, having a less extensively organised vasculature to begin with (36), are used to conditions of low oxygenation, scarce nutrients and abnormal blood supply, that they are more predisposed to an aggressive survival phenotype and are able to regrow in micro-environmental conditions to which the SW1222 tumours are not suited. Qualitative assessment of the neo-angiogenesis of the SW1222 tumours suggests a regular pattern of PA signal as seen in baseline images. This difference in vascular pathophysiology, which affects outcome to treatment with VDAs, is observable with PAT and could potentially be a powerful application of PAT in the clinic, used to assess tumour vascular state, and therefore expected outcome, in different patients. What is also useful for clinical practice is noting the pharmacodynamic effect of VDA action, i.e. when the tumour has re-vascularised, and therefore the interval with which patients need to be re-dosed in order to inhibit tumour growth. Interpretation of the data would be improved however by further analysis, such as vessel detection algorithms and texture analysis of grey scale values. Even with the approach used here however, I have demonstrated that large avascular areas within the tumour need to be repopulated with tumour tissue before outward growth can occur.

#### **4.4.3 Efficacy of vascular targeted treatment can be observed with PAT**

Having shown that PAT can detect vascular disruption and inward regrowth of the tumour vessels following treatment with a high dose of OXi4503, it is valuable to note that PAT can also detect smaller changes in vascular disruption within the tumour, as demonstrated by reduced doses of the VDA. The shift in PA values within tumour voxels at 48 hours, seen in

**figures 4.10 and 4.11**, show that lower doses of OXi4503 had a lesser effect than the highest 40mg/kg dose. Microscopy images at this time point (**figure 4.12**) show that the effect of vascular disruption was greatest in the 40mg/kg group and 10mg/kg group, with no blood vessels or perfusion present in the core of the tumours. Morphological staining by H&E shows these regions to be necrotic, with less densely packed nucleic staining. The lowest treatment group of 1mg/kg appears to be similar to sham dosed tumours, suggesting a very minor response to treatment. These reflect the PA signal obtained *in vivo*, where the greatest changes are seen in the 40mg/kg and 10mg/kg groups, with a smaller reduction in the 1mg/kg group. A similar effect is noted by Hill et al, 2002, where 1mg/kg of OXi4503 causes a reduction of 50% of functional vascular volume compared to greater than 80% for doses above 10mg/kg (19). This translates *in vivo* to a retardation of tumour growth in a dose dependent manner, as can be seen in **figure 4.13**. The growth curves for 40mg/kg, 10mg/kg, and 1mg/kg are separated on typical response curves seen in other models, what is shown here for the first time is that measures of PAT can distinguish, based on voxel comparison to baseline data, between effective and non-effective doses of the same vascular targeted drug. This again demonstrates the potential utility of PAT in the clinic for monitoring response to vascular targeted treatment. Also of interest is that, although not fully back to baseline values, around 50% 'haemoglobin positive' voxels spread across the tumour ROI are needed for re-growth. Whilst this study has concentrated on the response to VDA treatment, other vascular targeted agents such as anti-angiogenic therapies using humanised antibodies (37), and small molecules that attempt to normalise the tumour vascular microenvironment (38), would also be prime candidates for investigation with PAT.

## 4.5 Conclusion

In this chapter I have shown that PAT can be used effectively for monitoring response to vascular disruption with OXi4503. The resultant change in PA signal can be used to assess initial state of vascularisation and likelihood of achieving efficacy, and also relapse of the halt that is placed on tumour growth. As such it could be translated to the clinic to be used as a marker of vascular targeted therapies in patients. Further work on other vascular targeted therapies is a future aim of this research. I have also shown that different vascular pathophysiologies will respond differently to the same dose of drug, and that PAT can image these different vascular states in a longitudinal manner. Whilst many different vascular pathophysiologies will exist in patients, and the response to different vascular

targeted drugs and treatment strategies will vary considerably, the future use of PAT in the clinic is potentially a very powerful tool for determining patient response.. Further work on the analysis of the acquired data, such as determining the exact structure of the effected vasculature, is ongoing. However, it has also been noted that the internal vasculature returns from the periphery of the tumour at the surviving rim with neo-angiogenesis from the surrounding normal skin vasculature.

In order to further analyse the acquired data for this vasculature structure, more in depth studies correlating these PAT data with histology could be performed. For a quantitative measure histological staining for blood vessels could be accompanied by tissue micro-vessel density determination tissue slices and compared to PAT data sets. Two issues would arise from this comparison that would further complicate analysis; the first is that histological assessment of micro-vessel density would only be in two dimensions whilst the PAT is in three. The second problem would be that even if three-dimensional histology was not required, and the signal from only a section of the PAT data used to match the tissue section, the tissue deformation *ex vivo* would complicate correct alignment of both data sets. Fiducial markers would need to be implemented and shown to correlate precisely between data sets.

Whilst initial studies are promising, and the future potential of the use of PAT in the clinic is to some degree demonstrated, this research also shows some problematic areas that need addressing. Real time imaging is not currently possible with optical PAT. The imaging window, whilst large for *in vivo* optical studies, is small when compared to clinical used systems such as CT, MRI, SPECT and PET. Whole body imaging is not possible with this system, making difficult the assessment of deep sited or widespread disease. Models of cancer that are orthotopically located, such as within the liver to reflect metastasis, are therefore hard to image. As orthotopic locations have a tumour microenvironment that better imitates the clinical situation the response to therapy may be different to that which occurs in the subcutaneous location.

For all these reasons this research in to the pathological vascular microenvironment of tumours was next assessed by MRI parameters associated with blood supply to the tumour, both in subcutaneous and liver metastasis orthotopic models. This is presented in the following chapters.





## 4.6 References

- (1) Brubaker LM, Bullitt E, Yin C, Van DT, Lin W. Magnetic resonance angiography visualization of abnormal tumor vasculature in genetically engineered mice. *Cancer Res* 2005;65:8218-23.
- (2) Bullitt E, Lin NU, Smith JK, Zeng D, Winer EP, Carey LA, et al. Blood vessel morphologic changes depicted with MR angiography during treatment of brain metastases: a feasibility study. *Radiology* 2007;245:824-30.
- (3) Nishimura S, Hirai T, Shigematsu Y, Kitajima M, Morioka M, Kai Y, et al. Evaluation of brain and head and neck tumors with 4D contrast-enhanced MR angiography at 3T. *AJNR Am J Neuroradiol* 2012;33:445-8.
- (4) Zou Z, Ma L, Cheng L, Cai Y, Meng X. Time-resolved contrast-enhanced MR angiography of intracranial lesions. *J Magn Reson Imaging* 2008;27:692-9.
- (5) Pipe JG. Limits of time-of-flight magnetic resonance angiography. *Top Magn Reson Imaging* 2001;12:163-74.
- (6) Lin CY, Siow TY, Lin MH, Hsu YH, Tung YY, Jang T, et al. Visualization of rodent brain tumor angiogenesis and effects of antiangiogenic treatment using 3D DeltaR2-muMRA. *Angiogenesis* 2013;16:785-93.
- (7) Valable S, Lemasson B, Farion R, Beaumont M, Segebarth C, Remy C, et al. Assessment of blood volume, vessel size, and the expression of angiogenic factors in two rat glioma models: a longitudinal in vivo and ex vivo study. *NMR Biomed* 2008;21:1043-56.
- (8) Lemasson B, Valable S, Farion R, Krainik A, Remy C, Barbier EL. In vivo imaging of vessel diameter, size, and density: a comparative study between MRI and histology. *Magn Reson Med* 2013;69:18-26.
- (9) Peng SL, Chen CF, Liu HL, Lui CC, Huang YJ, Lee TH, et al. Analysis of parametric histogram from dynamic contrast-enhanced MRI: application in evaluating brain tumor response to radiotherapy. *NMR Biomed* 2012.
- (10) Coenegrachts K, Bols A, Haspeslagh M, Rigauts H. Prediction and monitoring of treatment effect using T1-weighted dynamic contrast-enhanced magnetic resonance imaging in colorectal liver metastases: potential of whole tumour ROI and selective ROI analysis. *Eur J Radiol* 2012;81:3870-6.
- (11) Miles KA, Lee TY, Goh V, Klotz E, Cuenod C, Bisdas S, et al. Current status and guidelines for the assessment of tumour vascular support with dynamic contrast-enhanced computed tomography. *Eur Radiol* 2012;22:1430-41.
- (12) Bisdas S, Surlan-Popovic K, Didanovic V, Vogl TJ. Functional CT of squamous cell carcinoma in the head and neck: repeatability of tumor and muscle quantitative measurements, inter- and intra-observer agreement. *Eur Radiol* 2008;18:2241-50.

- (13) Ng CS, Kodama Y, Mullani NA, Barron BJ, Wei W, Herbst RS, et al. Tumor blood flow measured by perfusion computed tomography and <sup>15</sup>O-labeled water positron emission tomography: a comparison study. *J Comput Assist Tomogr* 2009;33:460-5.
- (14) Goh V, Halligan S, Gartner L, Bassett P, Bartram CI. Quantitative colorectal cancer perfusion measurement by multidetector-row CT: does greater tumour coverage improve measurement reproducibility? *Br J Radiol* 2006;79:578-83.
- (15) Tai JH, Tessier J, Ryan AJ, Hoffman L, Chen X, Lee TY. Assessment of acute antivasular effects of vandetanib with high-resolution dynamic contrast-enhanced computed tomographic imaging in a human colon tumor xenograft model in the nude rat. *Neoplasia* 2010;12:697-707.
- (16) Korpanty G, Carbon JG, Grayburn PA, Fleming JB, Brekken RA. Monitoring response to anticancer therapy by targeting microbubbles to tumor vasculature. *Clin Cancer Res* 2007;13:323-30.
- (17) Seshadri M, Sacadura NT, Coulthard T. Monitoring antivasular therapy in head and neck cancer xenografts using contrast-enhanced MR and US imaging. *Angiogenesis* 2011;14:491-501.
- (18) Lang SA, Moser C, Gehmert S, Pfister K, Hackl C, Schnitzbauer AA, et al. Contrast-enhanced ultrasound (CEUS) detects effects of vascular disrupting therapy in an experimental model of gastric cancer. *Clin Hemorheol Microcirc* 2014;56:287-99.
- (19) Hill SA, Tozer GM, Pettit GR, Chaplin DJ. Preclinical evaluation of the antitumour activity of the novel vascular targeting agent Oxi 4503. *Anticancer Res* 2002;22:1453-8.
- (20) Chan LS, Malcontenti-Wilson C, Muralidharan V, Christophi C. Effect of vascular targeting agent Oxi4503 on tumor cell kinetics in a mouse model of colorectal liver metastasis. *Anticancer Res* 2007;27:2317-23.
- (21) Eklund L, Bry M, Alitalo K. Mouse models for studying angiogenesis and lymphangiogenesis in cancer. *Mol Oncol* 2013;7:259-82.
- (22) Carmeliet P, Jain RK. Angiogenesis in cancer and other diseases. *Nature* 2000;407:249-57.
- (23) Tozer GM, Prise VE, Wilson J, Cemazar M, Shan S, Dewhirst MW, et al. Mechanisms associated with tumor vascular shut-down induced by combretastatin A-4 phosphate: intravital microscopy and measurement of vascular permeability. *Cancer Res* 2001;61:6413-22.
- (24) Goertz DE, Yu JL, Kerbel RS, Burns PN, Foster FS. High-frequency Doppler ultrasound monitors the effects of antivasular therapy on tumor blood flow. *Cancer Res* 2002;62:6371-5.
- (25) Hori K, Saito S, Kubota K. A novel combretastatin A-4 derivative, AC7700, strongly stanches tumour blood flow and inhibits growth of tumours developing in various tissues and organs. *Br J Cancer* 2002;86:1604-14.

- (26) El-Emir E, Boxer GM, Petrie IA, Boden RW, Dearling JL, Begent RH, et al. Tumour parameters affected by combretastatin A-4 phosphate therapy in a human colorectal xenograft model in nude mice. *Eur J Cancer* 2005;41:799-806.
- (27) Sheng Y, Hua J, Pinney KG, Garner CM, Kane RR, Prezioso JA, et al. Combretastatin family member OXi4503 induces tumor vascular collapse through the induction of endothelial apoptosis. *Int J Cancer* 2004;111:604-10.
- (28) Salmon HW, Siemann DW. Effect of the second-generation vascular disrupting agent OXi4503 on tumor vascularity. *Clin Cancer Res* 2006;12:4090-4.
- (29) Hua J, Sheng Y, Pinney KG, Garner CM, Kane RR, Prezioso JA, et al. Oxi4503, a novel vascular targeting agent: effects on blood flow and antitumor activity in comparison to combretastatin A-4 phosphate. *Anticancer Res* 2003;23:1433-40.
- (30) Tozer GM, Kanthou C, Baguley BC. Disrupting tumour blood vessels. *Nat Rev Cancer* 2005;5:423-35.
- (31) Razansky D, Deliollanis NC, Vinegoni C, Ntziachristos V. Deep tissue optical and optoacoustic molecular imaging technologies for pre-clinical research and drug discovery. *Curr Pharm Biotechnol* 2012;13:504-22.
- (32) Brunner J, Beard P. Pulsed photoacoustic Doppler flowmetry using time-domain cross-correlation: accuracy, resolution and scalability. *J Acoust Soc Am* 2012;132:1780-91.
- (33) Pedley RB, Tozer G. Vascular Disruptive Agents for the Treatment of Cancer. In: Meyer, T, (ed.). Springer Verlag 2010:49 - 75
- (34) Chaplin DJ, Pettit GR, Hill SA. Anti-vascular approaches to solid tumour therapy: evaluation of combretastatin A4 phosphate. *Anticancer Res* 1999;19:189-95.
- (35) Kanthou C, Tozer GM. Microtubule depolymerizing vascular disrupting agents: novel therapeutic agents for oncology and other pathologies. *Int J Exp Pathol* 2009;90:284-94.
- (36) El EE, Qureshi U, Dearling JL, Boxer GM, Clatworthy I, Folarin AA, et al. Predicting response to radioimmunotherapy from the tumor microenvironment of colorectal carcinomas. *Cancer Res* 2007;67:11896-905.
- (37) Shahneh FZ, Baradaran B, Zamani F, Aghebati-Maleki L. Tumor angiogenesis and anti-angiogenic therapies. *Hum Antibodies* 2013;22:15-9.
- (38) Goel S, Duda DG, Xu L, Munn LL, Boucher Y, Fukumura D, et al. Normalization of the vasculature for treatment of cancer and other diseases. *Physiol Rev* 2011;91:1071-121.

# Chapter 5 Magnetic resonance imaging parameters associated with tumour vascular pathophysiology

---

## 5.1 Introduction

As described in the concluding remarks of the previous chapter, this research in to the pathological vascular microenvironment will now concentrate on MRI parameters associated with tumour development, and especially those that provide a functional response marker to therapeutic tumour vascular disruption. The advantage of this is a more immediate translational possibility, given that MRI scanners are widespread within hospitals and routinely used to assess patients. In addition, a larger area can be imaged compared to PAT, which opens up the possibility of using more relevant orthotopically sited tumour models. Given the importance of the pre-clinical model for translation to the clinic (1) and the ability to measure functional responses from imaging studies (2), it is envisaged that MRI will provide additional insights in to the response of tumours to VDAs that, when compared to PAT, is currently of increased translational relevance. The basic description of how MRI is used to visualise biological function was discussed in the Introduction to this thesis; this chapter will therefore introduce in more detail the specific vascular-associated parameters affected by VDA treatment, the MRI sequences developed to quantify them, and an initial demonstration of feasibility in subcutaneous tumours. An initial review will highlight the current work published in this area, and where advances can be made in understanding VDA mechanism of action and patient response to treatment.

### 5.1.1 MRI of tumour vasculature

Imaging of blood vessels using MRI angiography was noted in the previous chapter; it was established that certain vascular associated parameters, such as vessel size (3), density (4) and permeability (5, 6), could be determined using MRI angiography, however the use of an external contrast agent is a confounding factor when assessing tumour response to therapy. Endogenous contrast that is inherent to the tumour microenvironment provides a more direct assessment that eliminates the potential errors introduced through use of exogenous agents. A number of MRI techniques have been previously used to assess tumour response to therapy; measurement of acute response to VDA therapy in particular has mainly been assessed by intrinsic susceptibility contrast MRI (7) and diffusion MRI (8).

Another parameter than can be used to assess function is perfusion in biological tissue using arterial spin labelling (ASL) MRI (9). This has mainly been used for imaging the brain and cerebral blood flow (10), with little application to tumours outside of the head. These three functional parameters, perfusion using ASL, intrinsic susceptibility and diffusion weighted MRI, are described in the following sections.

### **5.1.1 Arterial spin labelling**

ASL is an MRI technique developed primarily to quantitatively measure cerebral blood flow, using the water in blood as an endogenous tracer (11-13). A pulsed ASL sequence called FAIR (Flow-sensitive alternating inversion recovery) has been designed to acquire pairs of images after global and slice selective inversion pulses (14, 15), thereby magnetically 'tagging' blood outside of the area of interest and generating an image of the flow of this blood into the tissue. This can then be used to generate quantitative maps of perfusion based on the inflow of blood (9). Assessment of vascular perfusion in solid tumours with ASL has received some interest, but generally only within the brain; ASL has been used to measure perfusion of brain metastases in patients (16-18) and in animal models (19, 20), as motion artefacts can be accounted for. In other locations outside of the brain motion artefacts, susceptibility differences caused by magnetic field inhomogeneity and visceral fat, coupled with a generally low rate of tumour perfusion, have made ASL challenging. One reported application of ASL in mouse xenograft models showed that it can be used to assess response to the anti-angiogenic agent Sorafenib, with significant reduction in blood flow seen at day 3 post-treatment (21). Another recent study looked at early response to anti-angiogenic treatment with Bevacizumab, also in subcutaneous tumour models, and found significant reduction in flow at 24 hours when compared to baseline measurements of perfusion (22). Response to vascular therapy is therefore possible with ASL, and should be suited to imaging response to vascular disruption with OXi4503. The time-course of action of OXi4503 may also provide a better model in which to study tumour haemodynamics with ASL, as blood flow will be affected at a much earlier point. Coupled to this is the ability of ASL to assess baseline measures of tumour blood flow, and therefore extent of tumour vasculature, with potentially improved predictive markers of therapy. ASL will therefore be developed as a marker of tumour perfusion first in the subcutaneous setting, before potentially being used in the colorectal liver metastasis model.

### 5.2.2 Intrinsic susceptibility MRI

IS-MRI is based on measuring the nuclear magnetic resonance transverse relaxation rate  $R2^*$  ( $R2^* = 1/T2^*$ ) (23). Transverse magnetisation is produced by applying a radiofrequency pulse to flip the longitudinal magnetisation into the transverse plane; this induces an MR signal in the receiver radiofrequency coil as all the protons are in phase. As the protons dephase the transverse magnetisation decreases, giving a measure of relaxation time  $T2$ , which represents  $1/e$  signal decay. Dephasing purely of spin-spin interactions is denoted as  $T2$ , but field inhomogeneities caused by susceptibility differences between different tissues also dephase the proton spin. This causes a faster relaxation of the transverse relaxation known as  $T2^*$ . The rate of this,  $1/T2^*$ , is known as  $R2^*$  and, in water molecules within blood at high magnetic field strengths, is predominantly determined by the oxygenation state of haemoglobin (24). This is because deoxyhaemoglobin is paramagnetic, which affects  $R2^*$ , whilst oxyhaemoglobin is diamagnetic, which does not affect the MR signal (25).  $R2^*$  can therefore be used to quantify deoxyhaemoglobin build-up via assessment of the transverse relaxation rate  $R2^*$ . Physiological interpretation of variations in such measurements can be challenging however, due to its potential dependence on numerous physiological processes. A strong relationship between deoxyhaemoglobin and  $R2^*$  has been demonstrated in animal models under different inspired oxygen concentrations (26), although the correlation between  $R2^*$  and oxygen pressure within solid tumours is harder to interpret, with poor relationships reported (27, 28). Interpretation of  $R2^*$  is further complicated by the observation that less hypoxic tumours, as assessed by pimonidazole adduct formation, have higher  $R2^*$  values (29). Prognostic ability of  $R2^*$  however has been shown for outcome to radiotherapy, based on different baseline values of  $R2^*$  (30).  $R2^*$  has also been shown to respond to vascular disruption with the research compound ZD6126 where, 35 minutes following dosing, the measured  $R2^*$  had increased by  $16 \pm 4\%$  from baseline values, with a significant decrease at 24 hours after dosing (7). This is consistent with vascular collapse due to therapy, and could provide prognostic markers for response to treatment. Initial phase I clinical trials with OXi4503 have been conducted (31), and although  $R2^*$  was performed on the patients the main parameter used for reporting response was DCE-MRI, with  $R2^*$  values not reported. As the interpretation of  $R2^*$  measurements is difficult, it is thought the combination with other markers, such as ASL and ADC described below, will further elucidate the reaction to dosing with VDAs and in particular OXi4503, and further validate the use of  $R2^*$  as a biomarker of response.

### 5.1.3 Diffusion weighted MRI

An MRI sequence that is weighted towards diffusion of water molecules can be created and used to assess tissue abnormalities that are not yet apparent on morphological imaging sequences. These sequences measure the Brownian motion of water molecules in the extracellular, intracellular, and intravascular space where movement is not restricted (32). This gives a measure of apparent diffusion coefficient (ADC), which is inversely related to the cellularity and integrity of tissue structure due to the restriction of space for water diffusion (33, 34). ADC can therefore be used as a measure of cellularity of the tissue and associated microstructural characteristics, such as fluid viscosity, membrane permeability, blood flow and tumour necrosis in response to therapy, as the structural integrity of the tissue is broken down. The sequence differentiates water movement by imaging paired diffusion gradients and changing a parameter known as 'b-value' multiple times; b-values are proportional to the gradient amplitude applied, the duration of this and the time interval between successive gradients. For static molecules the second diffusion gradient will rephase the protons without substantial loss of signal when compared to the first gradient; however, molecules that have moved will show different phase information for the second diffusion gradient when compared to the first. This attenuation in signal intensity is proportional to the degree of water motion. Diffusion weighted imaging (DWI) typically uses multiple b-values in the range of 0 to 1000 s/mm<sup>2</sup>, with the larger b-values providing the greatest signal attenuation, and is therefore biased towards slower water diffusion movements. By plotting the logarithm of the relative signal intensity measured against the b-values used, the slope of the resultant line describes the ADC value for that specific region. This is independent of scanner field strength and therefore comparable across systems, and results in a map of values across the region of interest. When using ADC to assess response to vascular disruption, necrosis is the main influence on ADC change, and studies have shown an increase due to CA4P therapy (8, 35, 36). Clinical use of ADC as a marker for VDA-induced necrosis, however, is restricted by a lack of consensus on data acquisition and processing (37). The combination of ADC measurements with both ASL and R2\* should provide insight into the tumour response to vascular disruption with OXi4503, as all parameters should be interlinked, thereby providing an overall picture of related responses. Also of interest would be acute measures of ADC in addition to just using the movement of water molecules as a marker of necrosis, as tumour blood vessel obstruction caused by VDA treatment should also have an effect on tumour ADC values.

#### **5.1.4 Hypothesis of vascular functional parameters in response to OXi4503**

The above mentioned functional parameters associated with tumour vascular function, ASL for tumour blood vessel perfusion,  $R2^*$  as a measure of deoxyhaemoglobin build-up as blood flow ceases, and ADC as an initial measure of vessel obstruction and tumour cell structure swelling, and subsequently as a measure of induced tumour necrosis, should all be interrelated in response to vascular disruption with OXi4503. Although all have to some extent been used to assess tumour response already, the combination of all three in response to the second generation VDA OXi4503 should provide greater understanding of the tumour microvasculature. It is envisaged that biomarkers, not only of response to treatment but also for prognosis of potential efficacy, will be forthcoming due to this increased understanding of the tumour vascular capability. These parameters will therefore be first established in subcutaneous models of colorectal carcinoma before progressing to the more clinically useful liver metastatic model, and always with a view to clinical translation of the assessment technique. The pulse sequences used to achieve this, and the experimental set-up employed, is described in the next section.



## 5.2 Methods

All CD1 nu/nu animals were acquired through UCL BSU and subcutaneous tumours established as previously described. All MRI imaging was performed at the UCL Centre for Advanced Biomedical Imaging on a dedicated small animal 9.4T Agilent VNMRS 20cm horizontal bore system (Agilent Technologies, Santa Clara, USA). Small gradients were used in conjunction with a 39mm birdcage coil (RAPID Biomed, Rimpar, Germany). Anaesthesia was induced with 4% Isoflurane in oxygen within the designated preparatory room before transfer to the MRI cradle for imaging. Anaesthesia was maintained at 1-2% Isoflurane via nose-cone, and a rectal temperature probe and respiration pillow put in place for physiological monitoring. In order to limit motion of the tumour, the flank of the animal was fixed in place using a fixative paste and tape. The MRI cradle was then placed in the centre of the bore of the magnet and animal temperature maintained at 36.8°C via a core body temperature-linked warm air blower (SA Instruments, USA). Monitoring of animal core temperature and respiration rate during image acquisition was performed via remote software within the MRI console room. For administration of substances, a heparin coated i.v. cannula line was placed in the tail vein of the mouse and a remote line placed outside the scanner bore. Baseline images were acquired before injection of either saline control or 40mg/kg of freshly made-up OXi4503 solution. For longitudinal studies the animals were placed in a heated recovery box after the imaging session, and returned to IVCs kept at the BSU holding room within CABI.

### 5.2.1 MRI pulse sequences

All MRI scan parameters were developed in conjunction with Dr Walker-Samuel (UCL CABI). In addition, the arterial spin labelling sequence used for perfusion was further modified in conjunction with Mr Ramasawmy (UCL CABI). A description of each sequence can be found below.

#### 5.2.1.1 High resolution morphological sequence

A multiple slice Fast-Spin Echo (FSE) sequence was used to obtain morphological information on the animal being imaged. This structural information was then used to plan subsequent data acquisition with other scans. This initial sequence was T2-weighted and respiratory-gated in order to obtain the best resolution possible. Sequence parameters included a field of view  $35 \times 35 \text{ mm}^2$  with a matrix size of  $256 \times 256$ . The repetition time between excitation pulses was set to  $TR = 1500 \text{ ms}$ , with  $n=4$   $180^\circ$  refocussing pulses applied (Echo train length=4) per TR. Effective echo time was  $TE=26 \text{ ms}$ . To cover the whole tumour area  $n=30$  contiguous  $0.5 \text{ mm}$  slices were acquired with  $n=2$  dummy scans and  $n=4$

averages per acquisition. For data planning, scans were visualised using the MRI scanner software VNMRJ (Agilent Technologies, Santa Clara, USA); for presentation of scans, the data was analysed with MATLAB (MathWorks, USA) and images visualised using Amira 5.4.0 software.

#### **5.2.1.2 Arterial spin labelling sequence**

Data for tissue perfusion was acquired by an arterial spin labelling sequence using a flow-sensitive alternating inversion recovery (FAIR) Look-Locker sequence (38). The sequence was single slice with 1mm thickness and a field of view of 30x30mm. Scan parameters included a matrix size of 128x128, a TE of 1.18ms, a time to inversion of the Look-Locker  $T_{\text{Look-Locker}}$  of 110ms with a repetition of the inversion  $TR_i$  of 13s, a  $TR_{\text{RF}}$  of 2.3ms, an angle  $\alpha_{\text{RF}}$  of 8°, 50 inversion recovery readouts, and 4 lines per segmented acquisition. A selective local inversion of 6mm thickness was performed across the area of interest of the tumour ROI, followed by a global inversion. Total scan time for each acquisition was around 14 minutes in duration. Maps of perfusion were calculated using the model suggested by Belle (39). Longitudinal relaxation time  $T_1$  of intravascular blood was based on previously measured value of 1900ms (40), which was acquired in the ventricular blood pool of the mouse heart. A blood-tissue partition coefficient of  $\lambda=0.95\text{mlg}^{-1}$  was used based on previously reported measurements from  $^{85}\text{Krypton}$  gas clearance experiments (41). A three parameter fit of the inversion recovery was therefore calculated which was corrected for the signal saturation caused by the FAIR acquisition sequence. Values of ASL were calculated per voxel of acquired data using MATLAB, with three dimensional visualisation of  $R2^*$  values across the tumour performed in Amira 5.4.0.

#### **5.2.1.3 Intrinsic susceptibility sequence**

Values of the MRI transverse relaxation rate ( $R2^*$ ) were acquired from a respiratory-gated, multiple-echo, multiple-slice gradient echo sequence (MGEMS). Sequence parameters included 8 echoes with a spacing of 2ms, a  $30\times30\text{mm}^2$  field of view, and 128x128 matrix size. Time to the first echo,  $TE_1$ , was 2ms, with a TR set to 280ms. A total of 15 slices of 1mm thickness were used to encompass the tumour region.  $R2^*$  was estimated using a maximum likelihood approach that took in to account the Rician distribution of the data (42). The tumour ROI was selected in Amira 5.4.0 and analysis performed with an in-house designed IDL programme. Values of  $R2^*$  were calculated per voxel of acquired data, with three dimensional visualisation of  $R2^*$  values across the tumour performed in Amira 5.4.0.

#### **5.2.1.4 Diffusion weighted imaging sequence**

To estimate the apparent diffusion coefficient of water molecule movement within the tumours, a diffusion weighted fast spin echo sequence (FSEdif) was established. Using the geometry from the FSE sequence, a 40x40mm field of view was placed covering the location of the tumour. A slice thickness of 1mm was used, with 20 contiguous slices acquired. The matrix size was 128x128 with TR set at 1500ms and TE set to 22ms. Diffusion gradients were set in the slice direction with b values of 2.5, 214, 413, 609, 805 and 1000 s/mm<sup>2</sup>. Analysis of acquired data was performed using a tumour selected ROI in Amira 5.4.0, and an in-house designed IDL programme to extract ADC parameters for each voxel of acquired data, with data fitted to a single exponential model on a pixel by pixel basis using a Bayesian maximum a posteriori approach. Three dimensional visualisation of ADC values across the tumour performed in Amira 5.4.0.

#### **5.2.2 In vivo procedure**

Animals were used for MRI experiments once tumour volume, as assessed by caliper measurement, had reached approximately 0.6cm<sup>3</sup>. Each imaging session was limited to three hours total anaesthesia time per mouse due to licence restrictions; imaging of cohorts of mice was therefore staggered over subsequent days. Initial studies of saline-dosed sham controls were acquired in order to gain experimental set-up experience and to demonstrate no change of measured parameters from baseline in n=2 SW1222 tumours. Studies of response to OXi4503 treatment were then performed in n=4 LS174T and n=6 SW1222 tumour bearing mice. Imaging sessions consisted of baseline acquisitions of R2\*, ASL and ADC followed by dosing via the remote i.v. line. The animal was then left within the scanner bore and acquisitions of R2\* and ADC acquired consecutively until 90 minutes post-dose, at which point a final measure of ASL was acquired and the animals returned to IVCs. The LS174T tumour bearing mice were terminated at this point. The SW1222 tumour bearing mice were imaged subsequently for longitudinal response to OXi4503 at days 1, 3 and 5 post-dose. One mouse was sacrificed on day 1 post-dose, one mouse at day 3 post-dose, and the remaining n=4 at day 5 post-dose. All tumours were excised at termination and fixed in 10% formalin for histological assessment.

## 5.3 Results

### 5.3.1 High resolution and segmentation

Imaging of the sham-dosed animals demonstrated the feasibility of work flow, data acquisition, correct sequence set-up and analysis of data. No significant changes from baseline were observed. In **figure 5.1** an example of the high resolution morphological scan raw data can be seen in panel **A**. The subcutaneous tumour is evident due to its location on the top of the animal's flank above the internal abdominal section. This spherical region is hypo-intense in signal, and is indicated here by the red arrow. An example of the Amira 5.4.0 workflow to segment the tumour region can be seen in panel **B**. The work area to the left of the image is a Amira 5.4.0 showing the different possible methods of segmenting materials based on voxel values; the area to the right highlighted in red shows the voxels designated as a region of interest. This can then be represented separately as in panel **C**, which shows the tumour volume rendered in orange above the high resolution MRI image slice. This tumour segmented area was then used to calculate values for functional parameter measurements.

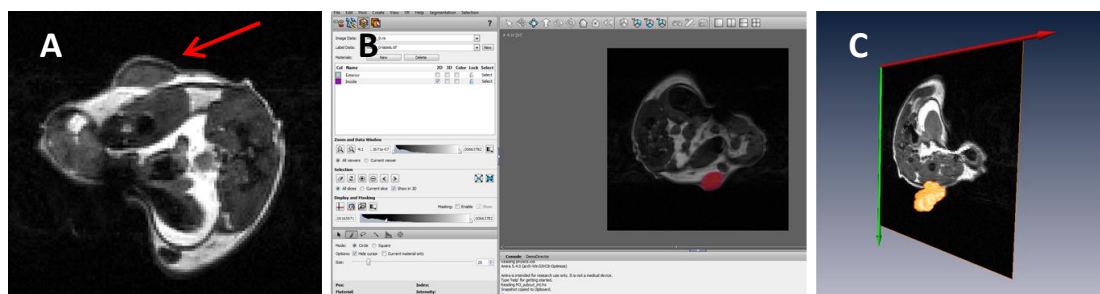


**Figure 5.1 High resolution morphological MRI images & segmentation**

Representative MRI image from a morphological FSE sequence of a subcutaneous tumour, with subcutaneous tumour highlighted by the red arrow (**A**), the segmentation of the tumour ROI using Amira 5.4.2 (**B**), and the three dimensional rendering of the tumour volume within Amira 5.4.0 (**C**) (n=2 animals used for development).

### 5.3.2 ASL acute

Measurements of tumour perfusion using arterial spin labelling in SW1222 tumours was unsuccessful and yielded corrupted data acquisition with no information. This data is not shown, as it was not possible to reconstruct any images or three dimensional volumes. It is possible that the low blood flow within the region of interest was not sufficient to produce the necessary contrast for ASL in subcutaneous SW1222 tumours. With LS174T tumour the results were similar, and although the data was not corrupted it none-the-less showed no change in values across the tumour and from baseline to post-dose imaging. An example of the LS174T data can be seen in figure 5.2. Each section from left to right shows a single 1mm slice through the tumour. The first row is from baseline values, with the second and third corresponding to 90 minutes after OXi4503. Each voxel shows the measured ASL in ml/g/min as per the colour bar included in the figure; no change is noted across the tumour. It is thought that the small area of the tumour leads to low perfusion which compromised correct ASL measurements, and that increased sequence acquisitions and averaging of data would allow this small ASL value to be obtained.

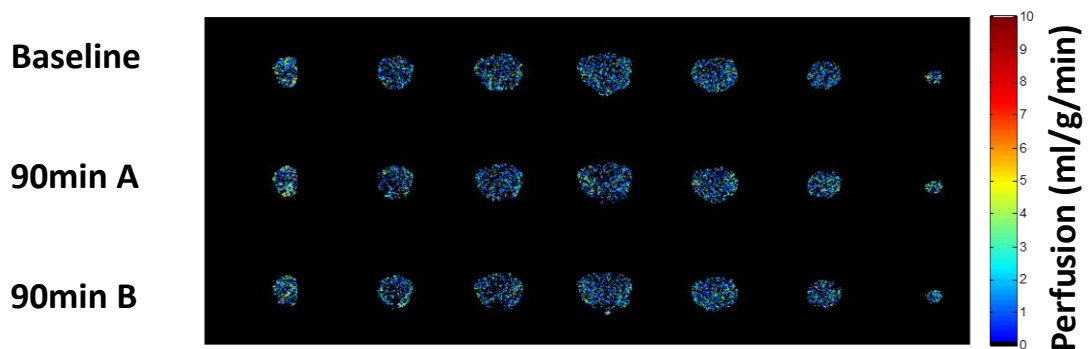


**Figure 5.2 Tumour perfusion maps**

Representative perfusion maps from an ASL sequence of a subcutaneous LS174T tumour (n=4). The top row indicates voxel perfusion measurements acquired at baseline, with the second and third rows showing the same tumour at 90min post 40mg/kg of OXi4503. Each row depicts 7 x 1mm slices that encompass the whole tumour from top to bottom.

### 5.3.3 R2\* acute

Data acquisition for values of R2\* across the tumour were attained and mapped. An example of this can be seen in **figure 5.3** for both SW1222 and LS174T tumours. The top row shows R2\* mapped across the tumour at baseline (**A**) and 90 minutes following administration of OXi4503 (**B**) in a representative tumour ROI (SW1222). A histogram of the values for all voxels from the example in **A** and **B** can be seen below each tumour R2\* map (**C** and **D**). The median value for baseline images is shown on the histogram by the T<sub>50</sub> value, which is used to demonstrate shift in the values at 90 minutes; a threshold at this T<sub>50</sub> value has been drawn and shows the percentage of voxels now above this value. In the example, an increase in values from baseline, expressed as a shift to the right of the distribution within the histogram, can be seen, with 52% of tumour voxels now above the median baseline value. From this whole tumour voxel-data the increase in median values and standard deviation from the mean across the whole cohort can be calculated for both tumour types; a continuous representation of this over the 90 minutes post-dose time period is shown in panel **E**, which depicts n=13 acquisitions of median R2\* value, with error bars denoting standard deviation, for SW1222 in blue and LS174T in red. SW1222 tumours show an initial decrease in value at the 5 minute time-point, followed by a sustained increase to 4.5% over baseline values at 90 minutes; LS174T tumours also show an initial decrease followed by an increase, however both are not as pronounced as the SW1222 tumours. At 90 minute no significant increase is noted, with the R2\* value being only 0.5% above baseline.

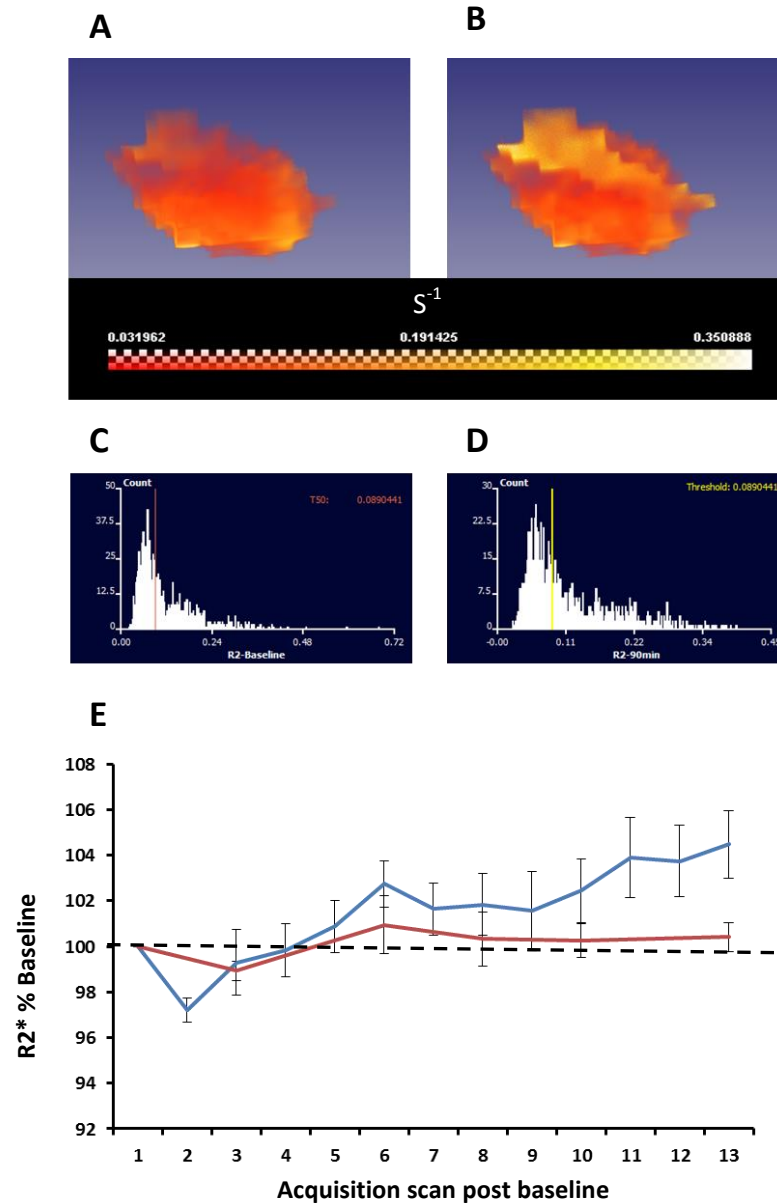


**Figure 5.3 Acute measurement of  $R2^*$**

Panel **A** and **B** show 3D representations of  $R2^*$  ( $S^{-1}$ ) mapped across tumour voxels at baseline and 90min after 40mg/kg OXi4503 i.v.. The change in signal intensity can be shown by voxel histograms as in panel **C** and **D** and used to assess percentage of tumour voxels above median baseline values. A graph of these values as percentage of baseline can then be constructed (panel **E**) for the n=6 SW1222 (blue line) and n=4 LS174T (red line) tumours.

### 5.3.4 ADC acute

Data acquisition for values of ADC across the tumour were mapped across the tumour region as previously shown for the R2\* measurements. An example of this can be seen in **figure 5.4** for both SW1222 and LS174T tumours. The top row shows ADC mapped across the tumour at baseline (**A**) and 90 minutes following administration of OXi4503 (**B**). A histogram of the values for all voxels can be seen below each tumour ADC map (**C** and **D**). No apparent change in ADC values is noted from baseline to 90 minutes post-dose. Median values and standard deviation from the mean over the 90 minute experiment are shown in panel **E**, with SW1222 tumours in blue and LS174T in red. As can be seen there is a reduction for both SW1222 and LS174T at the 90 minute time point, with values being 82% and 92% of baseline values respectively.

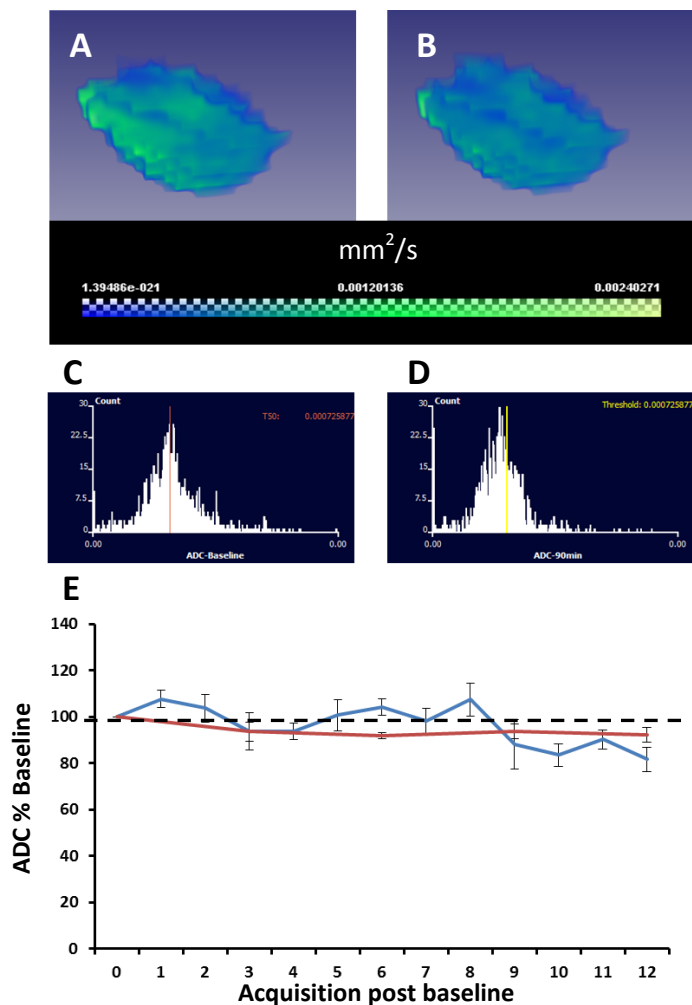


**Figure 5.4 Acute measurement of ADC**

Panel **A** and **B** show 3D representations of ADC mapped across tumour voxels at baseline and 90min after 40mg/kg OXi4503 i.v.. The change in signal intensity can be shown by voxel histograms as in panel **C** and **D** and used to assess percentage of tumour voxels below median baseline values. A graph of these values as percentage of baseline can then be constructed (panel **E**) for the n=6 SW1222 (blue line) and n=4 LS174T (red line) tumours.



### 5.3.5 Baseline vs 90min response

Measurements of both  $R2^*$  and ADC can be linked spatially within the same tumour, an example of which, performed in one SW1222 tumour, is shown in **figure 5.5 A** ( $R2^*$ ), **B** (ADC) and **C** (combination of  $R2^*$  and ADC). This allows regional comparison of tumour voxels over time, linking baseline values to values acquired post dose. Graph **D** of figure 5.6 shows an example of this, where initial  $R2^*$  values from an SW1222 tumour have been categorised into deciles and linked to the percentage change of ADC at 90minutes post dose with each decile. From this it can be seen that those voxels with the lowest  $R2^*$  values at baseline (deciles 1 to 5) will generally respond with a decrease in ADC at 90minutes, those with an above average baseline  $R2^*$  value (deciles 6 and 7) will show an increase in ADC, and those with the highest  $R2^*$  values (deciles 8 to 10) show only a slight reduction in ADC. Whilst this may be indicative of an association between  $R2^*$  and ADC values, comparisons across different tumours are complicated, and no definitive correlation was found across the group ( $n=6$  SW1222) over the time frame imaged.

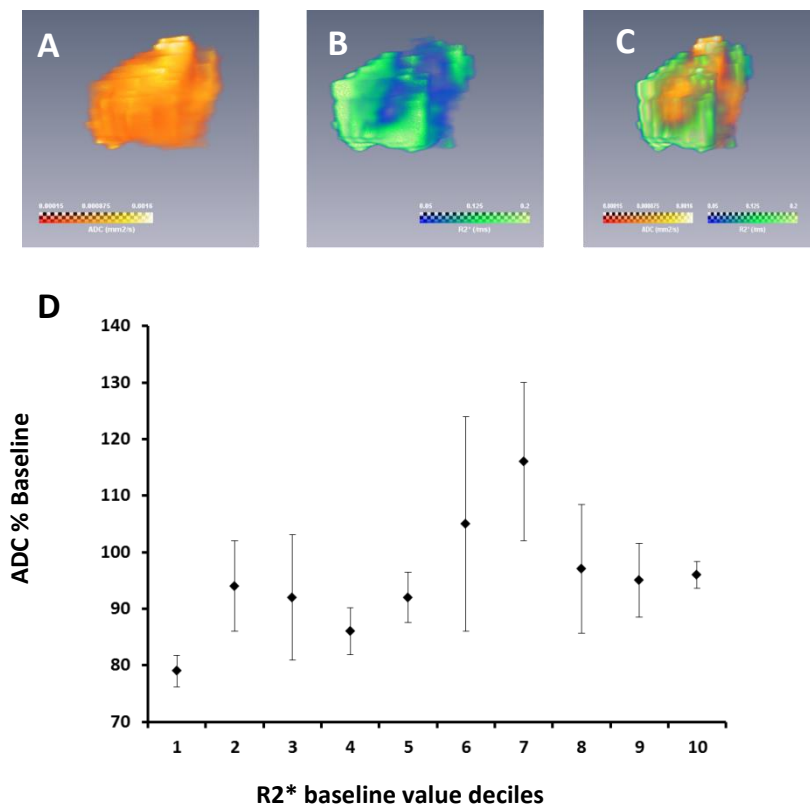


**Figure 5.5 Spatial correlation of  $R2^*$  and ADC values**

Panel **A** and **B** show 3D representations of  $R2^*$  at baseline and ADC at 90min post 40mg/kg OXi4503 i.v. mapped across the same tumour ( $n=1$  shown,  $n=6$  total). Panel **C** shows both  $R2^*$  and ADC mapped within the same image. Quantifying baseline  $R2^*$  in to deciles and plotting the change in ADC at 90min shows variation in results across the tumour, as seen in panel **D** (error bars denote mean $\pm$ SDM).

### 5.3.6 Longitudinal MRI assessment of response

Values for  $R2^*$  and ADC were acquired for the SW1222 tumours at 90 minutes, 1, 3 and 5 days post dose. As an example of value mapping across the tumour, values of ADC at baseline and at 24 hours post OXi4503 in an example SW1222 tumour can be seen in **figure 5.6 A and B** respectively. Histological assessment by H&E staining can also be seen for baseline and 24 hours in panels **C** and **D** of the same figure. Values of ADC show a marked increase from baseline values with more 'hot' areas of high ADC values. Morphological staining confirms the typical necrotic centre of OXi4503 treated tumours at 24 hours, with a rim of surviving cells, when compared to baseline. Values across the cohort of tumours over the 5 day longitudinal study are depicted by the box and whisker plots in **figure 5.7** that show median values across the tumour voxels. Graph **A** shows the results for  $R2^*$ , which show a slight increase in values from baseline to 90 minutes post dose, a widening of results but still within the same value range at 24 hours, and a significant decrease ( $p \leq 0.05$ ) from baseline values at 3 and 5 days post dose. Graph **B** shows the same layout for results of ADC. At 90 minutes post treatment there was a slight reduction in values and a narrowing in the range of results. All time points after this (days 1, 3 and 5), show significantly higher ( $p \leq 0.05$ ) ADC values. For both graphs, error bars denote maximum and minimum measurements, with boxes denoting the interquartile range and median values.

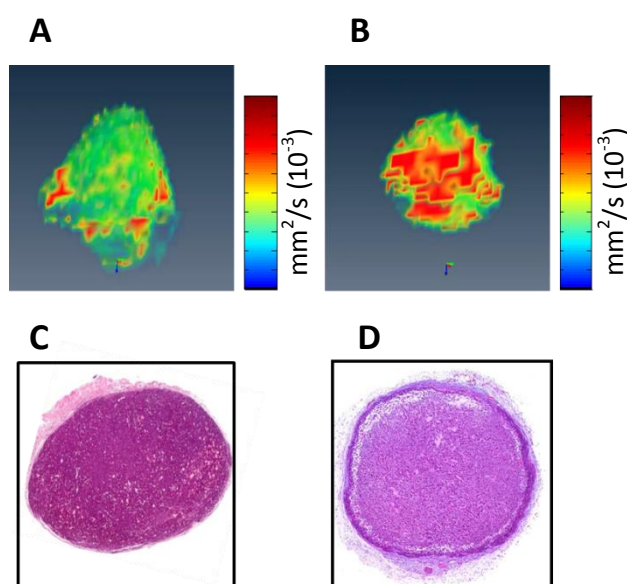


**Figure 5.6 Confirmation of longitudinal MRI feasibility**

Panel **A** and **B** show 3D representations of ADC in an SW1222 tumour at baseline and 24 hours after 40mg/kg OXi4503 i.v. mapped across the same tumour. Panel **C** and **D** represent morphological H&E images of baseline and 24 hours post drug respectively.

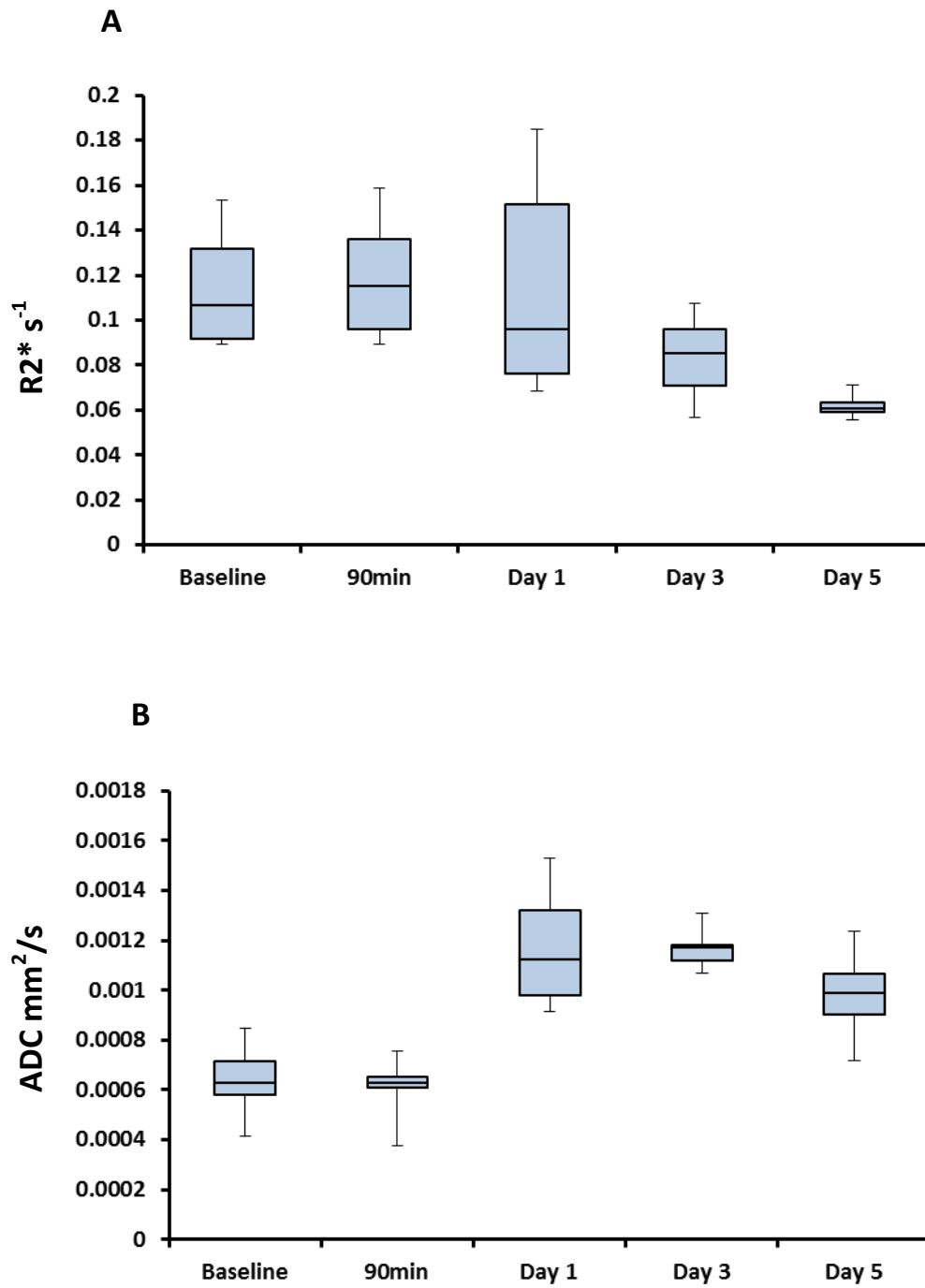


**Figure 5.7 Longitudinal  $R2^*$  and ADC measurements**

Graph A shows median values for  $R2^*$  and graph B median values for ADC across  $n=6$  SW1222 tumours at baseline, 90 minutes, 1, 3 and 5 days post 40mg/kg OXi4503 i.v. Error bars show maximum and minimum values, with boxes showing interquartile range and median values.

## 5.4 Discussion

### 5.4.1 MRI Sequences function as predicted

Arterial spin labelling for tissue perfusion, intrinsic susceptibility measures of  $R2^*$  and diffusion weighted measures of ADC have all been previously used to assess response to therapy, as discussed in the introduction to this chapter. Different MRI acquisition sequences can be employed to achieve each functional measurement, however, and sequences must be fully tested to ensure they achieve accurate results for each different MRI scanner used and with each new model tested. The aim of this chapter was therefore to assess the developed MRI sequences for ASL,  $R2^*$  and ADC in two subcutaneous colorectal models with different pathophysiologies, before progressing to the more clinically relevant liver metastatic model. The results shown in this chapter demonstrate that values for each sequence can be achieved in both these models. Values of  $R2^*$  and ADC in particular could be acquired and mapped across the 3D rendering of the tumour ROI. Perfusion as measured by ASL was more challenging, with results acquired for LS174T and sham-dosed tumours showing little change, and results from SW1222 tumours being corrupted to the point of being unusable. The sequence worked correctly on larger cross sections of mouse anatomy, however the small size of the tumour area and the low level of perfusion in subcutaneous tumours meant no functional perfusion measurement could be acquired with this model. The sequence was adapted by incorporating a MATLAB programme to reject severely corrupted data acquired in the Look-Locker train sequence, thereby eliminating 'ghost' artefacts and motion corruption, with the remaining images fitted by a non-linear least-squares method to generate T1 maps. It is thought that this, coupled with the larger cross section and increased blood flow in liver tissue, will provide non-corrupted and significant functional ASL measurements for the liver orthotopic model. Having determined that the developed MRI sequences work with the scanner and model used, there are a number of observations that can be drawn from the experimental studies conducted. These are discussed below.

### 5.4.2 Vascular shutdown can be observed using $R2^*$ and ADC

The interaction of  $R2^*$  and ADC should show the effect of dosing with OXi4503 and the resultant vascular destruction. From the literature, the vascular shutdown caused by OXi4503 will start to take effect from around 1 hour post dose, with around 50% reduction in actual blood flow, and maximum effects noted from around 6 hours to 24 hours post dose (43). With the related VDA compound CA4P (44) a significant reduction in blood flow can be seen at 5 minutes after dosing, with complete shutdown noted at 20 minutes (45). During the acute phase of vascular shutdown it is thought that the morphological and functional alterations to the endothelial cytoskeleton caused by VDAs, such as cell shape (46), are the main source of cessation of blood flow. With regards to  $R2^*$  this slowing of blood flow would have the effect of increasing the deoxygenated content of the blood within the tumour; the slow flow rate would provide more time for tumour cells to use up the available oxygen, with a resulting increase in paramagnetic deoxyhaemoglobin. This in turn would lead to an increase in the measured  $R2^*$  as the tumour blood flow eventually stops entirely. Over the 90 minutes measured, the  $R2^*$  for SW1222 tumours increases to around 4.5% over baseline, whilst in LS174T tumours only a modest 0.5% is observed. This potentially illustrates a more rapid slowing in vascular flow in the SW1222 tumours. This also fits in with reported literature that less hypoxic tumours have a higher  $R2^*$  value (29). This is probably due to the overall content of blood within the tumour vasculature, where SW1222 tumours, with a greater blood vessel network, subsequently have an increased percentage of deoxygenated blood affecting the  $R2^*$  measurement. This also links back to PAT and corrosion cast measurements that showed a greater vascular network within SW1222 tumours when compared to LS174T. This change in  $R2^*$  could also potentially be a product of altered blood volume within tumours following treatment. With values of ADC the acute measurements are unlikely to measure tumour cell necrosis, as it is presumed little tumour breakdown is occurring at this point. However, with blood flow stagnating within tumours and endothelial cell morphology becoming more rigid, it is possible that ADC would reflect the more restricted water movement by showing values that are reduced from baseline values. This is observed with the acquired data, where values have dropped to 82% and 92% of initial values for SW1222 and LS174T tumours. This shows that the initial effects of vascular shutdown can be assessed by  $R2^*$  and ADC. It is possible that the main effect of blood vessel occlusion was not noted however, as it was only possible to image up to 90 minutes after dosing due to the time required for experimental set-up and licence restrictions. Measurements at 6 hours would have potentially shown greater effect, however imaging of the animals within the same 24 hour period was not possible. The

opposing reactions of  $R2^*$  and ADC over the time frame imaged, however, show that both are linked in relation to mechanism of drug action. Spatially linking  $R2^*$  and ADC, as in **figure 5.5**, could demonstrate further the connection between voxels that show increased deoxyhaemoglobin (increased  $R2^*$ ) and occluded vessels (a decrease in water diffusion by ADC). No direct correlation was observed, but it is interesting to note that the greatest reduction in ADC occurred in those voxels that had the lowest baseline values of  $R2^*$ , i.e. most oxygenated, whilst those with the highest baseline levels of  $R2^*$ , i.e. the areas most deoxygenated initially, either showed little effect, which is presumably due to no reduction in blood flow, or an increased ADC, which is either related to increased water motion caused by the onset of necrosis or the breakdown of the tumour vasculature. Even though regional analysis proved no correlation, median values did reflect overall change in tumour functional parameters.

### 5.4.3 Longitudinal analysis

The action of OXi4503 was monitored longitudinally by imaging SW1222 tumours over a 5 day period, as seen in **figure 5.7**. Whilst it was originally planned to also image the LS174T tumours over this time frame, logistical issues in relation to scanner time and coordination with *in vivo* studies meant that this was not possible. Correlation of exact changes in both  $R2^*$  and ADC was also an initial aim of this study, but the deformation in the tumour 3D map over the course of time did not allow exact overlay of baseline and subsequent data sets. Micro-regional maps of values are therefore not shown due to co-registration problems. Measurement of  $R2^*$  also has the added difficulty in that scan parameters, such as shim values acquired, mean that direct comparison is not straightforward. Median values were therefore used to assess response to OXi4503 treatment over time, as they proved to be the most consistent in terms of reliability. Response to treatment should lead to a central necrotic core with little remaining vasculature, as shown by PAI; necrosis was observed through H&E staining. This in turn should lead to an increase in ADC values across the tumour, and a drop in  $R2^*$  as the haemoglobin is removed from the tumour core and cellular breakdown products become dispersed. This would be consistent with observed effects in PAT studies and other MRI experiments. These effects were indeed observed across the tumour cohort, with the expected increase in water diffusion shown by an increase in tumour ADC, and the tumour blood vessel destruction and removal shown by the drop in  $R2^*$  values. Whilst an increase in  $R2^*$  has been described previously using MRI following vascular disruption, this is in the acute phase of vessel shutdown where deoxygenated blood accumulates within the tumour blood vessels. In this study that time-

frame is extended to cover the subsequent days of recovery for the first time, with a subsequent drop in  $R2^*$  observed. The study therefore proved that the MRI sequences employed are capable of imaging not only the acute effects of vascular disruption with OXi4503, but also the longitudinal response.

## 5.5 Conclusion

The aim of this chapter was to determine and evaluate MRI sequences that would be capable of imaging tumour vasculature parameters associated with vascular disruption by the VDA OXi4503, using two colorectal cancer models. This was achieved by imaging subcutaneous tumours over an acute 90 minute period and follow-up of the same tumours at 24 hours and 3 and 5 days post dose. Although results of tumour perfusion by ASL were unsatisfactory in this setting, the experimental approach proved useful in that the sequence was seen to acquire data, but required modifying for further use. Sequences were modified and provided successful perfusion imaging in later experiments. Measures of  $R2^*$  and ADC were acquired with OXi4503 that reflected the known action of other VDAs. The response was consistent with the literature, and demonstrated a complex interaction between the two parameters. A combination of MRI functional measures of tumour response with PAT morphological response of the tumour vascular network would be extremely advantageous to the understanding of this complex interaction between cessation of blood flow, increase in deoxyhaemoglobin, blood vessel occlusion and onset of necrosis. Preliminary studies were carried out to check the feasibility of this, however coordinating two separate scanner schedules and timing *in vivo* study proved difficult, and the little data achieved (n=1 subcutaneous tumour) was hard to co-register accurately between the two modalities. Dual imaging would obviously be a powerful tool in this context, and further work will be conducted to achieve this aim; however the most immediate translational concern was to demonstrate that these functional parameters could be used in a more clinically relevant setting. The next chapter will therefore show the development of a model of colorectal liver metastases and the monitoring of response to OXi4503.

## 5.6 Reference List

- (1) Cook N, Jodrell DI, Tuveson DA. Predictive in vivo animal models and translation to clinical trials. *Drug Discov Today* 2012;17:253-60.
- (2) Brindle K. New approaches for imaging tumour responses to treatment. *Nat Rev Cancer* 2008;8:94-107.
- (3) Valable S, Lemasson B, Farion R, Beaumont M, Segebarth C, Remy C, et al. Assessment of blood volume, vessel size, and the expression of angiogenic factors in two rat glioma models: a longitudinal in vivo and ex vivo study. *NMR Biomed* 2008;21:1043-56.
- (4) Lemasson B, Valable S, Farion R, Krainik A, Remy C, Barbier EL. In vivo imaging of vessel diameter, size, and density: a comparative study between MRI and histology. *Magn Reson Med* 2013;69:18-26.
- (5) Peng SL, Chen CF, Liu HL, Lui CC, Huang YJ, Lee TH, et al. Analysis of parametric histogram from dynamic contrast-enhanced MRI: application in evaluating brain tumor response to radiotherapy. *NMR Biomed* 2012.
- (6) Coenegrachts K, Bols A, Haspeslagh M, Rigauts H. Prediction and monitoring of treatment effect using T1-weighted dynamic contrast-enhanced magnetic resonance imaging in colorectal liver metastases: potential of whole tumour ROI and selective ROI analysis. *Eur J Radiol* 2012;81:3870-6.
- (7) Robinson SP, Kalber TL, Howe FA, McIntyre DJ, Griffiths JR, Blakey DC, et al. Acute tumor response to ZD6126 assessed by intrinsic susceptibility magnetic resonance imaging. *Neoplasia* 2005;7:466-74.
- (8) Thoeny HC, De KF, Chen F, Vandecaveye V, Verbeken EK, Ahmed B, et al. Diffusion-weighted magnetic resonance imaging allows noninvasive in vivo monitoring of the effects of combretastatin a-4 phosphate after repeated administration. *Neoplasia* 2005;7:779-87.
- (9) Wells JA, Siow B, Lythgoe MF, Thomas DL. Measuring biexponential transverse relaxation of the ASL signal at 9.4 T to estimate arterial oxygen saturation and the time of exchange of labeled blood water into cortical brain tissue. *J Cereb Blood Flow Metab* 2013;33:215-24.
- (10) Zhou H, Chen M, Zhao D. Longitudinal MRI evaluation of intracranial development and vascular characteristics of breast cancer brain metastases in a mouse model. *PLoS One* 2013;8:e62238.
- (11) Morse OC, Singer JR. Blood velocity measurements in intact subjects. *Science* 1970;170:440-1.
- (12) Detre JA, Leigh JS, Williams DS, Koretsky AP. Perfusion imaging. *Magn Reson Med* 1992;23:37-45.



- (13) Detre JA, Subramanian VH, Mitchell MD, Smith DS, Kobayashi A, Zaman A, et al. Measurement of regional cerebral blood flow in cat brain using intracarotid  $2H_2O$  and  $2H$  NMR imaging. *Magn Reson Med* 1990;14:389-95.
- (14) Kwong KK, Belliveau JW, Chesler DA, Goldberg IE, Weisskoff RM, Poncelet BP, et al. Dynamic magnetic resonance imaging of human brain activity during primary sensory stimulation. *Proc Natl Acad Sci U S A* 1992;89:5675-9.
- (15) Kim SG. Quantification of relative cerebral blood flow change by flow-sensitive alternating inversion recovery (FAIR) technique: application to functional mapping. *Magn Reson Med* 1995;34:293-301.
- (16) Hirai T, Kitajima M, Nakamura H, Okuda T, Sasao A, Shigematsu Y, et al. Quantitative blood flow measurements in gliomas using arterial spin-labeling at 3T: intermodality agreement and inter- and intraobserver reproducibility study. *AJNR Am J Neuroradiol* 2011;32:2073-9.
- (17) Knutsson L, van WD, Petersen ET, Bloch KM, Holtas S, Stahlberg F, et al. Absolute quantification of cerebral blood flow: correlation between dynamic susceptibility contrast MRI and model-free arterial spin labeling. *Magn Reson Imaging* 2010;28:1-7.
- (18) Canale S, Rodrigo S, Tourdias T, Mellerio C, Perrin M, Souillard R, et al. [Grading of adults primitive glial neoplasms using arterial spin-labeled perfusion MR imaging]. *J Neuroradiol* 2011;38:207-13.
- (19) Silva AC, Kim SG, Garwood M. Imaging blood flow in brain tumors using arterial spin labeling. *Magn Reson Med* 2000;44:169-73.
- (20) Moffat BA, Chen M, Kariaapper MS, Hamstra DA, Hall DE, Stojanovska J, et al. Inhibition of vascular endothelial growth factor (VEGF)-A causes a paradoxical increase in tumor blood flow and up-regulation of VEGF-D. *Clin Cancer Res* 2006;12:1525-32.
- (21) Schor-Bardach R, Alsop DC, Pedrosa I, Solazzo SA, Wang X, Marquis RP, et al. Does arterial spin-labeling MR imaging-measured tumor perfusion correlate with renal cell cancer response to antiangiogenic therapy in a mouse model? *Radiology* 2009;251:731-42.
- (22) Rajendran R, Huang W, Tang AM, Liang JM, Choo S, Reese T, et al. Early detection of antiangiogenic treatment responses in a mouse xenograft tumor model using quantitative perfusion MRI. *Cancer Med* 2014;3:47-60.
- (23) Chavhan GB, Babyn PS, Thomas B, Shroff MM, Haacke EM. Principles, techniques, and applications of  $T2^*$ -based MR imaging and its special applications. *Radiographics* 2009;29:1433-49.
- (24) Thulborn KR, Waterton JC, Matthews PM, Radda GK. Oxygenation dependence of the transverse relaxation time of water protons in whole blood at high field. *Biochim Biophys Acta* 1982;714:265-70.

- (25) Christen T, Bolar DS, Zaharchuk G. Imaging brain oxygenation with MRI using blood oxygenation approaches: methods, validation, and clinical applications. *AJNR Am J Neuroradiol* 2013;34:1113-23.
- (26) Punwani S, Ordidge RJ, Cooper CE, Amess P, Clemence M. MRI measurements of cerebral deoxyhaemoglobin concentration [dHb]--correlation with near infrared spectroscopy (NIRS). *NMR Biomed* 1998;11:281-9.
- (27) Baudalet C, Gallez B. How does blood oxygen level-dependent (BOLD) contrast correlate with oxygen partial pressure (pO<sub>2</sub>) inside tumors? *Magn Reson Med* 2002;48:980-6.
- (28) Chopra S, Foltz WD, Milosevic MF, Toi A, Bristow RG, Menard C, et al. Comparing oxygen-sensitive MRI (BOLD R2\*) with oxygen electrode measurements: a pilot study in men with prostate cancer. *Int J Radiat Biol* 2009;85:805-13.
- (29) McPhail LD, Robinson SP. Intrinsic susceptibility MR imaging of chemically induced rat mammary tumors: relationship to histologic assessment of hypoxia and fibrosis. *Radiology* 2010;254:110-8.
- (30) Rodrigues LM, Howe FA, Griffiths JR, Robinson SP. Tumor R2\* is a prognostic indicator of acute radiotherapeutic response in rodent tumors. *J Magn Reson Imaging* 2004;19:482-8.
- (31) Patterson DM, Zweifel M, Middleton MR, Price PM, Folkes LK, Stratford MR, et al. Phase I clinical and pharmacokinetic evaluation of the vascular-disrupting agent OXi4503 in patients with advanced solid tumors. *Clin Cancer Res* 2012;18:1415-25.
- (32) Koh DM, Collins DJ. Diffusion-weighted MRI in the body: applications and challenges in oncology. *AJR Am J Roentgenol* 2007;188:1622-35.
- (33) Guo Y, Cai YQ, Cai ZL, Gao YG, An NY, Ma L, et al. Differentiation of clinically benign and malignant breast lesions using diffusion-weighted imaging. *J Magn Reson Imaging* 2002;16:172-8.
- (34) Gauvain KM, McKinsty RC, Mukherjee P, Perry A, Neil JJ, Kaufman BA, et al. Evaluating pediatric brain tumor cellularity with diffusion-tensor imaging. *AJR Am J Roentgenol* 2001;177:449-54.
- (35) Thoeny HC, De KF, Vandecaveye V, Chen F, Sun X, Bosmans H, et al. Effect of vascular targeting agent in rat tumor model: dynamic contrast-enhanced versus diffusion-weighted MR imaging. *Radiology* 2005;237:492-9.
- (36) Bohndiek SE, Kettunen MI, Hu DE, Witney TH, Kennedy BW, Gallagher FA, et al. Detection of tumor response to a vascular disrupting agent by hyperpolarized <sup>13</sup>C magnetic resonance spectroscopy. *Mol Cancer Ther* 2010;9:3278-88.
- (37) Hamstra DA, Rehemtulla A, Ross BD. Diffusion magnetic resonance imaging: a biomarker for treatment response in oncology. *J Clin Oncol* 2007;25:4104-9.
- (38) Campbell-Washburn AE, Price AN, Wells JA, Thomas DL, Ordidge RJ, Lythgoe MF. Cardiac arterial spin labeling using segmented ECG-gated Look-Locker FAIR:

variability and repeatability in preclinical studies. *Magn Reson Med* 2013;69:238-47.

- (39) Belle V, Kahler E, Waller C, Rommel E, Voll S, Hiller KH, et al. In vivo quantitative mapping of cardiac perfusion in rats using a noninvasive MR spin-labeling method. *J Magn Reson Imaging* 1998;8:1240-5.
- (40) Campbell-Washburn AE, Zhang H, Siow BM, Price AN, Lythgoe MF, Ordidge RJ, et al. Multislice cardiac arterial spin labeling using improved myocardial perfusion quantification with simultaneously measured blood pool input function. *Magn Reson Med* 2013;70:1125-36.
- (41) Rice GC, Leiberman DP, Mathie RT, Ryan CJ, Harper AM, Blumgart LH. Liver tissue blood flow measured by <sup>85</sup>Kr clearance in the anaesthetized rat before and after partial hepatectomy. *Br J Exp Pathol* 1977;58:243-50.
- (42) Walker-Samuel S, Orton M, McPhail LD, Boulton JK, Box G, Eccles SA, et al. Bayesian estimation of changes in transverse relaxation rates. *Magn Reson Med* 2010;64:914-21.
- (43) Sheng Y, Hua J, Pinney KG, Garner CM, Kane RR, Prezioso JA, et al. Combretastatin family member OXI4503 induces tumor vascular collapse through the induction of endothelial apoptosis. *Int J Cancer* 2004;111:604-10.
- (44) El-Emir E, Boxer GM, Petrie IA, Boden RW, Dearling JL, Begent RH, et al. Tumour parameters affected by combretastatin A-4 phosphate therapy in a human colorectal xenograft model in nude mice. *Eur J Cancer* 2005;41:799-806.
- (45) Tozer GM, Prise VE, Wilson J, Cemazar M, Shan S, Dewhurst MW, et al. Mechanisms associated with tumor vascular shut-down induced by combretastatin A-4 phosphate: intravital microscopy and measurement of vascular permeability. *Cancer Res* 2001;61:6413-22.
- (46) Galbraith SM, Chaplin DJ, Lee F, Stratford MR, Locke RJ, Vojnovic B, et al. Effects of combretastatin A4 phosphate on endothelial cell morphology in vitro and relationship to tumour vascular targeting activity in vivo. *Anticancer Res* 2001;21:93-102.

# Chapter 6 Functional MRI biomarkers of vascular disruption in a liver metastatic model of cancer

---

## 6.1 Introduction

In the previous chapter I have shown the development of three functional parameters associated with vascular function that can be assessed by non-invasive MR imaging. Subcutaneous models of cancer however only offer limited translational potential; orthotopic models of disease, in which the tumour grows at the correct anatomical location in which it would be found in patients, are generally considered to better reflect the clinical situation due to a more relevant microenvironment in which the tumours develop (1). This then provides a more reliable insight into the translational ability of the novel therapeutic tested or the preclinical imaging modalities used (2). As discussed in the introduction to this thesis, although there may be many different underlying causes of colorectal disease, one common factor is the high incidence of metastatic spread of the cancer cells to the liver; around a third of patients at diagnosis will present with detectable metastatic spread to the liver, with a further 50% of those with undetectable liver disease at presentation progressing to develop metastasis (3). This late stage of colorectal cancer is difficult to treat effectively, with metastatic spread being ultimately the main cause of mortality (4). Preclinical models of liver metastasis that mimic this clinical situation are therefore necessary for effective translation of therapies and imaging techniques. Many different models have emerged (5, 6); the most reproducible model that combines relative ease of set-up and spread through blood vessels to the liver parenchyma is direct injection of cancer cells in to the spleen of the animals (7). Following the subsequent development of the solid tumour deposits however can be difficult, as access to MRI scanners is both time-consuming and expensive. Bioluminescence has emerged as a useful way of following cells *in vivo* that is inexpensive, easy to use and has a high throughput (8). Transduction of cell lines with the luciferase gene is necessary, but allows longitudinal imaging of tumour progression. This chapter therefore aims to develop a model of colorectal liver metastasis by direct intrasplenic injection of luciferase transduced SW1222 and LS174T cells lines. This model will then be used to image the response to vascular disruption with OXi4503 using the functional vascular-associated MRI biomarkers described in the previous chapter.

## 6.2 Method

### 6.2.1 Validation of luciferase transduction

In order to image cells by bioluminescent imaging the colorectal carcinoma cell lines SW1222 and LS174T were first stably transduced via a viral vector with the firefly luciferase reporter gene. Transduction has the advantage that the reporter is constitutively active and longitudinally viable with no decrease in gene expression. This procedure was carried out by the laboratory of Dr Martin Pule at the UCL Cancer Institute. The firefly luciferase gene was co-induced with the cellular marker CD34, allowing analysis of transduction efficiency via fluorescence activated cell sorting (FACS). Analysis of non-transduced and luciferase transduced SW1222 and LS174T cell lines was performed on a CyAn ADP flow cytometer (Beckman Coulter), with measures of forward and side scatter used to identify viable single cell populations. This viable cell population was then measured for fluorescence to identify correct transduction of the luciferase gene in to the cell line. Quantitation of transduction efficiency by means of cell population was performed on the Summit software v4.3 (Beckman Coulter). Transduced cell lines were frozen for storage at passage 5 (SW1222) and passage 8 (LS174T). Further *in vitro* validation of successful gene transduction was performed using the PhotonImager (Biospace) to conduct assays of cell growth kinetics in comparison with parental cell lines, kinetics of luciferase bioluminescent activity, cell number to luminescence correlation, and lower limit of cell detection by bioluminescence. *In vivo* characterisation included the viability of transduced cells to form solid subcutaneous tumours with correct morphology, as assessed by H&E staining, and tumour growth curve kinetics compared to non-transduced cells.

### 6.2.2 Characterisation of liver metastasis model

In order to observe growth of the model in a longitudinal manner n=8 mice were injected intrasplenically with luciferase-transduced SW1222 cells under recovery surgery, as established in the methods section of this thesis. Animals were allowed to recover for 48 hours before imaging progression of the tumours commenced. Imaging by bioluminescence was achieved by injecting 30mg/kg i.p. luciferin and imaging at 15 minutes post dose. This was done every week up to four weeks after surgery. During this time imaging sessions on the 9.4T MRI scanner were also performed, with high-resolution T2-weighted sequences, as described in the previous chapter, used to acquire morphological scans that would enable volume measurements. During these scans, working up of diffusion, perfusion and deoxyhaemoglobin sensitive intrinsic susceptibility sequences was also performed. Liver

sections containing tumour deposits were excised at termination at 4 weeks post-surgery for histological analysis.

### **6.2.3 Functional assessment of response to vascular disruption**

For assessment of response to vascular disruption with the VDA OXi4503, n=12 mice were used to establish models of liver metastasis; n=6 with SW1222 cells and n=6 LS174T cells. A further n=5 were injected with SW1222 cells in order to be used as sham controls dosed with saline solution. Animals were monitored for tumour growth as described above. At around three weeks, when clearly defined individual tumours were distinguishable by bioluminescence imaging, animals were used for therapy response studies. Due to the time-intensive nature of this MRI scanning, it was performed over a number of consecutive days. Animals were positioned within the scanner and an i.v. line catheter placed in the tail vein and held in place with moulding paste and surgical tape. The line was left in place during localisation scans of the mouse abdomen to correctly place the image slice. Baseline measurements of ADC, ASL and R2\* were acquired using the sequences described in the previous chapter. Dosing of the mice was then performed remotely, and scans of ADC and R2\* acquired consecutively up until 90 minutes post dose, after which a final ASL perfusion scan was performed. Animals were then removed from the scanner and the tail vein catheter removed and checked for signs of an unsuccessful dose (i.e. a subcutaneous injection, pooled liquid outside the cannula, etc). SW1222 tumours were re-scanned at days 1, 3 and 5 post dose to observe longitudinal changes in functional parameters. Sham-dosed controls and LS174T tumours were scanned for the acute 90 minutes only. At experiment termination tumours were excised for histological assessment.

### **6.2.4 Analysis of results**

Measures of ADC, ASL and R2\* were analysed in Matlab and reconstructed in Amira software. The acquired data-sets were searched for acute (90 minutes) and longitudinal (up to 5 days) change in value; data-sets were also analysed for markers of response, both inter- and intra-parameter. Analyses based on size of tumour deposit and location was also performed, with results from all tumour voxels considered for potential significance.

## 6.3 Results

### 6.3.1 Expression of luciferase activity

Results from the flow cytometry of the SW1222 cell line can be seen in **figure 6.1**. The top section shows results for SW1222 cells and the lower section for LS174T cells. Panels **A** and **B** in each show acquired data for the parental non-transduced cells, with statistics of total count and percentage of total gated cells shown on the right of the row. Panel **A** shows the entire cell suspension plotted as forward scatter vs side scatter. From this a region **R1** is drawn around a healthy cell population. Panel **B** then shows the fluorescence of this population of healthy cells; for SW1222 cells 99% are within region **R4** of panel **B**, and for LS174T cells 98.65% are within region **R4**, showing that they are not fluorescent and therefore do not express the cell surface marker CD34.

Panels **C** and **D** show the same metrics for the luciferase transduced cell lines. The total events registered is maintained in a similar way to the non-transduced cells, with the percentage of total cells selected in the region **R1** also maintained to around 35% of total cells. The population of SW1222 and LS174T cells in the region **R4**, however, has decreased to 6.46% and 5.13% respectively, with 93.02% and 94.84% of this sub-population now within the region **R2** of panel **B**. This shows the cells to be positive for fluorescence and therefore expressing the cell surface marker CD34, which correlates to expression of the luciferase gene.

Following this, full characterisation of transduced cell lines was performed, including *in vitro* cell growth kinetics, time profile of cellular luciferase activity, correlation of bioluminescent signal to cell number, lower limit of detection, and *in vivo* comparison of subcutaneous growth between parental and transduced cell lines. No difference between transduced and parental lines was noted, and experiments proceeded to *in vivo* bioluminescent characterisation of the liver metastasis model (*in vitro* characterisation results can be found in appendix I of this thesis).

The n=8 mice injected intrasplenically with SW1222-Luc were imaged over the 4 week period by bioluminescence, an example of which can be seen in **figure 6.2**. Panel **A** shows a composite image of the whole group of mice at each time point, with the photon flux acquired superimposed over the photo of the animals in the scanner. As can be seen, the photon flux produced by the luciferase-expressing cells can be detected from day 2 onwards, and always located in the region of the abdomen and liver. Quantification of this photon flux is shown in panel **B** individually, with the growth of signal over time expressed

as  $\log_{10}$  of photon per second per  $\text{cm}^2$  per steradian. As can be seen in panel **B**, the signal in all animals increases over the 4 weeks. Panel **C** shows the average photon flux across the group of animals, with error bars denoting standard deviation of the mean.

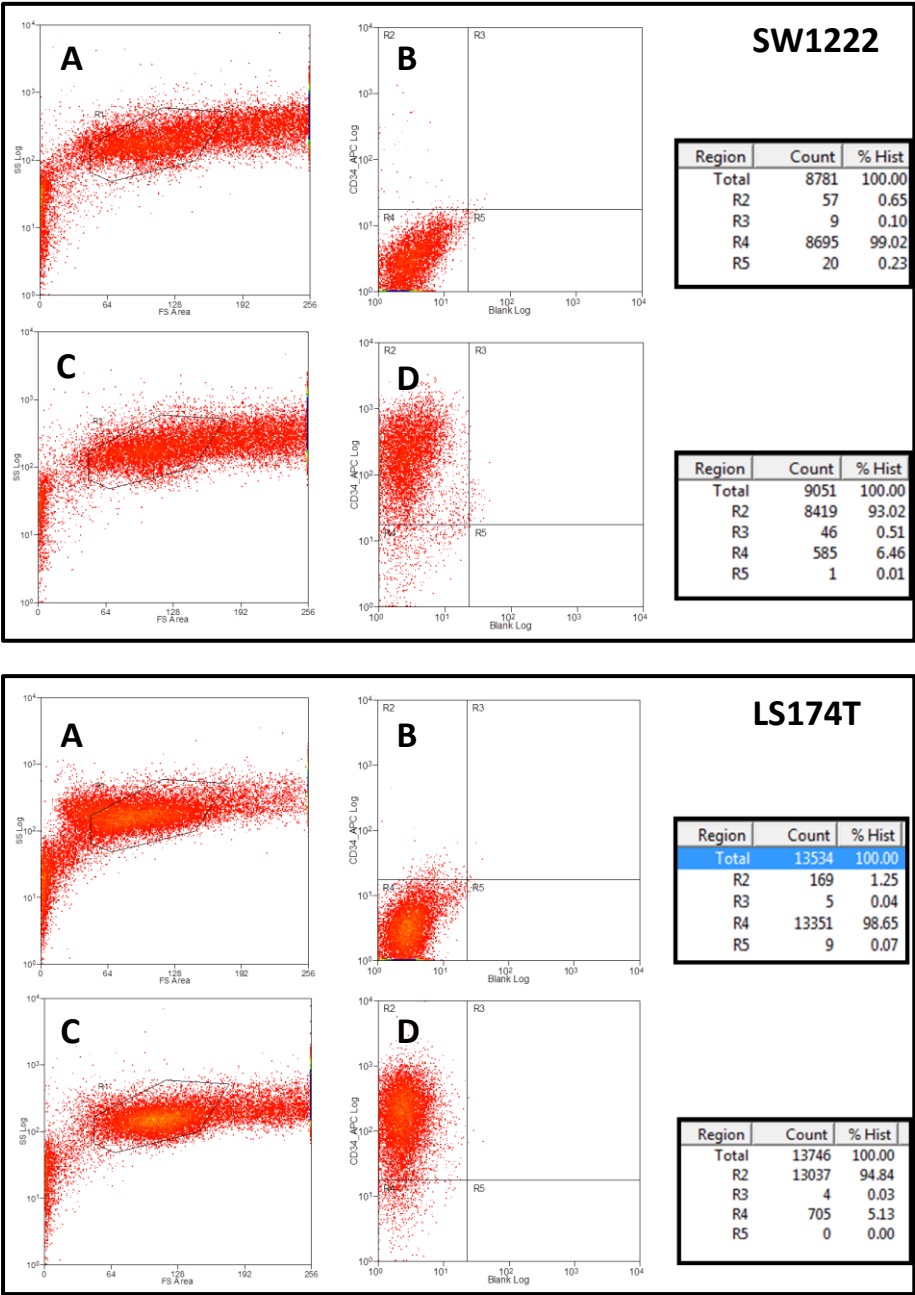


**Figure 6.1 Fluorescence activated cell sorting analysis of luciferase gene transduction**  
SW1222 cell line (first panel) and LS174T cell line (second panel): FACS analysis of parental (**A** and **B**) and luciferase-transduced cells (**C** and **D**). **A** and **C** depict healthy cell population selection, **B** and **D** depict sub-population fluorescence expression. Total cell count and % of total is shown to the right of each row.



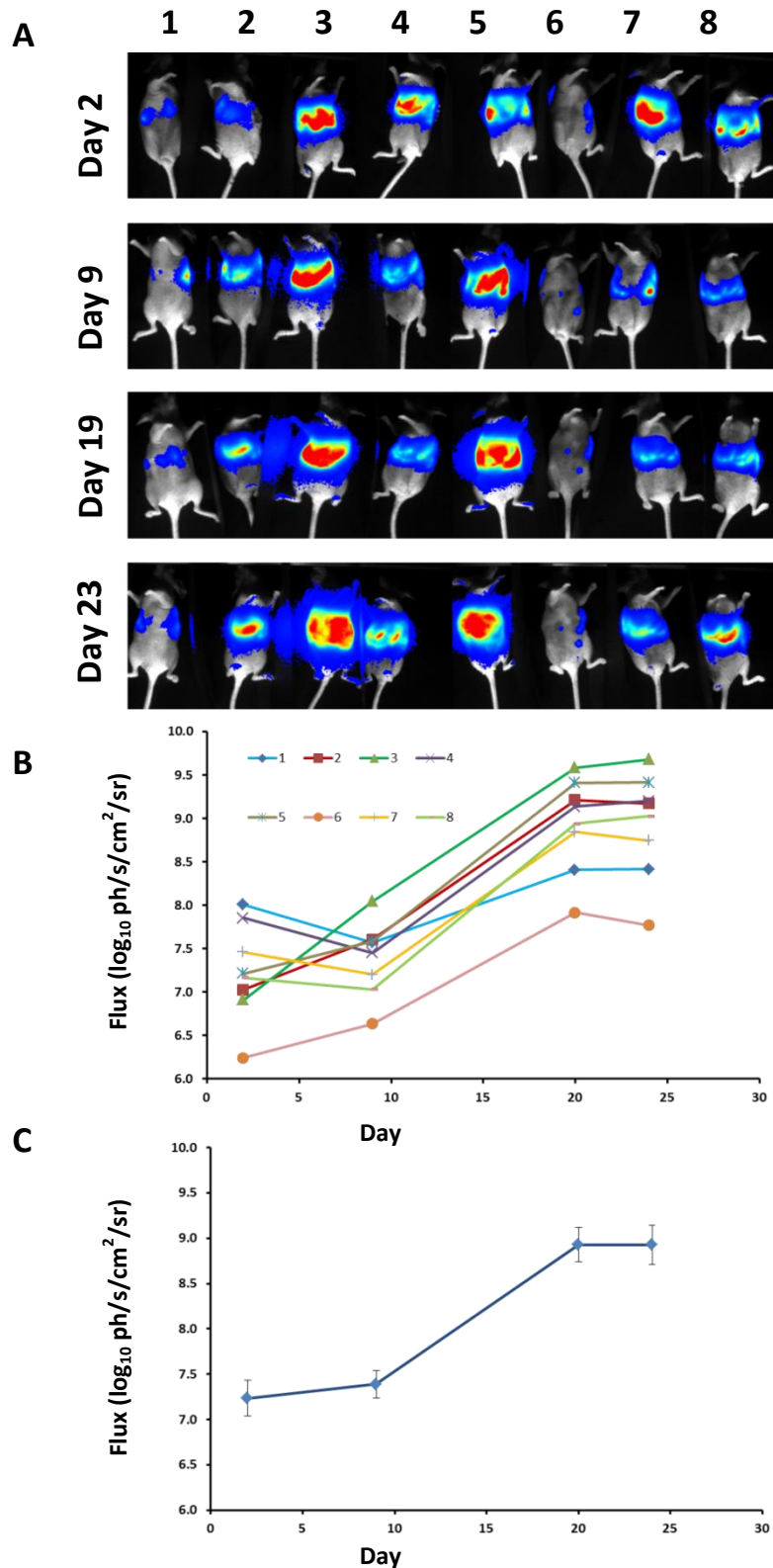


**Figure 6.2 Bioluminescence monitoring of liver metastatic burden**

Panel **A** shows  $n=8$  mice following intrasplenic injection of SW1222 cells at day 2, 9, 19 and 23. Images show bioluminescent photon flux superimposed on a photo background. Panel **B** shows calculation of  $\log_{10}$  of photon flux in ph/s/cm<sup>2</sup>/sr for all animals across all time points. Panel **C** shows the average with standard deviation of the mean denoted by error bars for the group.

### 6.3.2 Development of orthotopic model

High resolution T2-weighted scans of the n=8 SW1222 mice were acquired over the 4 week imaging period, an example of which can be seen in **figure 6.3**. The day at which each image was acquired is below the MRI section, with significant abdominal features highlighted by the arrows. Development of solid tumours within the liver is seen as areas of hyper-intense ‘white’ signal as opposed to normal uniform grey signal that is from liver tissue; tumour deposits are first seen as small spherical objects in one lobe of the example liver at day 14 following surgery. Tumour deposits increase in size until at day 27 the majority of liver area is taken over with tumour tissue. This can be segmented and a volume of total tumour burden calculated. An example of this is shown in **figure 6.4**, in which tumour deposits at weeks 2, 3 and 4 have been pseudo-coloured in orange. Tumour total burden across the group of mice can therefore be calculated, and is shown as percentage tumour burden within the liver in the lower right hand panel of **figure 6.4**.

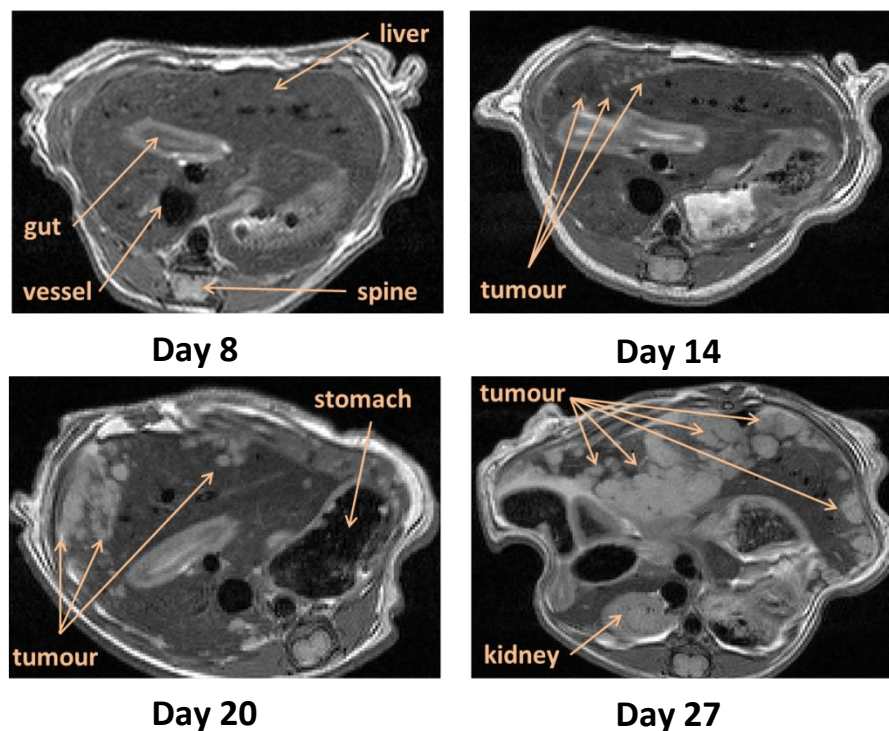


**Figure 6.3 Magnetic resonance monitoring of liver metastatic deposits**

High resolution T2-weighted MRI images of progression of the liver metastatic model shown over a 4 week imaging period (n=8 total); abdominal features such as organs are highlighted by the arrows. Tumours are seen as hyper-intense spherical regions within the liver lobes that increase in size over the time frame imaged.

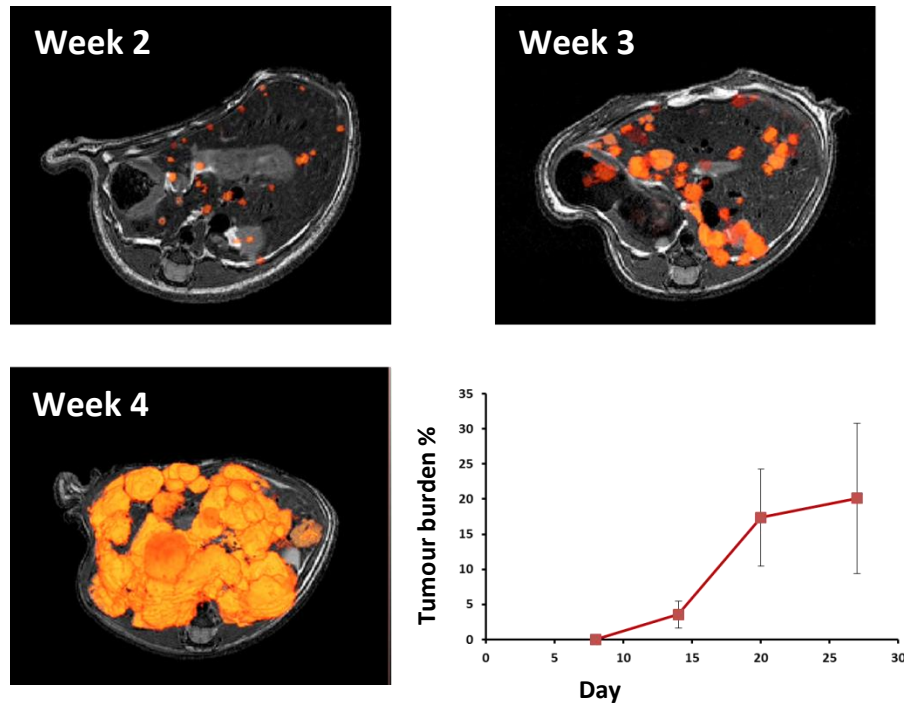


**Figure 6.4 Segmentation of tumour deposits and total tumour burden**

Images show orange pseudo-colouring of segmented tumour deposits from high resolution T2-weighted MRI images at weeks 2, 3 and 4 following surgery. Total liver burden can be calculated as percentage of the liver that is occupied by tumour tissue, a graph of which across the whole group can be seen in the lower right panel ( $n=8$ , error bars denote mean $\pm$ SDM).

### 6.3.3 Monitoring of functional response within tumour deposits

In order to demonstrate the applicability of the MRI sequences developed in the previous chapter to study of the liver metastatic model used here, an example of the mapping ability is shown in **figure 6.5**. This shows results from the ASL sequence (**A**) and IS sequence (**B**) from within the same liver mapped across 4 distinct tumour deposits both at baseline and 90 minutes post 40mg/kg OXi4503. For clarity these have been superimposed on high resolution T2-weighted images, and one of the deposits has been enlarged so as to clearly show the varied results mapped across the tumour voxels. Panels **C** and **D** show H&E staining of liver sections containing tumour deposits at 24 hours after dosing with saline control (**C**) or 40mg/kg of OXi4503 (**D**), which clearly shows a necrotic core with rim of surviving cells following dosing with OXi4503 and 'normal' healthy tumour cells with the saline control, demonstrating the efficacy of the i.v. line employed in this set-up. Results for the ADC sequence are not shown, as bulk motion within the imaging section due to peristaltic motion of the intestines and any residual respiratory motion not correctly gated out meant coupled with the small volume of the tumour deposits produced corrupted data sets, giving no useful measurement. Because of this only results for ASL and R2\* will be shown hereafter.

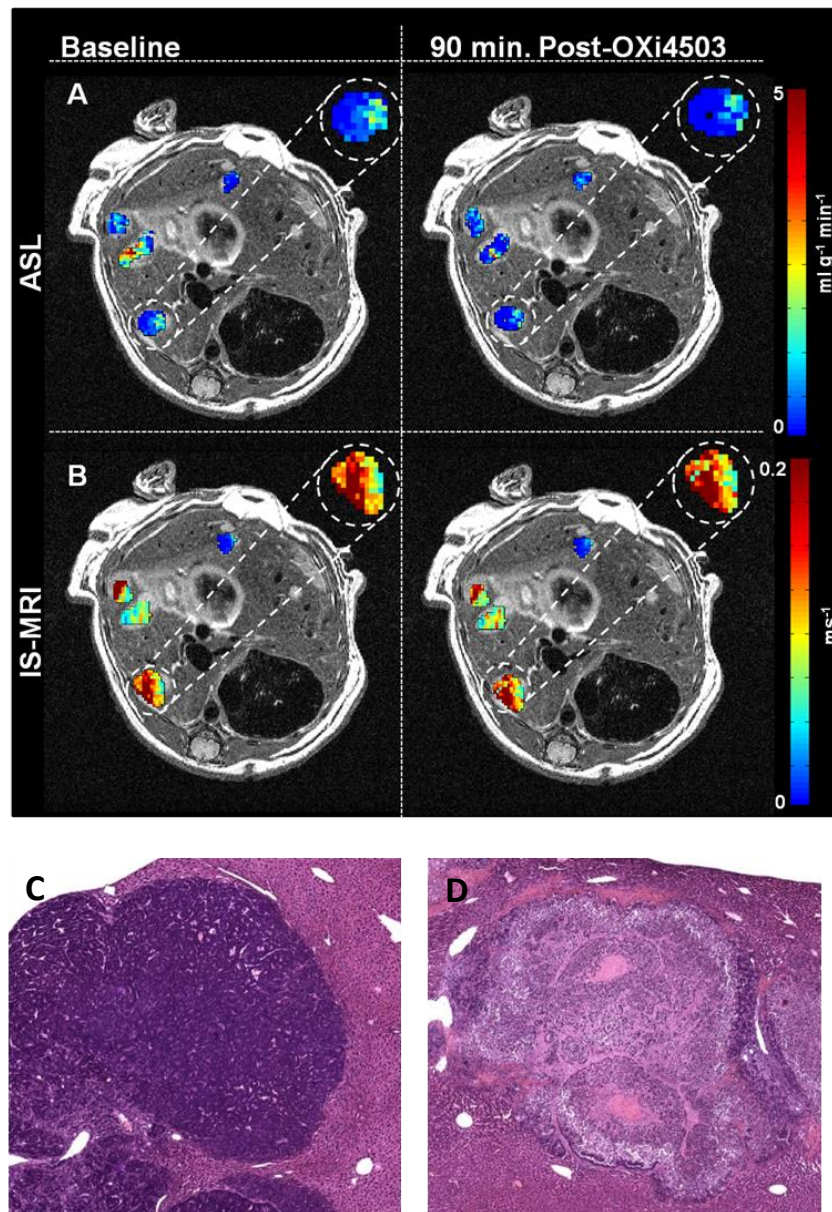


**Figure 6.5 Mapping of functional MRI measurements on to tumour deposits**

Functional measurements of perfusion (A) and increase in  $R2^*$  (B) using ASL and intrinsic susceptibility sequences at baseline and 90 minutes after 40mg/kg OXi4503 mapped across 4 distinct tumour deposits (n=1 shown, n=6 total for each of SW1222 and LS174T). Histological assessment of SW1222 response shows a sham dosed control liver section containing a viable tumour deposit (C) and a dosed liver section (D) at 24 hours post 40mg/kg OXi4503

### 6.3.4 Response of metastases to vascular disruption

Functional response to vascular disruption using OXi4503 in the liver metastatic model was performed in n=6 SW1222 and n=6 LS174T mice, with a further n=5 SW1222 animals sham dosed with saline. Distinct tumour deposits within the liver, clearly identified by high resolution T2-weighted imaging, were used to position the single slice ASL sequence; this was matched to the R2\* acquired data, providing n=22 distinct OXi4503 treated SW1222 tumours, n=12 LS174T tumours, and n=13 sham dosed SW1222 tumours. As seen in the previous chapter, use of the median functional value acquired from across the tumour voxels was used as indicative of response of the whole tumour. **Figure 6.6** shows box plots for values of ASL (**A**) and R2\* (**B**) in sham treated SW1222 tumours, with the central line denoting the median value, the boxes the inter-quartile range and the whiskers denoting minimum and maximum values. Two tailed paired T-Tests between values show no significant results across the 90 minute time frame acquired. The same box plot configuration has been used for both ASL and R2\* in SW1222 and LS174T, shown in panels **A** and **B** of **figures 6.7** and **6.8** respectively. Panel **C** in each of these figures shows the percentage of baseline median value of ASL in blue and R2\* in red plotted on the same graph, with error bars denoting standard error of the mean. As the SW1222 group was imaged for a longer time period, this is reflected in the graphs within **figure 6.7**. Perfusion of tumours, as measured by ASL, appears to decrease slightly at 90 minutes and 24 hours post dose, with a return to higher values seen at day 3 and 5. R2\* appears to increase slightly at 90 minutes, followed by a decrease at day 3 and 5. T-Tests for significant results however show that only 90 minute ASL and day 3 R2\* are significantly different from baseline values. All other time points show a non-significant spread of values.

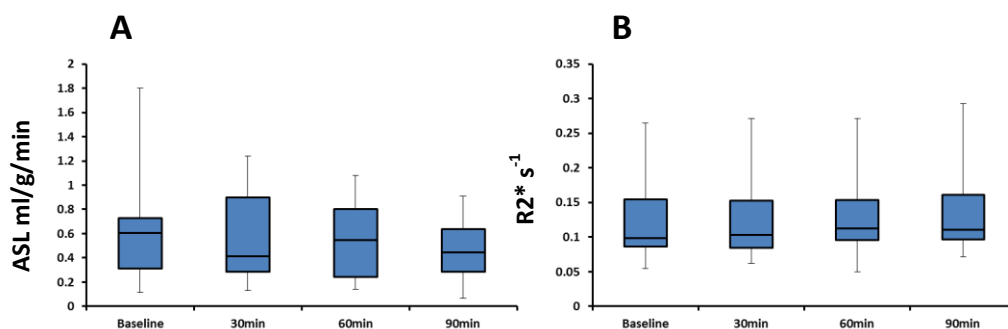


**Figure 6.6 Functional response of tumour deposits – Sham dose**

Graphs depict functional measurements of perfusion (**A**) and increase in R2\* (**B**) using ASL and intrinsic susceptibility sequences from baseline up to 90 minutes after saline sham dose (n=5). Box plots show the median value, interquartile range, and maximum and minimum of n= 13 distinct SW1222 tumour deposits.



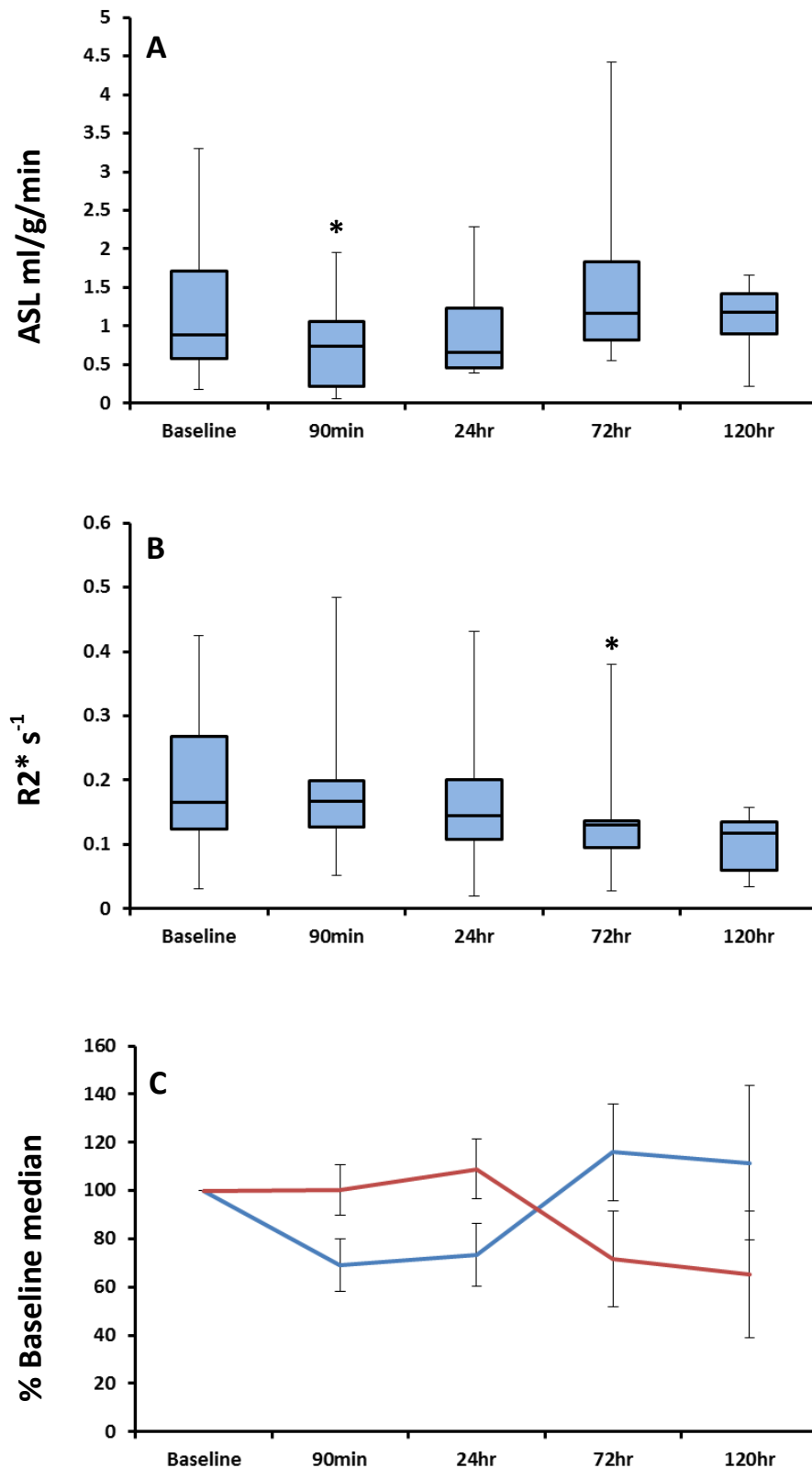


**Figure 6.7 Functional response of tumour deposits – SW1222**

Graphs of perfusion (A) and increase in  $R2^*$  (B) using ASL and intrinsic susceptibility sequences from baseline up to 5 days post 40mg/kg OXi4503 (n=6). Box plots show the median value, interquartile range, and maximum and minimum of n= 22 distinct SW1222 tumour deposits, with \* showing significance. Graph C shows average percentage of baseline values for  $R2^*$  in red and ASL in blue across the cohort, with error bars denoting standard error of the mean

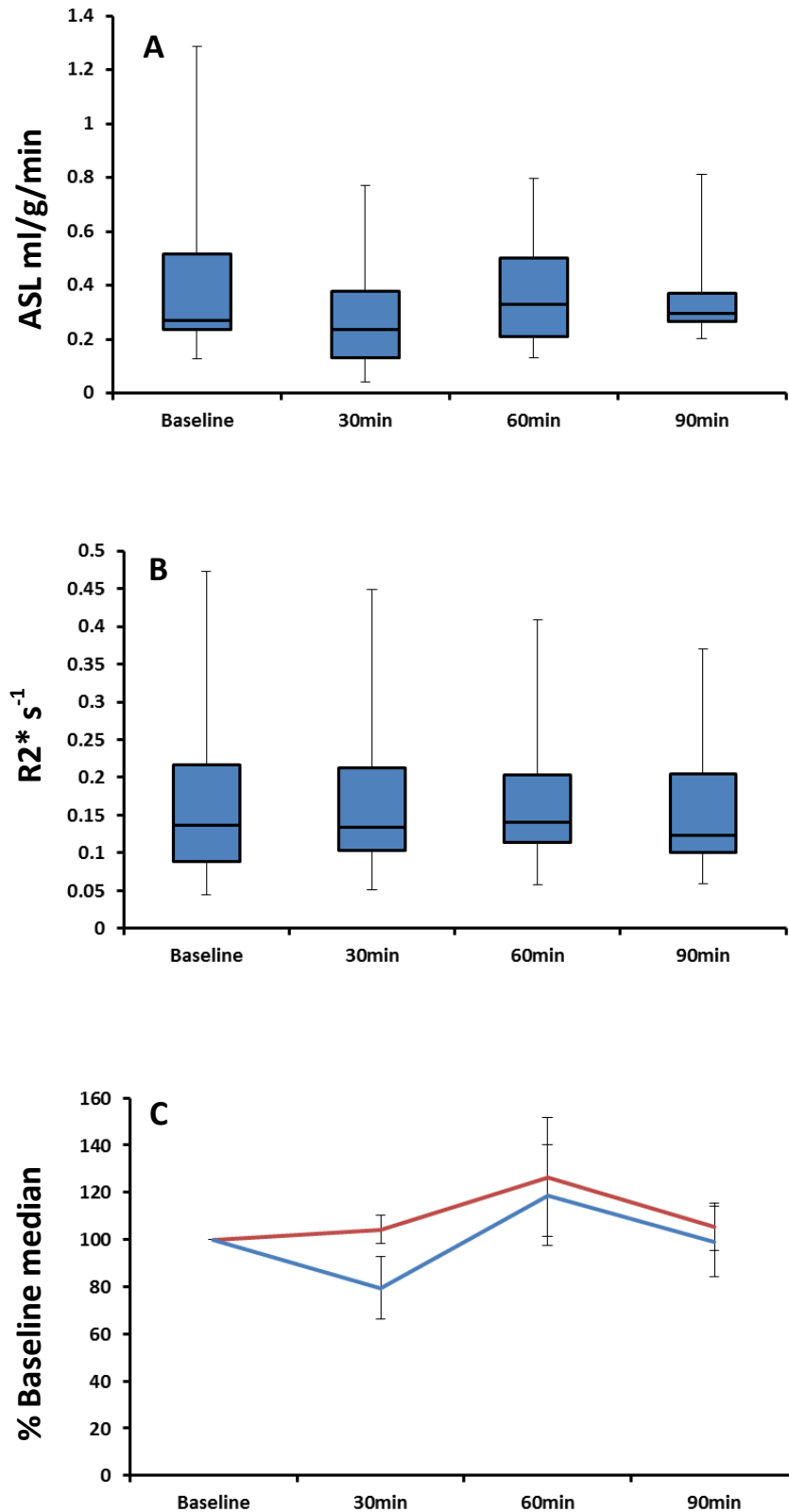


**Figure 6.8 Functional response of tumour deposits – LS174T**

Graphs depict functional measurements of perfusion (A) and increase in  $R2^*$  (B) using ASL and intrinsic susceptibility sequences from baseline up to 90 minutes after 40mg/kg OXi4503 (n=6). Box plots show the median value, interquartile range, and maximum and minimum of n= 12 distinct LS174T tumour deposits. Graph C shows average percentage of baseline values for  $R2^*$  in red and ASL in blue across the cohort, with error bars denoting standard error of the mean



Results for the LS174T tumours shown in **figure 6.8** depict the acute 90 minute imaging period. Although there is some suggestion of an increase in  $R2^*$  over the first 60 minutes of data acquisition the results demonstrate a range of values that show no significance when compared to baseline. As the cohort data showed no change, even though individual tumour deposits did alter functional readings of perfusion and increase of deoxygenated haemoglobin, correlations between the two parameters on an individual tumour deposit basis was examined. The scatter plots depicted in **figure 6.9** show the measured ASL perfusion value at baseline across the X axis against the change measured at 90 minutes post OXi4503 on the Y axis for both SW1222 (**A**) and LS174T (**B**). Both tumour types show a negative correlation with  $R^2$  values of 0.65 and 0.78 respectively, showing that those tumour deposits that show a change in perfusion levels are those that have the highest initial perfusion at baseline. The same graphs layout is reproduced for values of  $R2^*$  in **figure 6.10**. No association is observed in the SW1222 tumours, whilst in the LS174T tumours a negative correlation is observed with an  $R^2$  of 0.79. LS174T tumours with a high baseline  $R2^*$  appear to decrease in value at 90 minutes whilst those with a low initial value show an increase at 90 minutes. The third comparison in **figure 6.11** shows the change in perfusion by ASL at 90 minutes on the X axis compared to the change in  $R2^*$  at 90 minutes on the Y axis. Although there is a suggestion of correlation between an increase in  $R2^*$  relating to a decrease in perfusion in the SW1222 tumours, the  $R^2$  is only 0.34, whilst no association is noted in the LS174T tumours.

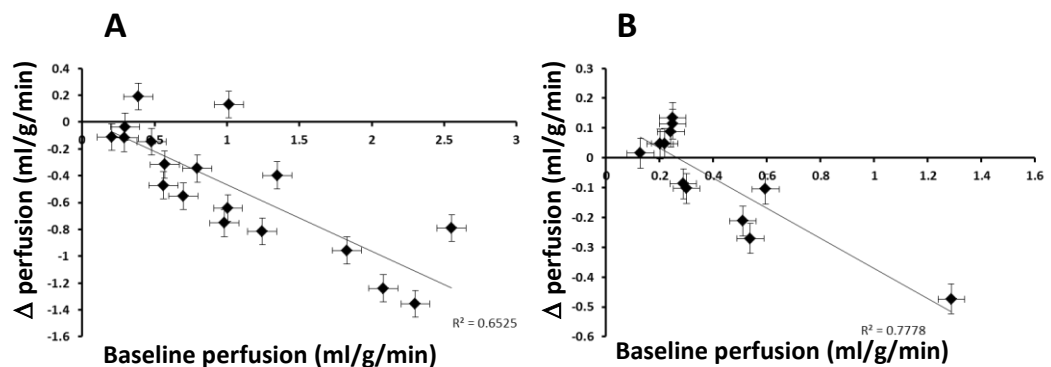


**Figure 6.9 Baseline vs change correlation in perfusion**

Graphs depict functional measurements of perfusion in SW1222 (**A**) (n=6 animals) and LS174T (**B**) (n=6 animals) tumours using ASL sequences. Median values per tumour deposit are shown for baseline measurements on the X axis with the change in perfusion at 90min on the Y axis. Error bars for individual points represent standard error of the median value acquired

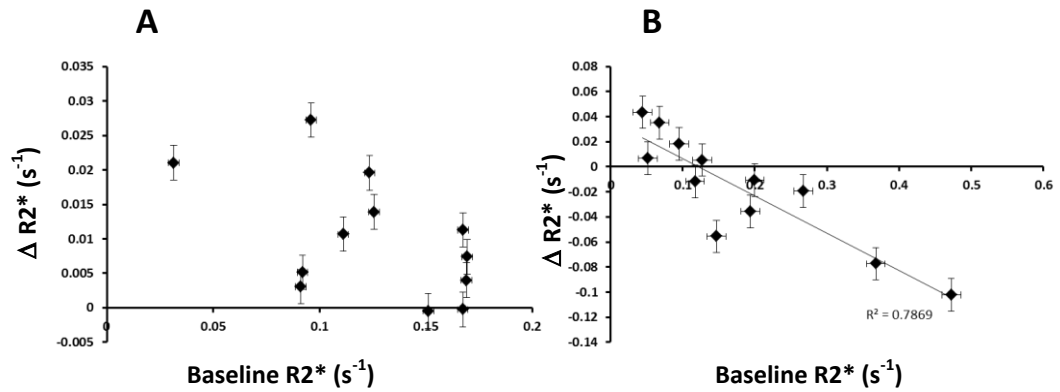


**Figure 6.10 Baseline vs change correlation in  $R2^*$**

Graphs depict functional measurements of  $R2^*$  in SW1222 (A) (n=6 animals) and LS174T (B) (n=6 animals) tumours using intrinsic susceptibility sequences. Median values per tumour deposit are shown for baseline measurements on the X axis with the change in perfusion at 90min on the Y axis. Error bars for individual points represent standard error of the median value acquired

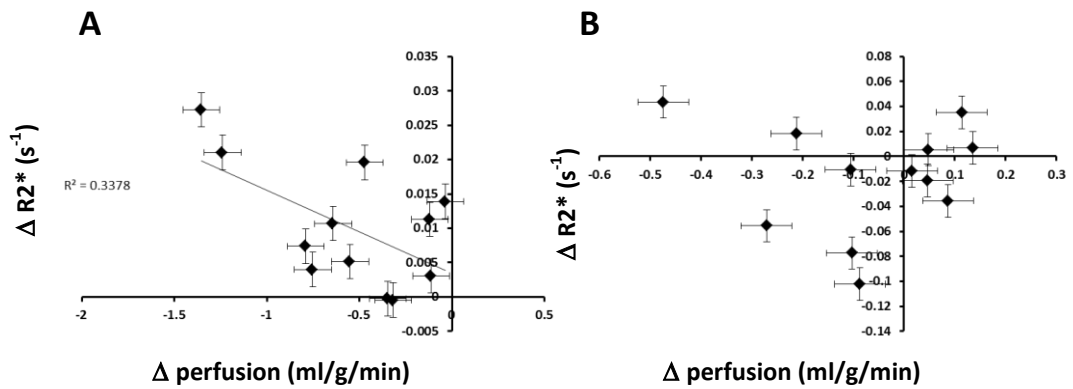


**Figure 6.11 Change in  $R2^*$  vs change in perfusion**

Graphs depict functional measurements of change in perfusion and  $R2^*$  in SW1222 (A) (n=6 animals) and LS174T (B) (n=6 animals) tumours using ASL and intrinsic susceptibility sequences. Median values per tumour deposit are shown for change in perfusion measurements on the X axis with the change in  $R2^*$  on the Y axis. Error bars for individual points represent standard error of the median value acquired

### 6.3.5 Effect of tumour location

Having observed differential effect of functional measurements of perfusion and R2\* within different tumours deposits, even if they were within the same animal and lobe of liver, further analysis was performed to understand these differences. Histological analysis was performed on larger sections to encompass more than one solid tumour deposit. Results from this varied, however as can be seen in **figure 6.12**; certain liver sections did contain multiple tumour deposits at 24 hours post OXi4503 that had reacted differently to dosing. Highlighted by black arrows in panel **A** are two SW1222 tumour deposits that show typical signs of necrosis within the core of the tumour, with a healthy rim of surviving cells. A further two tumour deposits are highlighted by the red arrows that show no sign of necrosis, with densely nucleated tissue that is characteristic of healthy growing tumours. Panels **B** and **C** show enlarged examples of tumour deposits found to be non-responsive and responsive respectively, both in a similar position on the edge of the liver.

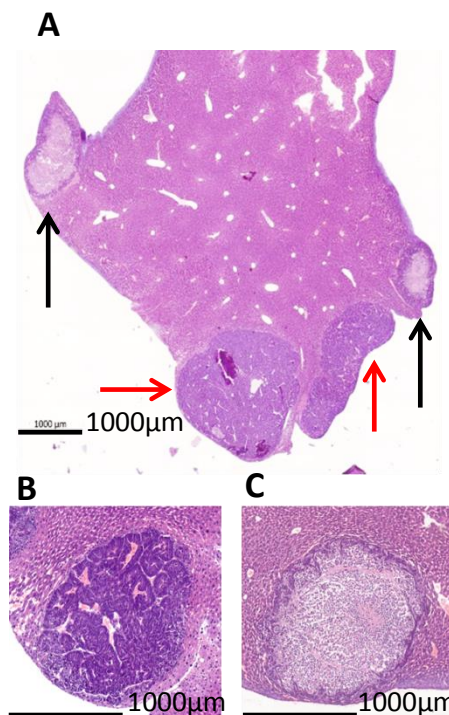


**Figure 6.12 Histological assessment of multiple tumours within a liver section**

Panels show H&E staining of a larger section of liver tissue containing multiple SW1222 tumour deposits. Highlighted in panel **A** by the black arrows are two deposits that have responded to 40mg/kg of OXi4503, whilst highlighted by the red arrows are two tumour deposits that have not. Panels **B** and **C** show further examples of cases of non-response and response, respectively. Black bars within images denote 1000µm

Further categorisation of the functional MRI data based on tumour deposit size did not show any correlation to observed effect. Where it was possible to categorise tumours based on location this was implemented, with tumours designated as either close to a large blood vessel, close to a small blood vessel, or close to the periphery of the liver lobe. An example of the segmentation used to achieve this can be seen in **figure 6.13** panel **A**, where a three-dimensional liver area has been segmented in Amira and represented by the maroon coloured structure. The major blood vessel networks within the liver have also been segmented and are represented in blue. All tumour deposits have been segmented and coloured in yellow, with three coloured differently to demonstrate categorisation based on location; the tumour in red is proximal to a large vessel, the tumour in green is proximal to smaller vessels, and the tumour in light blue is at the periphery of the liver lobe. The resultant change at 90 minutes in perfusion and  $R2^*$  can then be shown based on this grouping, with perfusion shown in blue and  $R2^*$  in red, for both SW1222 (panel **B**) and LS174T (panel **C**). For SW1222 tumours not much difference is seen in changes in  $R2^*$ , however there is a decrease of  $48\pm14\%$  for tumours close to large vessels, a more varied but also large decrease for tumour located close to small vessels of  $59\pm48\%$ , and a small and varied decrease at the liver periphery of  $17\pm28\%$ . Baseline perfusion measurements for these locations showed that those close to large vessels were better perfused at  $1.5\pm0.8\text{ml/g}^{-1}\text{min}^{-1}$ , compared to  $1.3\pm0.7\text{ml/g}^{-1}\text{min}^{-1}$  and  $0.6\pm0.3\text{ml/g}^{-1}\text{min}^{-1}$  respectively. However, for the LS174T tumours there was no difference noted in perfusion measurements, although those located close to large vessels had a significantly different increase in measured  $R2^*$  of  $74.7\pm23\%$  when compared to tumours located close to small vessels or the liver periphery. Initial values of  $R2^*$  for these tumours were significantly lower, at  $0.05\pm0.01\text{ s}^{-1}$ , when compared to tumours located close to small vessels ( $0.15\pm0.08\text{ s}^{-1}$ ) and liver periphery ( $0.25\pm0.1\text{ s}^{-1}$ ).

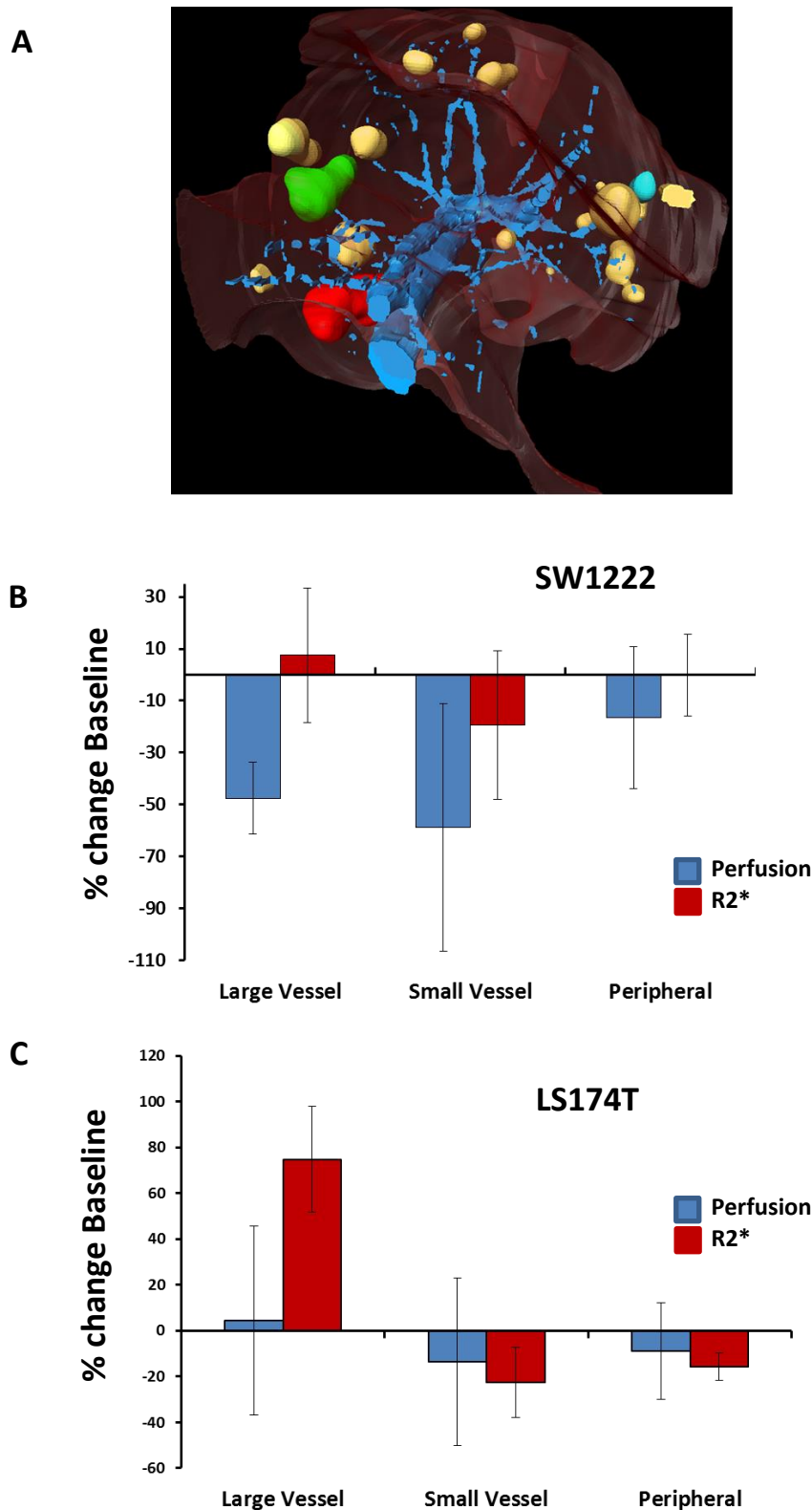


**Figure 6.13 Functional response of tumour deposits categorised by location**

Panel **A** shows a whole liver in 3D segmented for liver tissue (maroon), major blood vessels (blue) and tumour deposits (yellow). Three example tumours are shown in red for adjacent to 'large vessel', green for 'small vessel', and light blue for 'periphery'. Change from baseline value based on this categorisation can be seen in panel **B** for SW1222 (n=6 animals) and **C** for LS174T (n=6 animals), with ASL for perfusion in blue and R2\* in red.

## 6.4 Discussion

### 6.4.1 Correct transduction of cells lines was achieved

Bioluminescence is a useful preclinical *in vivo* tool that allows highly sensitive tracking of cells that express an introduced gene in a rapid, inexpensive and relatively easy manner (9-11); luciferase in particular, from the firefly *Photinus Pyralis*, has been extensively used in biomedical research (12, 13). In this chapter I have shown that the transduction of two colorectal carcinoma cell lines with the luciferase gene has been achieved, and that this does not affect growth characteristics of the cells *in vitro* or the progression of solid tumours *in vivo*. Luciferase expression was also not altered over time in the dividing cells or due to liquid nitrogen storage, as the cells were transduced with luciferase rather than transfected. This enabled monitoring of the developing tumours *in vivo* in a fast and inexpensive manner, and is similar to previous work using luciferase to monitor liver models of cancer that have used for different cell lines (14, 15). Bioluminescence was used here simply as a tool to monitor tumour progression, in order to time functional assessment of VDA treatment with MRI; translation to the clinic of bioluminescence is not a viable option, given that the cells need to be transduced externally to the patient in order to express the luciferase gene. However, previous work using bioluminescence as a marker of response to VDA treatment in its own right has shown that it may also be a useful translational tool for novel therapeutics that target tumour vasculature (16); Zhao et al have shown that dynamic response to CA4P can be monitored by luciferase activity, proving that correct transduction of cell lines, with no altered growth characteristics, may in the future prove a useful technique for assessing new vascular targeted therapies.

### 6.4.2 Functional MRI biomarkers can be measured on individual tumour deposits

Although previous work has shown response to OXi4503 in liver metastatic models of cancer (17) this is the first time that non-invasive imaging of vascular parameters across the whole liver has been assessed. Pre-treatment tumours showed variable baseline measurements of perfusion and R2\*, and a heterogeneous response to OXi4503 was observed in both ASL and IS-MRI techniques. Because of this observed heterogeneous response each metastasis was considered as an individual entity; caution is therefore needed in the interpretation of the statistical changes, as some effects may be affected by systemic changes within the whole animal. However, the ability to map these values across the tumour voxels, as with subcutaneous tumours shown in the previous chapter, demonstrates that these functional markers of response can be measured individually from

one tumour deposit to the next. This is the first time that arterial spin labelling has been used to measure perfusion in tumours outside of the brain; the use of hepatic ASL to assess response to VDA therapy in this liver metastatic model is therefore a novel approach to monitor vascular changes. A significant reduction in perfusion was observed at 90 minutes following administration of 40 mg/kg of OXi4503 in SW1222 tumours, which is consistent with the proposed vascular targeting action of the agent (18), and relates well to previously published *ex vivo* histological data of a similar VDA (19). It is interesting to note that at 24hr the value of ASL for the SW1222 tumours (**figure 6.7**) appears to measure perfusion within the tumour that should be centrally necrotic; this is possibly an effect of heterogeneous response observed, in that whilst some tumours will have no flow due to a necrotic core others were not affected at 24hr post-dose and therefore retain a flow measurement. Another possibility is that the area of tumour ROI is sufficient to include some of the tumour periphery and normal liver, which will still be perfused. Indeed, from the PAT experiments presented earlier in this thesis it appears that the remaining tumour periphery and surrounding normal tissue increases in haemoglobin presence following OXi4503 therapy. This flow to the periphery may explain some of the measured ASL in **figure 6.7**. A further possibility is of a potentially introduced bias for positive values during the post-processing of the acquired data; any negative values were automatically assigned a value of zero, given that a negative flow was not possible, which may skew the data towards a higher average value. This on its own however is not sufficient to explain the measured perfusion with ASL, and it is thought likely that it is a combination of the above.

An increase in  $R2^*$  from IS-MRI was also measured at 90min, which is consistent with previous studies (20). However, measurements taken at subsequent time-points showed no significant difference from baseline. The same was found for LS174T tumour measurements of ASL and  $R2^*$ . It is possible that the 90 minute time frame is not sufficient to observe any induced effects, however the more likely explanation is a heterogeneous response to treatment on a tumour-to-tumour basis. As these measurements were based on median values across tumour deposits and groups the range in values masks any potential biomarker effect of the measured parameters. In fact, when both SW1222 and LS174T tumour deposits are assessed individually it can be seen that high initial levels of perfusion correspond to those tumours with the greatest response to therapy; this suggests that tumours with high initial vascularisation stand are potentially sensitive to the actions of VDAs and indicates a potential prognostic ability of ASL measurement in tumours, i.e. not all tumours will have the same degrees of perfusion, but those that

possess high perfusion based on ASL measurements will respond effectively to VDA treatment. Tumour cell kill in response to therapy is also dependent on the absolute blood flow to the tumour and the length of time that this is shut down within the tumour. Further investigation of how these high-perfusion metastasis respond in this regard would be very informative. With  $R2^*$  there is no correlation between baseline and subsequent change within SW1222 tumours, and an inverse relationship with LS174T tumours, reflecting the differing vascular pathophysiologies between the two tumours. It is possible that the LS174T tumours with high initial  $R2^*$  reflect tumours with an already impaired vascular supply, leading to significant levels of deoxyhaemoglobin already present within the tumours. Low initial levels of  $R2^*$  would indicate a relatively well perfused tumour deposit to begin with which, when treated with OXi4503, actually increases the content of deoxygenated blood and therefore the measure of  $R2^*$ . This could explain the differences in response observed, and essentially show tumours at different stages of progression of necrosis. Given that a decrease in perfusion would lead to an increase in  $R2^*$  it is surprising that no correlation exists between the two parameters, even if there was a small indication of a negative correlation. This is potentially due to the timing of complete vascular shut down within the tumour vasculature and the subsequent consumption of the oxygen within the stopped blood. This highlights the complex vascular pathophysiological changes induced by VDAs and the need for multiple markers of response. It was not possible to exactly correlate the different histological tumour sections with the corresponding MRI data, as differential response was not initially expected, and subsequent liver deformation during tissue processing meant the link between actual tumour and MRI data was lost. In order to address this, in any future repeat of the study the individual solid tumour metastasis would need to be identified on excision during dissection (i.e. which lobe of the liver, position within the liver, etc) and placed in to separate labelled containers. In this manner any changes in tumour perfusion by a reduction in Hoechst 33342 perfusion, reduction in tumour vasculature by CD34 staining, the presence or not of a necrotic core, and any further histological assessment, could be linked back to the MRI data. Therefore responders and non-responders could be identified *ex vivo* and linked to the *in vivo* functional data. Current histology from 24 hours post dose however does indicate that different tumour deposits reacted differently to OXi4503.

#### **6.4.3 Effect of tumour location**

I have also shown within this chapter that tumour deposit location within the liver can affect functional response to dosing with OXi4503. H&E staining showed evidence of



different responses between metastases within the same liver; by categorising the location of tumour deposits within the liver relative to major blood vessels or the periphery, I have shown that for SW1222 tumours the reduction in perfusion was greatest and most consistent in metastases close to large vessels, similar but less consistent in metastases close to smaller vessels, and was smallest in those at the periphery of the liver. With LS174T tumours this categorisation shows that metastases close to large vessels will show an increase in  $R2^*$  whilst those less perfused, i.e. close to smaller vessels or the liver periphery, will not. This suggests that the pharmacokinetics of drug action may be influenced by micro-environmental factors such as tumour perfusion, and that the underlying tumour pathophysiology also has a role to play in determining which functional marker will show a change. This range of responses between metastases, dependent upon location and extent of growth, has been previously observed in the LS174T model, albeit with the use of radiolabelled antibodies (21), further validating this theory.

#### **6.4.4 Further work on hepatic ASL**

Liver metastases are arguably less suited to IS-MRI than subcutaneous tumour models, particularly as shimming of the  $B_0$  field can be challenging due to susceptibility artefacts propagating from surrounding lungs and gut, in addition to respiratory and peristaltic motion artefacts which can be difficult to control. As such, and given the mechanism of action of VDAs, ASL arguably provides a biomarker of therapeutic response that affords a less ambiguous interpretation than IS-MRI. Furthermore, I have shown that ASL can identify a heterogeneous response between tumour deposits within the same liver, and therefore has the potential to highlight those metastases that may respond positively to treatment versus those that will not. It can also identify a patient in which none of the tumours respond to the VDA, thus sparing them from unnecessary treatment. Targeting of different tumour pathophysiologies often requires a combination treatment approach for adequate response, especially with regards to VDAs (22). With optimisation of the combined biomarker approach, however, the two measures could provide a deeper insight into the mechanics of tumour response to therapy *in vivo*, by relating changes in blood flow to those in blood oxygen saturation.

A limitation of this study was the use of a single-slice acquisition for the arterial spin labelling sequence. This meant that only partial coverage of the liver was possible, and hence a number of metastases were omitted from analysis. Since this study was completed, a multi-slice adaption of the Look-Locker FAIR ASL sequence has been developed (23). Utilising the vessel-selective pseudo-continuous ASL sequences (24) could

also provide a direct method for separating the arterial and venous contributions to the liver blood supply, from which response biomarkers such as the hepatic perfusion index, a measure of the relative contribution of the two supplies in individual metastases, could be evaluated to further probe tumour pathophysiology (25).

## 6.5 References

- (1) Tseng W, Leong X, Engleman E. Orthotopic mouse model of colorectal cancer. *J Vis Exp* 2007;484.
- (2) Cunha L, Horvath I, Ferreira S, Lemos J, Costa P, Vieira D, et al. Preclinical imaging: an essential ally in modern biosciences. *Mol Diagn Ther* 2014;18:153-73.
- (3) Segal NH, Saltz LB. Evolving treatment of advanced colon cancer. *Annu Rev Med* 2009;60:207-19.
- (4) Macedo FI, Makarawo T. Colorectal hepatic metastasis: Evolving therapies. *World J Hepatol* 2014;6:453-63.
- (5) Tong Y, Yang W, Koeffler HP. Mouse models of colorectal cancer. *Chin J Cancer* 2011;30:450-62.
- (6) Heijstek MW, Kranenburg O, Borel Rinkes IH. Mouse models of colorectal cancer and liver metastases. *Dig Surg* 2005;22:16-25.
- (7) Lee WY, Hong HK, Ham SK, Kim CI, Cho YB. Comparison of colorectal cancer in differentially established liver metastasis models. *Anticancer Res* 2014;34:3321-8.
- (8) O'Neill K, Lyons SK, Gallagher WM, Curran KM, Byrne AT. Bioluminescent imaging: a critical tool in pre-clinical oncology research. *J Pathol* 2010;220:317-27.
- (9) Baker M. Whole-animal imaging: The whole picture. *Nature* 2010;463:977-80.
- (10) Contag CH, Ross BD. It's not just about anatomy: in vivo bioluminescence imaging as an eyepiece into biology. *J Magn Reson Imaging* 2002;16:378-87.
- (11) Sato A, Klaunberg B, Tolwani R. In vivo bioluminescence imaging. *Comp Med* 2004;54:631-4.
- (12) Fraga H. Firefly luminescence: a historical perspective and recent developments. *Photochem Photobiol Sci* 2008;7:146-58.
- (13) Close DM, Xu T, Sayler GS, Ripp S. In vivo bioluminescent imaging (BLI): noninvasive visualization and interrogation of biological processes in living animals. *Sensors (Basel)* 2011;11:180-206.
- (14) Zabala M, Alzuguren P, Benavides C, Crettaz J, Gonzalez-Aseguinolaza G, Ortiz de SC, et al. Evaluation of bioluminescent imaging for noninvasive monitoring of colorectal cancer progression in the liver and its response to immunogene therapy. *Mol Cancer* 2009;8:2.
- (15) Rajendran S, Salwa S, Gao X, Tabirca S, O'Hanlon D, O'Sullivan GC, et al. Murine bioluminescent hepatic tumour model. *J Vis Exp* 2010.
- (16) Zhao D, Richer E, Antich PP, Mason RP. Antivascular effects of combretastatin A4 phosphate in breast cancer xenograft assessed using dynamic bioluminescence imaging and confirmed by MRI. *FASEB J* 2008;22:2445-51.

- (17) Malcontenti-Wilson C, Chan L, Nikfarjam M, Muralidharan V, Christophi C. Vascular targeting agent Oxi4503 inhibits tumor growth in a colorectal liver metastases model. *J Gastroenterol Hepatol* 2008;23:e96-e104.
- (18) Siemann DW. The unique characteristics of tumor vasculature and preclinical evidence for its selective disruption by Tumor-Vascular Disrupting Agents. *Cancer Treat Rev* 2011;37:63-74.
- (19) El-Emir E, Boxer GM, Petrie IA, Boden RW, Dearling JL, Begent RH, et al. Tumour parameters affected by combretastatin A-4 phosphate therapy in a human colorectal xenograft model in nude mice. *Eur J Cancer* 2005;41:799-806.
- (20) Robinson SP, Kalber TL, Howe FA, McIntyre DJ, Griffiths JR, Blakey DC, et al. Acute tumor response to ZD6126 assessed by intrinsic susceptibility magnetic resonance imaging. *Neoplasia* 2005;7:466-74.
- (21) Dearling JL, Flynn AA, Qureshi U, Whiting S, Boxer GM, Green A, et al. Localization of radiolabeled anti-CEA antibody in subcutaneous and intrahepatic colorectal xenografts: influence of tumor size and location within host organ on antibody uptake. *Nucl Med Biol* 2009;36:883-94.
- (22) Pedley RB, El-Emir E, Flynn AA, Boxer GM, Dearling J, Raleigh JA, et al. Synergy between vascular targeting agents and antibody-directed therapy. *Int J Radiat Oncol Biol Phys* 2002;54:1524-31.
- (23) Campbell-Washburn AE, Zhang H, Siow BM, Price AN, Lythgoe MF, Ordidge RJ, et al. Multislice cardiac arterial spin labeling using improved myocardial perfusion quantification with simultaneously measured blood pool input function. *Magn Reson Med* 2013;70:1125-36.
- (24) Dai W, Garcia D, de BC, Alsop DC. Continuous flow-driven inversion for arterial spin labeling using pulsed radio frequency and gradient fields. *Magn Reson Med* 2008;60:1488-97.
- (25) Cuenod C, Leconte I, Siauve N, Resten A, Dromain C, Poulet B, et al. Early changes in liver perfusion caused by occult metastases in rats: detection with quantitative CT. *Radiology* 2001;218:556-61.

# Chapter 7 Conclusion

---

## 7.1 Vascular anatomy with photoacoustic tomography

The vascular anatomy and pathophysiology of tumours is of great importance for growth, metastatic spread and overall malignancy of cancer. As such, it has emerged as an area of cancer research that promises significant advances for treatment and survival of patients, with targeted therapy to tumour vasculature becoming ever more widespread and sophisticated. An understanding of the biology of this abnormal pathophysiological vascular state of tumours is required to fully appreciate the interaction of the tumour vasculature with its surrounding microenvironment, and to optimise therapies. In this thesis I have shown that the novel imaging modality of photoacoustic tomography can be used *in vivo* to accurately depict the localisation of haemoglobin within tumours, which corresponds to the location of the tumour blood vessels, and allows high resolution imaging of tumour vasculature in a non-invasive and non-ionising way. This is based on inherent measures of tissue haemoglobin, and is therefore possible without the use of exogenous contrast agents. By being able to clearly demonstrate the differences between two models of CRC, I have shown that this technique should be applicable to all types of solid tumours. I was able to show different vascular pathophysiologies *in vivo*, demonstrating that PAT is capable of detecting different levels of vascular abnormality. This has potential implications for accurately staging solid tumours, and following their growth and local tissue invasion, impacting on patient treatment strategies. What is more, the effect of angiogenic signalling was also observed in the surrounding tissue microenvironment by longitudinal PAT studies, as normal skin vasculature was modified into corkscrew tumour feeding vessels, and the normal tissue blood vessels were co-opted into the tumour. This ability to image baseline levels of vascularisation and degree of abnormality should have a great impact on understanding the adaptation of tumour vasculature in patients over time. The ability to image levels of oxygenation in tumours is another advantage to PAT imaging, and was demonstrated in this thesis in a qualitative manner. I have also been able to demonstrate the effects of vascular-targeted therapies on tumour blood vessels over time by PAT, using the VDA OXi4503, which has important implications for translation into improved clinical strategies. The effect of vascular disruption was clearly noted, with a difference in response between different vascular architectures also noticed, further highlighting the potential of PAT to assess inherent

degree of vascularisation and predicted response to treatment. Regrowth of tumour blood vessels over time was observed for the first time, showing an inward growth of vasculature from the surviving rim of tumour cells towards the necrotic tumour core. The ability to monitor the effect of a single treatment shows that PAT can be used as response marker that is capable of determining the need for further therapeutic intervention. Currently the potential clinical utility of PAT remains as a superficial imaging modality, because of a maximum imaging depth of around 1cm, motion artefacts from internal organ (e.g. peristalsis from intestines) and relatively long scan times of around 8 minutes. However, PAT does already have clinical potential, as well as preclinical translational use, in the assessment of melanoma, head & neck, and breast cancers and the system is being further developed for wider use.

### **7.1.1 Future PAT work**

Advancements in PAT system hardware are currently being developed at UCL Medical Physics. This includes smaller, more portable and patient friendly scanner design which would allow PAT imaging in humans, and further work on corroborating the translational research carried out in this thesis. The development of smaller systems also brings up the possibility of endoscopic PAT imaging, which would allow primary colorectal and oesophageal tumours to be investigated. Real-time imaging of blood flow within tissue is also being pursued.. From a basic translational science point of view, future work on imaging vascular targeted therapies other than OXi4503, including anti-angiogenic therapies and their effect on vascular normalisation, would provide important clinical information. . Fully quantitative analysis of acquired data is also urgently needed and is currently under investigation. Further possibilities include the tagging of therapeutics with contrast agents in order to image their biodistribution within the tumour. This may be possible with, for example, a fluorescent marker visible on PAT conjugated to a therapeutic antibody, permitting visualisation of antibody distribution whilst still having the inherent PAT marker of tumour response.

## **7.2 Translation of vascular associated MRI sequences**

Given that the use of PAT imaging is currently restricted to small animal preclinical studies, and that translation to clinical use will take some time to be fully applicable, it was decided to use MRI to assess vascular function. Whilst many MRI sequences exist that can image vascular function, most employ exogenous contrast agents. It was envisaged that vascular

function could be measured by MRI without contrast agents, based on inherent characteristics of the tumours, and that this would be complimentary to PAT imaging. As MRI is a system capable of acquiring whole body scans it was also thought that sequences could be designed that would be applicable to orthotopic models of disease, as this would give greater translational relevance due to the more physiological normal microenvironment. A liver model of orthotopic metastasis was used in this thesis; however one disadvantage of this was the inability to monitor, cheaply and efficiently, the development of the tumour deposits. Luciferase was therefore transduced in to the parental cell lines and shown to have no effect on tumour cell growth kinetics *in vitro* or *in vivo*. This permitted the use of bioluminescence scanning following the injection of luciferin, to observe the growth of the tumour cells within the liver and accurately time the more time consuming and technically challenging MRI experiments. The MRI sequences were first developed in subcutaneous models; the primary measure of tumour perfusion was initially not adequate, as the size of the voxel of interest was limited to the subcutaneous tumours, which was too small, and perfusion too low, to achieve reliable information. In the metastatic model the area of interest was increased to encompass the perfusion measurements from whole liver with subsequent areas of metastatic tumours defined by data segmentation; this, coupled with increased flow within the liver microenvironment allowed adequate measurements of tumour blood perfusion. Measurements of the apparent diffusion of water on the other hand, as an estimate of tumour necrosis, worked for relatively stable areas of interest such as subcutaneous tumours, but suffered from motion artefacts when in the more dynamic environment of the liver. For further studies this could be accounted for by decreasing the acquisition during the gated respiration window, i.e. being stricter on acquisition during respiratory phases. However, the peristaltic motion from the intestines could not be addressed, and the scan time would increase enormously. As this measure of necrosis was not performed to be associated with vascular function, but rather as a measure of the effective response to treatment, this was not considered too detrimental: ADC can be measured in humans, as has already been established. The novel aspect of this research was the application of ASL measurements coupled with  $R2^*$  for the vascular response of tumours. Although  $R2^*$ , measured by intrinsic susceptibility sequences, has been used in a different model and in response to a different agent, this was only over a very acute range. I have shown that  $R2^*$  and ASL can be used as measures in longitudinal studies as well as acute response to treatment, and that they can be used to map values across individual metastasis within the

same subject. This is a novel use of hepatic ASL, especially when in conjunction with  $R2^*$ . As with the PAT imaging studies, response to treatment varied according to the extent of vascular network within the tumour types. This was further demonstrated by the effect of tumour location within livers; given that a varied response was observed between metastases, and that perfusion by ASL appeared to be the more consistent in response from baseline to post-dose, another classification based on tumour blood perfusion was devised. It was assumed that tumours close to large liver blood vessels would have the greatest perfusion, compared to those next to smaller vessels or the periphery of the liver. When classified by these parameters, tumours that were well perfused, such as SW1222 tumours close to large vessels, showed the largest decrease in ASL. In contrast tumour types that were less well perfused to begin with, such as LS174T tumours, demonstrated an increase in the deoxyhaemoglobin within the tumour. For both CRC tumour types, SW1222 and LS174T, areas away from large vessels show less of a response, ostensibly due to decreased blood flow from normal tissue to, and pharmacokinetic action of the drug at, these locations. The response is therefore highly dependent on vascular function of the tumours, and the time at which the ASL or  $R2^*$  parameters are acquired. However I have demonstrated that both can be used to assess vascular function, and are probably best acquired in conjunction in order to fully understand the changes occurring within the tumour vasculature.

### **7.2.1 Future MRI work**

The heterogeneous response to treatment by metastases within the same liver was not expected, and warrants further investigation. Exact labelling of individual tumours would allow histological analysis to accurately corroborate, *ex vivo*, the changes in vascular parameters observed *in vivo*. It is possible that this is also simply a timing issue, with some metastases taking longer for vascular disruption and necrosis to be established. *In vivo* studies over longer consecutive time frames could potentially answer this question; however imaging sessions are limited due to animal experimentation regulations, which would make this study difficult to plan effectively. Since this work was conducted, multiple slice ASL has been developed which allows imaging of the whole liver, dramatically increasing the number of metastasis measureable. For future studies, this would need to be included in the experimental design



### **7.3 Concluding remarks**

One proposed area of research for this thesis was the combination of PAT and MRI imaging modalities. However, once both PAT and MRI sequences had been individually validated, it was not possible to achieve this to any degree of satisfaction. The combined information from PAT and MRI would provide measures of tumour response for structural tumour vascular network and cessation of blood flow, increase in deoxyhaemoglobin, blood vessel occlusion and onset of necrosis by PAT, whilst at the same time providing functional measurements of the vascular component in tumour voxels by MRI. This would have the advantage of simultaneously validating the functional MRI sequences, giving more emphasis to clinical utilisation, while also allowing further development of PAT as a clinical tool. Experiments were planned and performed, but a sufficient number of complete data sets were not obtained due to difficulty in performing these large multimodal experiments. Even with the limited amount of data acquired, co-registration proved difficult without the implantation of fiducial markers within the tissue, which needs to be addressed before future combined studies are performed. This would then prove to be a very powerful tool for assessing vascular targeted therapies, and is therefore planned for future work. However, even when used as individual modalities for assessing vascular function and response to treatment, this work demonstrates that both PAT and MRI vascular sequences are highly effective, with great potential within pre-clinical tumour vascular research, and also for translation into clinical trials.

# I Appendix

---

## I.I Cell growth kinetics

No differences in growth kinetics were noted through cell passages. Time to confluence and subcultivation ratio between the transduced and non-transduced cell lines were the same. Results from cell countess assessment of viability can be seen in **table 6.1** for the SW1222 cell line and **table 6.2** for the LS174T. As seen in these tables the viability of cells for each of the two lines was above 90% at each point evaluated, with average cell size between 9.8µm and 13.1µm.

SW1222	Passage	Viability	Average cell size
Non 1	12	96%	11.1µm
Non 2	18	97%	10.2µm
Non 3	22	92%	10.4µm
Luc 1	7	93%	12.9µm
Luc 2	15	98%	13.1µm
Luc 3	21	97%	10.9µm

**Table I.I** Viability of parental ('Non') and luciferase transduced ('Luc') SW1222 cells at varying passage number

LS174T	Passage	Viability	Average cell size
Non 1	16	96%	11.1µm
Non 2	17	95%	10.3µm
Non 3	19	97%	9.8µm
Luc 1	4	95%	11.0µm
Luc 2	7	97%	11.3µm
Luc 3	13	97%	10.0µm

**Table I.II** Viability of parental ('Non') and luciferase transduced ('Luc') LS174T cells at varying passage number

## I.II Kinetics of luciferase activity

Average photon radiance *in vitro* following addition of luciferin to the cell lines can be seen in **Figure I.I**. As representative images for all time-points within the n=3 experiments for both cell lines, panel **A** and **B** depict the acquired image of SW1222 cells within a petri dish with an overlay of photon emission data both before (**A**) and one minute after (**B**) the addition of luciferin. The first image serves as a baseline with no photon radiance, whilst subsequent images clearly show emission of photons from the centre of the sample. Regions of interest were drawn around the acquired data and quantification of the average photon radiance performed over the 30 minute time course. Graph **C** shows the average of the three experiments performed for the SW1222 *luc* cell line, with error bars denoting standard error of the mean. A peak photon radiance of  $2.5 \times 10^7$  can be observed at around three minutes post luciferin, after which there is a decrease in average radiance to roughly  $1.5 \times 10^7$  at 30 minutes post luciferin. The graph in section **D** shows results for the *in vitro* kinetics of luciferase activity in the LS174T cell line. Average radiance from the n=3 experiments is shown with error bars denoting standard error of the mean. A peak of  $2.5 \times 10^7$  is seen at around three minutes after addition of luciferin with a long steady decrease in radiance up to the 30minute mark, where radiance has dropped to around  $1.5 \times 10^7$ . Therefore results are very similar for the two colorectal cell lines.

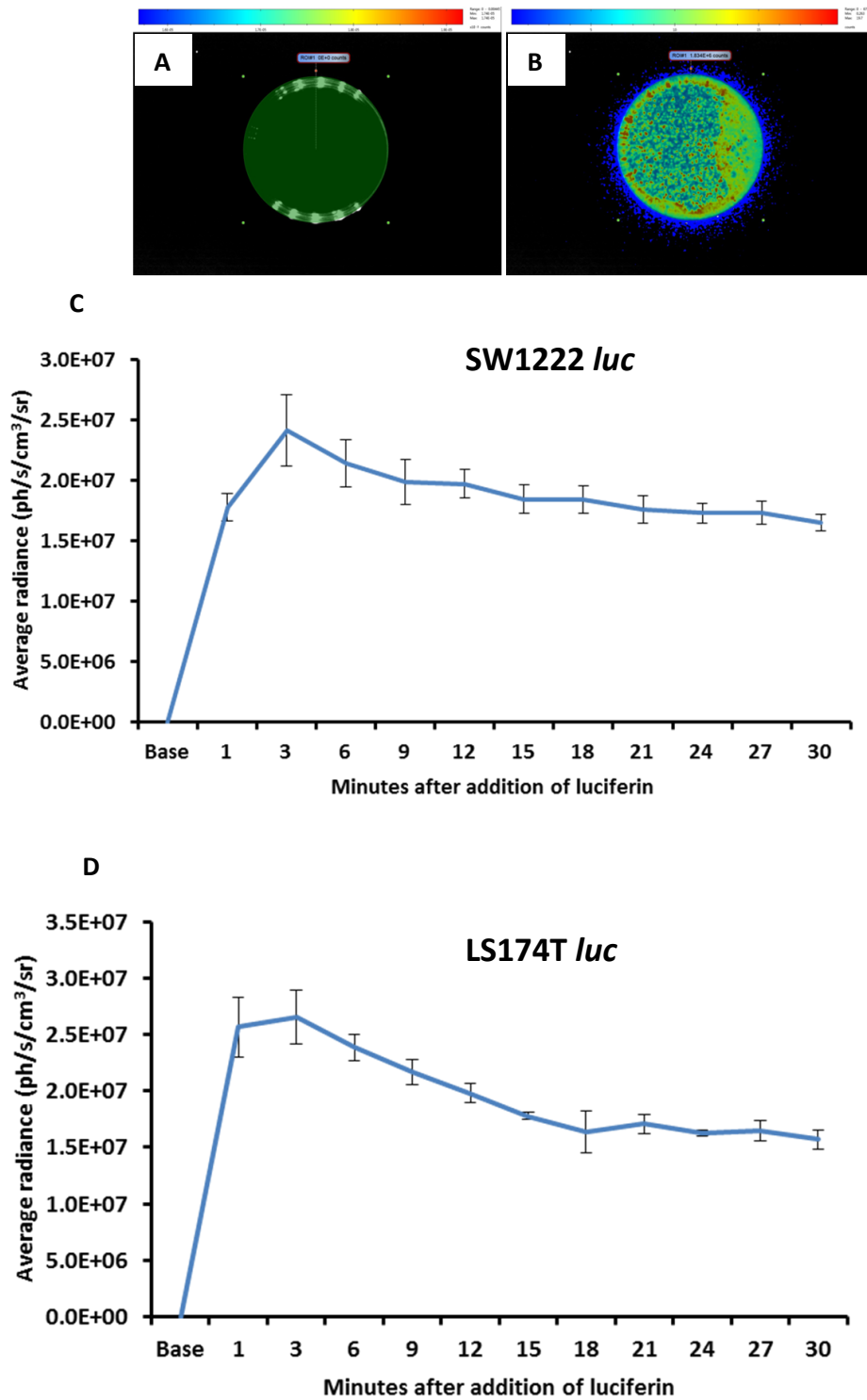


**Figure I.I** *In vitro* kinetics of luciferase activity. **A** shows an example of acquired data for SW1222 cells before addition of luciferin, **B** shows the same sample after addition of luciferin. Graph **C** (SW1222) and **D** (LS174T) show average radiance of cells up to 30min post luciferin with error bars denoting standard error of the mean

### **I.III Luciferase correlation to cell number**

Results from the experiments for correlation of photon radiance and cell number can be found in **Figure I.II**. Panel **A** is a photograph of one of the 96-well plates used, superimposed with the photon data acquired at one minute after luciferin addition, with regions of interest drawn around the triplicate cell concentrations. Both 1 and 5 minute acquisitions showed similar radiance. Cumulative data for the n=3 SW1222 plates can be seen in graph **B**, where a linear trend with an  $R^2$  of 0.98 was found between decreasing cell concentration and average radiance. Error bars denote standard error of the mean. All negative controls show no emission of photons.

For the LS174T cell line a similar pattern can be seen in graph **C**, where the decrease in cell concentration shows a linear correlation with decrease in photon average radiance. The  $R^2$  value for this correlation across the n=3 plates is 0.91. The trend is not as linear as with the SW1222 cell line in graph **B**, with higher concentrations between  $1 \times 10^5$  and  $8 \times 10^4$  showing variability in photon radiance, with a plateau effect observed at these concentrations. Negative controls show no emission of photons.

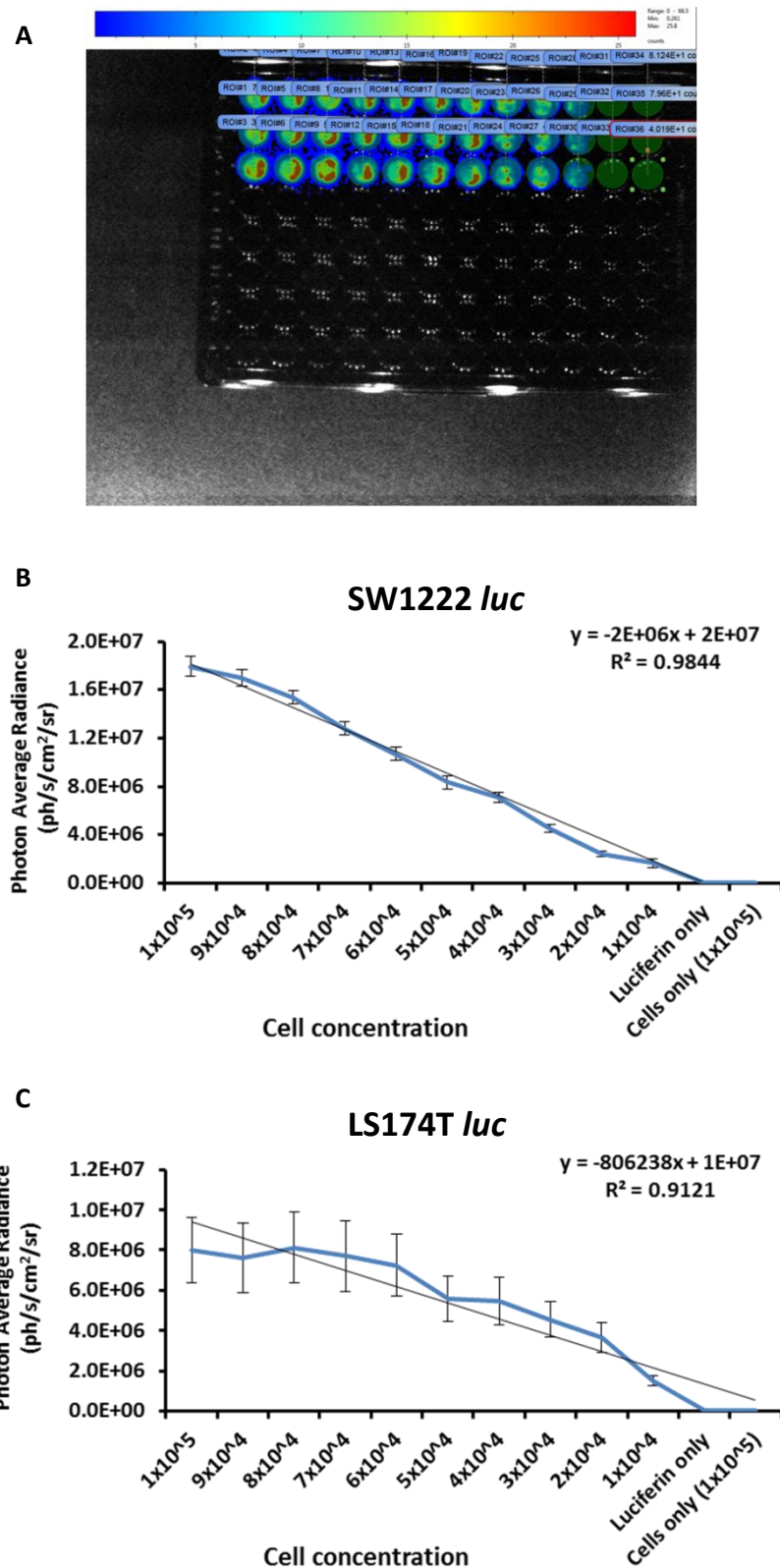


**Figure I.II** *In vitro* correlation between cell number and luciferase activity. **A** shows an example of acquired data for SW1222 with ROIs drawn around all concentrations. **B** shows cumulative photon radiance data for SW1222 cells, with graph **C** cumulative data for LS174T cells. Error bars denote show standard error

## I.IV Lower limit of luciferase detection

**Figure I.III** shows results for the lower limit of detection experiment for the SW1222 cell line. Panel **A** is an example of one of the  $n=3$  plates at 1 minute after addition of luciferin with overlaid photon radiance data acquired. Both the 1 and 5 minute time points showed similar results for cell number detection with no significant difference in average photon radiance. Panel **B** shows the average photon radiance of the  $n=3$  experiments in triplicate for a total of  $n=9$  sample concentrations for the SW1222 cell line. Error bars denote standard error of the mean. This bar graph shows that bioluminescence can be detected from as little as  $\approx 300$  cells, with concentrations below this being similar to negative controls.

The data for the LS174T cell line can be seen in panel **C**, which again shows cumulative quantification data for the bioluminescent signal from the different cell concentrations. This shows a slightly reduced sensitivity when compared to the SW1222 cell line, with the highest concentration of 10,000 cells giving an average radiance of  $\approx 7 \times 10^5$  ph/s/cm<sup>2</sup>/st compared to  $\approx 1.8$  ph/s/cm<sup>2</sup>/st for the SW1222 cell line (**Panel B**), however the lower limit of detection is still in the region of 300-600 cells.

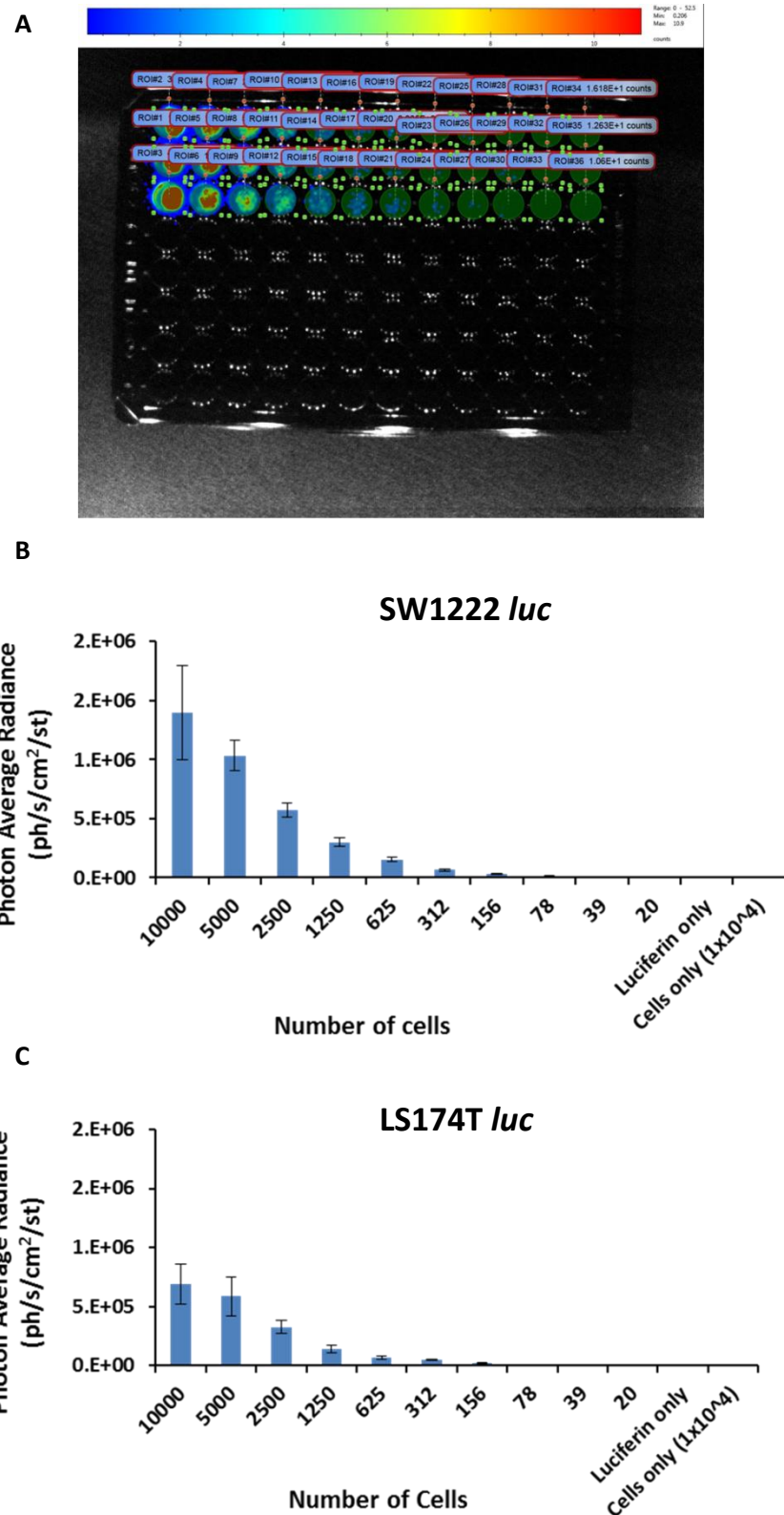


**Figure I.III** *In vitro* lower limits of cell detection. **A** shows an example of acquired data for SW1222 with ROIs drawn around all concentrations. **B** shows cumulative photon radiance data for SW1222 cells, with graph **C** cumulative data for LS174T cells. Error bars denote show standard error



## I.V Subcutaneous growth comparison

**Figure I.IV** shows *in vivo* subcutaneous tumour growth data from the luciferase transduced cell lines. Non-transduced cell lines showed no bioluminescence activity and are therefore not shown. **Panel A** (SW1222) and **C** (LS174T) show acquired data for the three mice expressing the luciferase gene, with the overlay of photon data clearly showing that the photon expression is only observed at the site of subcutaneous tumour formation. Graphs **B** (SW1222) and **C** (LS174T) show the kinetics of photon average radiance following i.p. injection of the substrate luciferin. Both graphs show a peak bioluminescence signal at 15 minutes post injection with a subsequent drop off in activity up to the 30 minute time point.

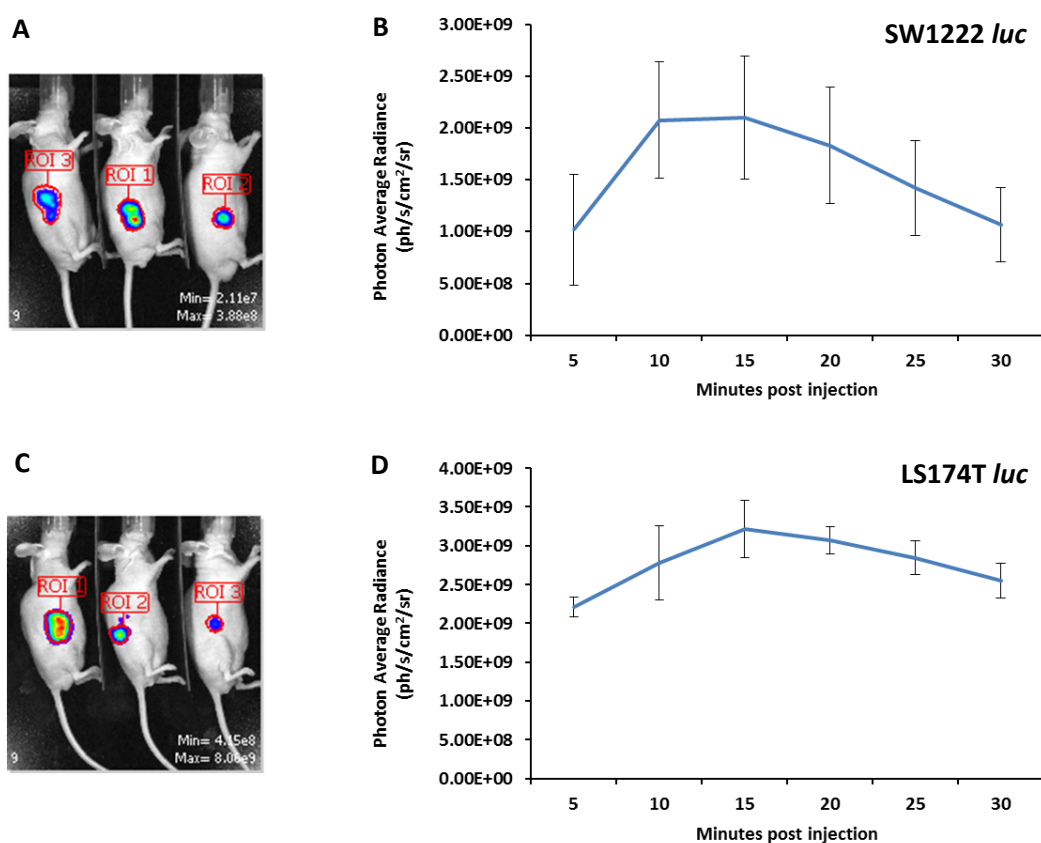


**Figure I.IV** *In vivo* subcutaneous average photon radiance. Panels **A** (SW1222) and **C** (LS174T) show examples of acquired data with ROIs drawn around areas of photon emission, correspondent with the site of solid tumour growth. Graphs **B** and **D** show average photon radiance post i.p. injection of luciferin up to 30 minutes post dose. Error bars denote show standard error of the mean.

**Figure I.V** shows the comparison between tumour progression over time as assessed by caliper measurement. Graph **A** represents the SW1222 cell line and graph **B** the LS174T cell line, with luciferase transduced cells shown in red and the non-transduced shown in blue. A similar rate of tumour growth is observed between transduced and non-transduced cells for both tumour types, with students T-Test showing no significant differences between groups.

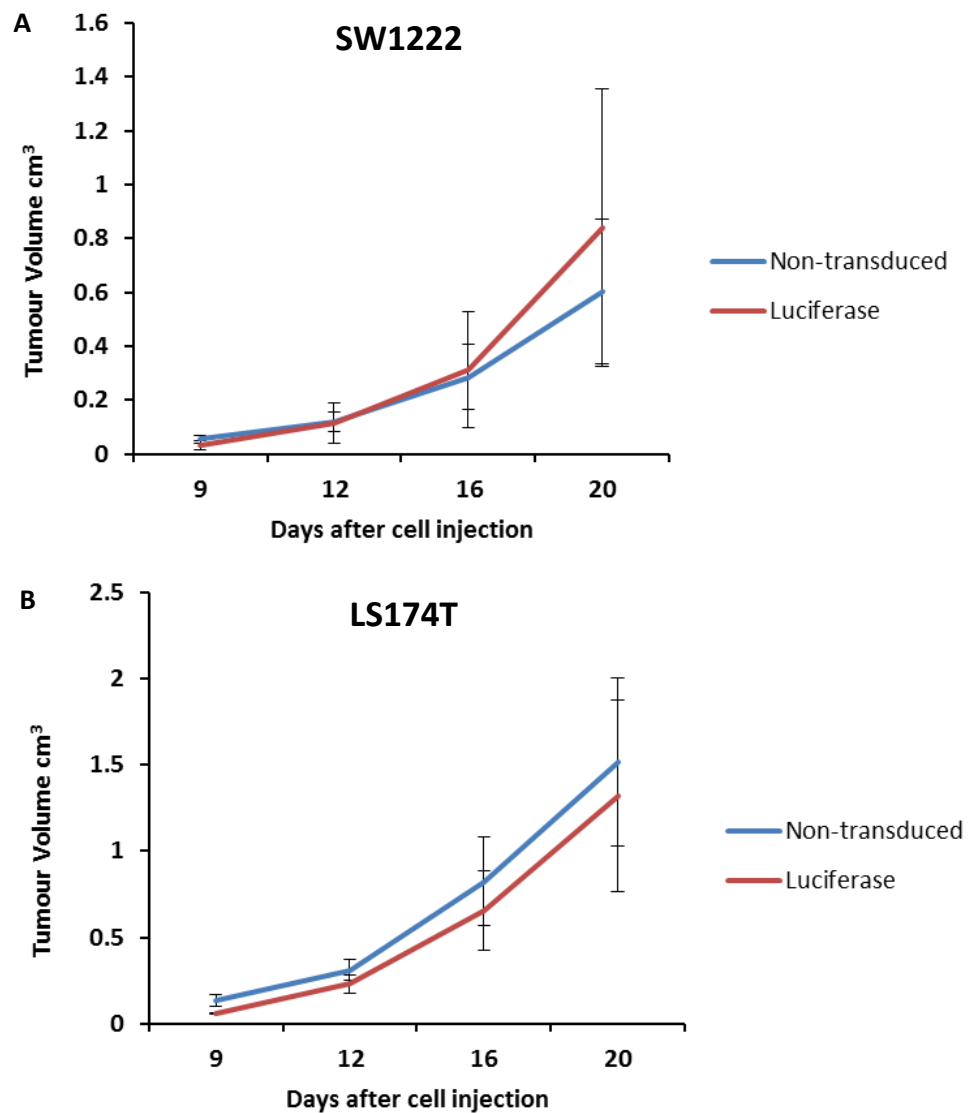


**Figure I.V** *In vivo* growth comparison. Caliper measurements of subcutaneous tumour growth comparing non-transduced (blue) and luciferase transduced (red) SW1222 (Graph **A**) and LS174T (Graph **B**) cell lines

**Figure I.VI** compares the average photon radiance emitted by the growing tumours versus the volume increase over time, with tumour volume in red and bioluminescence count in blue. Graph **A** depicts SW1222 *luc* tumours whilst graph **B** depicts LS174T *luc* tumours. Bioluminescence is able, in both tumour types, to detect tumour cells at day 2 post cell injection. By contrast, accurate measurement by calipers is only possible 7 day later, at day 9 post cell injection. Whilst there is a general trend between increasing tumour volume and increased generation of photons, there is no clear correlation between the two, with scatter plots of the two values showing no association. The higher number of cells present in a larger tumour does relate to an increased photon count, but exact estimation of tumour size based on photon radiance is not possible with the data generated.

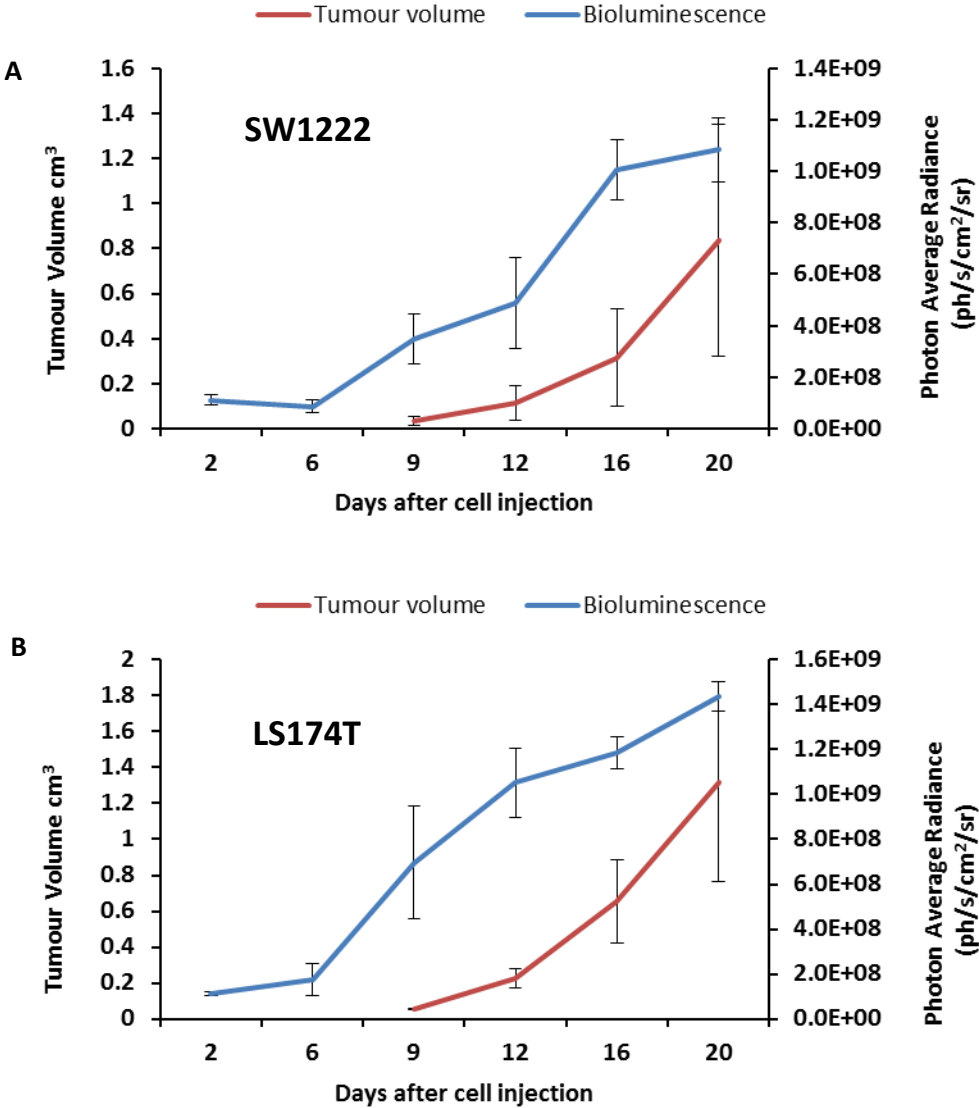


**Figure I.VI** *In vivo* growth comparison vs bioluminescence. Caliper measurements of subcutaneous tumour growth comparing non-transduced (blue) and luciferase transduced (red) SW1222 (Graph **A**) and LS174T (Graph **B**) cell lines